METAL REFINING REACTIONS IN RISING BUBBLES

A thesis presented for the degree of

Doctor of Philosophy

by

AMBROSE CHIKA EBIOGWU

John Percy Research Group

Department of Metallurgy and Materials Science

Imperial College of Science & Technology

London, SW7

October 1984

ABSTRACT

The behaviour of a third phase carried by a gas bubble rising in a liquid bath has been investigated using the 'Open Top Bubble' (OTB) technique. This technique simulates the spherical-cap bubble in a stationary frame of reference with the top of the bubble open, thus providing a direct visual access to the bubble base.

Using the water model of the OTB apparatus, the spreading and stripping characteristics of some liquids added to the bubble were studied. It was observed that the stripping of these reagents from the bubble base was dependent on their viscosity and spreading coefficient.

High temperature experiments were done using the open top bubble system in molten lead to produce a slag phase by gas-metal reaction. Injection of oxygen gas on to the lead resulted in the formation of PbO and the suppression of the ripples at the base of the bubble. The PbO dissolved and the oxygen activity in the lead bath was monitored by a gas reference solid electrolyte oxygen cell and consequently the oxygen solubility in lead was measured. The dissolution of molecular oxygen by the reaction $\frac{1}{2}O_{2(g)} = [O]$ (wt % in lead) was described by the standard free energy change ΔG^{o}, $J = -60693 - 21.88T$ ($450°C < T < 610°C$) the standard state being weight per cent [O] at infinite dilution. An analysis was also done for oxygen in the outlet gas using a suitable solid electrolyte cell. Both oxygen probes provided useful kinetic information on the reactions occurring in the system.

The high temperature system was also used to study the spreading and stripping characteristics of caustic soda-based slags in molten lead. Pure sodium hydroxide slags were observed to strip very slowly but not spread, whereas slags containing sodium nitrate did spread. Impurity antimony and tin were later added to the lead and the reactions of these impurities with caustic soda/sodium nitrate slags, as in the Harris process, were investigated. The reactive slags displayed some interesting spreading features.

The final stage of this work was centred on a design for the open top bubble in molten iron, using a graphite apparatus. This new system has considerable design advantages over the existing unit built in mild steel and would be invaluable in the study of steel refining reactions.

TABLE OF CONTENTS

LIST OF FIGURES

LIST OF TABLES

LIST OF SYMBOLS

A	Area
a	Activity (Raoultian)
C	Concentration (moles/cm^3)
Ca	Capillary number (= $\mu u/\Delta\sigma$)
d	Diameter
d_e	Diameter of volume equivalent sphere (= $(6V/\pi)^{1/3}$)
d_t	Column diameter
E	Electromotive force (volts)
Eo	Eotvos number (= $\Delta\rho g d^2/\sigma$)
F	Faradays constant (joules/volt)
Fr	Froude number
f	Activity coefficient (Henrian)
ΔG	Gibbs free energy change (joules/mol)
g	Gravitational acceleration
(g)	Gas phase
h	Activity (Henrian)
h_b	Bubble base depth
h_w	Bubble weir height
K	Equilibrium constant
k	Mass transfer coefficient (cm/sec)
(ℓ)	Liquid phase
M	Morton number [= $g\mu^4/(\rho\sigma^3)$]
N	Molar transport rate (moles/cm^2.sec)
P	Pressure (atm.)
R	Gas constant
Re	Reynolds number (=$\rho ud/\mu$)
(s)	Solid phase
T	Temperature

t	Time
u	Velocity
u_b	Bubble velocity
u_w	Bubble velocity in the vicinity of a wall
V	Volume
We	Weber number ($= \rho u^2 d/\sigma$)
wt %	Weight per cent
x	Mole fraction
μ	Viscosity
ρ	Density
$\Delta\rho$	Density difference
σ	Surface tension
$\Delta\sigma$	Surface tension difference
γ	Interfacial tension
θ_m	Maximum subtended angle
φ	Spreading coefficient
Δ	Flotation coefficient
β	Angular extent of spreading
τ	Shear stress

Subscripts

i	Interface
g	Gas
ℓ	Liquid
M	Metal
MO	Metal oxide
max	Maximum
min	Minimum
O	Oxygen
o	Initial

ox	Oxide
r	Ripple-return
s	Solid
sat	Saturation

Superscripts

b	Bulk
i	Interface

ACKNOWLEDGEMENTS

I wish to express my sincere thanks to Dr. Dave Robertson for his guidance as my supervisor, and for his support and contributions towards this project.

Thanks are also due to the following:

Prof. Jim Jeffes, for his useful discussions on this work.

Mr. Alec Neve and Mr. Alan Willis, for their technical advice and assistance in the running of the high temperature rig.

Miss Pam Martins and Mr. Jim Rossdale, for their advice on photography; and the entire staff of the Metallurgy Workshop for their help on many occasions.

Special thanks go to my parents Mr. and Mrs. A.O. Ebiogwu for their financial support and encouragement throughout the entire course.

The financial support of an Overseas Research Students Award for the 1983/84 academic session and a grant in aid from the British Steel Corporation, Teesside Laboratories are also gratefully acknowledged.

CHAPTER 1

INTRODUCTION

In many pyrometallurgical processes gases are injected beneath the liquid metal surface. The gases may be chemical reagents in their own right, as in the case of oxygen injection into molten iron to remove dissolved carbon as CO. Alternatively, the gas may be used simply as a carrier for a powdered reagent. An example is the injection of $CaO-CaF_2$ flux, using an argon carrier gas, to remove sulphur from molten iron. The gas bubbles also stir the liquid phases as they rise through them, thus generally preventing the establishment of concentration gradients within the bulk phases.

From a process engineering point of view it is obviously essential to understand the details of the fluid flow and the heat and mass transfer between the phases liquid metal, gas bubbles and slag.

1.1 GAS-METAL-SLAG REACTIONS

A feature of gas-metal reactions is that a slag film may be formed at the gas-metal interface. Such slag film formation has been studied by a number of investigators[1-8], and using various techniques.

Robertson and Jenkins[1] reacted drops of iron, iron-carbon, iron-silicon and iron-carbon-silicon alloys with pure oxygen gas using the levitation technique. The rapid formation of the slag film was recorded with a high speed camera and the reaction temeprature followed by a two-colour pyrometer. With pure iron, an oxide film spread rapidly across the drop within 3 m-sec producing an increase in specimen brightness due to the higher emissivity of the oxide layer. In iron-carbon alloys, near carbon saturation, the rate of diffusion of carbon to the gas-metal interface was sufficient to avoid the formation of iron oxide. The temperature rose smoothly during the decarburization process and later on, carbon boil started, increasing in intensity as the reaction progressed. Vigorous surface turbulence was also noted, with velocities reaching 2 m/sec. The iron-silicon alloys showed two different types of behaviour termed 'passive' and 'burning'. Passive behaviour was observed with high silicon alloys when a layer of impervious slag was formed which inhibited

further gas-metal reaction. At lower silicon levels the reaction was similar to that of pure iron and the temperature rose rapidly. An interesting feature of the burning reaction of iron-silicon alloys was that iron oxide formed in islands on the drop surface between the impervious silica layers. Iron-carbon-silicon drops initially behaved similarly to the iron-silicon alloys but later a violent reaction started which was caused by carbon boil and the ejection of drops from the melt.

Rao[2] also used the levitation technique in his study of the reactions of iron-carbon-chromium alloys in oxygen-argon gas mixtures, as is found in AOD stainless steel making.

The levitation technique is, however, not quite representative of the oxidation of a liquid metal by a bubble of oxidizing gas. The ratio of oxidizing gas to metal is greater for the levitated drop if the oxidizing gas is continuously passed over the surface and as such the extent of oxidation is much larger. Also the large temperature changes observed with levitated drops will not occur in a bubble since a bubble is surrounded by a much larger mass of liquid metal.

The 'absorption' of gaseous oxygen by pure liquid iron was studied by Emi and co-workers[3]. The vessel containing molten iron was initially evacuated and oxygen from a second chamber was allowed to react with the iron. The reaction rates were followed by pressure measurements. They found that the reaction proceeded in two stages:

(i) the oxygen gas reacted rapidly initially to form a thin oxide phase;
(ii) the rate of oxygen consumption decreased markedly once the oxide layer had thickened and become visible as a third phase.

The amount of oxide present at any given time was thus the result of two competing processes,viz: the growth of the oxide film and the simultaneous dissolution of oxygen in the melt. The rate of growth of the oxide film was found to be controlled by the rate of dissociation of oxygen gas into adsorbed atoms which were subsequently incorporated in the oxide.

Emi and Pehlke [4] used the same techniques to study oxygen absorption by iron-silicon and iron-aluminium alloys. Their results remained the same for alloys with less than 3% Si and 6% Aℓ. Above these levels the oxidation rate decreased considerably as soon as an oxide layer rich in silica (or alumina) had formed, the rate being controlled by ionic diffusion in the oxide layer.

Additional experimental evidence for the rapid spreading of the slag after the addition of oxygen has been obtained by Brimacombe[5]. He injected oxygen onto liquid tin, copper and iron and observed that a ring of oxide moved radially outwards from the position when the jet impinged onto the surface. The spreading occurred because the higher oxygen concentration lowered the surface tension of the metal.

Barton and Brimacombe[6] observed the effect of adding solid Cu_2S to the surface of a quiescent bath of molten copper. There was a spreading away of the molten sulphide from the solid, and the formation of ripples and waves. Sulphur is surface active in molten copper and strongly reduces the surface tension of copper.

Barton and Brimacombe[8] measured mass transfer rates to molten copper from a gas jet. They observed that the condition necessary for rapid spreading was oxygen starvation and this limited the area of oxide formation on the bath. They measured the mass transfer coefficients for oxygen in copper under spreading conditions which was some thirty six times the value for oxygen in silver. The difference was attributed to the effect of rapid spreading and interfacial turbulence.

1.2 BUBBLE HYDRODYNAMICS

Bubble phenomena are a frequently recurring research subject in the Chemical Engineering literature. The literature covers such fundamental aspects as bubble formation, bubble motion, mass transfer and liquid motion induced by bubbles.

1.2.1 Basic theory of bubble rise

The behaviour of a bubble which rises in an infinite extended and uncontaminated liquid can be characterized by its shape, its terminal velocity and its rising path, all of which must be considered simultaneously.

Three main types of bubble shapes are observed in liquids: spherical, ellipsoidal (or spheroidal) and spherical-cap. The shape a bubble assumes depends on the stresses or forces acting on the bubble surface, viz:

- the viscous stress ~ $\mu u_b/d_e$
- the inertia stress ~ $\rho_\ell u_b^2$
- the buoyancy force ~ $\Delta\rho g d_e^3$
- the surface/interfacial stress ~ σ/d_e

where u_b is the rise velocity of the bubble, $\Delta\rho$ is the liquid-gas density difference, μ and ρ_ℓ are respectively the viscosity and density of the liquid, σ is the surface tension, d_e is the diameter of volume-equivalent sphere.

The ratios between the different contributions are commonly expressed in terms of dimensionless numbers, some of which are:

$$\text{Reynolds number, Re} = \frac{\text{Inertial forces}}{\text{Viscous forces}} = \frac{\rho_\ell u_b d_e}{\mu}$$

$$\text{Eotvos number, Eo} = \frac{\text{Buoyancy forces}}{\text{Surface tension forces}} = \frac{\Delta\rho g d_e^2}{\sigma}$$

$$\text{Froude number, Fr} = \frac{\text{Inertial forces}}{\text{Buoyancy forces}} = \frac{u_b^2}{g d_e}$$

$$\text{Weber number, We} = \frac{\text{Inertial forces}}{\text{Surface tension forces}} = \frac{\rho_\ell u_b^2 d_e}{\sigma}$$

$$\text{Morton number, M} = \frac{We^3}{Fr.Re^4} = \frac{g\mu^4}{\rho\sigma^3}$$

The Morton number depends primarily on the viscosity/surface tension ratio of the liquid; M varies from very high values of about 10^6 for fluids like syrup through 10^{-2} for viscous fluids like mineral oil to about 10^{-10} for inviscid liquids like water and alcohols.

Grace[12] has given a generalized plot of Re vs Eo for Morton numbers in the range 10^{-14} to 10^8 (see fig. 1-1) from which it is possible to predict the shape and velocity of any size bubble in a Newtonian liquid, given the liquid properties. When surface tension forces dominate, the bubble surface area is as small as possible and the bubbles are spherical in shape. For large bubble sizes, the buoyancy forces become larger while the interfacial forces decrease, resulting in the flattening of the bubble; the final shape is then determined by the equilibrium between interfacial tension, the inertial and the buoyancy forces. Hence we have the ellipsoidal shape. For very large bubble volumes the interfacial tension forces become less significant and the bubble shape is fully determined by the ratio between the inertial and buoyancy forces. The bubble assumes a spherical-cap shape.

The boundary between the ellipsoidal and the spherical shape is arbitrary; only semi-empirical criteria are available, e.g. Grace[12] used the criterion

$$\frac{\text{minor axis}}{\text{major axis}} = 0.9$$

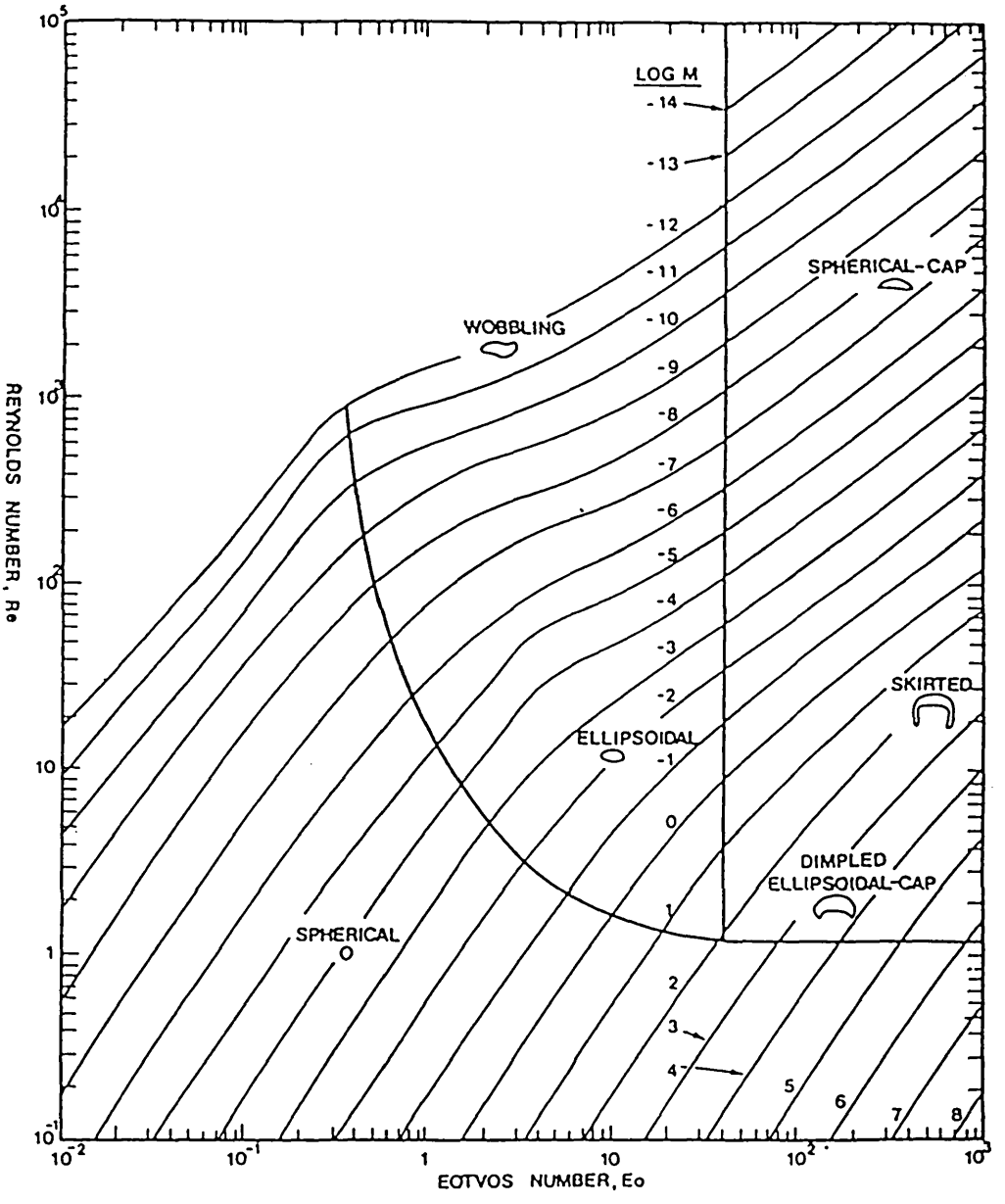

Fig. 1-1: Shape regimes for bubbles and drops in unhindered gravitational motion through liquids.

(After Grace[12])

A spherical-cap bubble has a nearly spherical upper surface and a lower surface fluctuating about a horizontal plane. The bubble geometry is fully determined by the frontal radius of curvature R, and the maximum subtended angle ϑ_m (see fig. 1-2), and related to the bubble volume V_b by

$$V_b = \pi R^2[2/3 - \cos \vartheta_m + (1/3)(\cos \vartheta_m)^3]$$

In liquids of low viscosities, spherical-cap bubbles develop an irregular or wobbling shape, the upper surface being rippled and the bottom indented a little upwards. At viscosities $\mu > 200$ cp they develop a skirt - a very thin gas sheet trailing behind the cap. These skirts have been discussed by Davenport, Richardson and Bradshaw[13]. In their study of the stability of gas envelopes trailed behind large spherical-cap bubbles rising through viscous liquids, Guthrie and Bradshaw[14] deduced that surface tension forces are likely to play an important part in skirt formation.

The spherical-cap bubble can be held with an open bottom as was used by Filla et al[15], and with an open top as shown by Conochie[16]; a technique also used in this work.

Spherical-cap bubbles rise with terminal velocities proportional to the square root of the bubble diameter. Davies and Taylor[11] confirmed this by a fluid dynamic analysis assuming that the upper surface of the bubble was perfectly spherical and that the flow around the bubble could be described as a potential flow. They further assumed that the pressure within the bubble is constant everywhere and that interfacial tension did not affect the bubble behaviour and arrived at the relationship:

$$u_b = (2/3)\ (g.R)^{\frac{1}{2}} \quad \text{for small } \vartheta_m$$

Experimental results have been found to be in good agreement with this result for ϑ_m values up to 50° (about the opening angle of a spherical-cap bubble) and Re > 40.

After Davies and Taylor many investigators[17-20] have tried to give an even better theoretical explanation of the hydrodynamic behaviour of spherical-cap bubbles. Most of the results fit experimental data as well as those of Davies and Taylor; Collins[17] calculated a rise velocity given by the

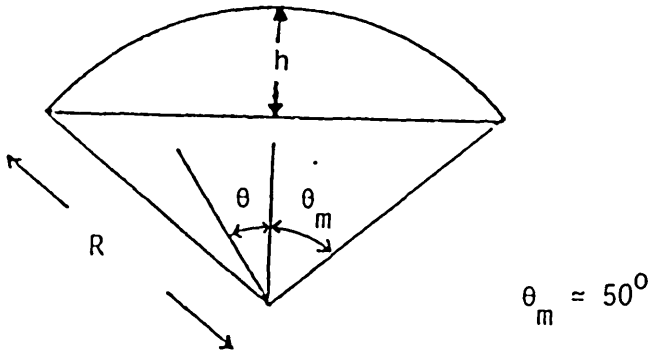

Fig. 1-2: The spherical-cap bubble

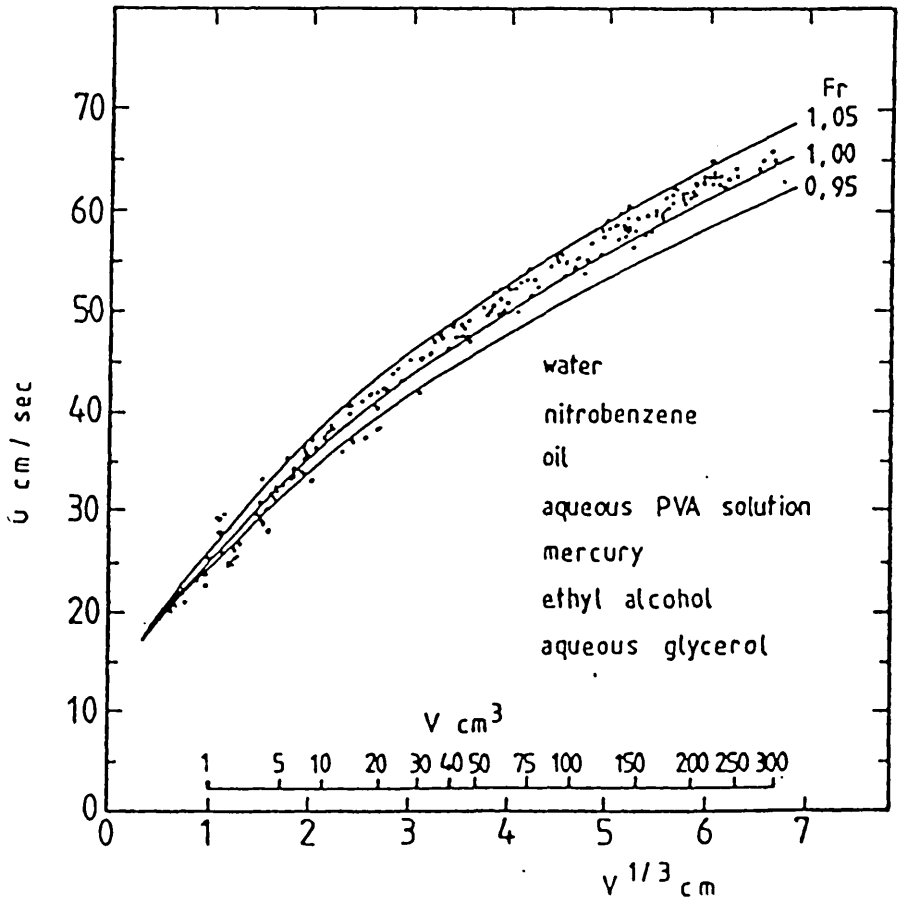

Fig. 1-3: Rise speed of spherical-cap bubbles in different liquids.

(After Wegener and Parlange[18])

relationship:

$$u_b = 0.645\ (g.R)^{\frac{1}{2}}$$

The importance of wall effects was highlighted in the works of Haberman and Morton[19] and later confirmed by Uno and Kinter[20], who developed a relationship considering wall effects:

$$u_w/u = 1.094\ (1 - (d_e/d_t))^{0.765}$$

where u_w is the bubble velocity in the presence of a wall, u is the velocity in an infinite medium and d_t is the column diameter. This relationship is in good agreement with experiment.

1.2.2 Wake phenomena

For a complete description of the bubble hydrodynamics information is needed to discuss the flow behind the bubble. For clean spherical bubbles there will be flow in the bubble surface all the way round. However, for ellipsoidal and spherical-cap bubbles, the flow will not behave this way but will separate at a certain distance from the top of the bubble; the exact position of separation being dependent on the bubble shape. In the spherical-cap bubble this separation occurs at the bubble rim. The fluid region between the streamlines at the point of separation and the bubble rear surface is called the wake. If the streamlines meet again the wake is said to be closed, if not it is open. The wake behind spherical-cap bubbles is closed for Re < 110. For Re > 110 in skirtless bubbles, the wake is open and turbulent.

For spherical-cap bubbles rising in nitro-benzene, Davies and Taylor[11] showed flash photographs of a turbulent region behind the bubble whose margin appears as a continuation of the bubble curvature. No details of the flow pattern were visible but they believed the wake was enveloped by a potential flow.

Slaughter and Wraith[21] observed the wake to consist of a toroidal vortex moving with the bubble, and a streaming cyclindrical tail extending along the rise path. The vortex part of this wake is spheroidal and compares with the observation

of Davies and Taylor while the tail part corresponds to the downstream disturbance discussed by Maxworthy[22].

Coppus[23] studied wake properties of spherical-cap gas bubbles rising in water and water-glycerine solutions using tracer photography and described qualitatively the wake structures in the laminar, transitional and turbulent flow regimes. In the laminar flow regime, the wake consists essentially of a toroidal vortex. In the transitional flow regime, vortex rings and highly turbulent zones change into each other while vortex shedding hardly occurs. In the turbulent flow regime, vortices are shed at regular time intervals to form a vortex street.

1.2.3 Metallurgical bubbles

In this work attention is generally focussed on bubbles greater than 5 cm^3 in volume.

Large bubbles in liquid metals are spherical-cap in shape and behave in much the same way as similar bubbles in other liquids. Paneni and Davenport[24] studied 'two-dimensional' bubbles in water and mercury and confirmed the dynamic similarity between their rise in liquid metals and aqueous systems, but showed some interesting differences in their basal rims. The bubble surface in mercury was far more rippled than that in water. They[24] also measured rise velocities of up to 5-10% higher in mercury. This discrepancy was attributed to initial stabilization problems.

In their work with liquid silver and mercury, Davenport, Bradshaw and Richardson[25] measured the rise velocities and sizes of spherical-cap bubbles. They observed that bubbles of equivalent volume in mercury and water were of the same height but their basal radii were about 20% smaller in liquid metal. Taking wall effects into account they observed the same rise velocity in silver as in water. Later work by Guthrie and Bradshaw[26] found excellent agreement in the measurements made in liquid silver and in water.

1.2.4 Third phase in rising bubbles

The presence of a third phase in a gas bubble submerged in a liquid (phase 1) may result in the formation of three interfaces, i.e. phase 1/gas, phase 3/gas and phase 1/phase 3.

In their study of matte entrapment and flotation in molten slags, Minto and Davenport[27] characterized three modes of behaviour of the third phase:

(i) A complete film coverage of the inside of the bubble.
(ii) Phase 3 dispersed in phase 1.
(iii) Phase 3 drops are attached to bubbles of gas in a flotation mode.

They used criteria based on minimum surface energy to distinguish between the three mdoes by the use of the three interfacial energy values. The criteria used are:

(a) if the film or spreading coefficient

$$\varphi = \gamma_{1/g} - \gamma_{3/g} - \gamma_{1/3} > 0$$

then a film is energetically stable; and

(b) if the flotation coefficient

$$\Delta = \gamma_{1/g} - \gamma_{3/g} + \gamma_{1/3} > 0$$

then flotation will occur.

Both film formation and drop flotation are favoured by high values of the liquid/gas interfacial energy ($\gamma_{1/g}$). A large value of $\gamma_{1/3}$ tends to inhibit film formation which requires a large liquid/phase 3 interface. Droplet flotation tends to reduce this interfacial area by contact of the third phase drop with the bubble and hence flotation is favoured in systems with high liquid/phase 3 interfacial energies ($\gamma_{1/3}$). As $\Delta > \varphi$, if a film is stable flotation will occur, but the analysis does not decide between the two criteria.

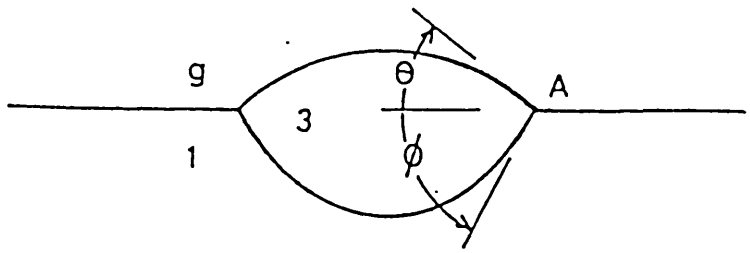

Fig.1-4: A third phase at an interface

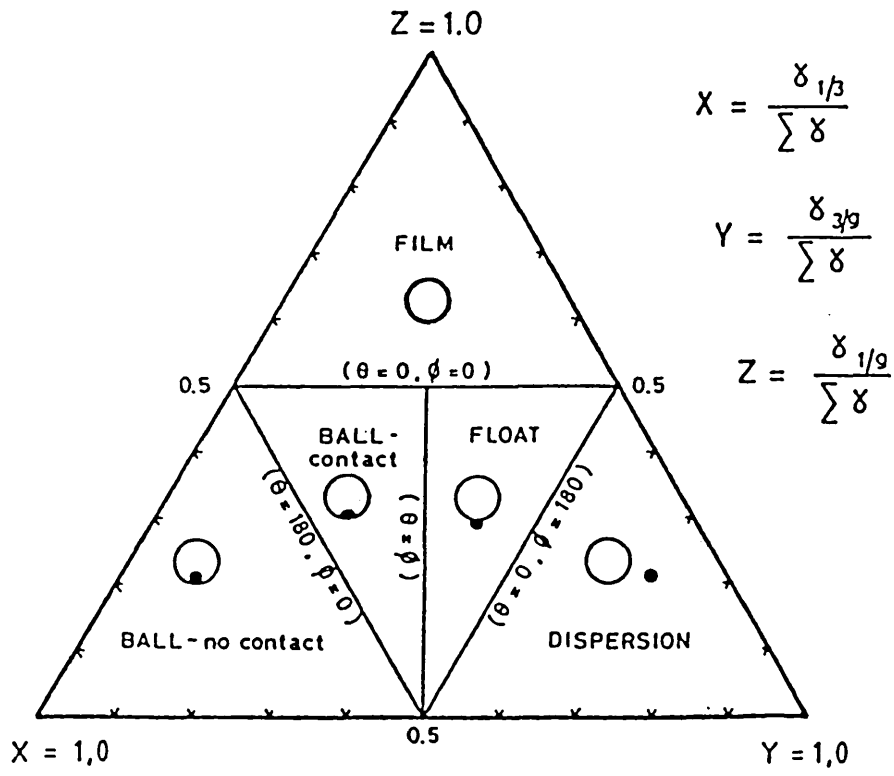

Fig. 1-5: The ternary interfacial energy diagram

(After Conochie and Robertson[30])

Using contact angle analysis and ignoring density effects, Conochie and Robertson[36] distinguished five modes of behaviour of the third phase (fig. 1-5):

(1) Phase 3 is spread as a thin film between phase 1 and gas.
(2) Phase 3 is only in contact with phase 1, i.e. phase 3 is dispersed in phase 1.
(3) Phase 3 is only in contact with the gaseous phase, i.e. phase 3 is dispersed in the gas.
(4) As a ball in gas with contact with phase 1.
(5) Flotation in phase 1 in contact with gas.

An additional aspect of film behaviour arises from possible interaction of the film with the flow of phase 1 around the bubble. The fluid dynamics are dependent on the size of the bubble. Very small bubbles have a rigid interface hence there will be no effect of fluid motion on the slag film. Larger bubbles are spherical-cap in shape and have a moving interface, hence as the spreading film tries to move over the top surface of the bubble the surface tension force is opposed by the shear induced by the liquid flow past the film (fig. 1-6). The angular extent of the stagnation region is thus determined by a balance between the film spreading force and the shear forces exerted by the external liquid.

Conochie and Robertson[35] have discussed the spreading of a third liquid phase using the theory first developed by Weber[28] and derived the following relationship:

For total coverage ($\beta = 0°$)

$$d_e^{5/4} < 1.42 \; \Delta\sigma / (\rho\mu)^{\frac{1}{2}} \; g^{3/4}$$

Stripping

The third phase carried by a rising bubble may strip from the bubble into the bulk liquid.

Engh and his co-workers[31] studied the removal of oxygen from steel by submerged injection of $CaO-CaF_2$ slags using argon as the carrier gas. They showed that the reaction kinetics were much slower than would have been the case if all

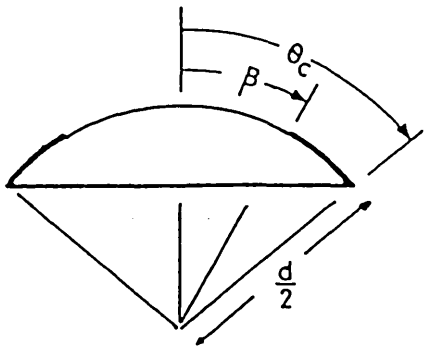

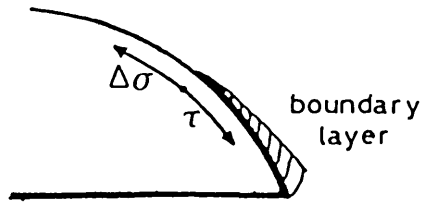

$C_a = \mu . U / \Delta\sigma$

Re = Reynolds no.

$$\Delta\sigma = \frac{d}{2} \int_{\beta}^{\theta_c} \tau \, d\theta$$

where:

τ = shear stress exerted on film by liquid

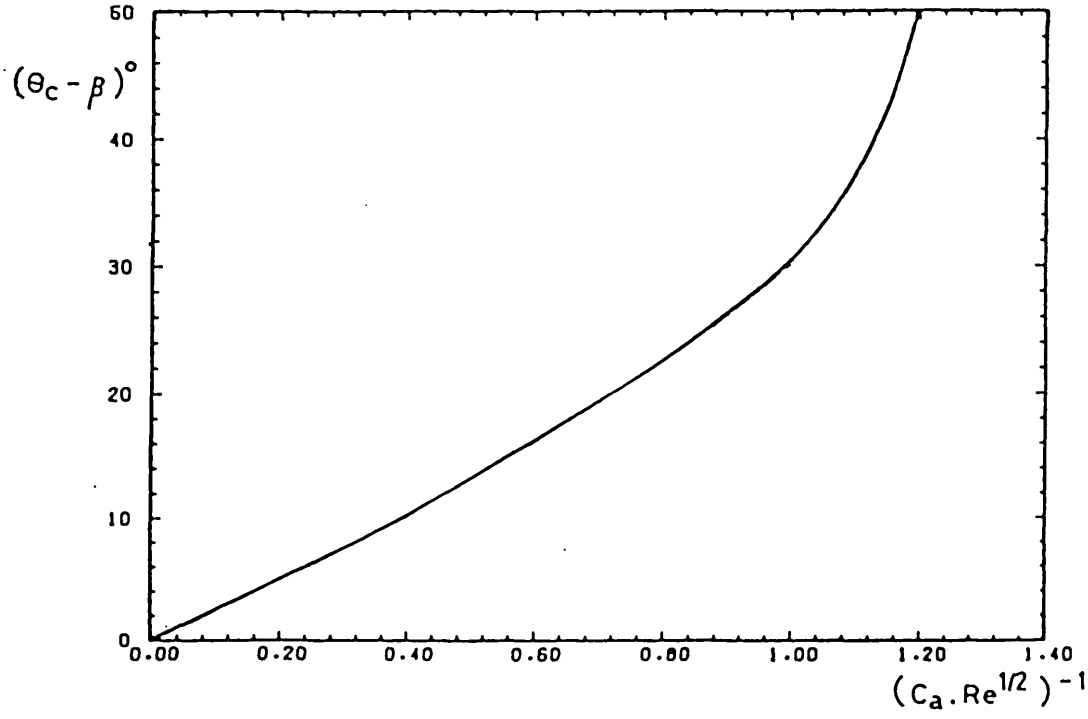

Fig. 1-6: Film coverage of a spherical-cap bubble

(After Weber[28])

the particles had been dispersed in the melt. They suggested that most of the slag powder remained associated with the bubbles during their rise. On the other hand, they also found that injection of slag powder was far superior to simply adding slag on the melt surface and gas stirring.

In their study of the kinetic mechanisms in desulphurization of molten iron using magnesium vapour, Irons and Guthrie[33] investigated the kinetics of magnesium vapour dissolution in molten iron. They reported that a major portion of the desulphurization occurred away from the bubble interface and proceeded via a heterogenous reaction in the bulk of the metal. They postulated that MgS phase, formed at the surface of the ascending bubbles, was stripped from the bubble surfaces and provide nucleation sides for further desulphurization.

To obtain more information about the behaviour of reagents carried by bubbles rising in liquid metals, Conochie and Robertson[35] developed the 'Open Top Bubble' (OTB) technique. The technique simulates the spherical-cap bubble but leaves the top of the bubble open. This system has the unique advantage of providing direct visual access to the bubble base, as well as working in a stationery frame of reference.

Using the OTB technique Robertson and co-workers[29] have shown that solid particles which are wet by the liquid will be entrained in the bubble wake even if their density is below that of the liquid. They also showed that liquid films are unlikely to remain inside large bubbles, even when they have a strong tendency to spread, because they will be stripped from the basal rim.

Wiafe[32] measured the critical stripping of various liquids in a water OTB and deduced that stripping was primarily dependent on the viscosity of the third liquid phase. He reported that there was a'critical depth' at which stripping began.

The behaviour of the third phase associated with a rising bubble is of interest for three main reasons:

(1) The mass transfer between the third phase in the bubble and the liquid phase will be dependent on the interfacial area between them.

(2) Continued reaction of the gas bubble with the liquid will be affected by the proportion of the bubble covered by the reaction product.

(3) The residence time of the third phase in the melt will depend on whether it rises with the bubbles or is dispersed in the melt.

The work reported here was carried out using the 'Open Top Bubble' technique as detailed in the next sections.

1.3 LEAD REFINING ('SOFTENING')

The removal of the elements chiefly responsible for hardening lead (antimony, tin and arsenic) is termed 'softening'. This may be accomplished by preferential oxidation due to differences in the free energies of formation of the oxides of these metals and lead. Two main types of softening are usually employed:

(a) Neutral softening

This is a high temperature oxidation process (with air as the oxidizing agent) in which most of the impurities are removed as a liquid slag, although in the last stages the major product is PbO, giving a solid dross requiring to be skimmed off. At temperatures above 600°C, the order of formation of the oxides is SnO_2, As_2O_3, Sb_2O_3, PbO, as predicted by their free energies of formation. However, since these impurities are in dilute solutions in lead, the free energies of formation of the oxides are decreased. PbO will thus be formed to dilute the acidic oxides and enable the reaction to proceed to an adequate extent. Fig. 1-7 shows the antimony content in a lead-antimony-oxide slag as a function of its content in the lead in equilibrium with the slag, according to data from Zunkel and Larson[51].

(b) Basic softening

This process (also known as the Harris process) consists in oxidizing the impurities in lead in the presence of a caustic soda slag, such that they form their respective sodium salts. The NaOH, as well as entering into chemical combination with the impurities,also act as a suspension medium for them, thereby facilitating their removal from the lead. An excellent account of the modern practice of the Harris process is given by Emicke and his co-workers[52]. A more recent review is also available from Davey[53].

The oxidizing agents are sodium nitrate and/or air. Air alone is a weak oxidizer[54] and the resulting rate is low. According to the account by Emicke[52], when lead is brought in contact with NaOH and air through pumping, the impurity arsenic, tin and antimony in the lead are partly oxidized:

$$4As + 5O_2 + 12\ NaOH \rightarrow 4Na_3AsO_4 + 3H_2O$$

$$Sn + O_2 + 2NaOH \rightarrow Na_2SnO_3 + H_2O$$

$$4Sb + 5O_2 + 12\ NaOH \rightarrow 4Na_3SbO_4 + 3H_2O$$

At sufficiently high concentrations, As and Sn can react in the NaOH even without oxidation[53]:

$$2As + 6NaOH \rightarrow 2Na_3AsO_3 + 3H_2$$

$$Sn + 2NaOH \rightarrow Na_2SnO_2 + H_2$$

In this case the lower valency forms (arsenite and stannite) of the sodium salts are formed.

However the main reactions occur using sodium nitrate as a strong oxidizing agent, forming the higher valency salts in each case:

$$2As + 2NaNO_3 + 4NaOH \rightarrow 2Na_3AsO_4 + N_2 + H_2O$$

$$5Sn + 4NaNO_3 + 6NaOH \rightarrow 5Na_2SnO_3 + 2N_2 + 3H_2O$$

$$2Sb + 2NaNO_3 + 4NaOH \rightarrow 2Na_3SbO_4 + N_2 + H_2O$$

Any lower valency salts formed by displacement of hydrogen are also oxidized by sodium nitrate, so that the products are sodium arsenate, stannate and antimonate. Although the order of oxidation is As, Sn, Sb and then Pb, in practice As and Sn are removed together before Sb, which is scarcely oxidized at all until As and Sn are reduced to very low values (see fig. 1-8).

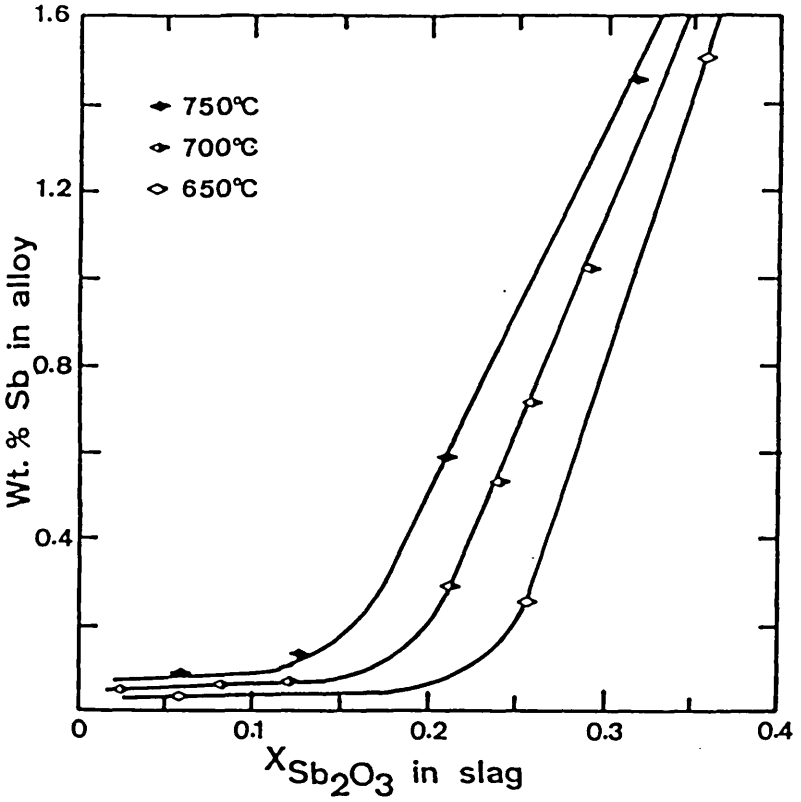

Fig. 1-7 Equilibrium antimony contents of Sb-Pb alloys in contact with $PbO-Sb_2O_3$ slags.

(After Zunkel and Larson[51])

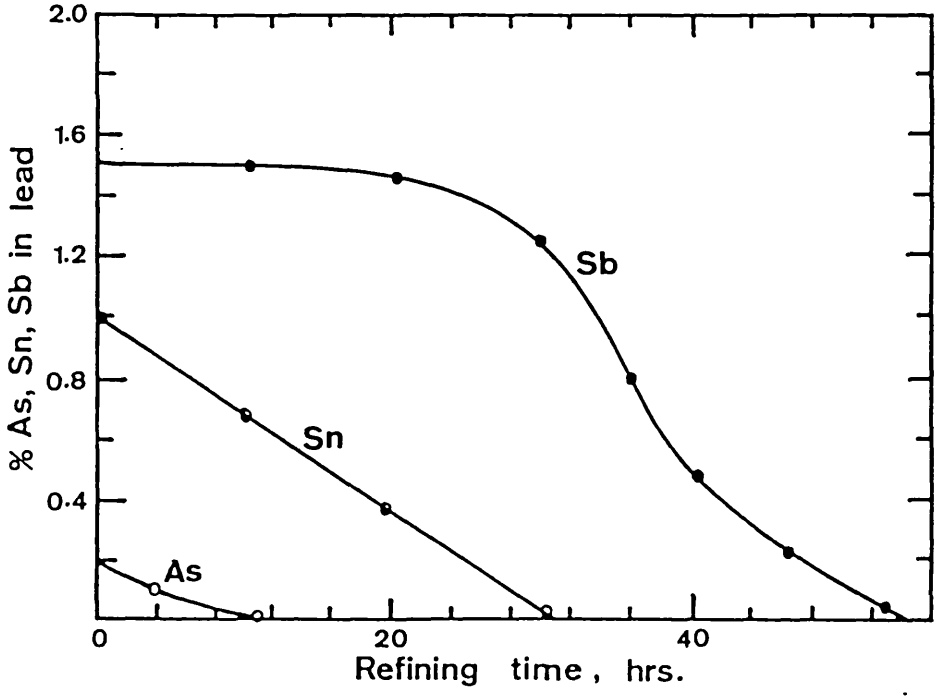

Fig. 1-8: The removal of As, Sn and Sb from lead by the Harris process.

(After Emicke[52])

CHAPTER 2

EXPERIMENTAL

The open top bubble technique simulates the spherical-cap bubble in a stationary frame of reference but leaves the top of the bubble open. Liquid in a container is made to flow inwards in a circular weir to form the sides of the bubble. This flow over the weir is a potential flow, as is the flow around the frontal surface of a spherical-cap bubble (fig. 2-1). The wake structure is similar to that behind a spherical-cap bubble and there is also a basal wobbling as observed in spherical-cap bubbles. The flow system thus achieved is a reasonable representation of fluid flow around the lower part of a spherical-cap bubble.

The power of this technique has been utilized in the study of third phase behaviour in rising bubbles. The experiments were done using both the room temperature model (water model) and the high temperature model, using molten lead. A design for the OTB in carbon saturated iron was also completed. This could be used in the study of some steel making reactions.

2.1 FLUID FLOW IN OTB

Liquid circulation in the open top bubble rig is induced by a centrifugal pump. In the room temperature model, built in perspex (fig. 2-2), the pump (b) drives liquid in the right-hand tank up the left through the perforated plates (c), installed to reduce turbulence, and allowed to flow over an inner circular weir forming a bubble at (a). The bubble base level at (a) is controlled using a valve (e).

The flow of water over the weir was estimated from the height of the free surface above the weir (h_w) as measured with a micrometer and the flow characteristic curve given by Conochie[16] (fig. 2-4). The flow-rate can be varied by adjusting the bypass weir (d). The flow profiles over the ciruclar inflow weir, for different weir heights, are given in the same work[16].

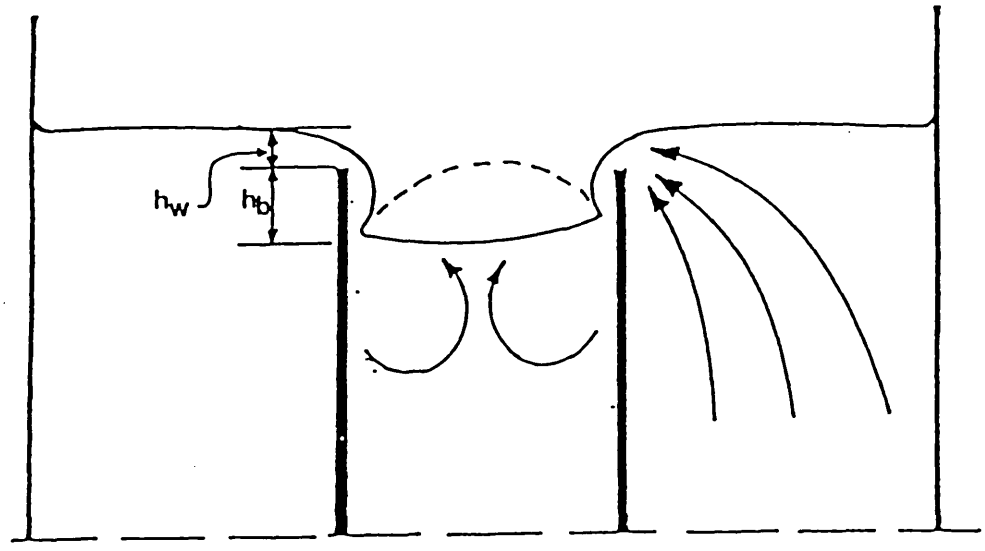

Fig. 2-1: The open top bubble concept

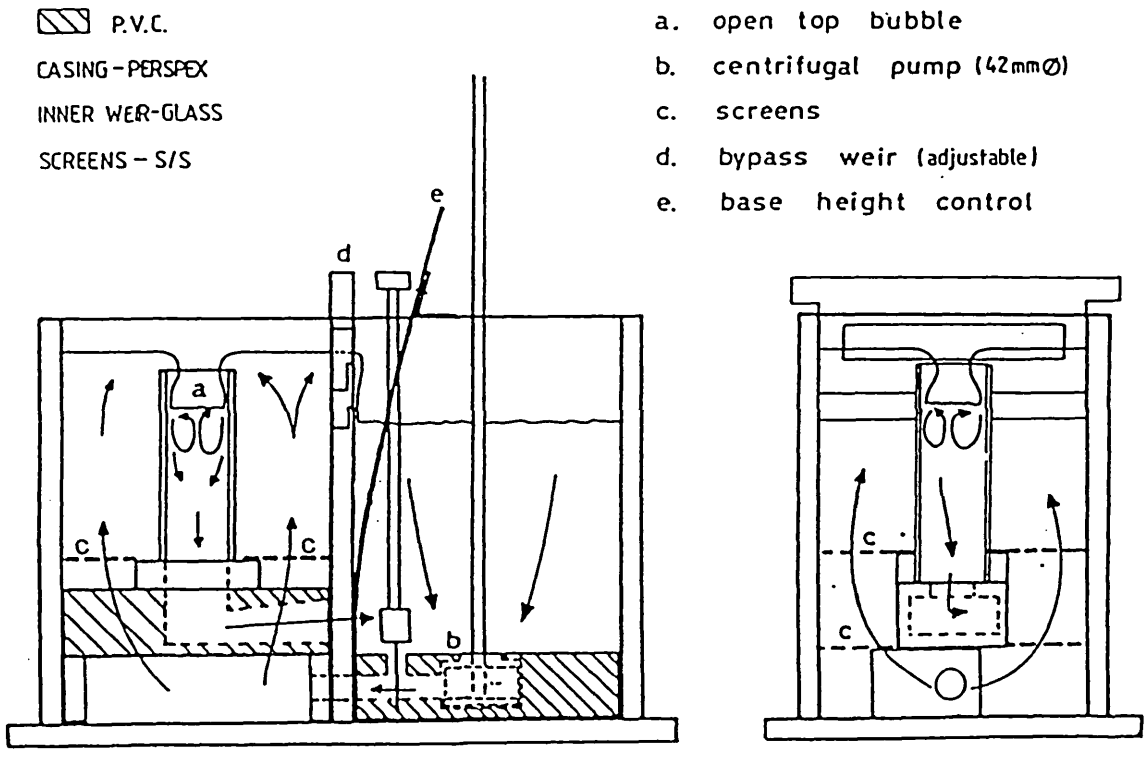

Fig. 2-2: The room temperature open top bubble model

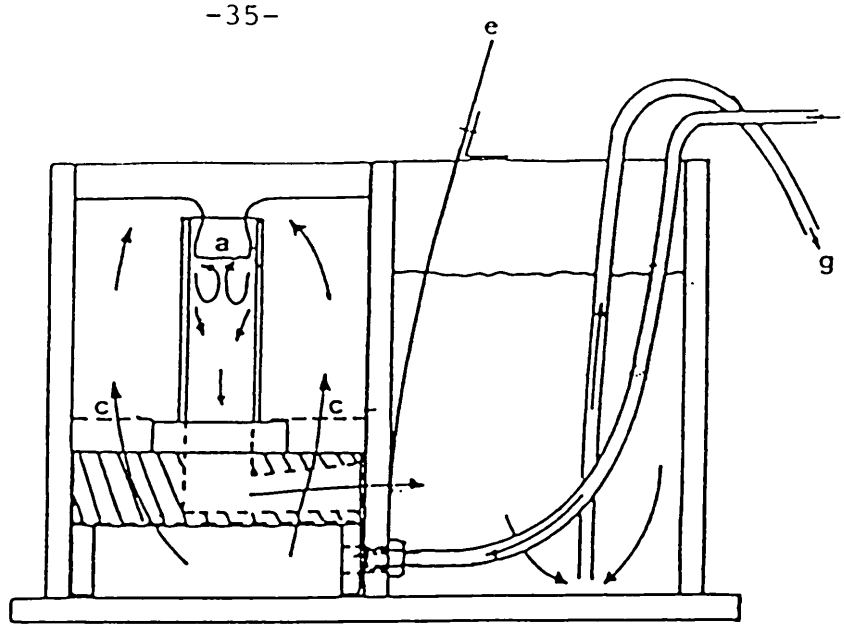

f. water inlet
g. siphoned water

Fig. 2-3: The room temperature open top bubble - Fresh water supply arrangement

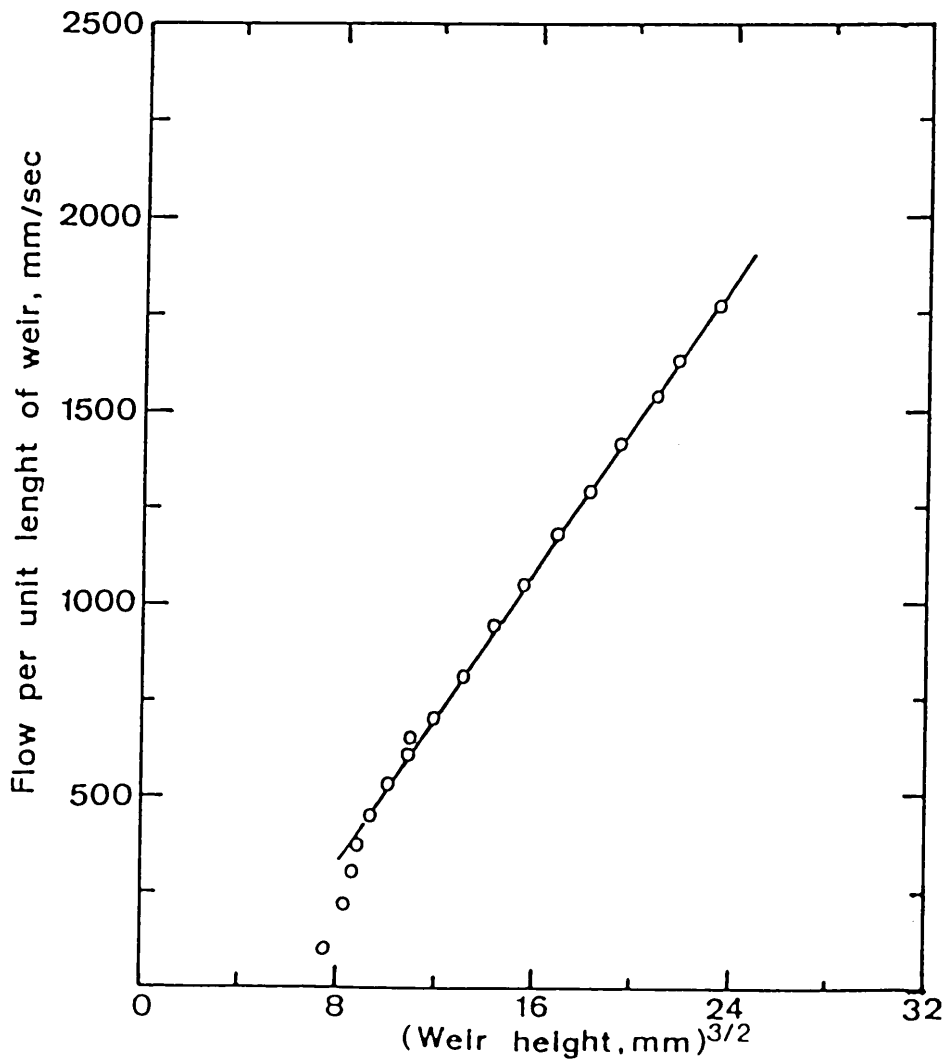

Fig. 2-4: Weir flow characteristics (After Conochie[16])

A later modification on the room temperature open top bubble rig (fig. 2-3) was such that continuous fresh water from the tap was supplied to form the bubble using the tube (f). The contaminated water resulting from the stripping of the third phase at bubble base was simultaneously siphoned out using tube (g), thus maintaining a relatively clean bubble surface throughout the runs. The only problem encountered was the difficulty in reaching a balance between the flow into the rig and the flow out of it. The flow rate was varied by increasing or reducing the inflow using the tap valve and at the same time increasing or reducing the pressure head on the siphon.

2.2 OXIDATION EXPERIMENTS

High temperature experiments were done with liquid lead to produce slag by gas/metal reaction, using the molten lead open top bubble apparatus. The layout of the apparatus was such that the basic shape of the bubble produced was unchanged from that in the water model, but the design was modified to satisfy the engineering requirements of a high temperature, atmosphere-controlled rig. A cross-section through the rig is shown in fig. 2-6. A detailed description of the layout, design criteria and operational procedure have been given by Conochie[16].

30 kg of grade A chemical lead (99.9% Pb) was heated in a mild-steel container. The temperature in a Kanthal A resistance furnace wascontrolled by two 'Eurotherm' PID/SCR/10 controllers with chromel-alumel type K thermocouples. The liquid metal temperature was measured with another chromel-alumel thermocouple, which was checked against the boiling point of water and the melting point of lead.

A schematic drawing of the experimental apparatus is presented as fig. 2-5. Fig. 2-6 shows details of the bubble profile, the locations of the oxygen probes and liquid lead levels.

2.2.1 Recommissioning the lead rig

The high temperature open top bubble rig was recommissioned after a two year shut down. All aspects of the system were carefully checked. First, the furnace was heated to melt the lead and the thermocouple removed to enable the lid to come off. The apparatus was then cooled and the lid removed. All seals and 'O' rings were changed, including the faulty pump shaft seal. The lead splashes on the radiation shield and on the lid were also scraped back into the pot before the lid was replaced.

The furnace temperature was then slowly taken up to about 400°C and allowed to run at this temperature for a couple of days during which all the furnace components 'broke in' evenly and the external components were checked

very carefully. A steady but slow flow of forming gas (10% H_2; 90% N_2) was allowed in to effect a slow deoxidation of the molten lead. Vertical and horizontal adjustments were carried out to ensure vibration-free running of the pump. Stabilized zirconia oxygen probe was slowly immersed into the lead and its terminals connected through a 'Vibron' 33B-2 electrometer to a 'Servoscribe' 1S chart recorder to continuously monitor the oxygen potential of the molten lead bath.

During some of the experiments pure hydrogen was used as the deoxidant and sufficient deoxidation was achieved within a few hours of its use. However, for most of the work forming gas (25% H_2, 75% N_2) was used as the deoxidant and good results were obtained.

2.2.2 Gaseous injection into the OTB

Oxygen was added to the liquid metal in pulses. The volume of oxygen that was injected was set by a combination of the flow rate through the rotameter labelled R2 and the time determined by the timer T1, both of which were connected to the injector through a peristaltic change-over valve (fig. 2-5). The peristaltic change-over valve allowed a timed pulse of oxygen to enter the apparatus and automatically switched over to direct the oxygen flow to exhaust while it admitted the purging gas. The oxidation sequence was such that a timed pulse of oxygen (as set by the timer T1) was followed by purging gas (high purity argon or oxygen-free nitrogen), at first at strong purge and then reset to weak purge (set by timer T2). The strong purge ensured that no oxygen was left behind in the injector and the weak purge maintained a neutral atmosphere above the melt during the oxygen dissolution process. The injector was positioned so that the injected gases were blown straight onto the bubble base.

Before each experiment the volume of oxygen that was to be injected in a pulse was measured by two different techniques: measurement of the pressure change when an oxygen pulse was injected into a flask of known volume and

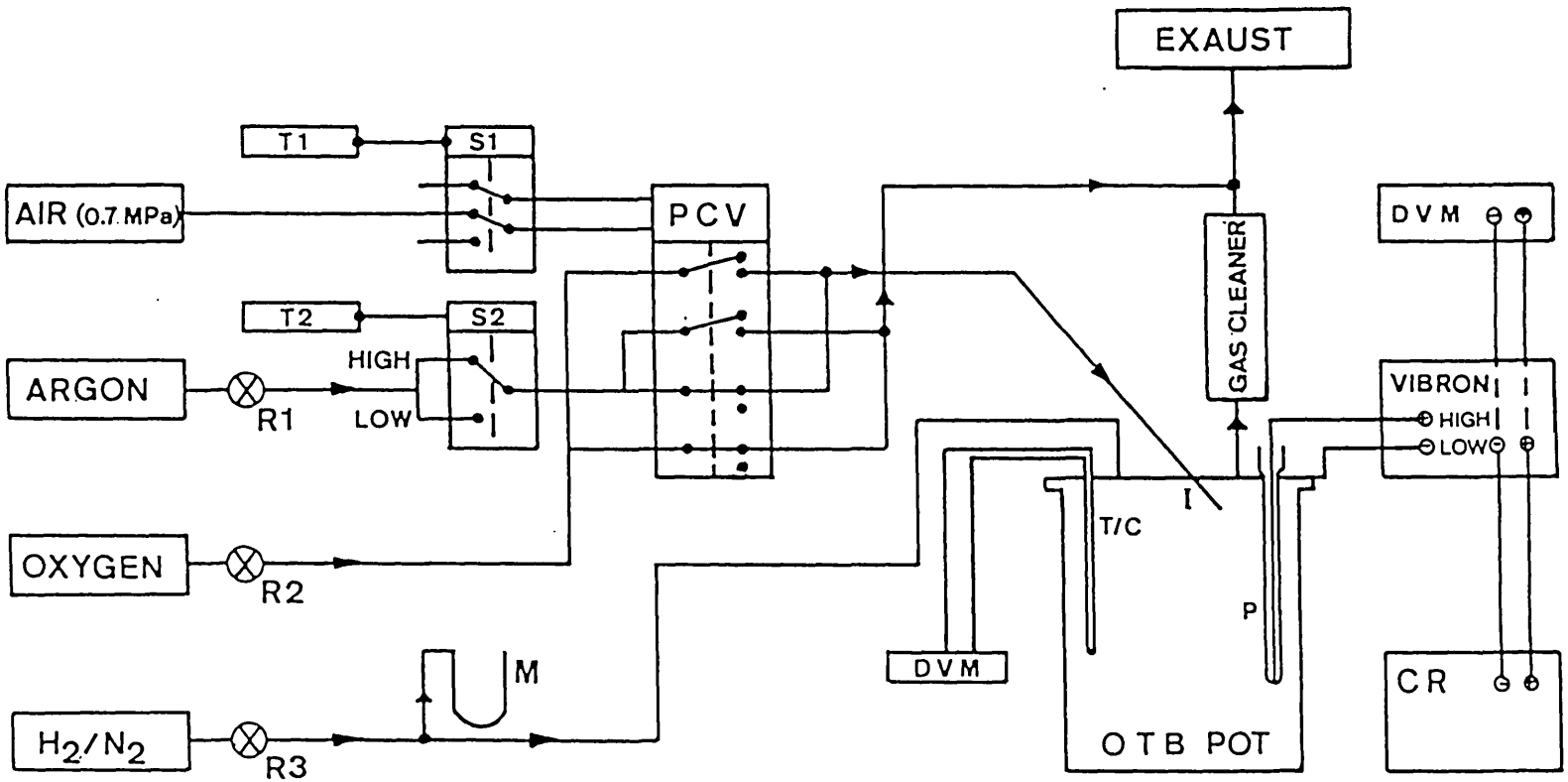

Fig. 2-5: Schematic drawing of the experimental apparatus

T_1, T_2	Electronic timers	PCV	Peristaltic changeover valve
S_1, S_2	Solenoid switches	DVM	Digital voltmeter
R_1, R_2, R_3	Rotameter control valves	OTB	Open top bubble
I	Stainless steel injector	CR	Chart recorder
P	Oxygen probe	T/C	Chromel-alumel thermocouple
M	Water manometer	Argon purge:	High = 600 ml/min
			Low = 120 ml/min

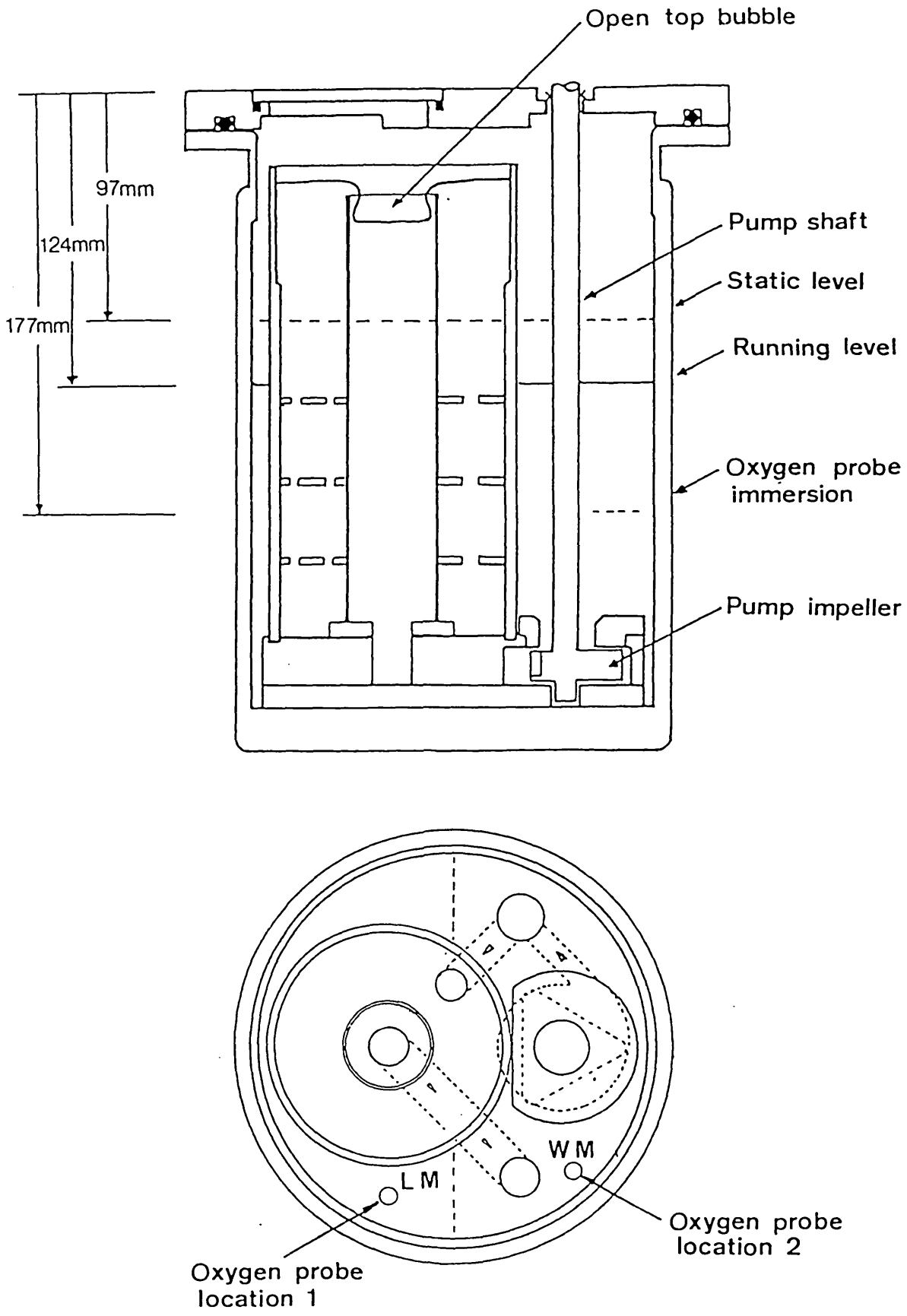

Fig. 2-6: The lead OTB pot

direct measurement with a soap film meter. The values that were obtained were reproducible to within ±2% relative error, after careful checks.

Prior to each oxidation experiment, the liquid lead was thoroughly deoxidized using forming gas (75% N_2, 25% H_2). The gas chamber of the lead pot was then purged for at least 15 mins using high purity argon or oxygen free nitrogen gas at high purge (600 ml/min). This was to ensure that any residual hydrogen from the forming gas was flushed out.

Each addition of an oxygen pulse caused oxide to form on the lead surface, and this suppressed the ripples at the bubble base. A new pulse of oxygen was added soon after the riples had returned. Oxygen addition was stopped when any further pulse ceased to yield a measurable change in the cell potential within a 5-minute period. Oxygen was then allowed to flow steadily into the reactor until a steady emf (the saturation emf at that temperature) was reached.

2.3 THE OXYGEN PROBE

Changes in the oxygen potential of the liquid lead and the outlet gas were monitored using stabilized zirconia oxygen probes. The liquid metal probes were immersed in the lead at locations shown in fig. 2-6. Gas phase oxygen potential was monitored in a separate furnace positioned near the lead pot, in place of the gas cleaner (fig. 2-5).

Each oxygen probe was connected to a chart recorder through a 'Vibron 33B-2' electrometer. The connections from the probes to the Vibrons were made using non-microphonic coaxial cables. Use was made of the electrometers' back-off units to improve accuracy and sensitivity.

2.3.1 Probe design and contruction

Fig. 2-7 shows a cross-section through a liquid metal oxygen probe. The assembly of each probe required extreme care. The zirconia/yttria tube was sealed onto a suitably machined brass head using 'Araldite'. A length of platinum wire with a bundle at the end was then put into the tube and held in place using a single bore alumina push rod. A PTFE ring was carefully attached to the outside of the push rod such that it provided a gas seal between the rod and the brass head. This seal prevented the incoming reference gas from leaking into the outlet stream without passing through the tip of the probe. A small spring was used to keep the platinum electrode firmly in contact with the solid electrolyte and to allow for differential thermal expansion when the probe tip was heated. The platinum wire was then passed through a standard coaxial connector which was subsequently screwed into the brass holder using a PTFE tape seal. The probe was later slowly lowered into the lead pot and finally sealed by soldering the platinum wire into the connector.

The design of the gas phase probe was slightly different from that of the liquid metal probe. The gas probe required an external contact and had to be operated at a higher temperature in order to obtain a reasonably fast and reversible response.

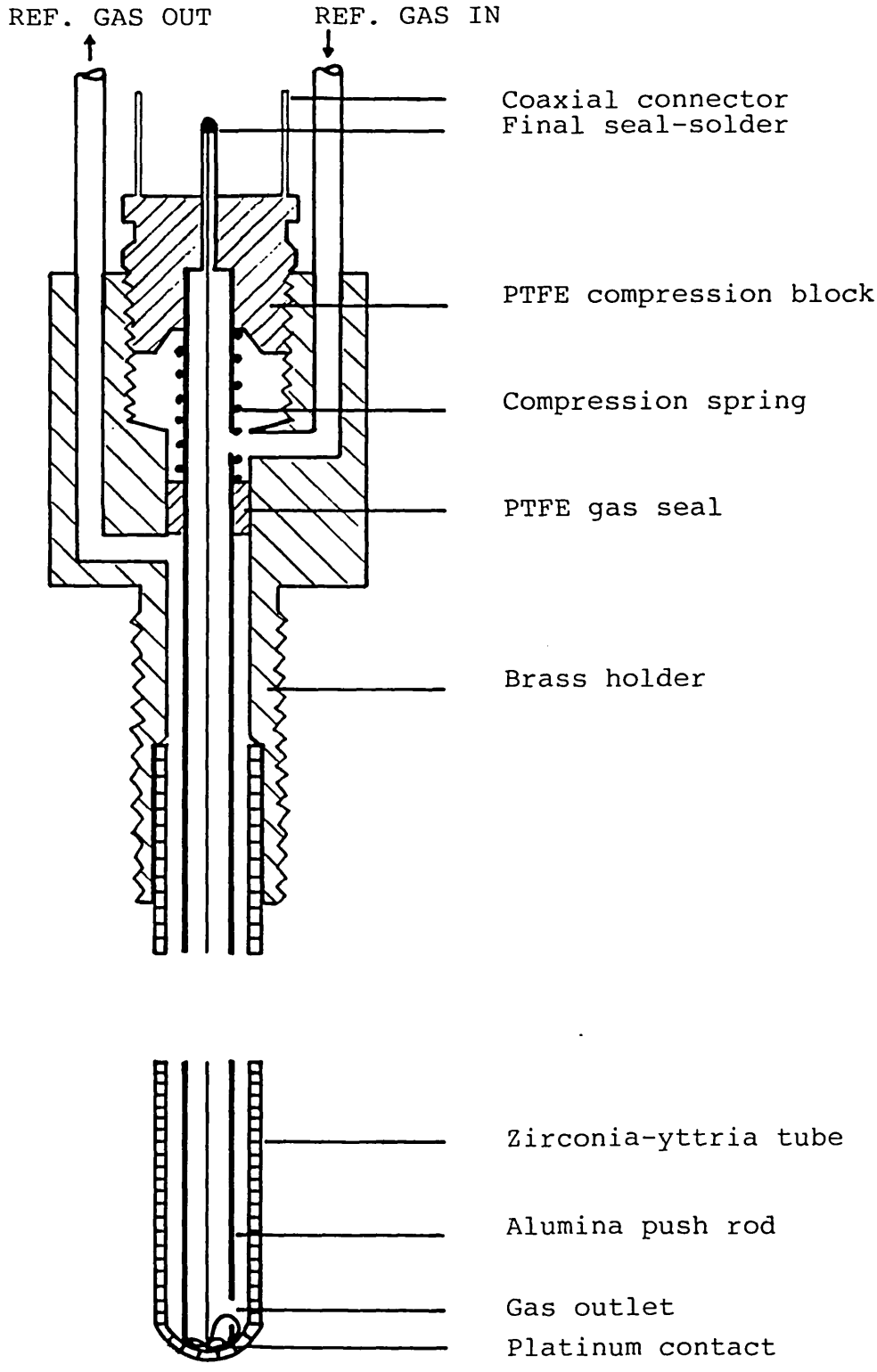

Fig. 2-7: The liquid metal oxygen probe

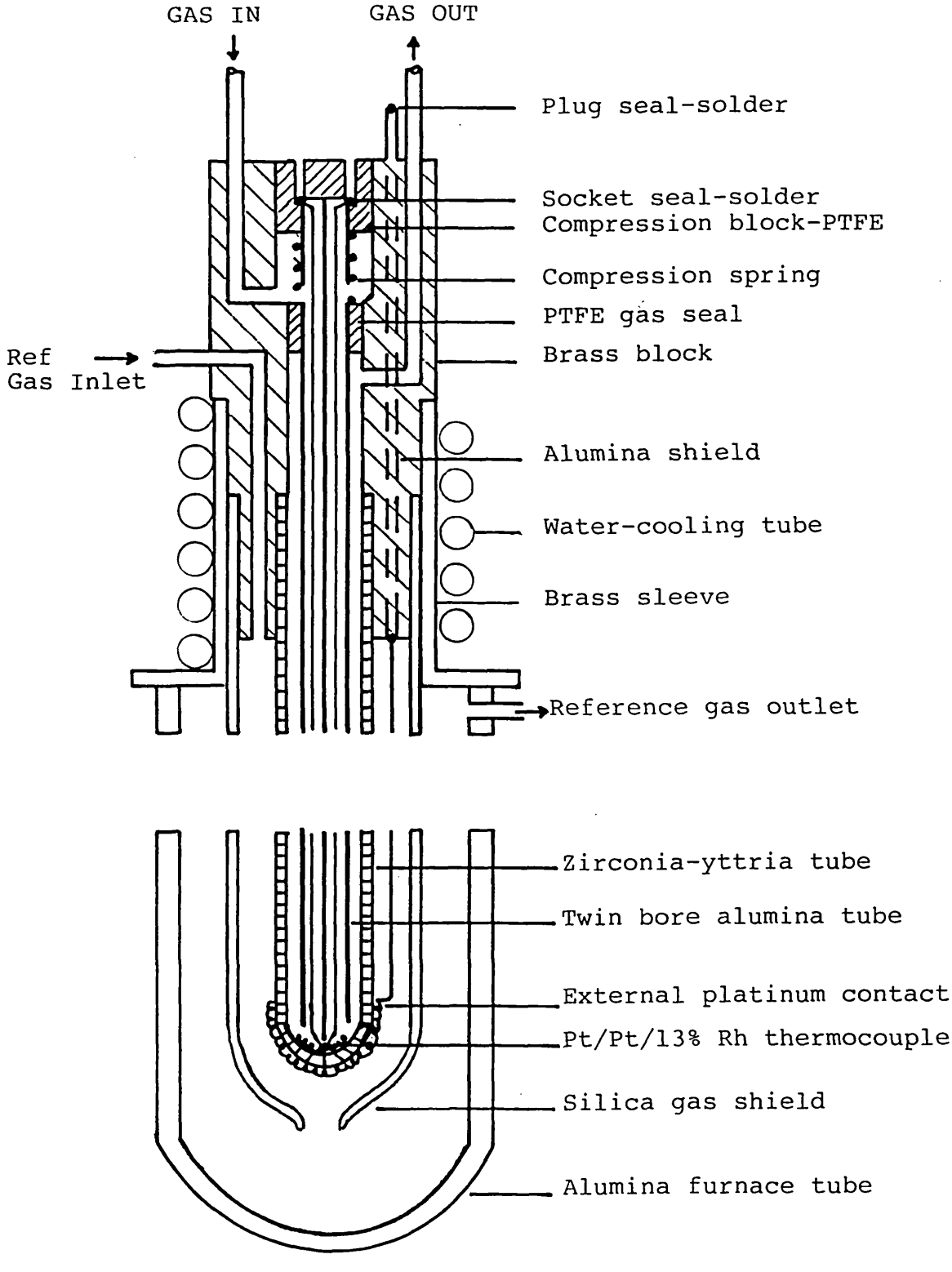

Fig. 2-8: The gas phase oxygen probe

A cross-section through the probe and its furnace is shown in fig. 2-8. The probe was designed such that it incorporated a thermocouple which measured the temperature of the flue gas. The platinum wire of the Pt/Pt; 13% Rh thermocouple was also the negative electrode of the electrochemical cell. The external contact (positive electrode) was made of platinum gauze spot-soldered onto the tip of a platinum wire and attached to the probe tip using platinum paste. This was then fired over night in a furnace at 1200°C, to ensure firm contact between the platinum and the solid electrolyte tube.

The assembly of the inside of the gas probe was similar to that of the liquid metal probe, discussed earlier. The platinum wire of the positive electrode (external contact) was passed through a hole in the brass probe holder, using an alumina sleeve and later sealed with 'Araldite'. The probe was connected to the lead pot in such a way that the measured gases went through the inside of the solid electrolyte, while a steady stream of the reference gas was maintained on the outside. This arrangement eliminated accumulation of gases inside the probe and a small residence time was ensured. The silica tube shielding the external portion of the zirconia stabilized tube ensured that the reference gas touched the tip of the probe before escaping from the furnace. The seals holding the solid electrolyte and the silica tubes to the brass head of the probe were protected using water-cooled copper tube. The probe was heated in a specifically designed furnace (see Appendix A-3).

2.3.2 Probe performance tests

Various tests were made to check on the behaviour of the oxygen probes.

The performance of the liquid metal probes were checked first, with the use of air and pure oxygen as reference gases, at various temperatures. Typically observed responses are shown in fig. 2-9. The observed response speed increased with the temperature of the metal. At 490°C a change of 26 mV was obtained when the reference gas was

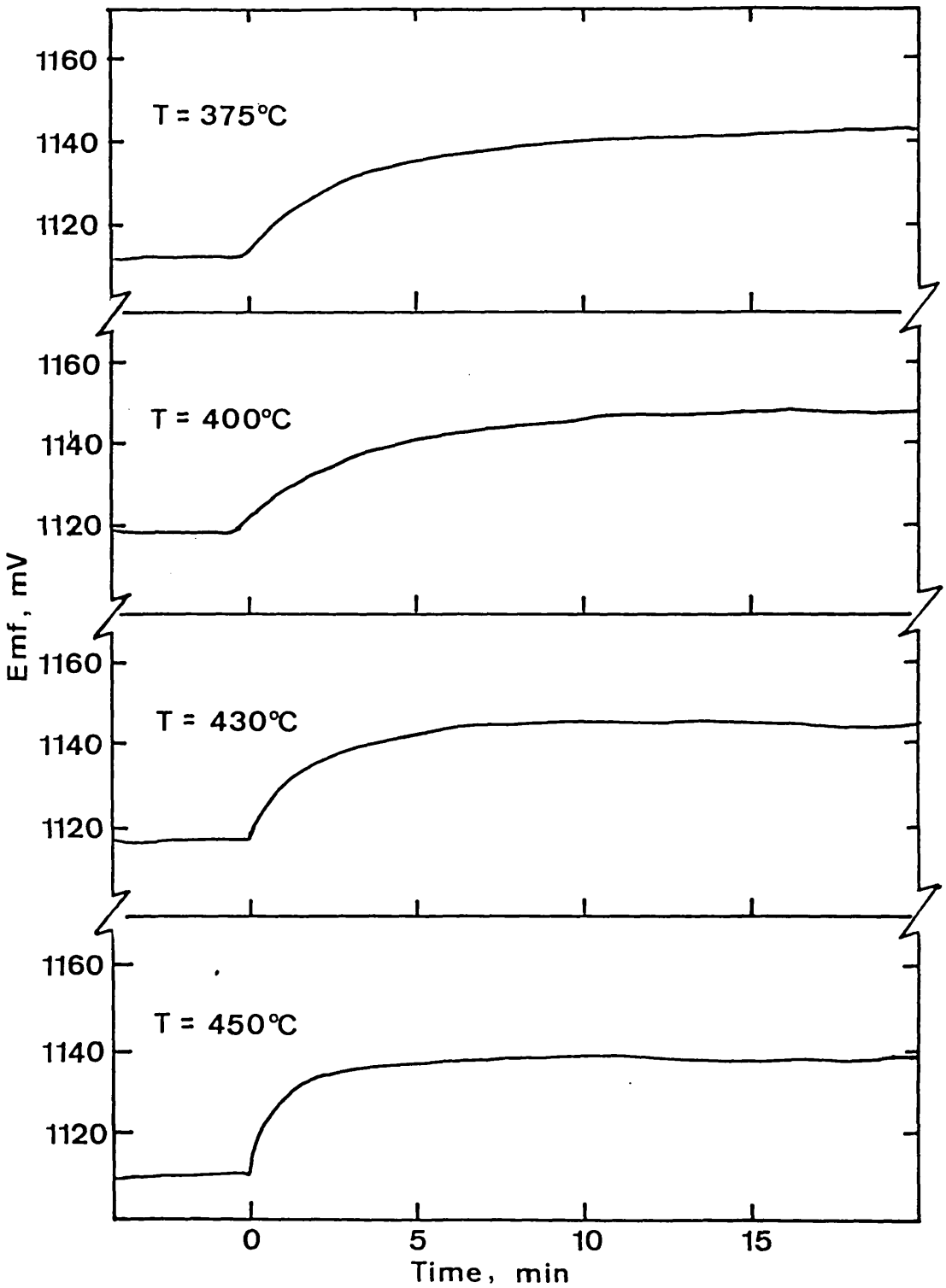

Fig. 2-9: The response of the liquid metal probe to change in the reference gas (from air to oxygen) at different temperatures.

changed from air to oxygen. This value agreed very well with the calculated value of 25.7 mV.

The probe potentials for Pb/PbO equilibrium were also measured at various temperatures (see fig. 2-10). The measured values agreed with the calculated values to within 2 mV, after correction had been made for the iron-platinum thermoelectric effect.

Initial tests on the gas phase oxygen probe produced unexpected results. The measured oxygen potentials of the gases leaving the lead pot were substantially higher than was expected. Reversing the flow of the gases produced a different result; an even higher oxygen potential. It was subsequently established that there was a leak in the initial seal used in joining the stabilized zirconia tube to the brass probe holder. The flue gas was diffusing out through the leak, thereby diluting the reference gas and resulting in lower probe potential measurements.

The seal was replaced and satisfactory results obtained thereafter. At 750°C, a change in the reference gas from air to oxygen produced an emf change of 31 mV (see fig. 2-11). This compared well with a calculated value of 34.4 mV. Fig. 2-12 shows a typical response of the gas phase probe to argon purging of the gas atmosphere of the lead pot, after lead deoxidation using forming gas.

The gas phase oxygen probe was operated at a temperature of 750°C throughout the duration of the experiments.

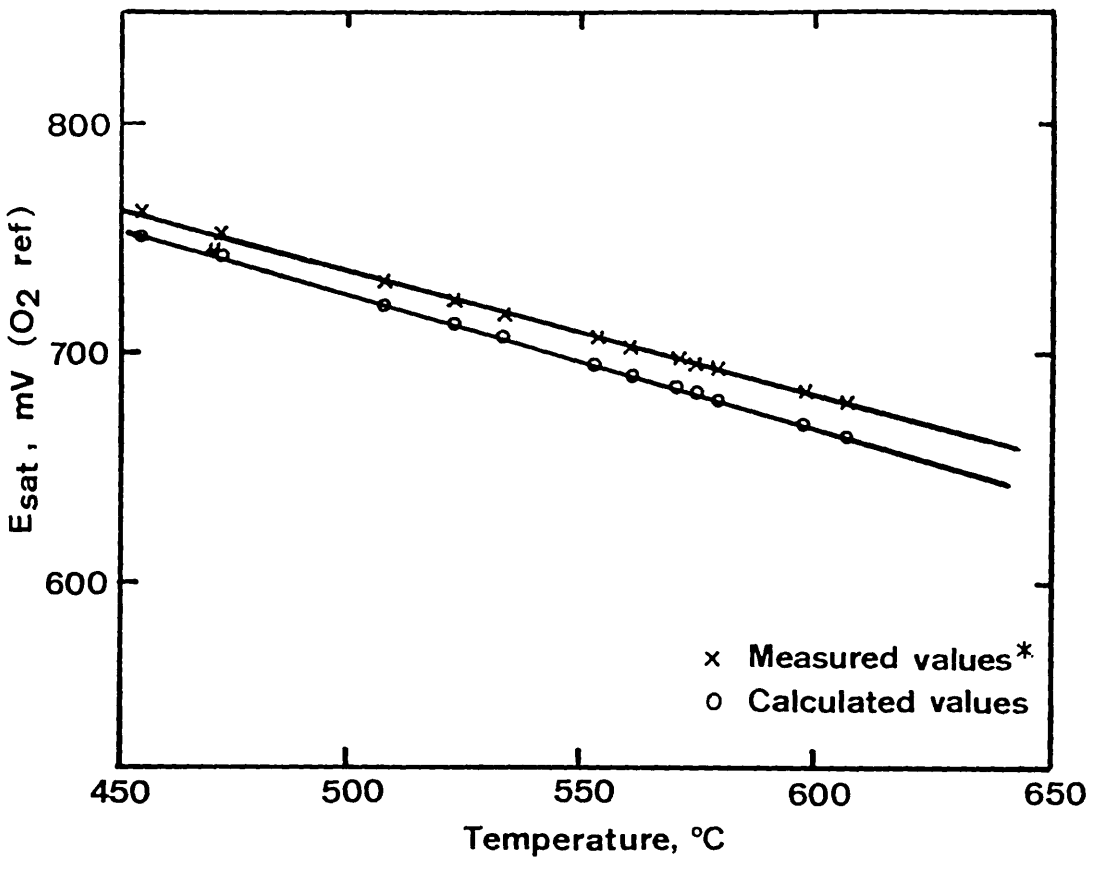

Fig. 2-10: Oxygen cell potential for Pb/PbO equilibrium

*Before correction was made for Fe/Pt thermoelectric effect

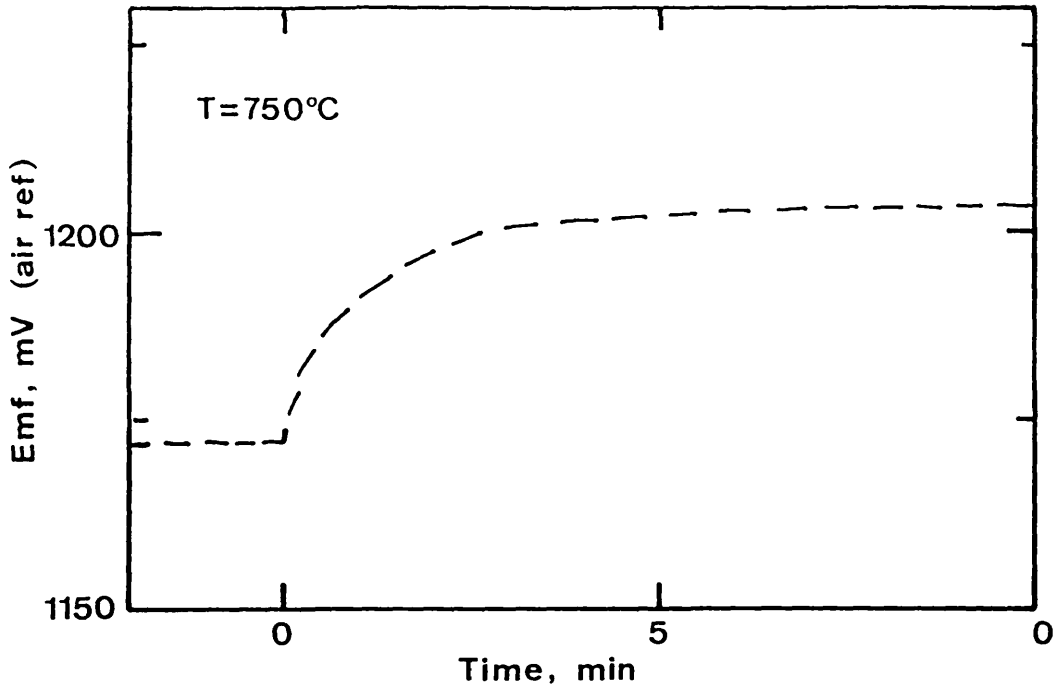

Fig. 2-11: The response of the gas probe to change in the reference gas from air to oxygen.

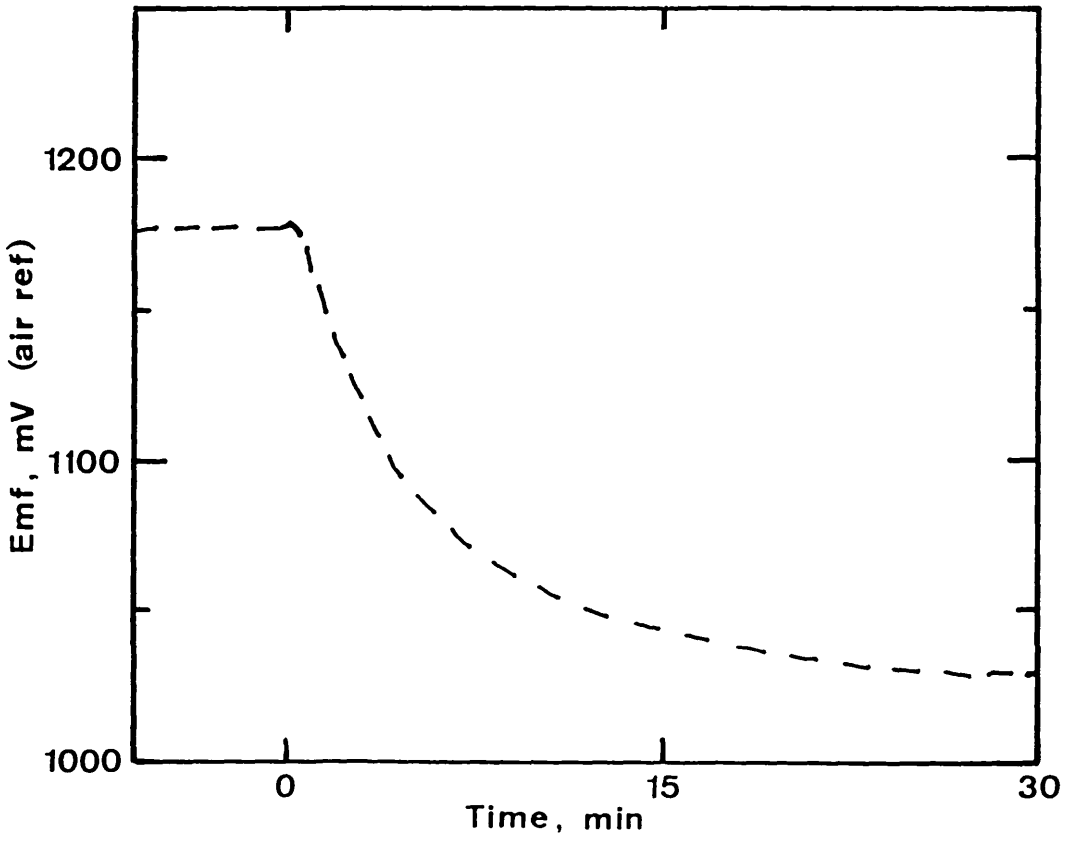

Fig. 2-12: The response of the gas probe to the purging of the gas atmosphere of the lead pot with argon, after lead deoxidation using forming gas.

2.4 SLAG ADDITION

2.4.1 Reagents used

1. Sodium Hydroxide (NaOH)

   Suppliers: British Drug Houses Chemicals Ltd.
   Grade: Analar
   Minimum assay: 98%

2. Sodium Nitrate ($NaNO_3$)

   Suppliers: Hopkin and Williams Ltd.
   Grade: Laboratory reagent

3. Lead Oxide (PbO)

   Suppliers: Hopkin and Williams Ltd.
   Grade: Analar

2.4.2 Preparation of reagents

NaOH slag

The caustic soda slag samples were made by weighing out about 5 gms of NaOH granules into a gold crucible of approximately 15 mm diameter and 75 mm length. The crucible and contents were then lowered into a tube furnace operating at about 300°C. The furnace temperature was then slowly taken up to 500°C and left for about 15 mins. This was to ensure that the caustic soda lost most of its dissolved water.

The molten slag was subsequently quenched on an 18 mm thick brass block which had numerous closely packed 6 mm holes bored through its breadth. The brass block rested on a sheet of copper plate in such a way that the liquid slag ran through the holes and solidified therein. The resulting slag pellets were removed by pushing them out through one end of the brass slab, using a mild steel rod. These pellets were then broken down to the required weights and stored in sealed glass containers kept in a dessicator containing freshly oven-dried silica gel.

NaOH - $NaNO_3$ slags

Granules of sodium hydroxide and sodium nitrate were weighed to the desired weight fractions in the gold crucible and lowered into the tube furnace. The furnace temperature was later slowly raised (as in the NaOH slag preparation) to 500°C and kept for about 15 mins. While in the furnace the melt was slowly stirred using an alumina rod to ensure good mixing. Care was taken in raising the furnace temperature in order to prevent the loss of sodium nitrate by decomposition.

The slag was subsequently cast into pellets and stored, in the same way as was done for the NaOH slag.

A check made on the weight loss during melting in three separate experiments showed a maximum decrease in weight of 0.7 % (see appendix A-4). This change may be largely due to the loss of the water in the reagents. Decomposition of the $NaNO_3$ would have been marked by the evolution of brown NO_x fumes but these were not observed or detected by smell.

$NaNO_3$ slag

These slags were also prepared in the same way as the NaOH slags. The operating temperature was, however, reduced to 400°C in order to avoid any decomposition. No fumes of NO_x oxides were observed during the slag preparation. Powder X-ray diffraction pattern of the prepared slag pellets (shown in Table E of appendix A-6) compared very well with that of the as-received sample.

PbO-NaOH slag

A suspension of PbO in caustic soda was prepared by stirring a few grams of yellow PbO powder into molten NaOH in the gold crucible at 500°C. The melt was stirred using an alumina rod and was later quenched on the brass slab. Most of the added PbO sedimented to the bottom of the crucible as a reddish brown lead oxide. The cast pellets were, however, deep yellow in colour and were stored in the same way as the other slags in a dessicator.

2.4.3 The solid dispenser

Slag additions to the open top bubble were made using a solid dispenser which was built in pyrex. The dispenser was designed such that it provided addition of the slag into the atmposphere-controlled lead pot without air leaks, as well as providing an inlet for the inert gas. A schematic representation of the solid dispenser is shown in fig. 2-13.

Connection of the dispenser to the lead pot was made through the port K shown in fig. 2-14. The tail,E of the dispenser was passed through the sleeve,J in the modified window unit, M. The contact between the glass E and the ring, I was sealed with an 'O' ring while the threaded ends of the sleeve, J were wrapped with PTFE tape before coupling.

The modified window unit was water-cooled and was mounted in place of the original flat window using an 'O' ring seal. The setting was such that the port, K on the modified window was vertically above the centre of the bubble (see fig. 2-14). This new arrangement restricted illumination of the inside of the lead pot but allowed a fairly good visualization of the OTB. The bubble was viewed at an angle of 30° to the vertical through a 38 mm diameter pyrex disc which was clamped to the window unit with a brass disc and utilized an 'O' ring seal. The entire arrangement was later tested for leaks and was found to be gas tight.

Prior to the start of a slag addition experiment the lead was deoxidized using forming gas (25% H_2, 75% N_2). The slag pellet was charged into the dispenser by holding down rod A and raising Cl using the sliding seal B, which was protected by a smear of silicone grease. The gas chamber of the dispenser was subsequently purged using high purity argon which had been dried by passing it through a silica gel drying column. The gas entered the dispenser at H and left through the valve F at G. Care was taken to avoid pressure build-up or gas suck-back in the dispenser by passing the gas leaving at G through a glass bubbler containing heavy machine oil. Typical argon flow-rates used were of the order of 600 ml/min and the purging was complete in about 5 mins.

A	-	Glass rod
B	-	Sliding seal
C1,C2	-	Glass cones
D	-	Valve; sliding fit
E	-	Dispenser tail
F	-	Valve; stop cork
G	-	Gas outlet
H	-	Gas inlet

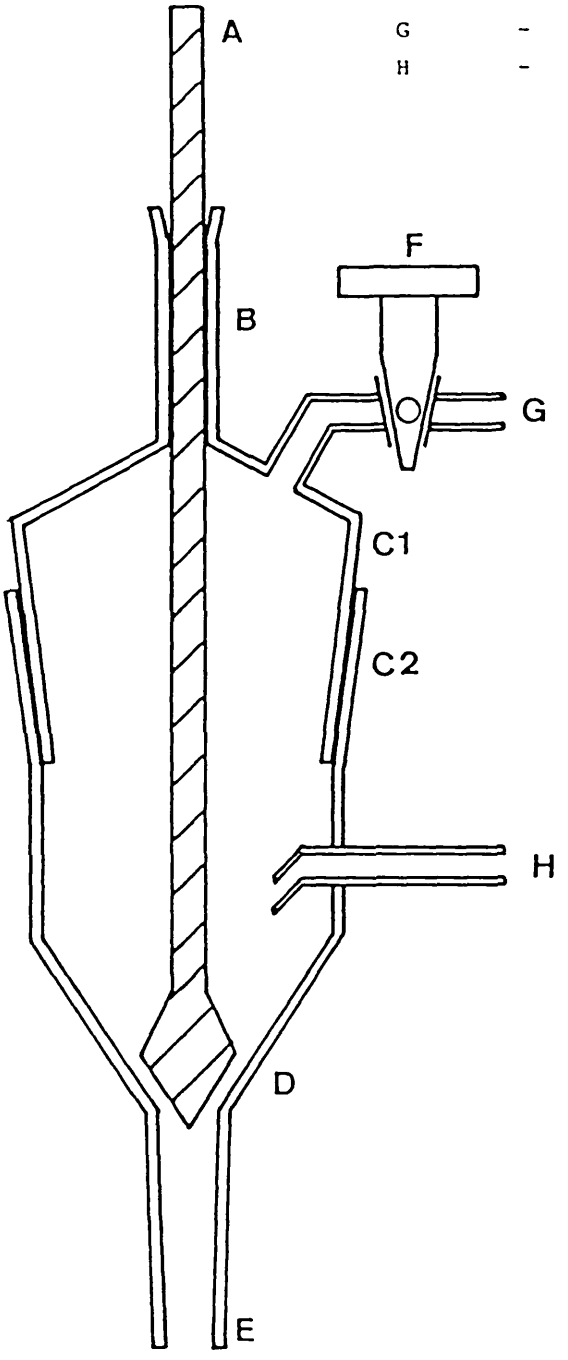

Fig. 2-13: The solid dispenser (schematic diagram)

I - Brass ring with 'O' ring seal
J - Brass sleeve
K - Port opposite OTB
L - Glass window
M - Modified window unit
N - Reactor lid

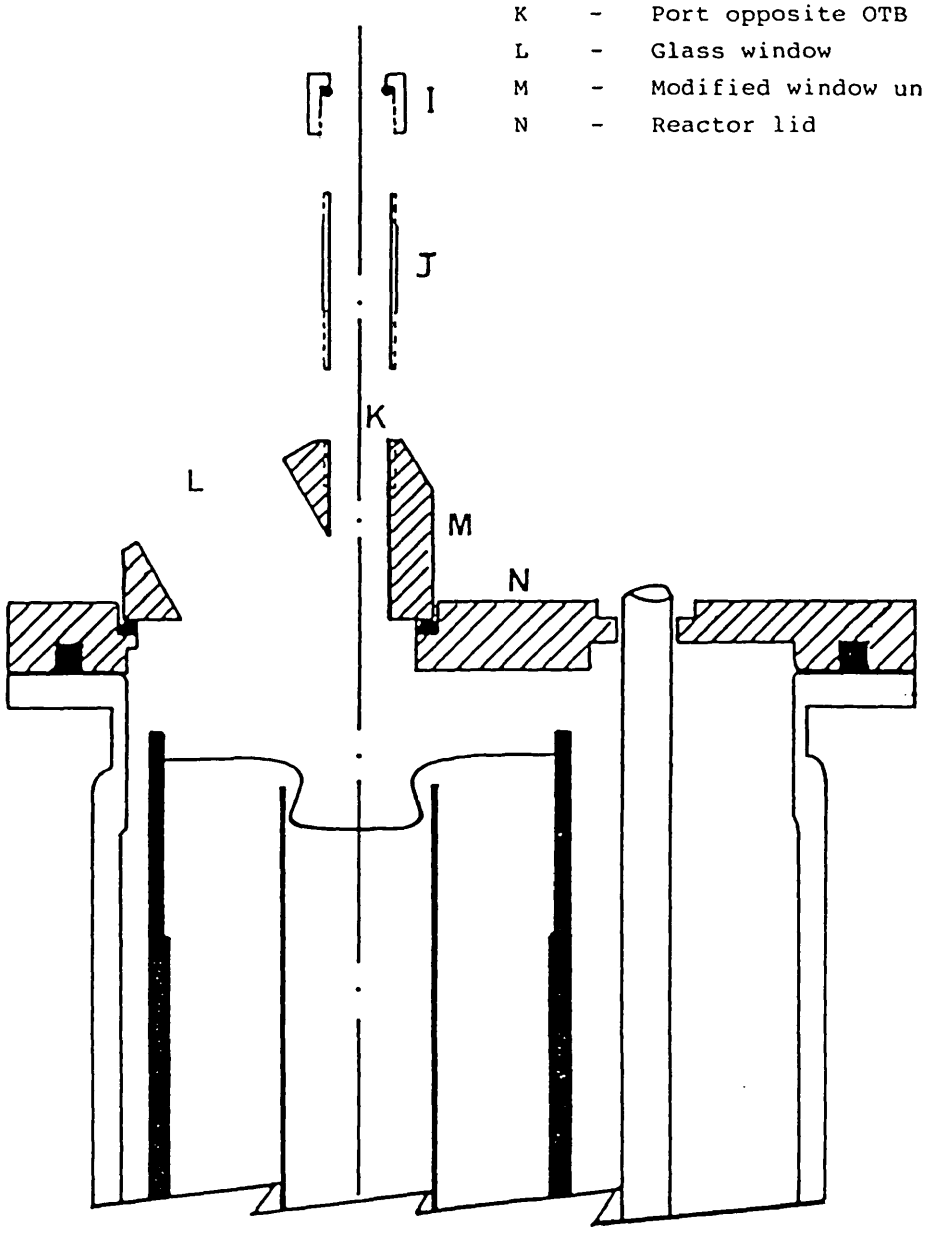

Fig. 2-14: The lead OTB pot - New arrangement for slag additions

After the purging of the gas volume of the dispenser the rod A was lifted slightly (~5 mm) while holding the upper cone in place at C and the tap F closed. This diverted the flow of the inert gas to pass through the lead pot. The flow of the forming gas was stopped and consequently the inert gas purged the gas chamber of the lead pot. The purging of the lead pot continued until the probe potential of the outlet gas reached a steady value (see fig. 2-12). The slag pellet was then allowed to fall through E into the OTB by raising the 'stopper rod', A.

2.4.4 General

The lead apparatus was operated at a temperature of 450°C throughout the duration of the slag addition runs and the subsequent lead refining experiments. The bubble was formed initially from a surface cleaned by flooding over the outer weir. Oxygen potential changes in the liquid lead and in the outlet gas were monitored throughout the duration of the experiments, using the appropriate solid electrolyte cells. A series of photographs of the open top bubble were also taken to help illustrate the behaviour of the slags in the bubble. In some runs a movie camera was used.

Details on the photographic technique are as follows:

Camera type:	Leica
Film type:	Ilford HP5
Exposure:	1/500
F stop:	F8
Lighting power:	350 watts
Movie camera:	Bolex Paillard H16 Reflex
Film speeds:	16, 24 pps
F stop:	F22

2.5 OTB IN Fe-C

The long-time objective of this work had been to engineer the open top bubble in molten iron and use it to study some reactions at iron-making temperatures. This would yield results of particular interest to steelmakers and in the general area of gaseous and powder injection metallurgy.

The studies with both the room temperature and molten lead systems had provided information on the fluid flow in an open top bubble and on working with reactive metal systems at high temperatures. This experience has been used in the design of a new OTB unit which would be used in molten iron.

The main objective of the design was to develop a simple system geometry which will work in molten iron-carbon alloy using graphite as the material of construction and utilize some of the existing parts of the OTB rig. The advantages of using graphite more than offset its limitations. It is very cheap, easily machinable and has good thermal shock resistance.

2.5.1 Description of the rig

The assembly drawing for the new OTB apparatus is shown in fig. 2-15. The apparatus was designed such that most of its components in contact with the molten metal were made in graphite, while those above the liquid metal level were made in mild steel, aluminium or brass. The main components of the apparatus are as follows.

1. The bubble generator

This forms the main chamber through which the liquid metal flows to the centrifugal pump. Its main features are illustrated in fig. 2-16. The generator consists of the circular weir (E), the pump shaft casing (J) and the pump chamber (F). Both the weir and the pump shaft casing were also designed to act as supports for the perforated screens (D) inserted to stabilize fluid flow in the system, as well as locate the generator inside the graphite pot (A). The pump shaft casing is the main support holding the bubble generator

in the liquid metal and was designed to withstand the buoyancy force on the generator when immersed in the liquid iron-carbon alloy.

2. The centrifugal pump

Liquid circulation in the new apparatus is induced by a centrifugal pump. A cross-section through the pump chamber is shown in fig. 2-17. The pump shaft is made out in graphite while the impeller is in 'Pyrophylite' (a compound consisting mainly of $A\ell_2O_3$ and SiO_2). The graphite portion of the pump drive shaft was designed to run in close contact with its graphite casing so as to prevent wobbling.

3. The secondary water-cooled lid

This lid was designed in mild steel to locate the graphite pot of the apparatus as well as to reduce heat transfer to the lid. On the surface of this mild-steel water-cooled ring are three studs designed to serve as a guide in locating the existing brass lid of the lead apparatus.

4. The upper segment

The upper section of the apparatus consists mainly of metallic parts, viz. the water jacket (P), the platform (Q), the bubble adjustment screw (R), the mild steel extensions of the pump drive shaft (H) and its casing (I); shown in fig. 2-15.

The pump shaft casing (I) is connected to its mild steel extension using a 'Pyrophylite' ring. The water jacket (P) was included to cool the steel shaft casing and hence minimise heat transfer to the platform (Q). The pump shaft itself will be cooled by forcing compressed air down the narrow track (K).

The platform (Q) was designed to be fairly massive to reduce any vibrations due to the pump drive system mounted on its top surface. Within the platform is the bubble adjustment screw designed such that the level of immersion of the bubble generator in the liquid metal can be varied without affecting the pump alignment, as set by the screws (W).

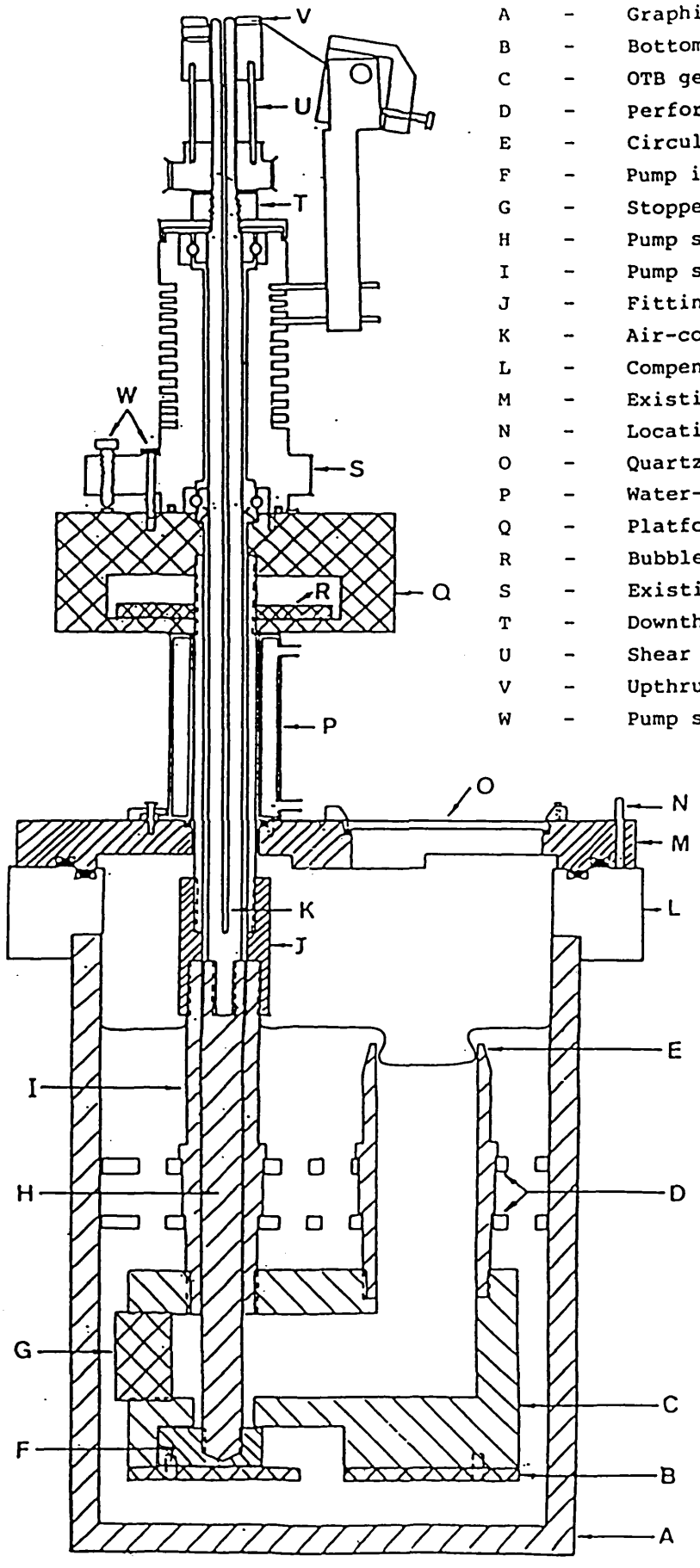

A	-	Graphite pot
B	-	Bottom plate
C	-	OTB generator
D	-	Perforated screens
E	-	Circular weir
F	-	Pump impeller
G	-	Stopper
H	-	Pump shaft
I	-	Pump shaft casing
J	-	Fitting ring
K	-	Air-cooling channel
L	-	Compensating ring
M	-	Existing water-cooled ring
N	-	Locating stud
O	-	Quartz window
P	-	Water-cooled jacket
Q	-	Platform
R	-	Bubble level adjustment screw
S	-	Existing pump unit
T	-	Downthrust plate
U	-	Shear pins
V	-	Upthrust bearing
W	-	Pump shaft alignment screws

Fig. 2-15: OTB in Fe-C (proposed assembly)

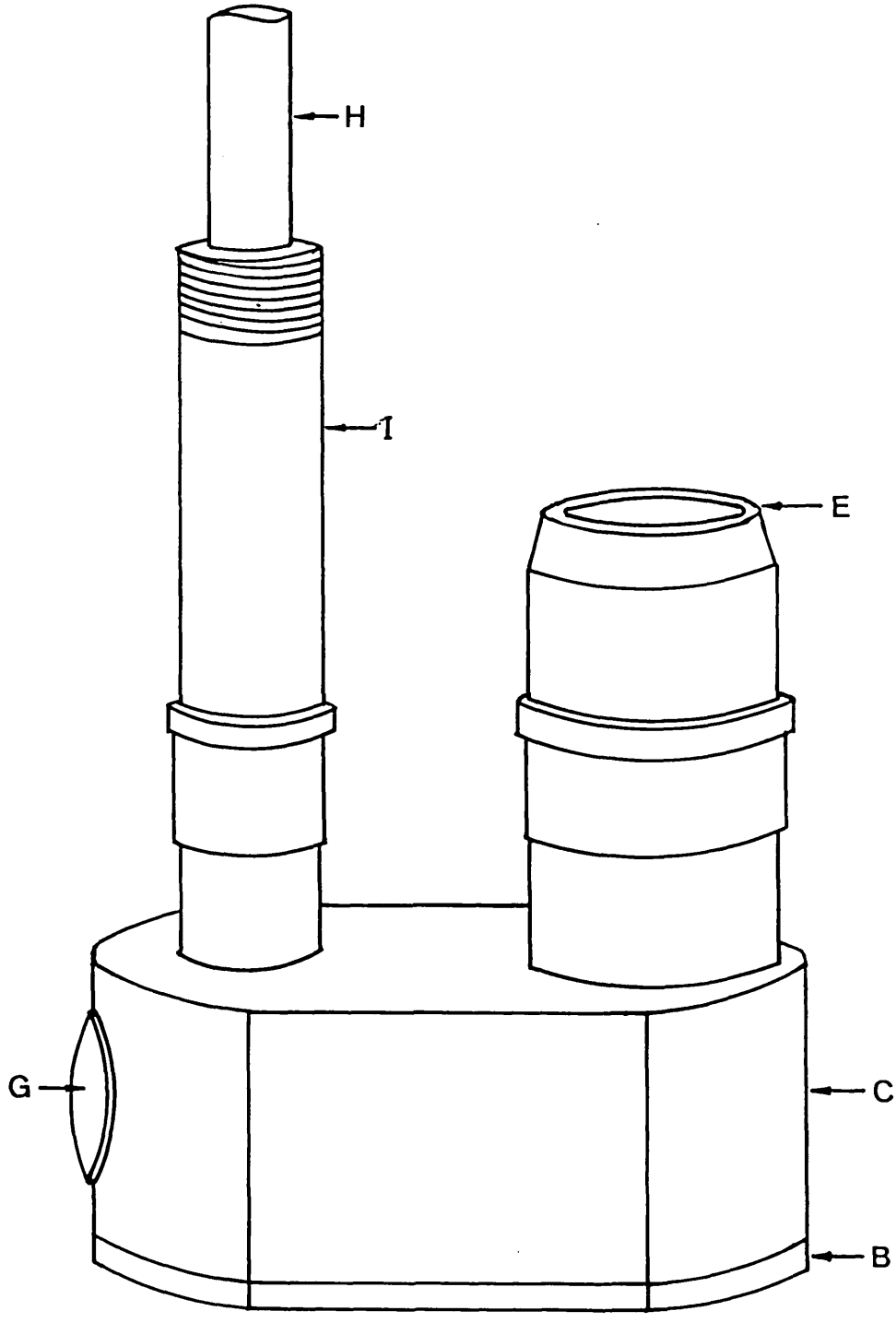

Fig. 2-16: The open top bubble generator

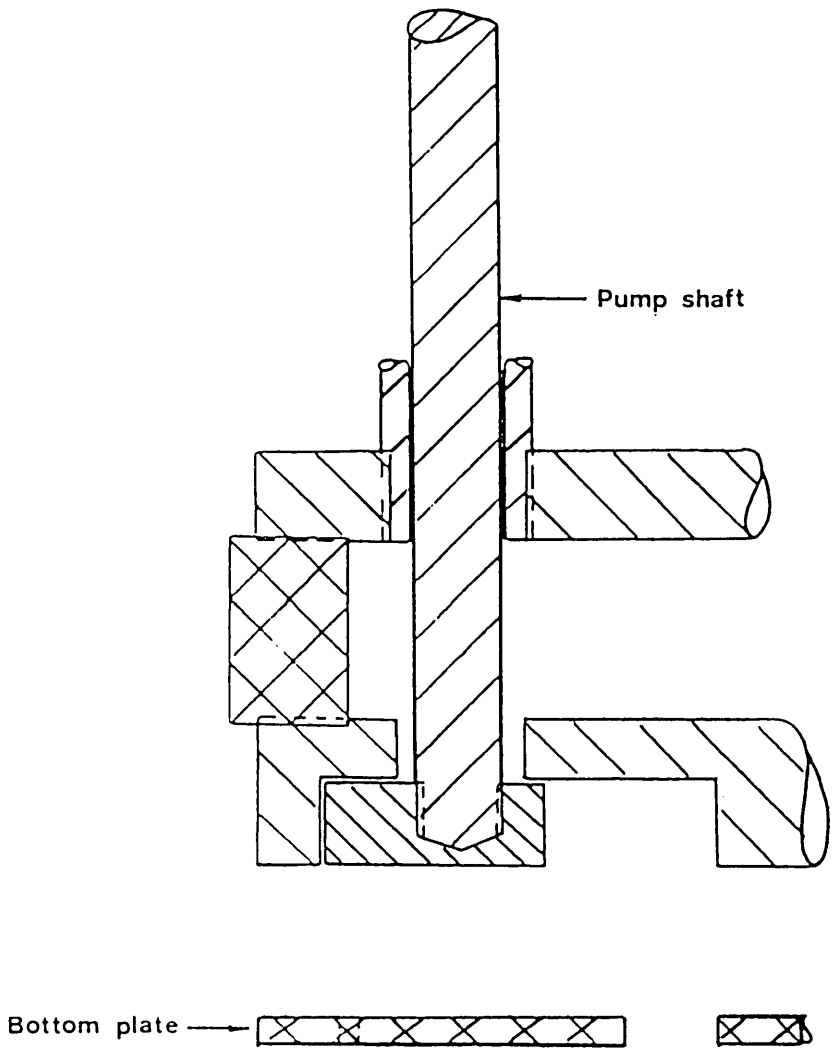

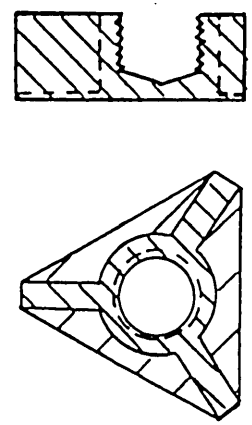

PUMP IMPELLER

Fig. 2-17: Details of the pump chamber of the new OTB unit

2.5.2 Setting up the new apparatus

The new OTB unit has certain engineering advantages over the existing unit built in mild steel. Prominent amongst these advantages is the absence of valves and bearings in the region of the molten metal. The open top bubble will be created ina fashion exactly opposite to that in the existing rig. Bubble 'velocity' will be varied by raising or lowering the bubble generator as need be, using a control screw. The new design also utilized some of the existing infrastructures (e.g. the brass lid and the pump housing). Heating will be done using an existing induction furnace.

A model of the new OTB apparatus built to the above design was made in perspex and operated in water. Studies on this model showed that the main features of the resulting open top bubble were the same as in the existing apparatus. The bubble parameters (weir height and bubble depth) could be varied changing the immersion depth of the bubble generator. Work has been completed on most of the components of the high temperature apparatus. Whilst the setting up of this system would present many potential engineering problems, with skill and ingenuity the above design could probably be made to operate in molten iron. There was insufficient time for the author to start on this work.

CHAPTER 3

RESULTS AND THEIR INTERPRETATION

3.1 THIRD PHASE IN OTB AT ROOM TEMPERATURE

Solid particles and liquid droplets were injected into the room temperature open top bubble to simulate particle injection and slag formation as in injection steel-making. The main idea behind these experiments was to study the behaviour of particles and/or slag films carried by rising bubbles in metal baths.

The main stages of spreading are defined below, as they occurred in order of increasing bubble base heights:

- Total spreading (TS), when the third phase covers all bubble surfaces.
- Wall spreading (WS), when the third phase covers the bubble base and sides, but not the top side.
- Basal spreading (BS), when only the bubble base is covered by the third phase.
- Stripping (ST), the turbulent trailing-off of the third phase from the bubble base into the wake.

Aluminium flake particles were used in the solid stripping experiments. The data are given in fig. 3-1. It was observed that at low bubble 'velocities', once total spreading was achieved, any extra aluminium flakes added were stripped from the bubble base. As the bubble base was lowered (i.e. increasing bubble 'velocity')there was a gradual change from total spreading to basal spreading followed by a change to stripping. At very low flowrates basal spreading occurs over a wide range of bubble base heights before the onset of stripping. At such low flow-rates it was also observed that the particles covering the bubble base circulate within horizontal vortices of variable diameters in the base of the bubble.

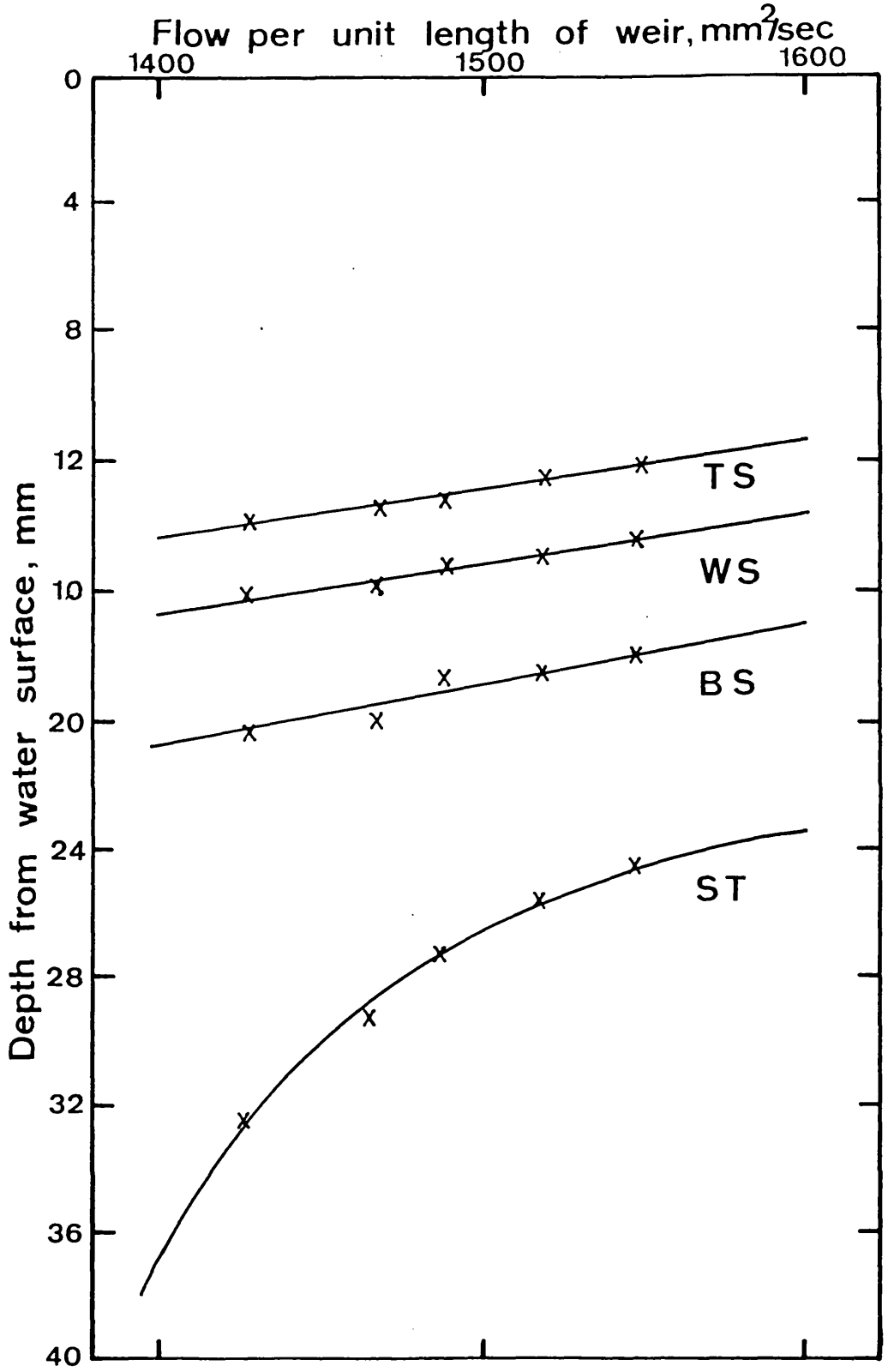

Fig. 3-1: Stripping of a third phase - Solid particle phase

Liquid stripping experiments were done with Octanol (OCT), Light Machine Oil (LMO), and Heavy Machine Oil (HMO), in their order of increasing viscosity but decreasing spreading coefficients. Stripping rates were measured to increase initially with flowrate but reached a constant value at about 1800 mm^2/sec (fig. 3-2). Octanol was observed to strip nearly as soon as it was put in, whereas heavy machine oil took a considerable bubble 'velocity' to strip.

From the above measurements it was not clear whether it was viscosity or spreading that was most critical in stripping. Wiafe[32] used an additional liquid (Heptanoic acid, $\Delta\sigma$ = 36.4 dynes/cm, μ = 4.5 cP) in his measurement of the 'critical depth' of stripping and concluded that the viscosity effect was paramount. Data obtained from this work (fig. 3-2) suggest an important influence of spreading. Since viscosity affects the rate of spreading for a given $\Delta\sigma$ the two are not independent.

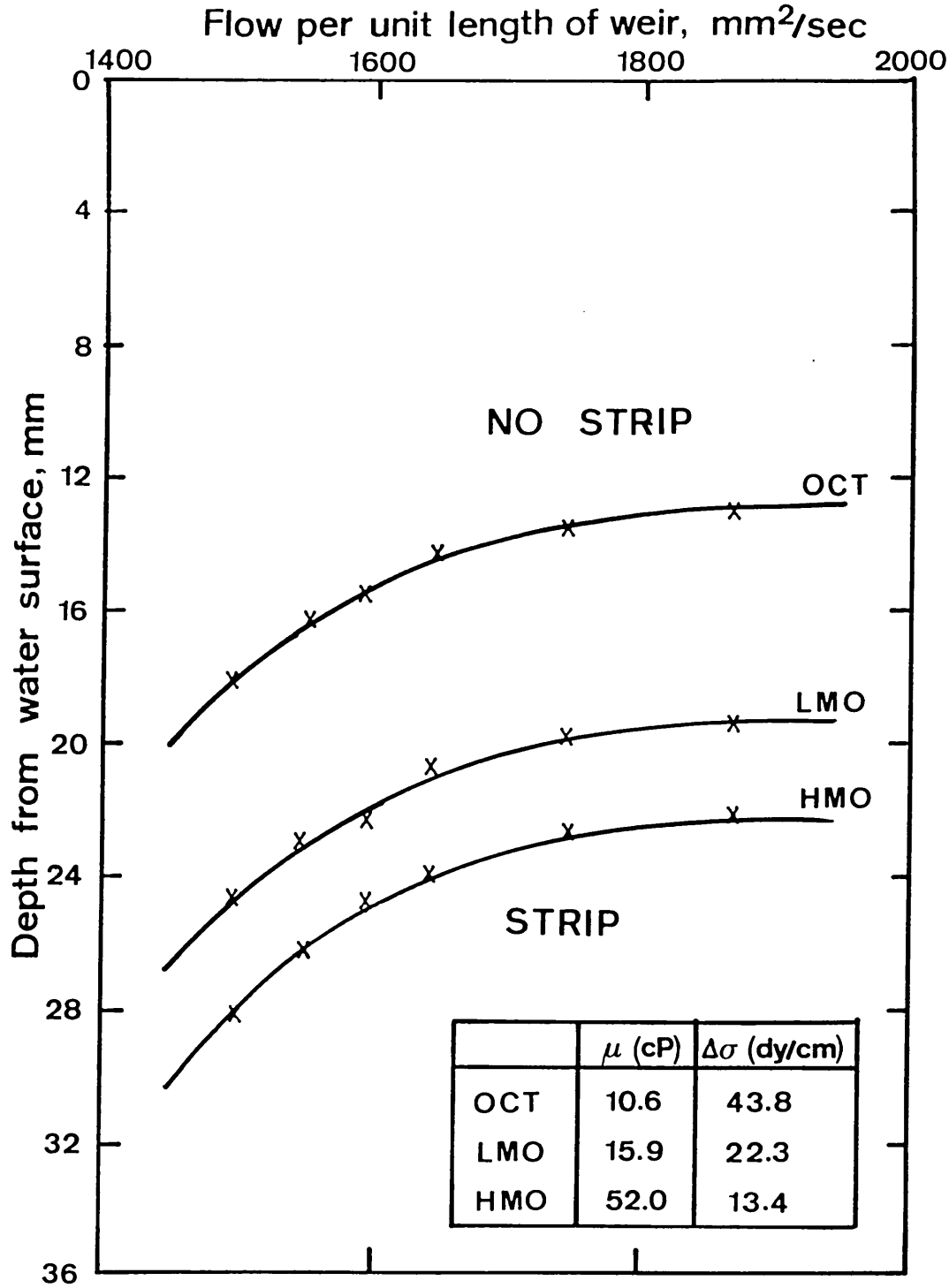

Fig. 3.2: Stripping of a third phase - Liquid phase

3.2 OXYGEN GAS ADDITION TO LEAD OTB

The main aims of the oxidation experiments were:

(i) To observe the formation and behaviour of the slag phase formed by oxygen gas injection inside the open top bubble.

(ii) To measure the oxygen solubility in liquid lead.

(iii) To study the kinetics of oxygen dissolution in liquid lead.

The reaction of molecular oxygen with liquid lead can be represented by the equations

$$Pb(\ell) + \tfrac{1}{2}O_2(g) \rightarrow PbO(s) \qquad (3.1)$$

Below oxygen saturation in lead, solid lead oxide will react to yield liquid lead and dissolved oxygen:

$$PbO(s) \rightarrow Pb(\ell) + [0] \text{ (in } Pb(\ell)) \qquad (3.2)$$

further oxidation of the lead oxide via the reaction

$$3PbO(s) + \tfrac{1}{2}O_2(g) \rightarrow Pb_3O_4(s) \qquad (3.3)$$

is a possibility but requires oxygen pressure in excess of 0.25 atmospheres at 450°C.

Using equations (3.1) and (3.2), the appropriate equilibrium for oxygen dissolution would then be written as

$$\tfrac{1}{2}O_2(g) \rightarrow [0] \text{ (in } Pb(\ell)) \qquad (3.4)$$

Taking activity equal to wt%[0] at infinite dilution to be the standard state, the equilibrium constant for reaction (3.4) is

$$K = h_0/p_{O_2}^{\frac{1}{2}} = f_0 \text{ wt\% } [0]/p_{O_2}^{\frac{1}{2}} \qquad (3.5)$$

where h_0 and f_0 are the Henrian activity and activity coefficient of oxygen, respectively.

Alcock and Belford[34] have shown that oxygen in liquid lead obeys Henry's law up to 700°C, so that eqn. (3.5) reduces to

$$K = (\text{wt\% } [0])/p_{O_2}^{\frac{1}{2}} \qquad (3.6)$$

3.2.1 Observations and probe response types

Typical behaviour of the open top bubble during the pulse oxidation experiments are summarized in Table 3-1.

Each additional oxygen pulse caused a suppression of the basal ripples in the bubble. The time taken for the ripples to return (ripple return time) ranged from about 10 seconds to several minutes and was dependent on the temperature of the liquid lead, bubble 'velocity' and the amount of oxygen in solution.

Initial pulses only 'darkened' the bubble surface and the ripples returned soon after the end of the oxygen addition. Later pulses gave rise to dark oxide flakes, seen to thicken with successive pulses, passing through a spectrum of colours and later turning golden brown. The oxide formation started from the bubble base and progressively spread across the whole lead surface. At high temperatures some grey oxides formed during the initial oxygen pulses. These persisted in the bubble base, forming a thin film which made ripple return take longer and difficult to observe.

Thermodynamic calculations

The activity of oxygen in the lead was measured using an oxygen probe. The cell used is represented by:

Pt contact	$O_2(g)$ 1 atm.	$ZrO_2 - y_2O_3$ solid electrolyte	[0]	Iron pot contact

The overall cell reaction is

$$\tfrac{1}{2}O_2(g) \rightarrow [0] \text{ (in Pb}(\ell)), \Delta G_1^{\circ} \qquad (3.4)$$

TABLE 3.1

Oxygen Injection - Bubble Appearance
(Run A_7; T = 570°C)

No. of pulses	Ripple-return time, t_r (secs)	C/C_{sat}	Appearance on Oxygen Injection
1	10	10^{-4}	Ripple suppresion due to formation of a dark 'oily' film.
16	13	0.09	Formation and growth of brown oxide flakes at bubble base.
33	35	0.48	Oxide flake surrounded by a purple tinge.
40	67	0.67	Greenish appearance surrounding oxide island.
42	120	0.76	A spectrum of green/purple films on whole lead surface.
44	260	0.84	Golden brown colour begins to appear.

At oxygen saturation in lead the reaction becomes

$$\tfrac{1}{2}O_2(g) + Pb(\ell) \rightarrow PbO(s) \ , \quad \Delta G_2^o \tag{3.1}$$

for which the reversible cell potential, E_{sat} is given by

$$E_{sat} = -\frac{\Delta G_2^o}{2F} \tag{3.7}$$

where F is Faraday's constant (~96480 joules/volt) and ΔG_1^o dand ΔG_2^o are Gibb's free energy changes of reactions (3.4) and (3.1), respectively. Using thermodynamic data from Kubaschewski and Alcock[74], ΔG_2^o is given by

$$\Delta G_2^o, \ J = \begin{cases} -224890 + 110.04T \ (600 \leqslant T,K < 760) \\ -223007 + 107.53T \ (760 \leqslant T,K < 1150) \end{cases} \tag{3.8}$$

Below oxygen saturation, reaction (4) takes place with a free energy change given by

$$\Delta G_1^o = -RT \ \ell n \ a_{[O]} \tag{3.9}$$

and the cell potential, E given by

$$E = -(RT/2F) \ \ell n \ a_{[O]} \tag{3.10}$$

At oxygen saturation, $a_{[O]} = a_{[O \ sat]}$ and

$$E_{sat} = -(RT/2F) \ \ell n \ a_{[O \ sat]} \tag{3.11}$$

$$\therefore \quad E-E_{sat} = -(RT/2F) \ \ell n \ (a_{[O]}/a_{[O \ sat]}) \tag{3.12}$$

Since oxygen in lead obeys Henry's law in the temperature range of interest[34], eqn. (3.12) may be expressed in concentration terms, thus:

$$E-E_{sat} = -(RT/2F) \ \ell n \ (C/C_{sat}) \tag{3.13}$$

Probe response types

Typical responses monitored by the oxygen probe during pulse oxidation are shown in figs. 3-3, 3-4 and 3-5. The electrical potential was plotted from high to low in order to give the correct sense of the increase in oxygen potential of the lead.

Two main types of probe responses were observed, depending on the oxygen potential in the lead. Fig. 3-3 shows the probe response to pulse oxidation at a very low oxygen potential in lead; a rapid rise in oxygen potential followed by a slow decay. This response is known as type A response.

The trace obtained from the probe response during the middle course of the same run is shown in fig. 3-4. This is the type B response; a rise in oxygen potential and a steady value after oxygen dissolution.

Type A response is consistent with the oxidation and removal of impurities in the lead, in a classic refining reaction, as well as the reaction of the dissolved oxygen with the mild steel container. The amount of oxygen dissolved in the lead, as measured by the oxygen probe, was determined by two competing reactions:

(i) the oxygen supply reaction

$$\tfrac{1}{2}O_2(g) + Pb(\ell) \rightarrow PbO(s) \rightarrow Pb(\ell) + [0] \qquad (3.14)$$

followed by

(ii) the much slower oxygen consumption reaction,

$$[0] + [B] \rightarrow BO(s) \qquad (3.15)$$

for any impurity B dissolved in the lead.

The reaction of the mild steel pot may occur via any of these processes:

$$4PbO + 3Fe \rightarrow Fe_3O_4 + 4Pb \qquad (3.16)$$

$$4[0] + 3Fe \rightarrow Fe_3O_4 \qquad (3.17)$$

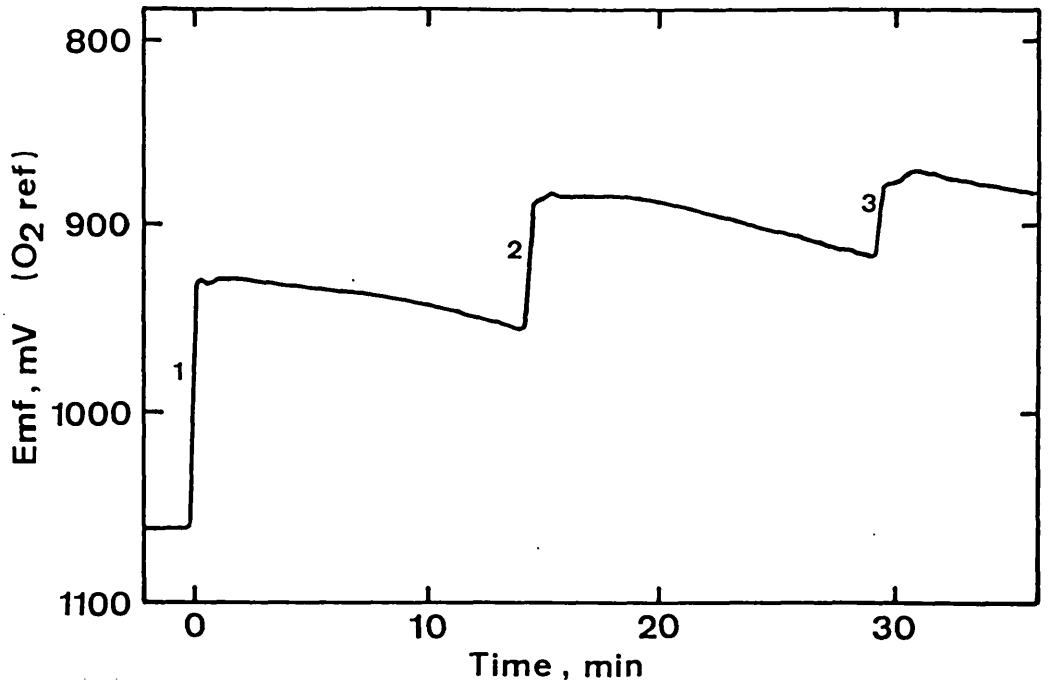

Fig. 3-3: Probe response to the addition of 2-second pulses of 20 ml pure oxygen at a low oxygen potential in the lead. Run 2, T = 500°C.

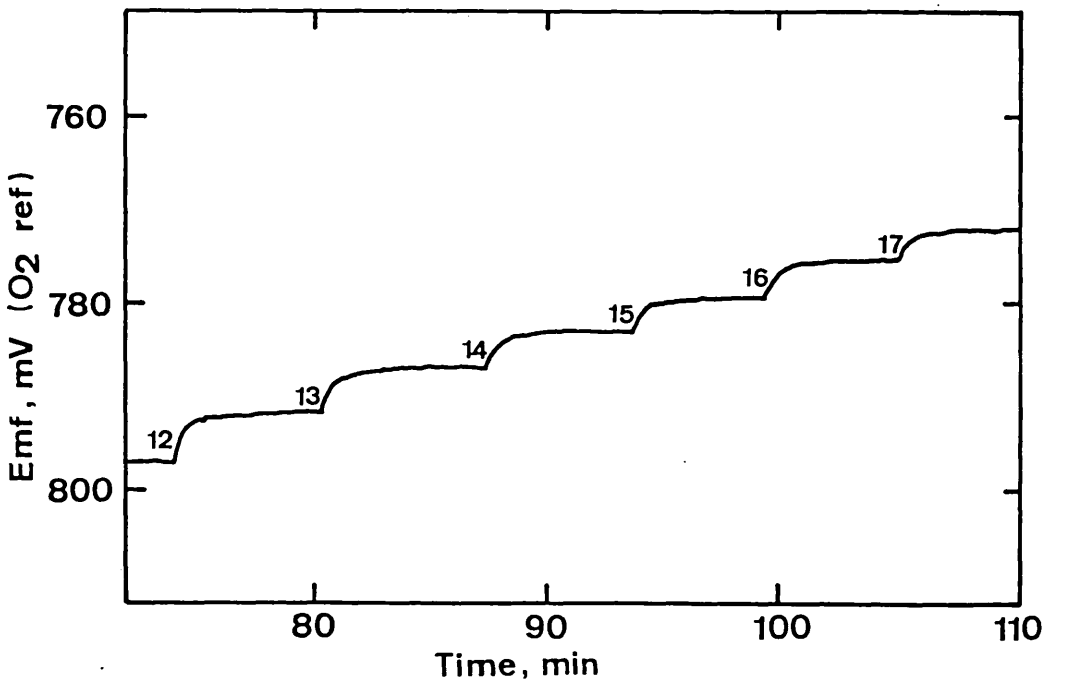

Fig. 3-4: Probe response to the addition of 2-second pulses of 20 ml pure oxygen at a medium oxygen potential in the lead. Run 2, T = 500°C.

The oxygen potential diagrams given in figs. 3-6 and 3-7 are very useful in understanding (a) the role of the impurities in lead and (b) the mild steel container reaction with the added oxygen. The iron in the container was present at unit activity and iron must have been present at reduced activities in lead. Fig. 3-7 also shows that iron in lead could be effectively removed by oxidation. This may have led to the formation of the grey oxide which was observed in the open top bubble after oxygen addition.

In addition to the iron impurity, the lead also absorbed hydrogen from the forming gas at low oxygen potentials, which would later react with the added oxygen via the process:

$$[O] + 2[H] \rightarrow H_2O(g) \qquad (3.18)$$

After deoxidation, there was in fact water condensation on the glass window mounted on the water-cooled lid of the OTB apparatus. Smithells[75] gives a figure for solubility of hydrogen in lead at 500°C of 9.8×10^{-2} ppm. Hanson[78] quoted one value of 8.9×10^{-2} ppm at 500°C and another value $<10^{-2}$ ppm.

Oxidation of the iron pot to Fe_3O_4 must also have occurred over the working range of oxygen potential, the rate being limited by the properties and thickness of the magnetite layer. The working range of the oxygen potential in the lead was between $C/C_{sat} = 1$ (the Pb/PbO equilibrium potential) and $C/C_{sat} \sim 10^{-5}$.

When lead at 450°C was being reduced with forming gas after oxygen saturation, the oxygen probe potential would rise over night from oxygen saturation at about 755 mV (oxygen reference) to the range 1100-1150 mV and stabilize. Comparing this with the Fe/Fe_3O_4 equilibrium potential at the same temperature (fig. 3-7), it was deduced that the lower limit of oxygen potential was probably set by the reduction of Fe_3O_4 to Fe on the walls of the container. When the pot was opened after cooling there was evidence of a brown magnetite layer on the inside surface of the iron container. This layer would have been partially reduced during deoxidation and would slowly form during the oxidation experiments.

Type B response represents only the oxygen supply reaction to the lead, i.e.

$\frac{1}{2}O_2 \rightarrow [O]$, via PbO

This response occurred after the removal of the dissolved impurities and after a significant layer of magnetite had formed, limiting further oxygen consumption via the formation of Fe_3O_4 on the container walls.

The experimental conditions for the transition from probe response type A to type B changed from one experiment to another. Hence the transition was thought to be dependent on one or more of the following features:

(i) Increased contamination over the period the apparatus had been used. Conochie[16] showed in his early runs that type A response was not observed.

(ii) Varying times of deoxidation, affecting the amount of iron oxide reduced back to metal.

(iii) The time allowed between oxygen pulses varied, and in most cases equilibrium between dissolved oxygen and impurity was not reached before the next oxygen pulse.

(iv) Changes in the operating temperature which affect the amount of impurity materials that can be dissolved in the lead.

(v) Occasional drossing of residual oxides floating on the lead surface which helped in 'refining' the lead.

3.2.2 Mixing characteristics of the HOTB pot

The oxygen probes immersed in the liquid lead were located such that they reflected on the mixing characteristics of the open top bubble pot: Probe 2 was located in the well mixed region of the pot (WM) and Probe 1, in the less mixed region (LM), as shown in fig. 2-6. Their responses to pulse oxidation of the lead were measured simultaneously, as shown

in fig. 3-5. The results display four important features:

(i) The oxygen concentrations rose to about the same level at both positions.

(ii) At very low oxygen potentials in the lead ($C/C_{sat} \leq 10^{-3}$), oxygen depletion due to impurity reaction was faster in the well mixed region of the lead pot, and hence a faster probe potential decay was registered in that region (fig. 3-5A).

(iii) In the low to medium oxygen potential range $10^{-3} < C/C_{sat} \leq 0.2$, type A response persisted but with no appreciable variations in the oxygen potential decay rates in the different regions of the apparatus. The oxygen depletion rate was thus independent of the mixing rates in this oxygen potential regime (fig. 3-5B).

(iv) At oxygen levels in the range $0.2 < C/C_{sat} \leq 1.0$, the probe's responses to pulse oxidation of the lead changed to type B, but were still independent of the probe location and hence the mixing rates in the apparatus.

The above results obviously have implications on oxygen dissolution in the lead and the subsequent impurity reaction.

At very low oxygen potentials in the liquid metal, the lead would be laden with impurities and its mild steel container substantially reduced. Thus the initial probe potential decay resulting from impurity reaction with the added oxygen was seen to be very strong, gradually getting weaker with subsequent oxygen additions. In the well mixed region, owing to the larger degree of turbulence caused by the rapid mixing, the dissolved oxygen is in faster contact with both the impurities and the container walls, thus accounting for the faster oxygen consumption in the region.

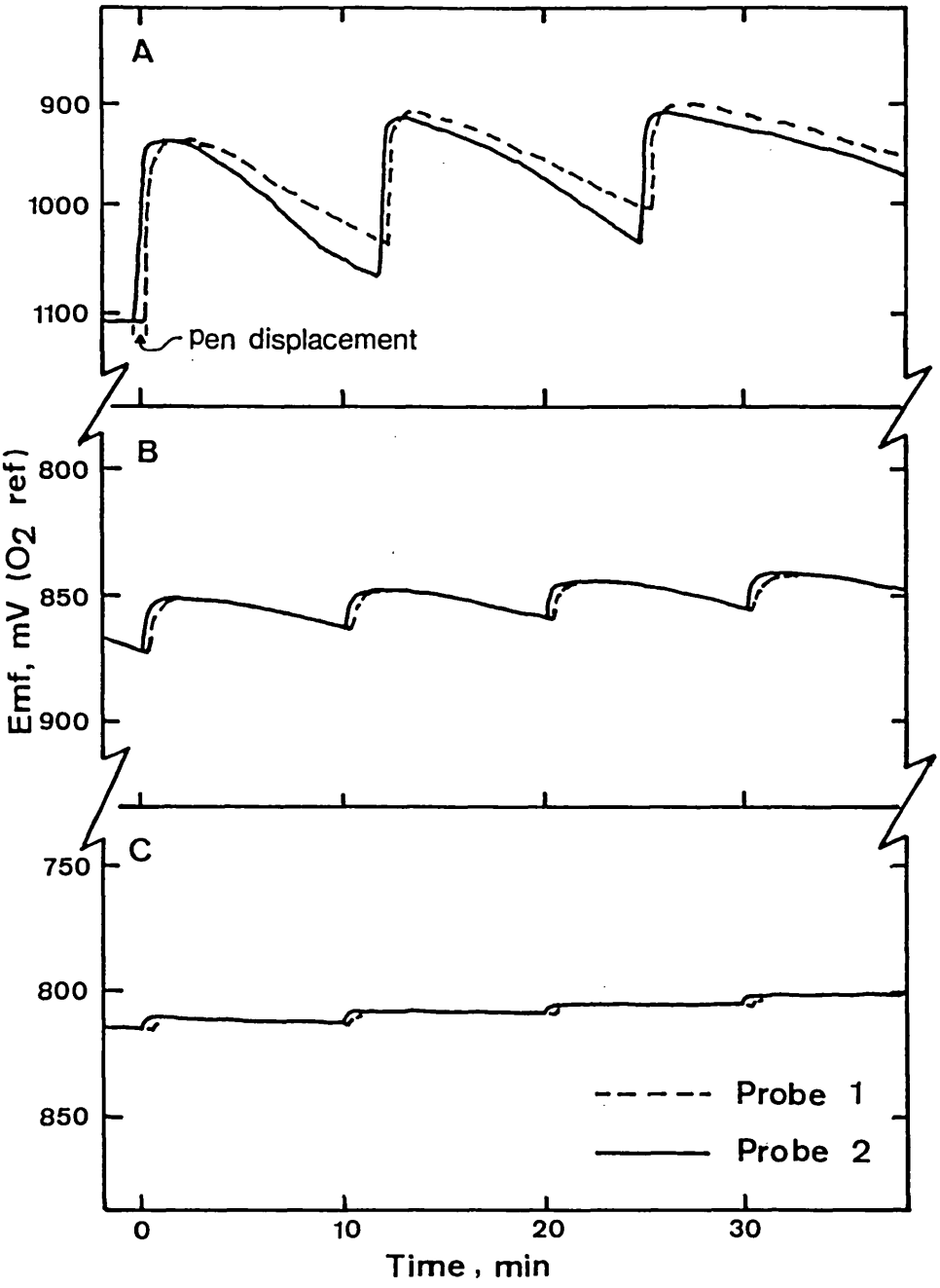

Fig. 3-5: Probe response to the addition of 2-second pules of 16.5 ml pure oxygen to the lead, reflecting on the mixing characteristics of the HOTB. Run 4, T = 450°C.

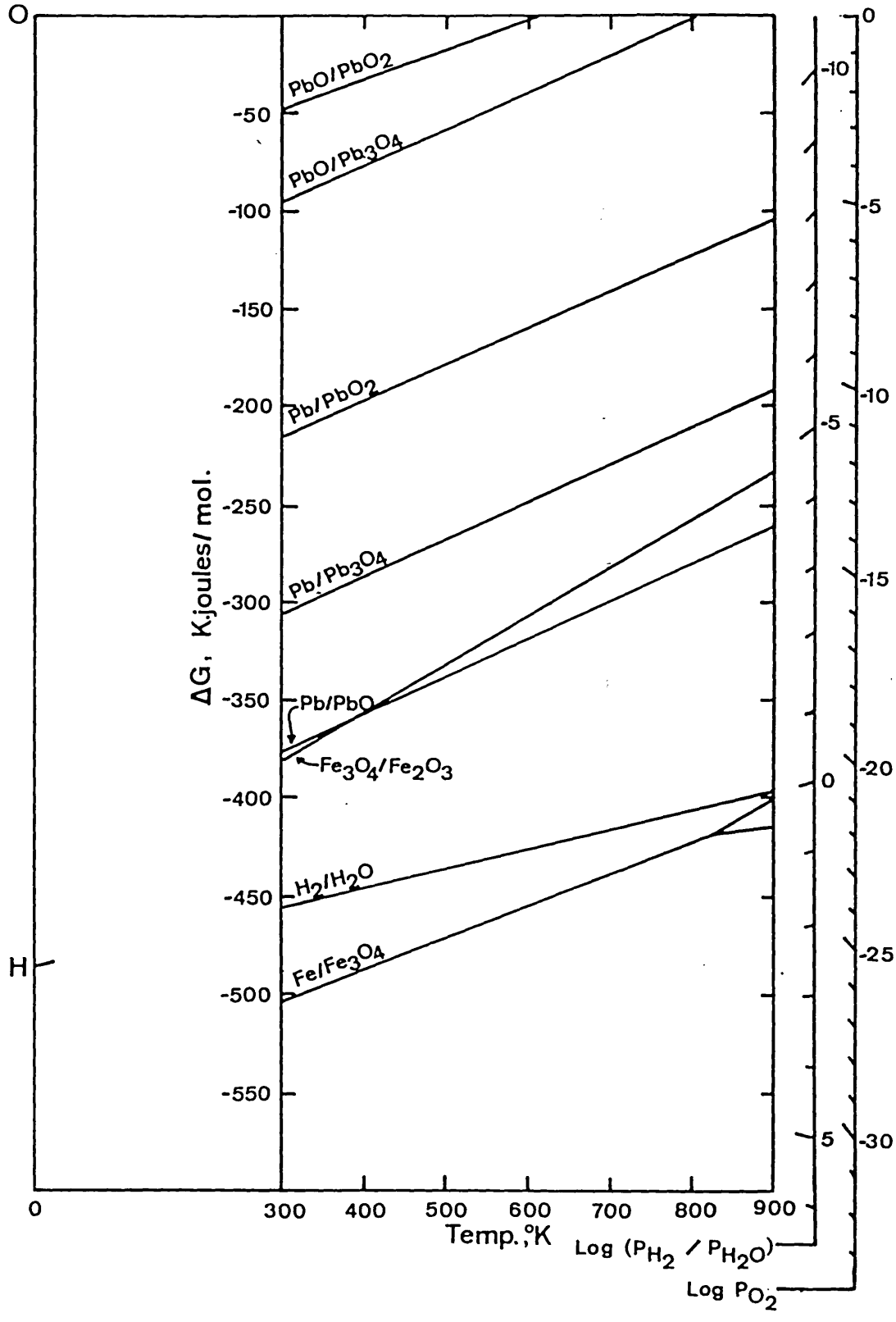

Fig. 3-6: Gibbs free energy diagram for selected oxides, per mole of oxygen consumed.

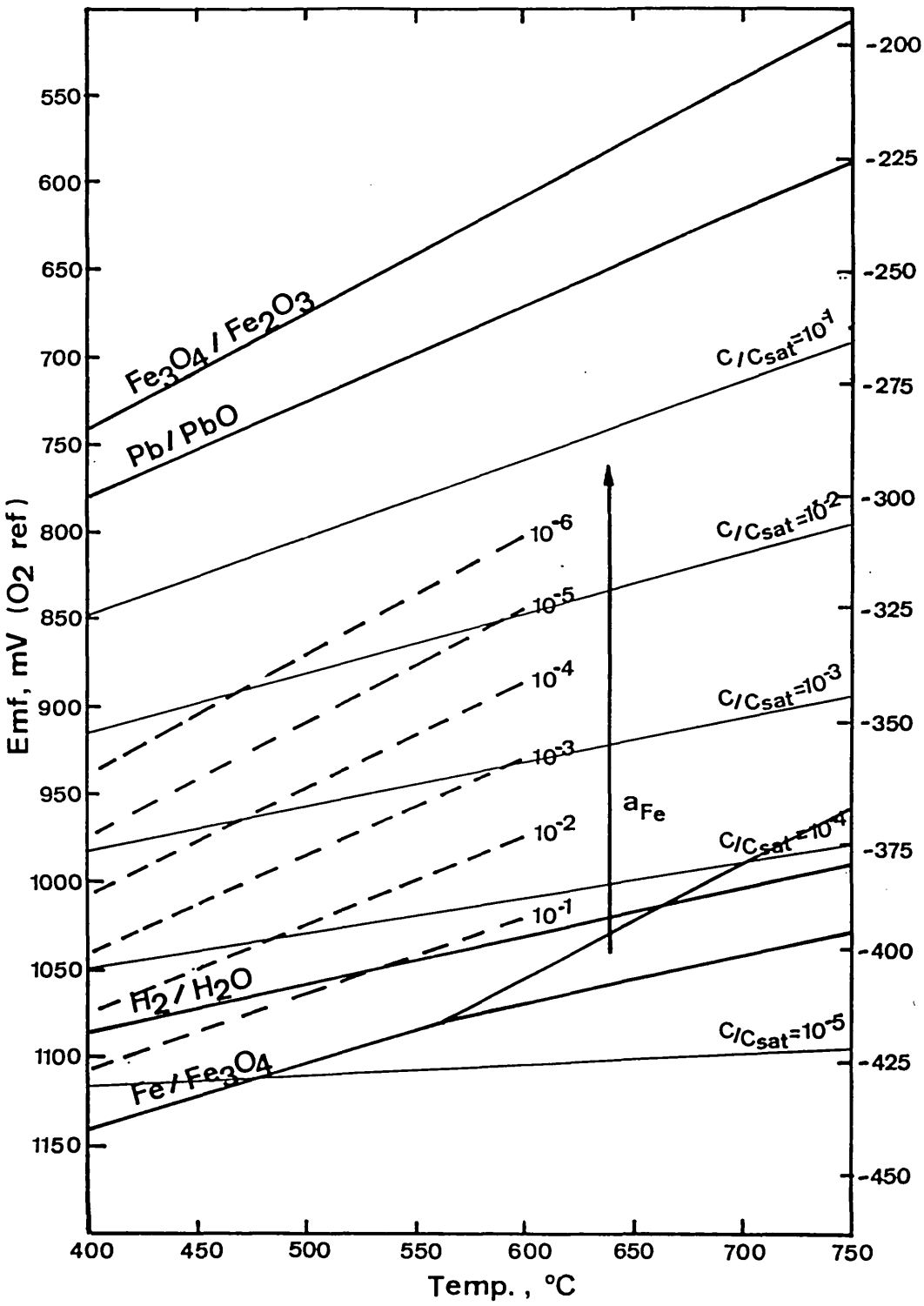

Fig. 3-7: Oxygen cell potential diagram for the relevant oxides in the HOTB pot.

Conversely, oxygen transport in the less mixed region would be slower.

With successive oxygen pulses, most of the dissolved impurities in the lead would be oxidized and a thin magnetite layer probably formed on the inside walls of the container. The rate controlling step in the oxygen consumption reaction would then be the rate of Fe^{3+} ion diffusion through the magnetite layer, and not its bulk transport rate. Hence the decay in the oxygen probe potential became independent of the mixing rate in the pot.

Oxygen probe response in the medium to high potential regime ($0.2 < C/C_{sat} < 1.0$) is typically type B: a rise in oxygen potential after oxygen addition, to a steady level. By this time nearly all the impurities in the lead had been oxidized (see fig. 3-7), the iron activity in lead being less than 10^{-7}. Also a sizeable layer of magnetite would have formed on the container walls, thus reducing the ability of oxygen to diffuse through the layer to an insignificantly low value. The oxygen probe response to input oxygen was thus respresentative of a direct supply of oxygen to the lead, as shown in fig. 3-5C).

3.2.3 Oxygen solubility measurements

The method used for calcualting the oxygen solubility in liquid lead is illustrated in fig. 3-8. The number of pulses of oxygen added is plotted against the amount of oxygen in solution in the lead, as measured by the oxygen probe. A line of best fit is then drawn through the points within the range $0.3 < C/C_{sat} < 0.8$ and extrapolated to C/C_{sat} values of 0.0 and 1.0. The volume of oxygen required to saturate the given mass of lead at the given temperature is then obtained as the product of the slope of the line and the volume of oxygen delivered per pulse.

The validity of this technique lies in the efficient oxygen utilization in the region $C/C_{sat} < 0.8$. Data for $C/C_{sat} < 0.3$ showed a smaller change in Emf than was predicted for simple oxygen absorption and this was attributed to the previously discussed impurity effect. Analysis for oxygen in

the outlet gas (see section 3.2.5) showed that when C/C_{sat} exceeded 0.8 oxygen was not completely reacted, which explains the smaller change in C/C_{sat} per pulse that is apparent near saturation.

In principle, the solubility of oxygen can be determined from the oxygen probe potentials before and after a single pulse, together with the probe electrical potential at oxygen saturation, but it was obviously preferable to use a series of oxygen pulses to cover most of the range of oxygen content.

Data for run A_7 in fig. 3-8a show that a 10 minute delay resulted in an increase in the oxygen potential of the system. A check was made on the leakage of air into the system. A check on all runs and subsequent plot of ΔE (pulse Emf change; $E_i - E_{i+1}$) versus the number of pulses for runs A_6 and A_7 suggested irreproducibility of pulses and apparent leakage of oxygen through the change-over valve as shown in fig. 3-9. This fault was rectified by changing the silicone rubber tubing in the valve and increasing the air pressure to the valve to ensure perfect cut-offs. The valve performed very well thereafter.

Oxygen solubility in lead was measured in the temperature range 450-610°C. The results obtained are summarized in Table 3-2 and plotted in fig. 3-12.

Oxygen solubility during steady addition

An attempt was made to measure the solubility of oxygen in liquid lead with continuous addition of the gas. Oxygen was introduced into the open-top bubble at low but steady flow rates of 4-15 ml/min. The solubility values that were obtained when this technique was employed were lower than those from the previous measurements, the difference narrowing as the oxygen flowrate decreased (see figs. 3-10 and 3.11). It was also observed that for the same flowrate the oxygen solubility measured in the 'bubble mode' was higher than that measured when the system was run in the 'overflow mode'.

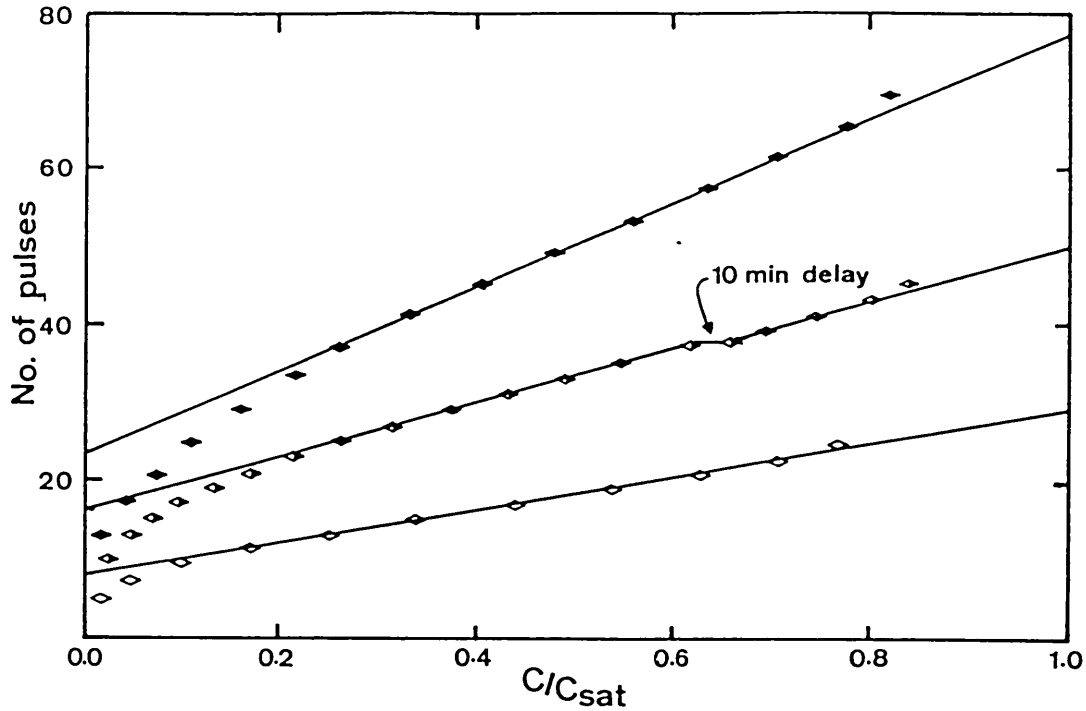

(a) ◇ Run A_2, T = 509°C; ◆ Run A_7, T = 570°C;
◆ Run A_5, T = 595°C.

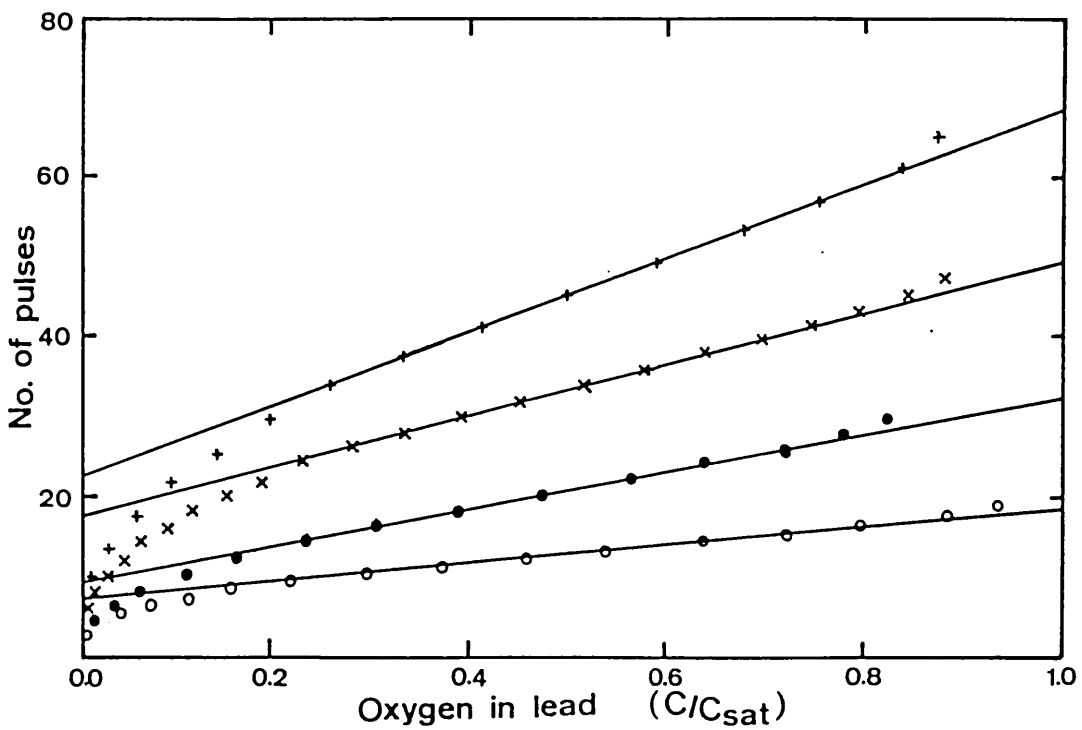

(b) o Run C_5, T = 470°C; • Run C_1, T = 532°C;
× Run C_4, T = 574°C; + Run C_3, T = 606°C.

Fig. 3-8: Method used to calculate oxygen solubility in lead (pulse oxidation technique).

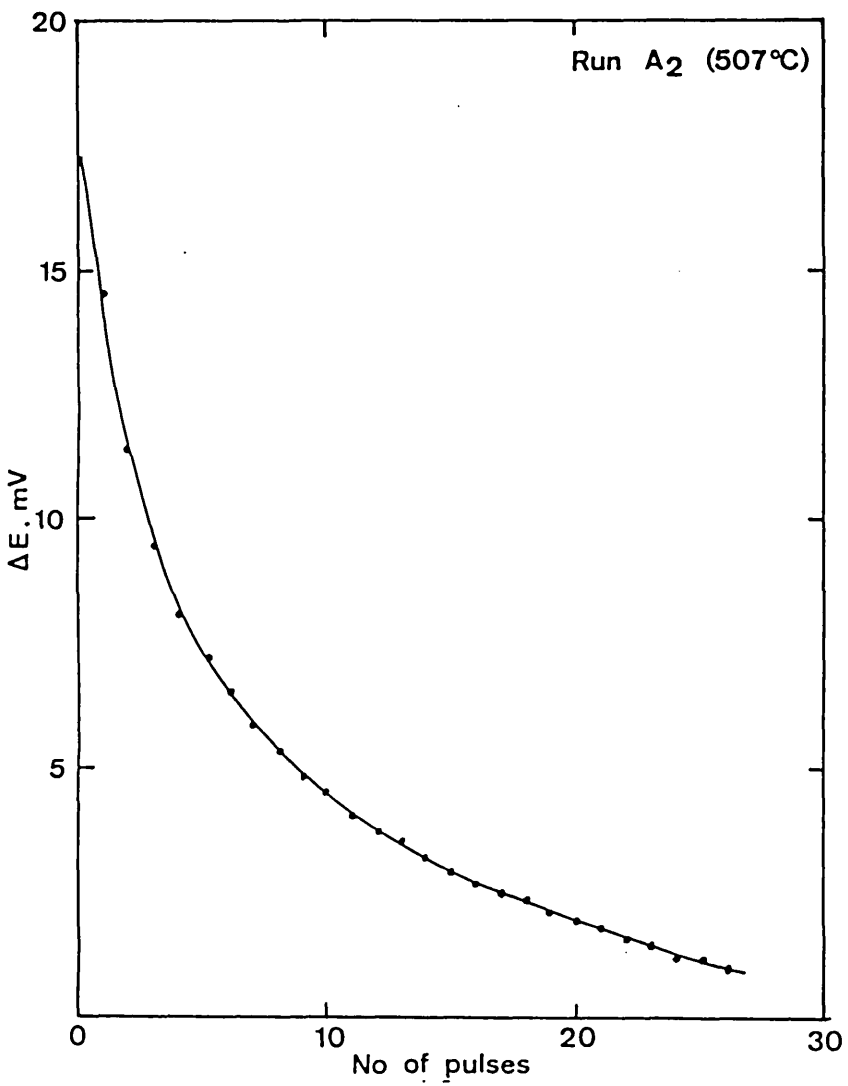

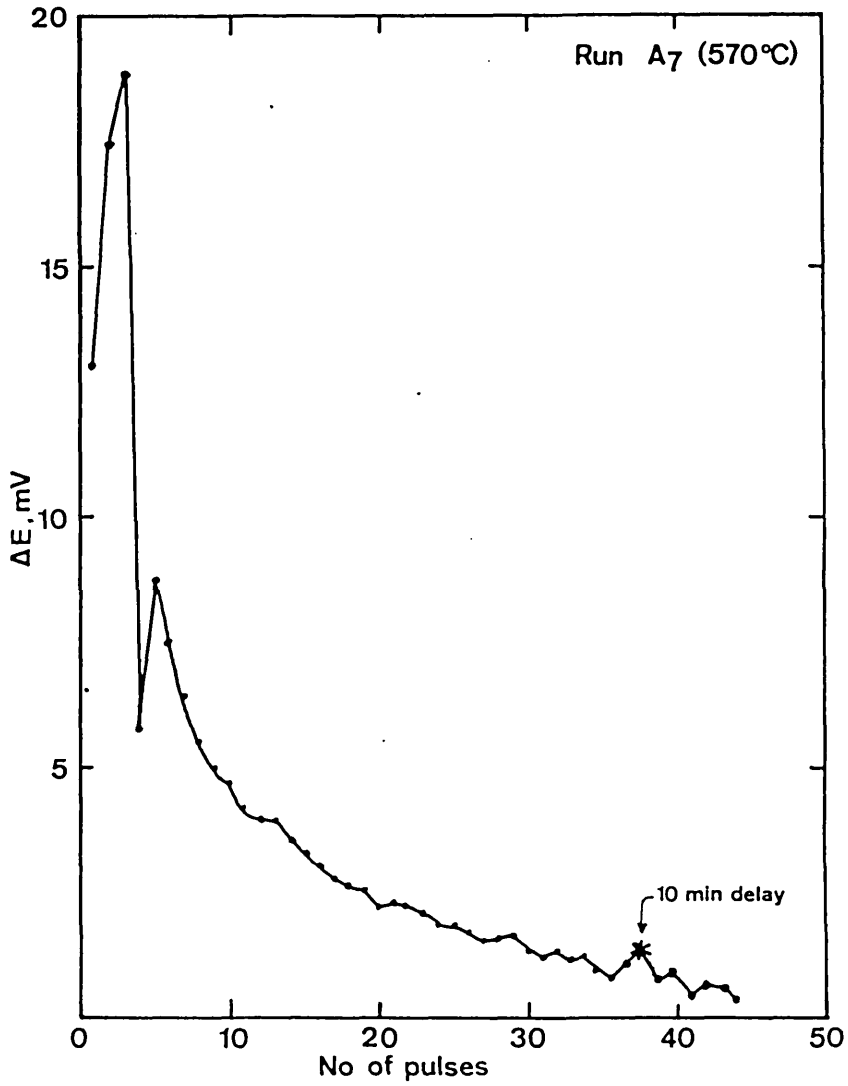

Fig. 3-9: Changes in cell emf per unit oxygen pulse addition to the lead.

TABLE 3-2

Summary of Runs - Oxygen Solubility

RUN	TEMP ^{o}C	PULSE VOL (ml at STP)	V_{sat} (ml at STP)	Wt % [O] ($X 10^3$)
A_1	507	12.14	265	1.23
A_2	507	12.14	258	1.20
A_3	522	12.14	330	1.54
A_4	580	12.14	556	2.60
A_5	595	12.14	665	3.10
A_6*	552	12.14	345	1.61
A_7*	570	12.14	430	2.01
B_1	578	14.71	581	2.71
C_1	532	16.67	385	1.80
C_2	560	16.71	490	2.29
C_3	606	16.71	769	3.60
C_4	574	16.81	551	2.57
C_5	472	16.81	190	0.89
C_6	455	16.80	142	0.67

*Substantial pulse irreproducibility observed.

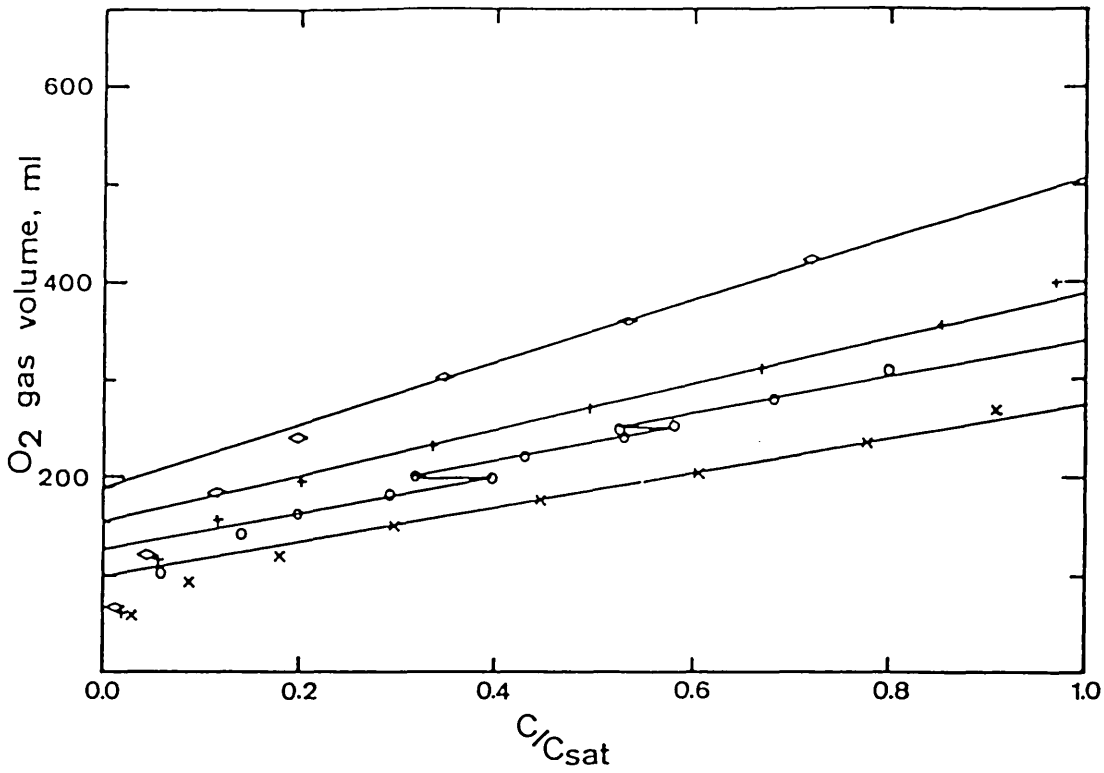

Fig.3-10: Method used to calculate oxygen solubility in lead (steady oxidation technique); T = 520°C, × Run D_3, o Run D_5, + Run D_7, ◇ Run A_3

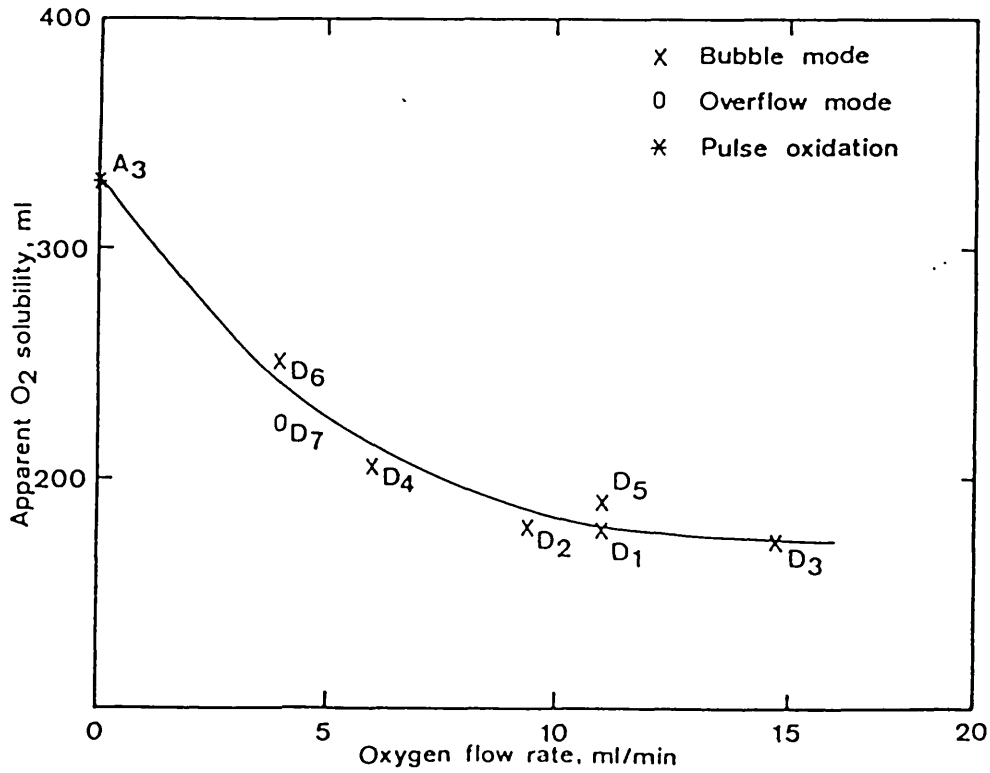

Fig. 3-11: Changes in the apparent oxygen solubility as a function of oxygen flow rate (T = 520°C).

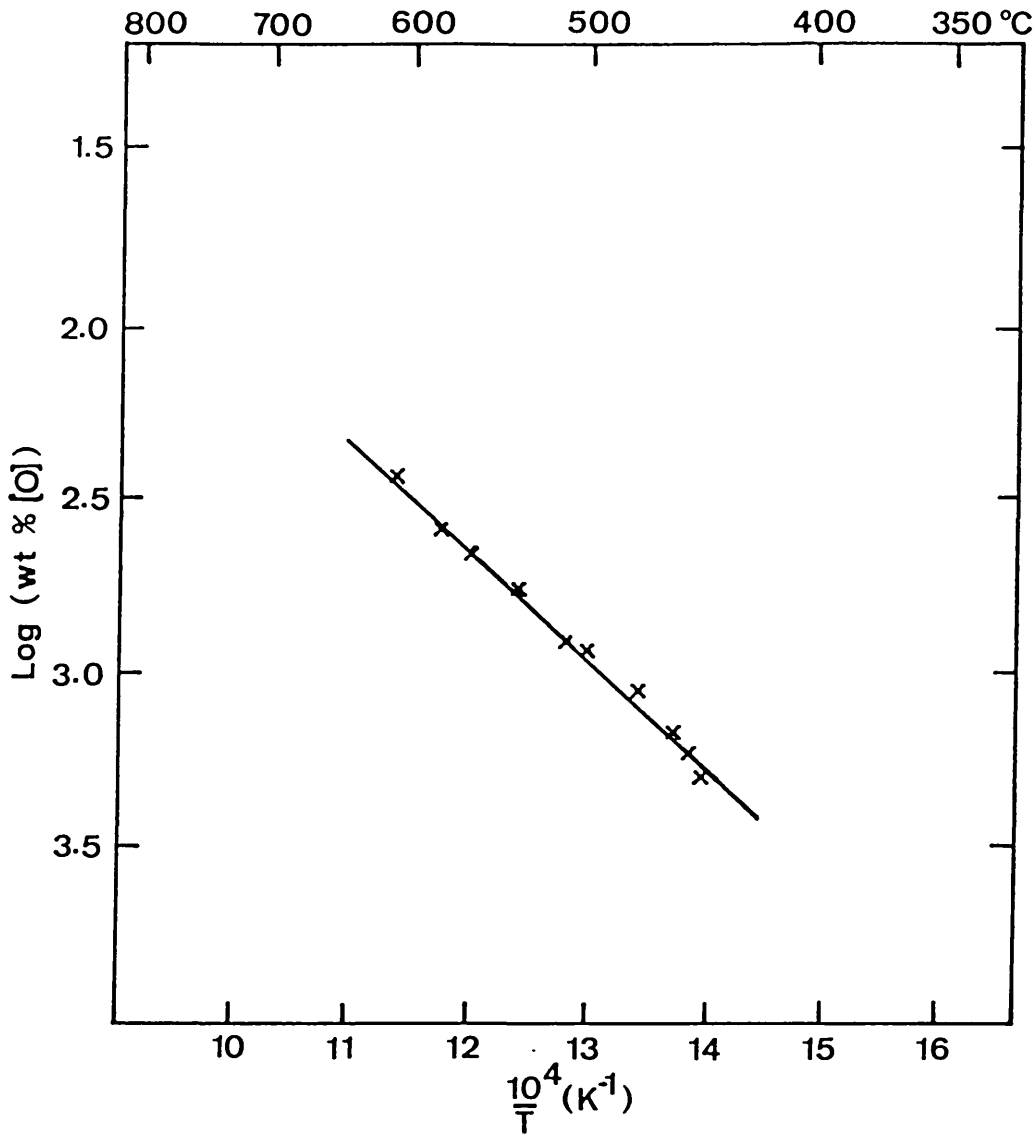

Fig. 3-12: Oxygen solubility in molten lead

These results led to a check on the oxygen potentials that were measured by the probe during the runs. Oxygen flow into the bubble was stopped at various intervals during run D_5 and the probe reading in millivolts was observed to drop slightly during each stoppage, indicating a gas-phase potential effect. The presence of unreacted oxygen in the gas atmosphere was causing the probes to give a millivolt reading that was too low (equivalent to too high an oxygen potential). In the overflow mode the probe immersion depth in the lead bath was less than it was in the bubble mode, thereby exposing a greater probe length to the oxidizing gas atmosphere. This explained the lower apparent oxygen solubility measured in the overflow mode (run D_7 in fig. 3-11).

Shielding the probe with a silica tube improved matters but silica tubes were observed to crack before the end of a run. Best results were obtained with the intermittent pulse technique in which the gas atmosphere above the lead was constantly diluted by the inert gas.

3.2.4 Mass transfer in HOTB

The mass transfer from oxygen to liquid lead in the presence of an oxide film involves three main steps:

(i) Diffusion of oxygen in the gas phase to the oxide/gas interface.
(ii) Growth of the oxide film as controlled by the ionic diffusion in the oxide layer.
(iii) Oxygen diffusion from the gas/oxide interface into the liquid lead.

In the presence of an oxide layer the rate of transfer of oxygen per unit area into the lead is given by

$$N_\ell = k_\ell (C_{sat} - C)$$

$$= k_\ell \ C_{sat}(1-C/C_{sat}) \qquad (3.19)$$

where k_ℓ is the liquid phase mass transfer coefficient. This rate is independent of the rate of transfer of oxygen through

the gas phase. Since only a very low oxygen potential is necessary to form an oxide film on lead (10^{-19} at 500°C) and also since it was observed that an oxide film was formed immediately on oxygen injection, it must be assumed then that oxygen is freely available at the gas/oxide interface. Once a slag film had been formed the rate of oxygen transfer to the liquid lead is controlled by the liquid phase mass transfer.

Since the bulk system is well stirred, the rate of change of oxygen concentration is given by

$$(dC/dt) = (k_\ell A/V)\ (C_{sat} - C) \tag{3.20}$$

where C is the oxygen concentration at a time t,
A is the surface area vailable for mass transfer,
k_ℓ is the liquid phase mass transfer coefficient,
C_{sat} is the interfacial oxygen concentration, i.e. the saturation concentration of oxygen as set by the Pb/PbO equilibirum.

Rearranging and integrating between the limits C_o at t = 0 and C at t = t:

$$\ell n \left[\frac{C_{sat}-C}{C_{sat}-C_o}\right] = -\frac{A}{V}\ k_\ell t \tag{3.21}$$

For the oxygen probe,

$$E-E_{sat} = -(RT/2F)\ \ell n\ (C/C_{sat}) \tag{3.22}$$

$$\frac{A}{V}\ k_\ell t = \ell n \left\{\frac{[1-\exp\ 2F(E_{sat} - E_o)/RT]}{[1-\exp\ 2F(E_{sat} - E)/RT]}\right\} \tag{3.23}$$

The accuracy of the above equation in the determination of k_ℓ A/V depends very much on the accuracy in the measurements of the various Emfs. There was considerable scatter in the set of values obtained for any one run and also the average mass transfer rates obtained for all the runs were significantly lower than those reported by Conochie[16]. The temperature dependence of the mass transfer coefficient is shown in fig. 3-13.

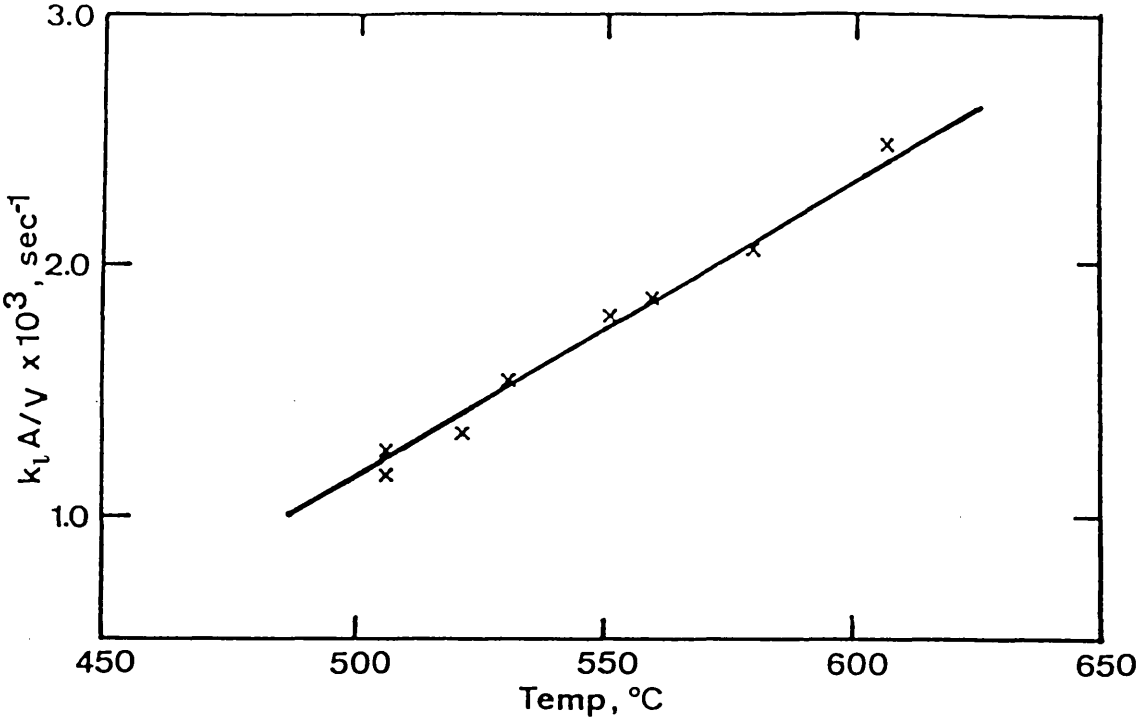

Fig. 3-13: Liquid phase mass transfer coefficient

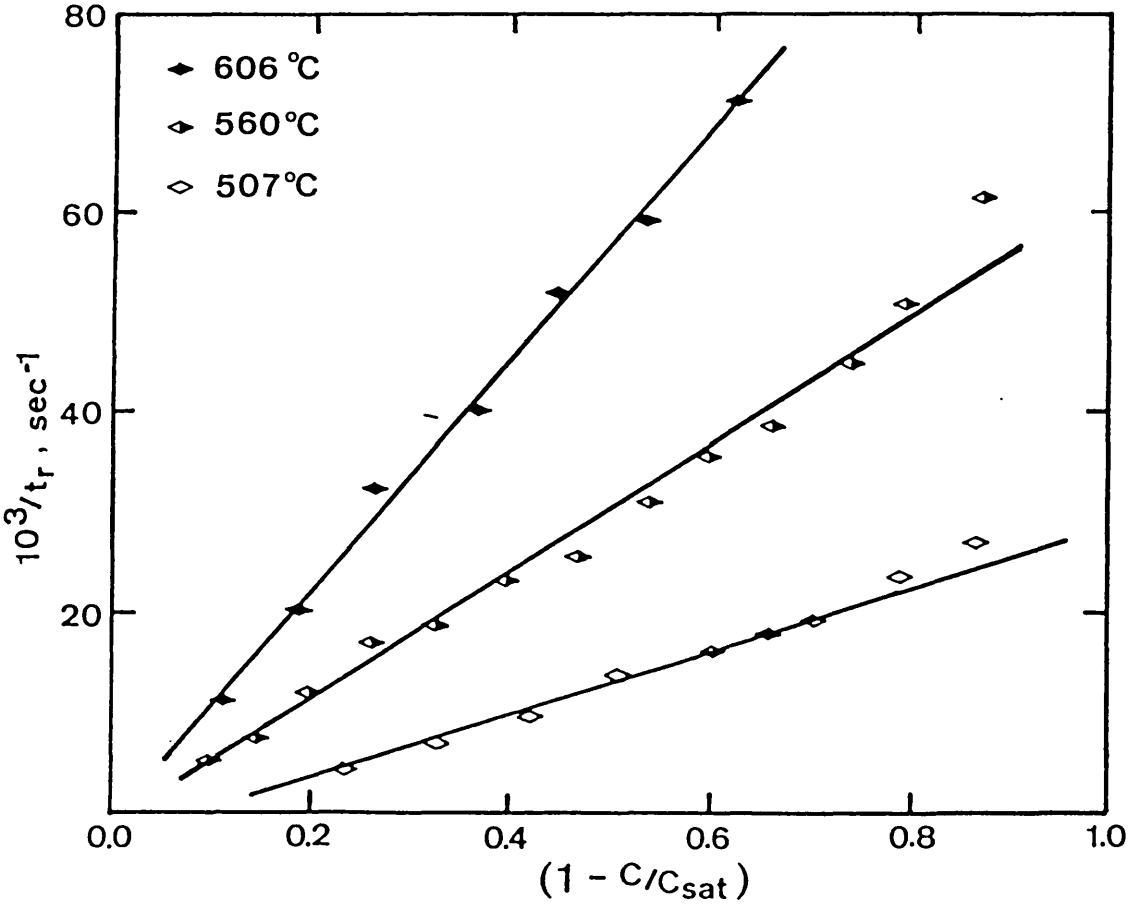

Fig. 3-14: Oxygen dissolution and ripple return

The most likely cause of the lower values of k_ℓ A/V is that the large quantities of iron oxides produced over many runs which accumulate on the surface of lead in the sump have 'blocked' part of the interfacial area.

Oxygen dissolution and ripple return

The time taken for ripple return after an oxygen pulse addition to the OTB was fairly constant up to about $C/C_{sat} = 0.2$ and then increased steadily up to oxygen saturation in the lead. This is consistent with a first order reaction controlled by liquid phase mass transfer, i.e.

$$\text{Rate} = Ak_\ell (C_{sat} - C) \qquad (3.24)$$

When the bulk oxygen concentration C was small in relation to C_{sat}, the rate would be approximately constant, as observed. Assuming all the oxygen forms PbO, a constant amount of oxide would be formed and provided the amount was small in relation to the amount required for saturation, the ripple return time would be inversely proportional to the rate of oxide dissolution. Thus a plot of t_r^{-1} vs C/C_{sat} would be linear as shown in fig. 3-14, and could be used to estimate the mass transfer coefficient. Expressing the rate and concentration in terms of volumes of oxygen;

$$\frac{\text{Pules } O_2 \text{ vol}}{\text{Ripple return time, } t_r} = \left[\frac{A}{V} k_\ell\right] \left[1 - \frac{C}{C_{sat}}\right]$$

x total O_2 volume required for saturation.

$$\frac{1/t_r}{1-C/C_{sat}} = \left[\frac{A}{V} k_\ell\right] \left[\frac{V_{sat}}{\text{Pulse } O_2 \text{ volume}}\right] \qquad (3.25)$$

Thus using the slopes in fig. 3-14 and the solubility data in table 3-2, $(A/V)k_\ell$ can be estimated. At 606°C the value of $(A/V)\, k_\ell$ is calculated to be 2.5×10^{-3} sec^{-1} (cf. 2.43×10^{-3} sec^{-1} estimated earlier, using eqn.(3.23)).

3.2.5 Oxygen in outlet gas

The oxygen content of the outlet gas was monitored at a temperaturs of 750°C using the gas phase oxygen probe described in section 2.3. The probe gave reproducible values for apparent oxygen potentials in the range $1.0 < p_{O_2} < 10^{-25}$; the lower limit measured for forming gas or pure hydrogen. Using high purity argon the apparent oxygen potential was 10^{-15}.

The outlet gas oxygen probe responded very quickly to changes in oxygen potential in the OTB pot. Oxygen input into the liquid metal pot was reflected as a sharp rise in the outlet gas oxygen potential followed by a relatively slow decay. The magnitude of this change depended on the volume of oxygen injected, the amount of oxygen in solution in the lead and the purge rate of the injected oxygen by argon.

Figs. 3-16 and 3-17 show an assembly of typical gas phase oxygen probe responses on a log scale of oxygen potential. Fig. 3-15 shows theoretical and actual curves for pulse injection of oxygen into a reactor, followed by a flow of an inert purging gas. The theoretical curves are for a flow of the oxidation gas with no consumption of oxygen by chemical reaction. The response curve is dependent on the temperature of the gas in the perfectly mixed volume. Curve A assumes the gas temperature to be the average of the lid and the liquid lead temperatures.

Gas volume mixing model

The gas volume of the OTB apparatus was 1740 ml, into which was inejcted between 9 and 20 ml of oxygen gas at room temperature. The initial gas phase oxygen concentration is dependent on the gas temperature in the rig. For the gas in the rig at liquid metal temperature (450°C), 16.5 ml of oxygen injected at room temperature would expand to 40.0 ml at constant pressure, resulting in a gas phase oxygen concentration, $C_o = 2.3 \times 10^{-2}$. The lower limit is set by assuming the gas in the rig is at room temperature (25°C), giving $C_o = 9.5 \times 10^{-3}$; here C_o has the units of

mole fraction. Assuming the injected gases were well mixed in the OTB pot gas volume a uniform mean gas temperature of 237.5°C (= (450 + 25)/2°C) could be assumed for which $C_o = 1.6 \times 10^{-2}$. With a purge rate of 600 STP ml/min by the inert gas, the mean residence time at the mean gas temperature is $\bar{t} = 1.7$ min.

For a perfectly mixed reactor, the decay in tracer concentration in the outlet stream after a tracer addition is given by

$$C/C_o = e^{-t/\bar{t}} \qquad (3.26)$$

Substituting for $\bar{t}$ at the mean gas temperature we obtain

$$\log_{10} C/C_o = 0.26t \text{ (min)} \qquad (3.27)$$

A plot of C/C_o as a function of time is shown in fig. 3-15 (curve A). Similar procedures have been used in the calculations for curve B (for the gas at room temperature).

The actual curves show that a large fraction of the input oxygen was consumed by rapid reactions with the lead. Near oxygen saturation in the lead, the area under the actual curve was still much less than that of the theoretical curve. This behaviour may be attributed to one or more of the following factors:

(i) Continuous utilization of the injected oxygen in the formation of lead oxides, even after oxygen saturation of the liquid metal.

(ii) Further oxygen consumption by the mild steel container.

Gas probe response slopes

Considerable effort was put into the investigation of the gas probe response slopes shown in figs. 3-16 and 3-17. The apparent oxygen potential in the input argon was measured at 10^{-15} with a slow response. This was much lower than BOC quoted values for oxygen in argon of less than 4 vpm. Other impurities were given as: N_2 < 15 vpm, H_2 < 1 vpm and hydrocarbons 1 vpm. It was thought that the reason for the

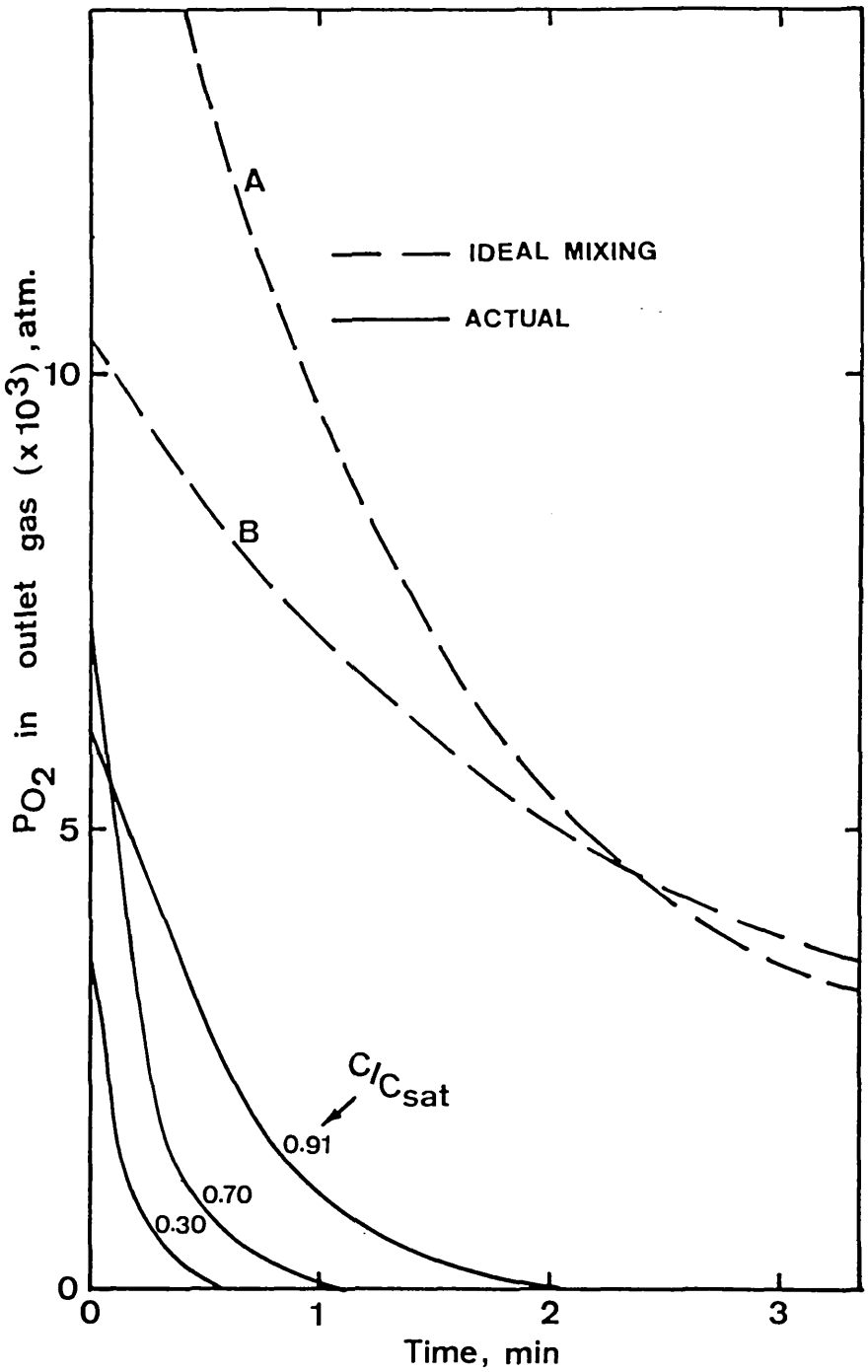

Fig. 3-15: Linear plot of gas phase oxygen potential decay; A (Gas temperature = 237.5°C), B (Gas temperature = 25°C). Pulse O_2 vol. = 16.5 ml (STP)

low apparent oxygen potential measured in argon was that the impurity oxygen reacted with the hydrogen and hydrocarbons while the argon gas was passing through the heated probe, hence the measured potential was set by H_2/H_2O and CO/CO_2 in the gas mixture. For argon passing through the OTB pot containing freshly deoxidized lead at very low oxygen potential and then through the gas probe, the response was far more rapid and the apparent oxygen potential measured was in the region of 10^{-21}. It was concluded that in passing over the deoxidized lead the oxygen content of the argon had been lowered by reactions of the impurity oxygen in the gas with the deoxidized lead and its iron container and also the pick-up of the residual hydrogen in the pot. The minimum attainable oxygen potential in the outlet gas was thus dependent on the reducing conditions within the lead pot.

At very low oxygen potentials in the liquid metal, the lead pot is itself very reactive and hence oxygen utilization in the pot very high. A pulse of oxygen injected into the lead bath is reflected as a small sharp peak in the outlet gas oxygen potential. This peak increased in magnitude with successive oxygen pulses, finally reaching a maximum of the same order of magnitude as the initial oxygen concentration expected as a result of mixing of the injected O_2 gas with inert gas in the rig.

Also associated with the increase in the peak response of the outlet gas probe is the occurrence of transitions during the potential decay. The decay in outlet gas oxygen potential was observed to occur in two stages, resulting in two main types of transition:

(i) Transition I:

A change in the oxygen potential decay rate in the region of the measured potential for cylinder argon. This transition was primarily dependent on the oxygen potential of the liquid metal as illustrated in fig. 3-16.

(ii) Transition II:

A change in the oxygen potential decay rate in the region $10^{-12} < p_{O_2} < 10^{-8}$. Transition II occurred for higher oxygen contents of the lead (see fig. 3-17).

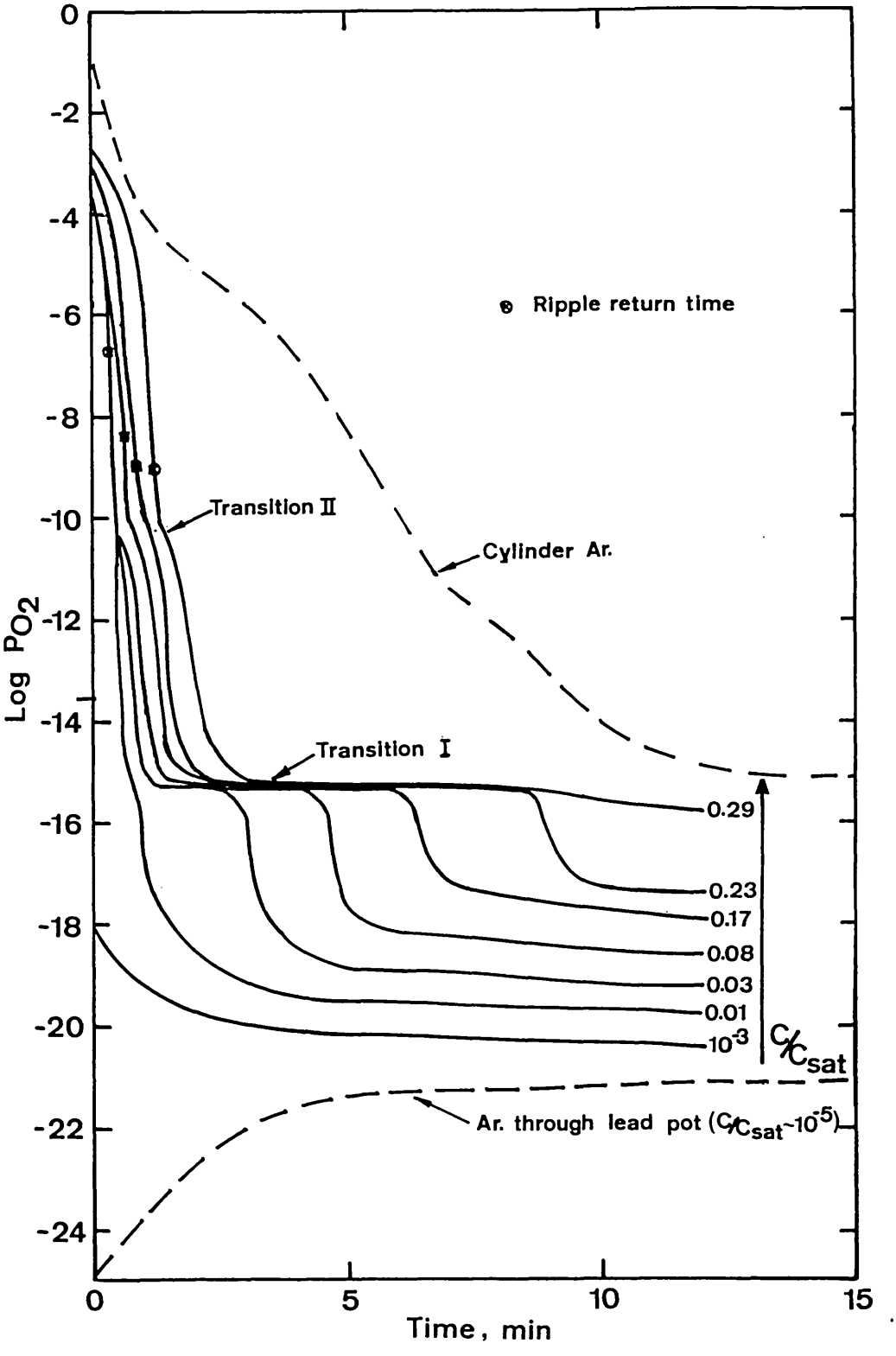

Fig. 3-16: Log plot of gas phase oxygen potential decay: Injection sequence - O_2 pulse (2s) followed by high Ar purge (10 ml/s). Pulse O_2 vol. = 9 ml (STP)

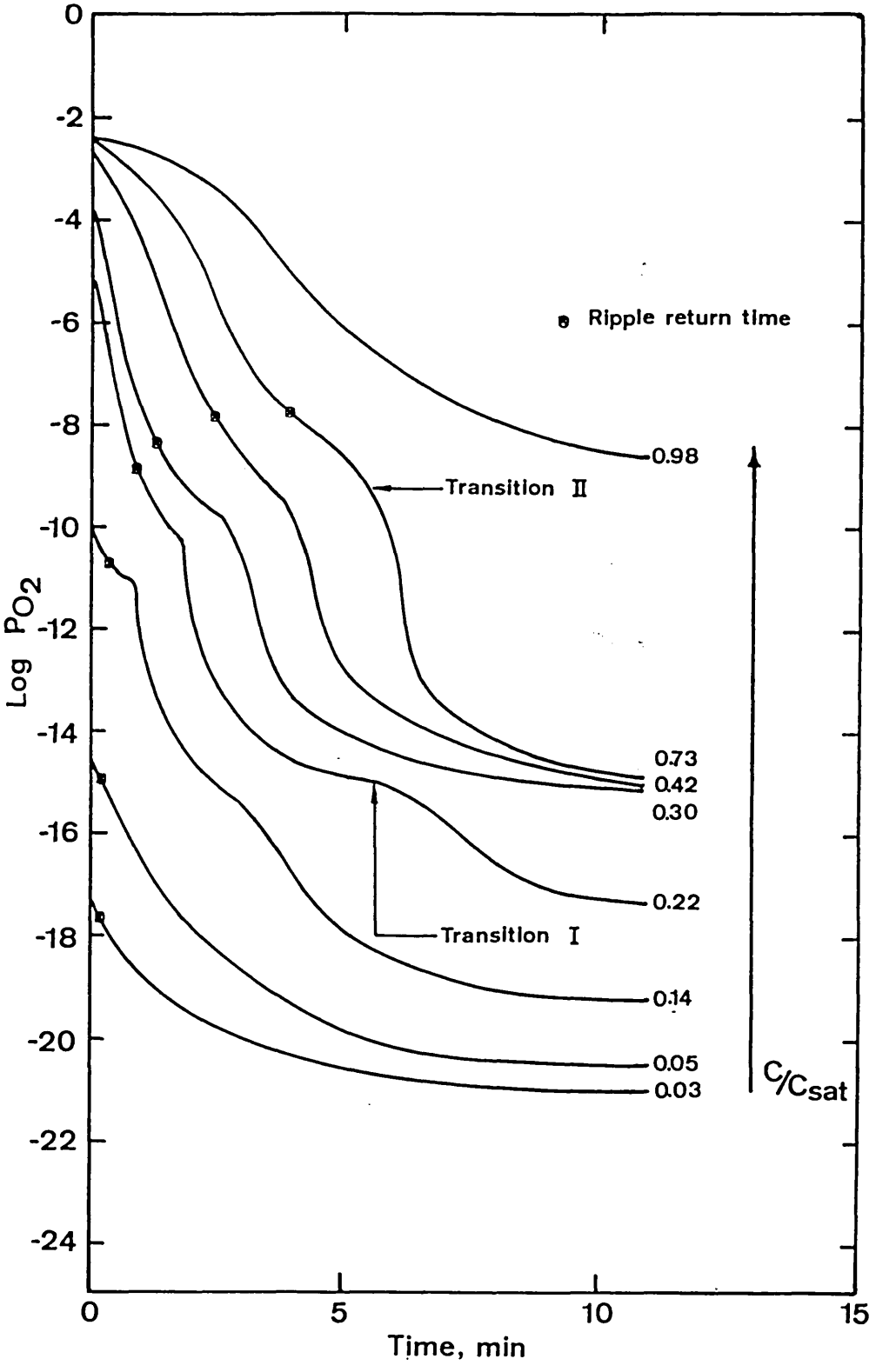

Fig. 3-17: Log plot of gas phase oxygen potential decay: Injection sequence - O_2 pulse (2s) followed by high Ar purge (2s), reset to low purge (2 ml/s).
Pulse O_2 vol. 9 ml (STP)

Transition I was observed at low oxygen potentials in the lead. The transition is consistent with the reaction and subsequent removal of the impurity oxidants in the gas phase while it is passing through the reactive lead pot, as discussed earlier. This transition was not observed at very low oxygen potentials in the lead ($C/C_{sat} < 10^{-2}$), where it was thought that because of the highly reducing conditions in the OTB pot and the likely presence of hydrogen in its gas atmosphere, the reactions of any oxidizing impurities in the gas phase would have occurred very quickly. As the oxygen level in the lead increased, the lead and its container gradually became less reducing thereby limiting both the rate and extent of reduction and also the oxygen potential decay. At $C/C_{sat} > 0.3$ transition I ceased to occur and the outlet gas oxygen potential settled in the region of that measured for a direct supply of cylinder argon to the oxygen probe, without passing through the lead pot. This was consistent with the changing of the liquid metal oxygen probes from type A response to type B response, after the passivation of the iron pot, as discussed in section 3.2.

Transition II occurred at high gas phase oxygen potentials. During its initial stages it was measured at oxygen potentials of about 10^{-11} at 750°C. With subsequent increases in the liquid metal oxygen potential this increased to about 10^{-9} atm.

The likely cause of type II transition was the formation and subsequent dissolution of PbO after oxygen addition to the lead. The transition began to show when an oxide film remained on the lead surface for a significant period of time. The gas phase oxygen potential decayed shortly after oxide dissolution. The duration of the transition was dependent on the ripple-return time in the OTB as well as the purge rate of the gas atmosphere by the inert gas (see fig. 3-17). The fact that this transition was not observed near oxygen saturation in the lead is consistent with this hypothesis. A detailed chemical analysis of the outlet gas at various stages through the lead pot and the probe would be necessary to give a quantitative account of the changes in the potential.

3.3 SLAG ADDITIONS

The behaviour of liquid slags in rising bubbles, as is often encountered in metallurgical processes, was investigated using the open top bubble technique in molten lead. The slags were added as solid pellets which were then observed to melt inside the OTB. Three main types of slags were used in this investigation, viz. NaOH, NaOH-$NaNO_3$ and $NaNO_3$ slags. The reactions of these slags with the lead were followed by monitoring the oxygen potentials of the liquid metal and the outlet gas. Their spreading and/or stripping behaviour are characterised by the sequence of photographs taken during the experiments. Typical observations are illustrated by the photographs in figs. 3-18, 3-19 and 3-25 , and also by plates A, B and C. In some experiments the observations were recorded using a movie camera. Details of the experimental conditions are shown in Table 3-3. (p. 114)

3.3.1 NaOH addition

Each addition of a caustic soda slag to the OTB resulted in a slight suppresssion of the ripples at the bubble base. The ripples reappeared soon after the slags had melted. Typical observations are shown by the photographs of run S_2 shown in fig. 3-18. Frame 1 shows the OTB before the addition of the NaOH pellet. The strong rippling at the bubble base and walls is clearly visible. Frame 2 shows the bubble 5 seconds after the addition of an NaOH slag pellet. The ripples in the bubble slowly reappeared after the slag had melted, as shown in frames 3 to 6. The slag pellet took about 10 seconds to melt.

During the initial period after the slag pellet had melted, it sat immobile at one end of the bubble base (frame 3) and stripped very slowly. There were also fluctuations in the bubble base depth during this period. After about 3 minutes, the amount of slag in the bubble had reduced considerably and its colour had begun to darken. Subsequently, the remaining slag in the OTB became very mobile, darting about the basal surface of the bubble. This behaviour continued until the end of the experiment, the

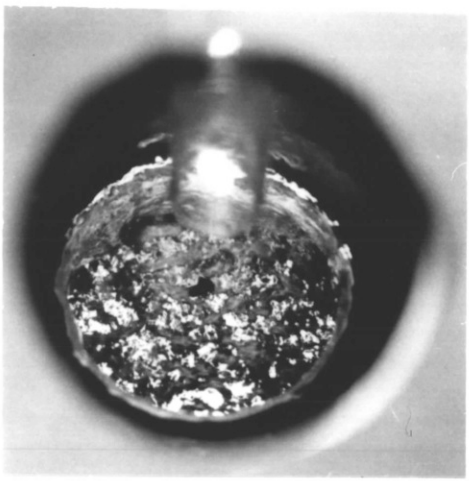

1· Before addition

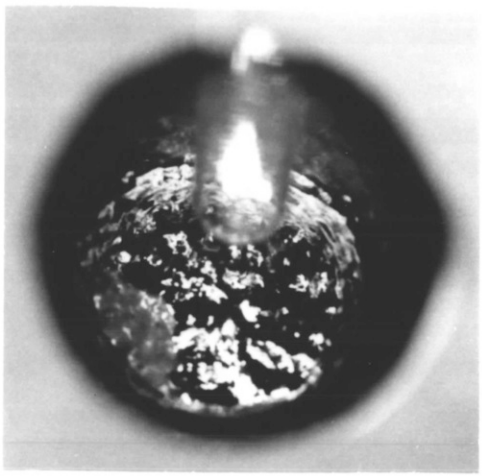

4· t = 3 min

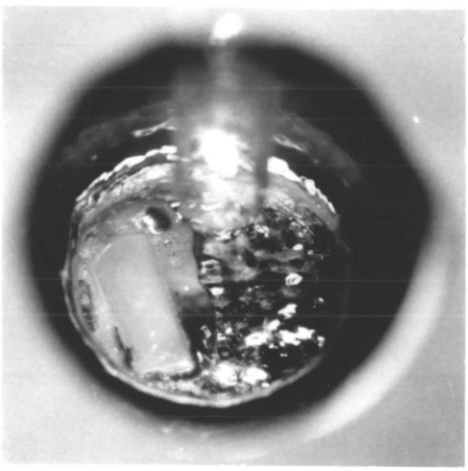

2· After addition, t ≃ 5 s

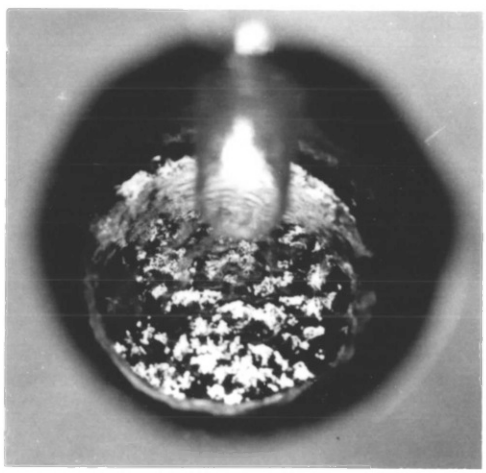

5· t = 6 min

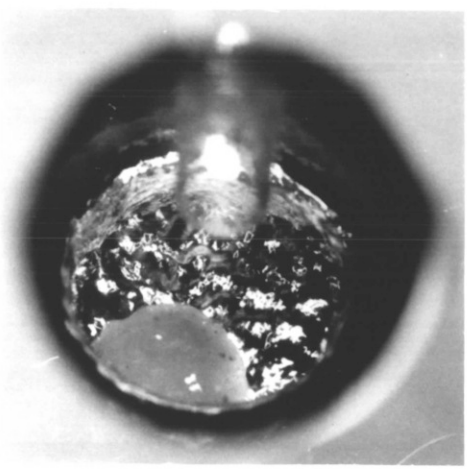

3· t = 40 s

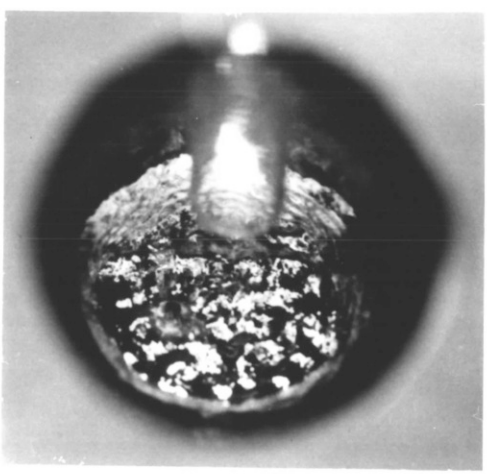

6· t = 10 min

Fig 3-18 Typical behaviour of NaOH slag in the O T B (Run S2)

slag only changing slightly in size and turning deep brown in colour.

The oxygen potentials of the system changed very little throughout the duration of each NaOH addition experiment. Oxygen potential in the liquid metal was unaffected by NaOH slag additions. The gas phase oxygen potential displayed a sharp increase in potential immediately after each addition of the slag, which decayed shortly after, and settled in the region of its original starting value. This response was observed during the melting of the added slag pellet and was thought to be caused by the gas evolution observed in the region of the melting slag (as shown in plate B). Typical response of the oxygen probes are shown in fig. 3-27A. A detailed investigation into the gas phase probe response is given in section 3.4.3.

The reaction of caustic soda with the steel pot

During the interval between runs S_4 and S_5, patches of reddish-brown oxides were seen on the surface of the mild steel container above the static lead level inside the OTB pot. This observation raised questions about the reactions that could occur between the added caustic soda and the mild steel container, at the experimental temperature (450°C).

Various tests were made to investigate this observation. New pulse oxygen addition experiments produced results which differed considerably from the usual (see figs. 3-19 to 3-24). At very low oxygen potentials in the lead, initial oxygen pulses gave rise to a new type of probe response; type C response - a small increase in oxygen potential followed by a very slow decay.

A typical type C response is shown in fig. 3-20 (run G_1). The variations in the gas phase oxygen potential (also shown in the same figure) were similar to those observed for the earlier pulse oxidation runs. Fig. 3-21 compares type C response with the previously observed type A response. Three main differences could be observed between the two response types:

(i) The magnitude of the increase in oxygen potential in a type C response is much smaller than was observed for the corresponding type A response at the same initial oxygen potential in lead and using the same pulse volume of oxygen.

(ii) The probe potential decay in type C responses were considerably slower than for a corresponding type A response.

(iii) In type C response, the probe potential change to input oxygen increased with the number of added oxygen pulses, whereas in type A response the probe potential change decreased with increase in number of added pulses. With subsequent oxygen pulses, type C response gradually changed to type A response (see figs. 3-22 to 3-24).

The photographs in fig. 3-19 illustrate typical slag films formed in the open top bubble after oxygen addition to the lead, in the type C response regime. Ripple return times were significantly longer than previously observed. This was caused by the presence of a thin film of powdery yellow oxides, which had appeared inside the bubble soon after oxygen addition. The oxide film can be clearly seen in frames 3 and 4, floating on the bubble base.

Type C response was consistent with the oxidation of a very reactive impurity in the lead by the added oxygen and hence connected with the oxide film observation discussed above. At very low oxygen potentials the impurity would be present in lead at a finite activity and would react much more readily with the added oxygen than the oxygen would go into solution in the lead. With subsequent oxygen additions to the lead the impurity level would be substantially reduced and further reactions would occur via the mechanism proposed for type A response discussed in section 3.2.1.

The liquid lead was later oxidized by opening the lid of the OTB apparatus and the lead surface cleaned by drossing the residual oxides. The system was later reassembled and

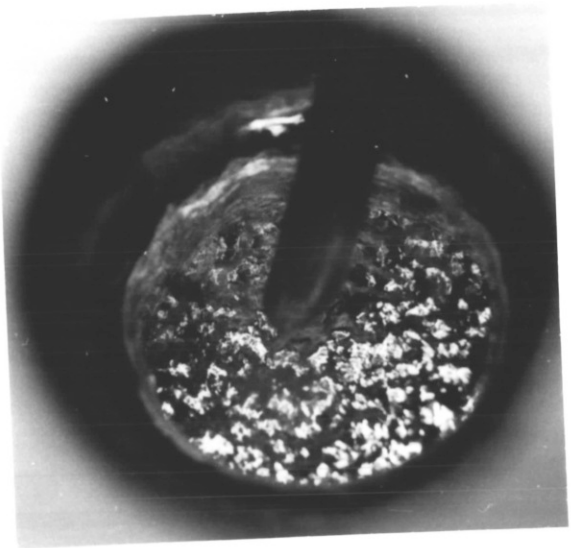

1. Before O_2 injection

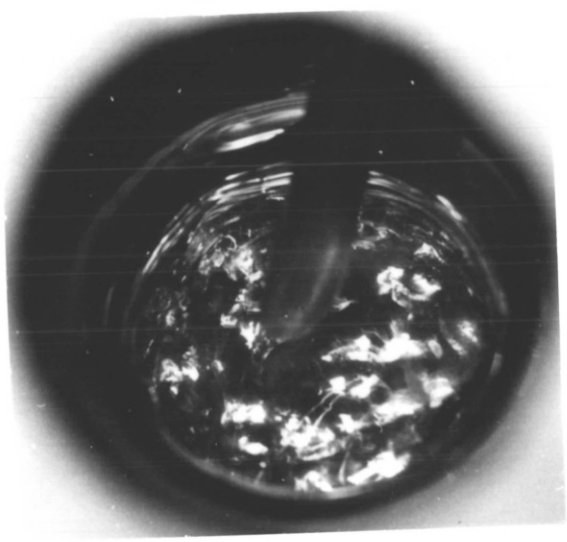

2. t = 10 s

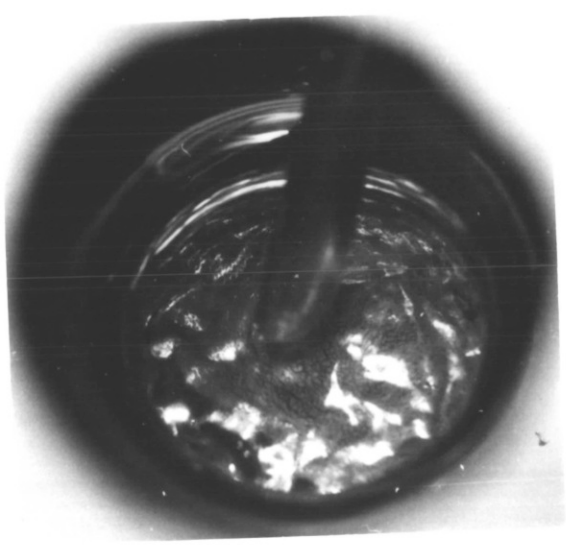

3. t = 30 s

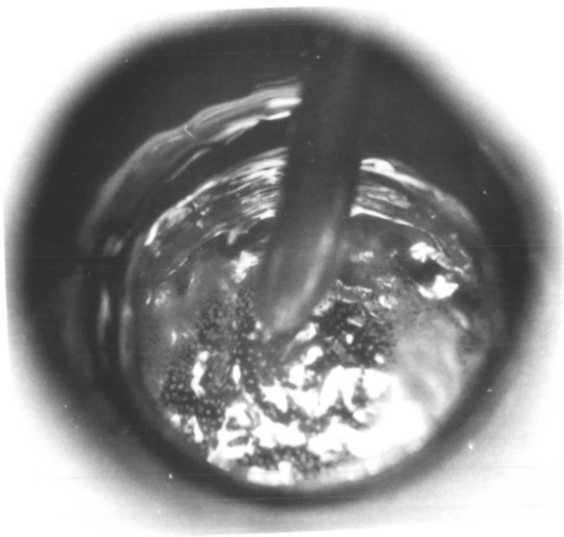

4. t = 2 min

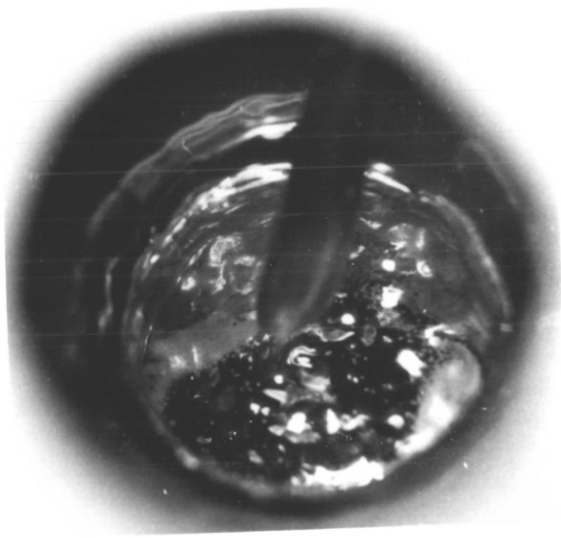

5. t = 5 min

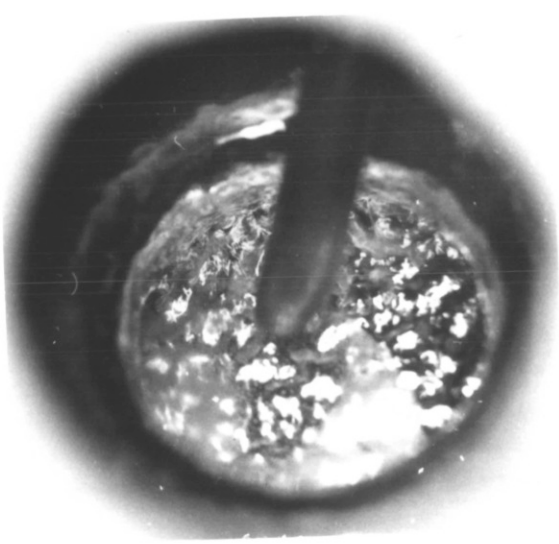

6. t = 10 min

Fig 3-19 Typical slag films formed by oxygen addition to the O T B after the NaOH slag additions (Run G4)

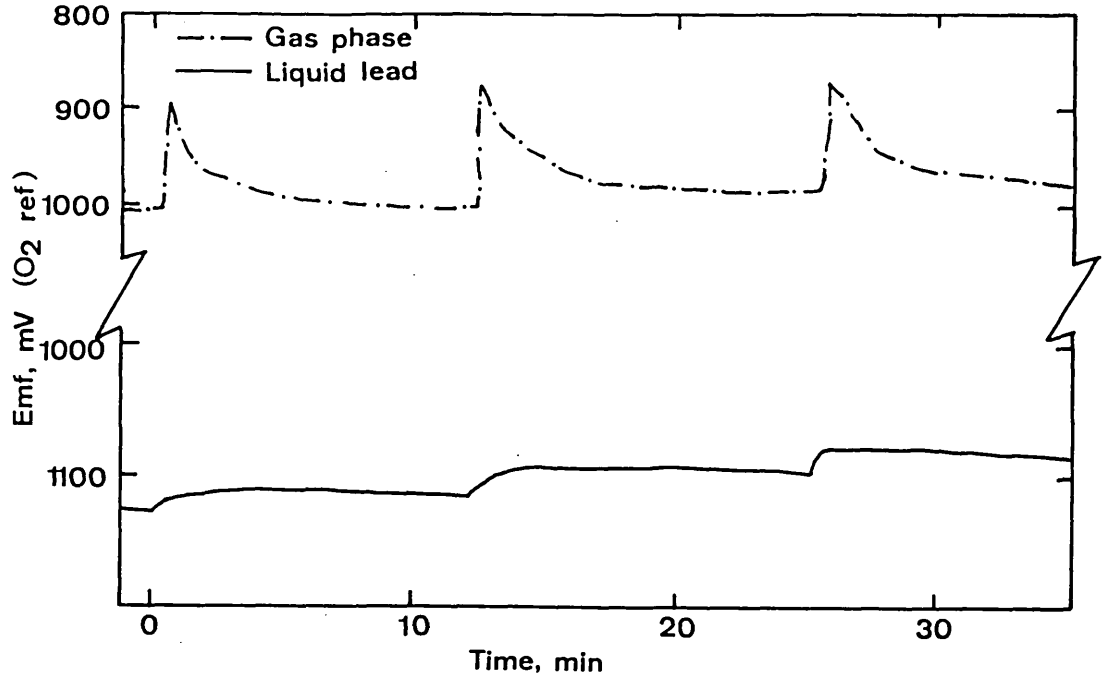

Fig. 3-20: Typical type C response curve (Run G_1)

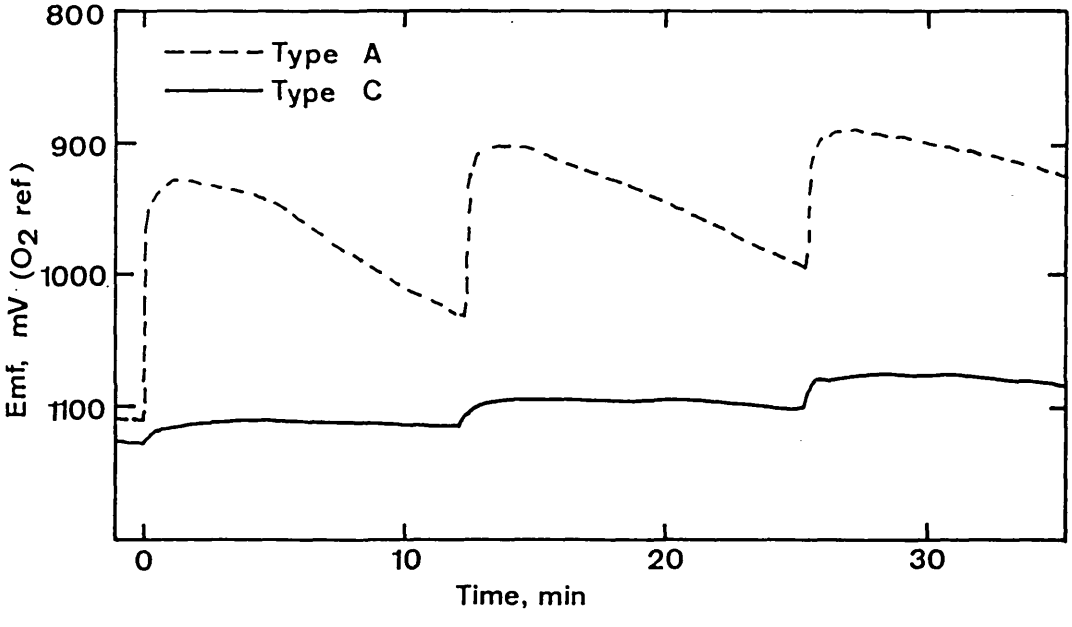

Fig. 3-21: Comparing oxygen probe responses to the addition of 16.5 ml oxygen pulses before and after NaOH addition.

the lead was subsequently deoxidized with forming gas (25% H_2, 75% N_2). Pulse oxygen injection experiments were later repeated. Results obtained show that the probe responses to initial oxygen input were still type C but with larger potential changes and a quicker transition to type A response (see fig. 3-22). In run G_4, shown in fig. 3-23, the lead was deoxidized using pure hydrogen gas and the probe response to initial oxygen pulse reverted to typical type C response. Apparently, the hydrogen had reduced more of the remaining impurity oxides into the lead and may have itself gone into solution in the lead, at such low oxygen potentials, hence the larger amount of oxygen consumed by type C response in this run.

The effect of an increased oxygen pulse volume on type C response is also shown in fig. 3-24. The comparatively rapid change from type C response to type A response is obvious.

It was thought that the new impurity in the lead was sodium, which may have been a product of the reaction of the added caustic soda with the OTB pot. NaOH may oxidize lead to PbO[58]. Its reaction with PbO does not occur at the experimental temperature (450°C)[56-58]. Newman and co-workers[64] interpreted its reaction with iron as

$$Fe + 2NaOH \rightarrow NaFeO_2 + NaH + \tfrac{1}{2}H_2 \qquad (3.28)$$

with a possibility of the sodium hydride decomposing according to the reaction

$$NaH + NaOH \rightarrow Na_2O + H_2 \qquad (3.29)$$

Powder X-ray diffraction patterns for drossed oxide samples taken from the OTB pot after NaOH addition and the subsequent oxygen injection experiments confirmed the formation of sodium ferrite (see tables A and B in appendix A-6). The reaction thought to be taking place slowly in the reactor was

$$2NaOH + Fe \rightarrow NaFeO_2 + [Na] + 2[H] \qquad (3.30)$$

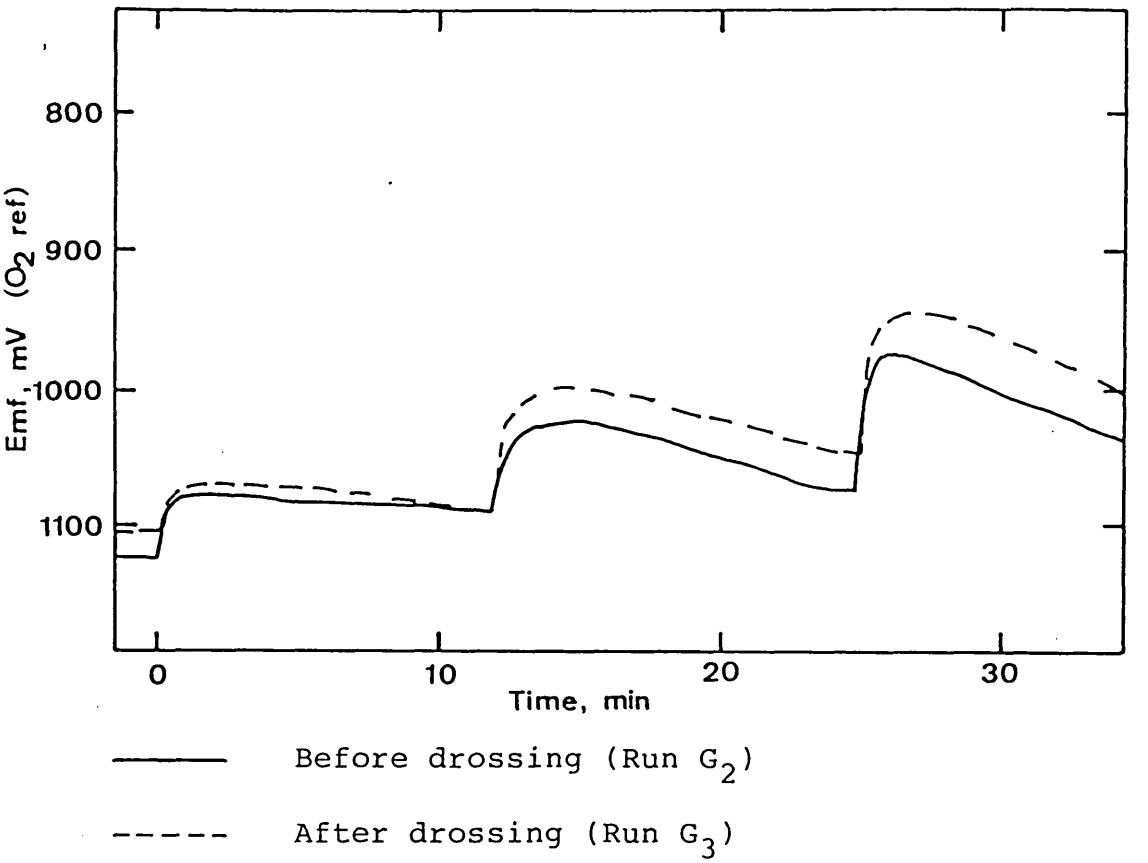

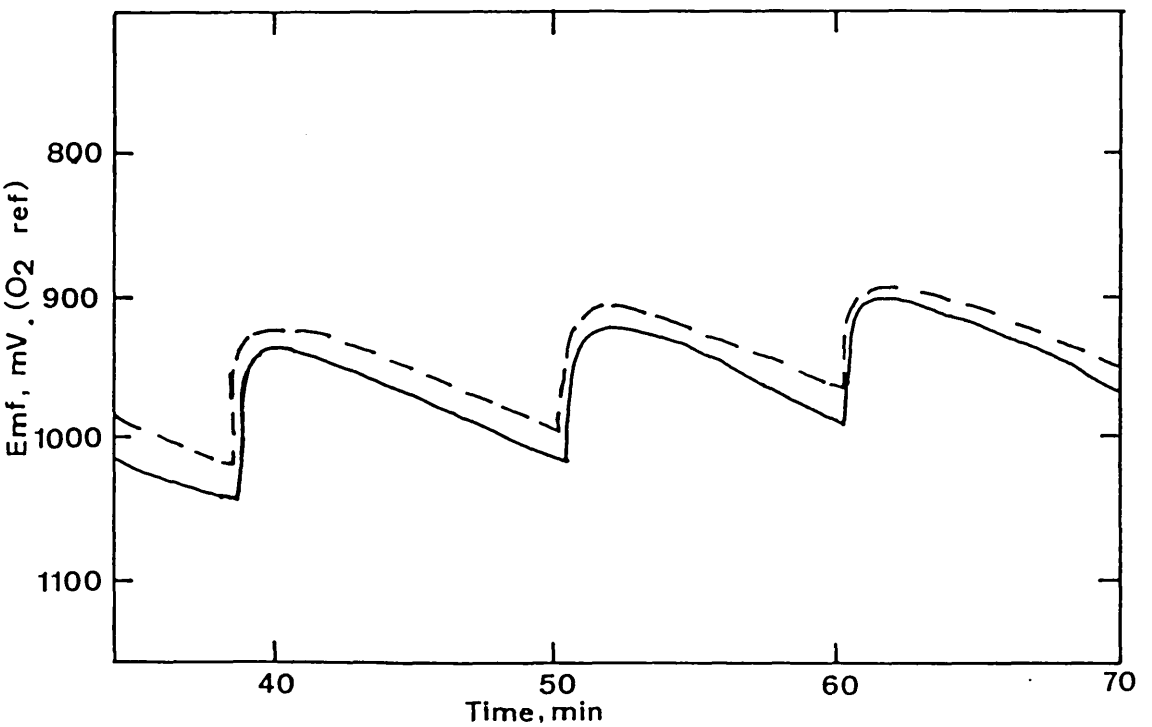

Fig. 3-22: The effect of the drossing of impurity oxides in the lead on type C response.

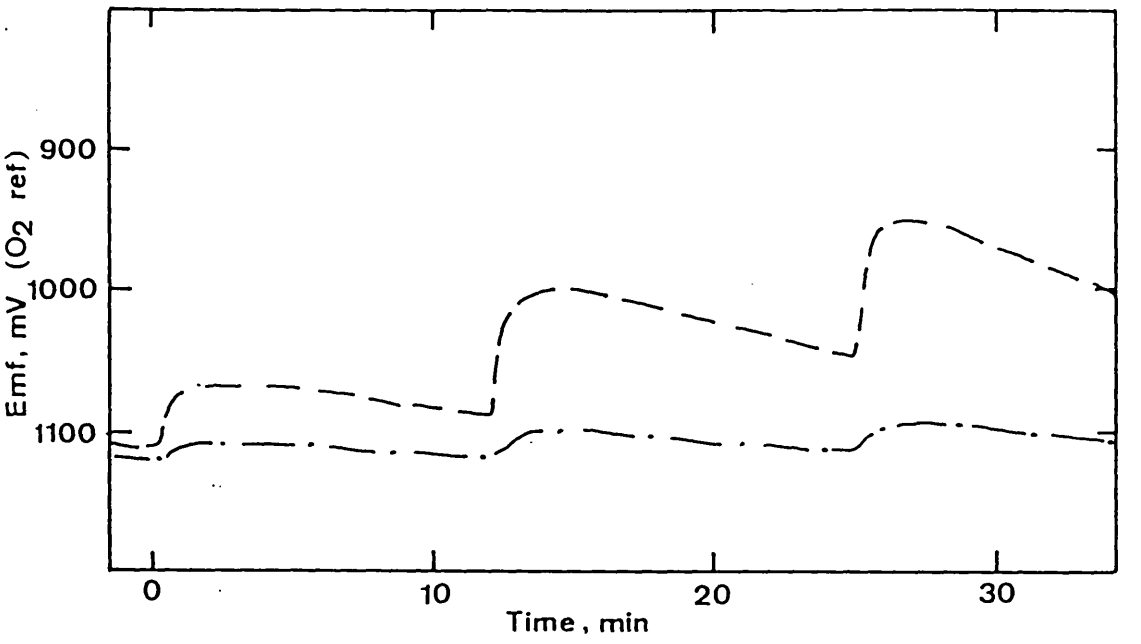

—·— After reduction using forming gas (Run G_3)

– – – – After reduction using hydrogen (Run G_4)

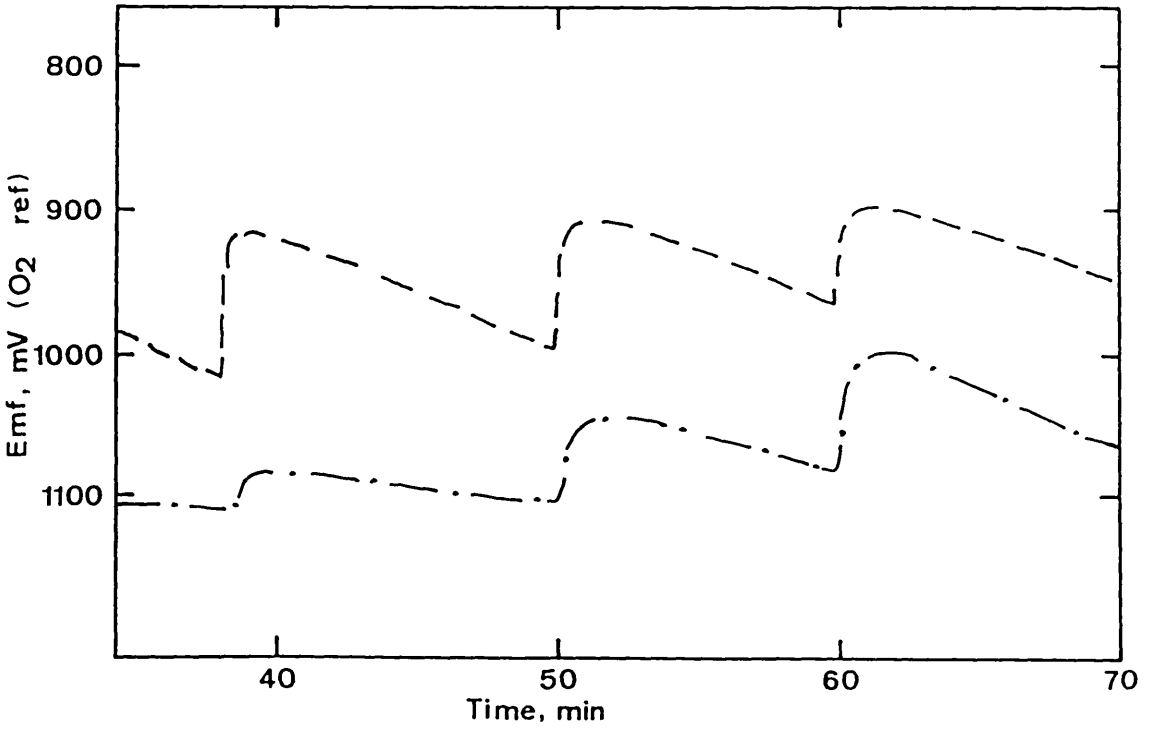

Fig. 3-23: The effect of the deoxidant gas on type C response.

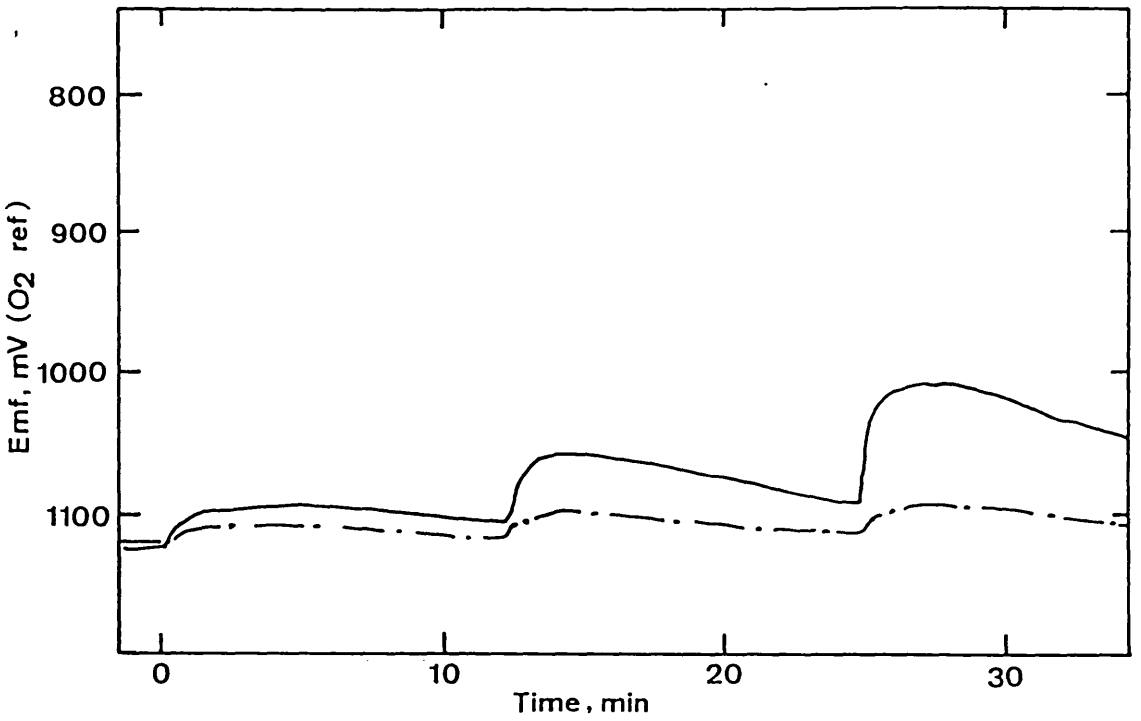

Pulse volume = 16.5 ml at stp. (Run G_4)

Pulse volume = 30.0 ml at stp. (Run G_5)

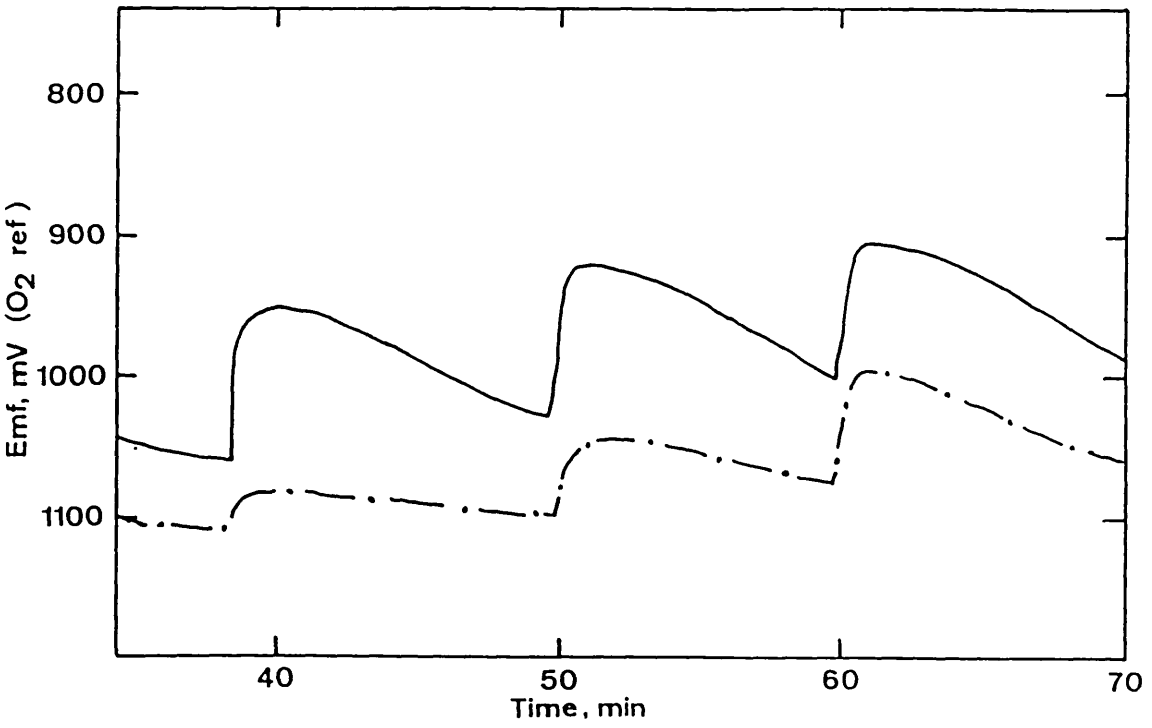

Fig. 3-24: The effect of oxygen pulse size on type C response after drossing and reducing with hydrogen.

Analysis for sodium and iron in the lead samples taken from the OTB pot at low oxygen potential in the lead suggests that these impurities were not significantly present in the lead (see Table 3-5). Further work would need to be done in order to identify what was responsible for type C response. Analysis of the powdery yellow oxide film formed in the OTB during type C response would provide useful information towards a detailed explanation of the response.

3.2.2 $NaOH-NaNO_3$ addition

The typical behaviour of $NaOH-NaNO_3$ slags in the OTB is illustrated by the photographs in fig. 3-25. At low slag mass loadings in the bubble, the observed behaviour differed slightly as shown by plate A.

The addition of an $NaOH-NaNO_3$ slag pellet to the OTB resulted in the immediate suppression of the ripples in the bubble. Each pellet melted soon after its addition forming a thin brown film which spread rapidly covering the entire bubble surfaces as shown in frame 3 of fig. 3-25. The film thickness subsequently increased and its colour gradually darkened. Soon after a bulk solid began to form at the bubble base changing the bubble shape to a conical shape, with the solid slag bulk sitting at the apex of the 'conical bubble' (see frames 7 to 9 in fig. 3-25). The bubble depth subsequently increased with time until the solid bulk at the tip stripped into the liquid metal. This stripping took place between 8 and 15 minutes after the slag addition, depending on the weight of slag and the bubble parameters. After stripping the bubble shape returned to normal, with a thin layer of brown oxide particles covering its basal surface, as shown by frame 12.

During the melting of the $NaOH-NaNO_3$ slag pellet in the OTB, gas bubbles were seen to evolve from the region of the melting slag. This resulted in a sharp decrease in the outlet gas oxygen potential which later slowly increased towards its original starting oxygen potential, after the gas evolution had stopped. The liquid metal oxygen potential was also affected by the addition of $NaOH-NaNO_3$ slags. The lead

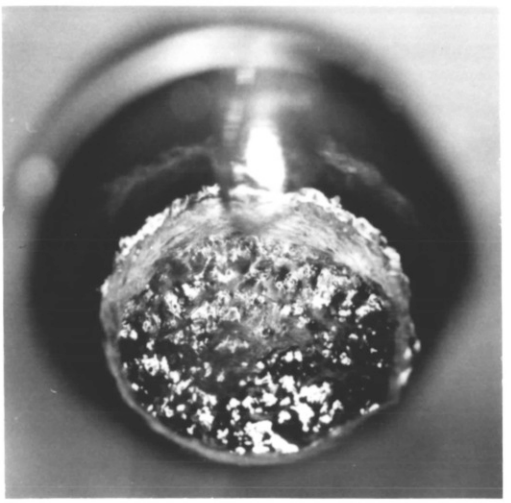

1· Before addition

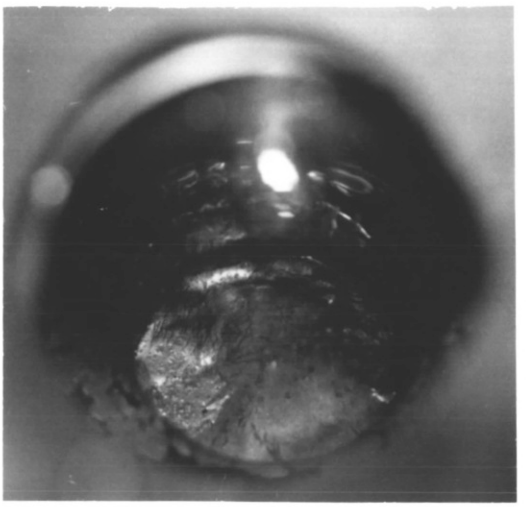

4· t = 30s

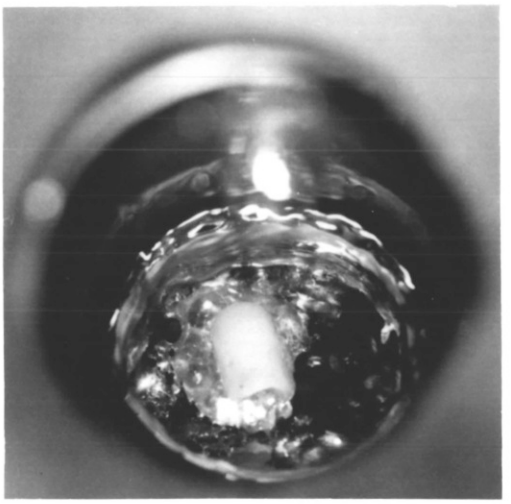

2· After addition, t = 5s

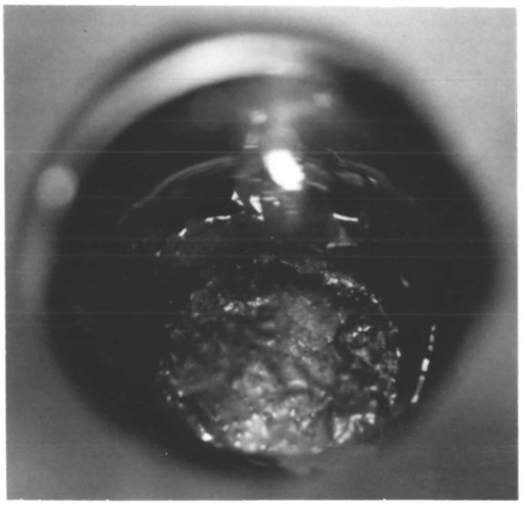

5· t = 1 min

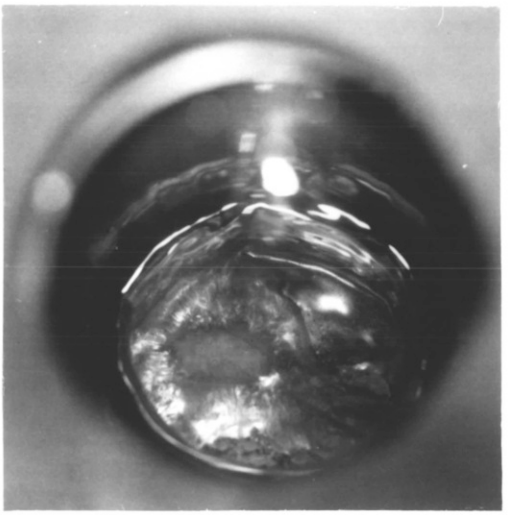

3· t = 10s

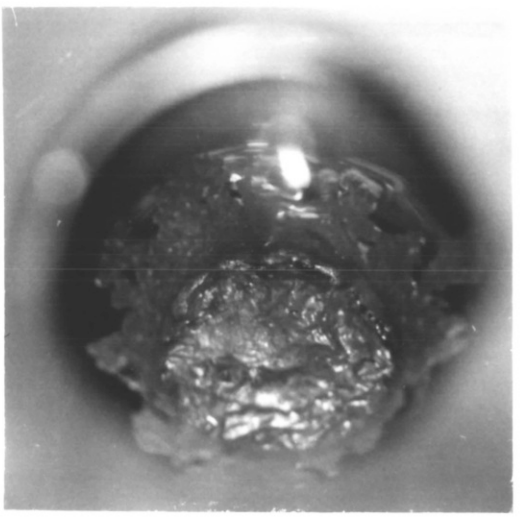

6· t = 1½ min

Fig 3-25 Typical behaviour of $NaOH - NaNO_3$ slag in the O T B *(Run S8)*

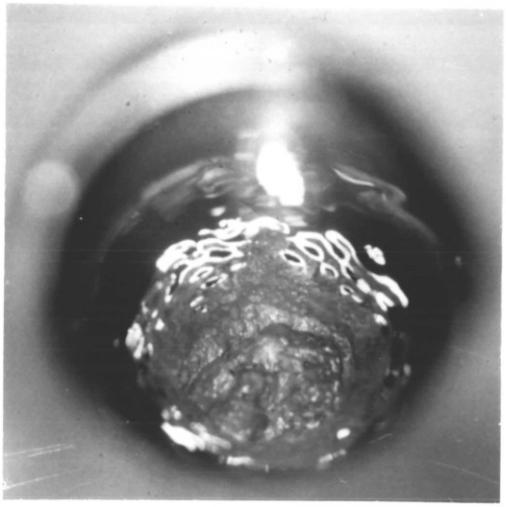

7. t = 2 min

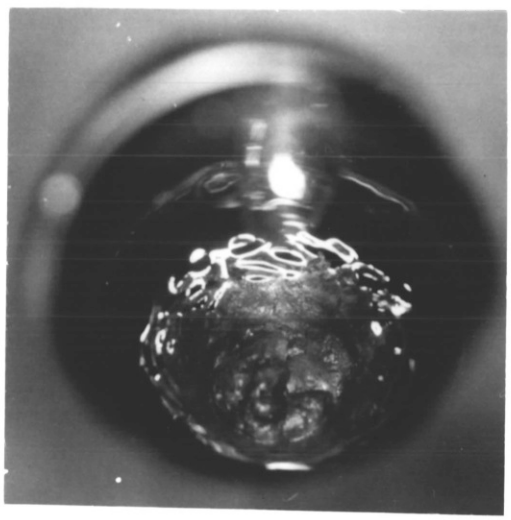

8. t = 2 1/2 min

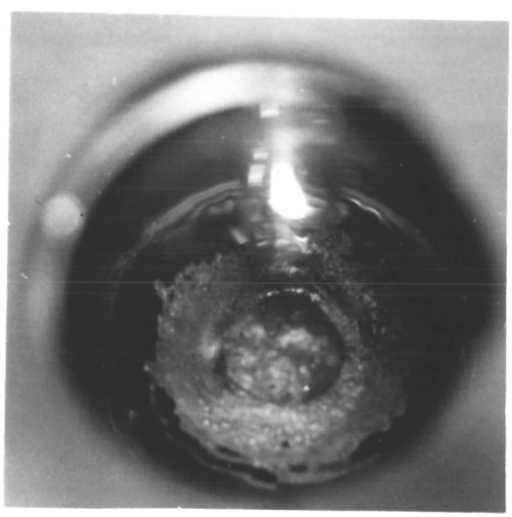

9. t = 4 min

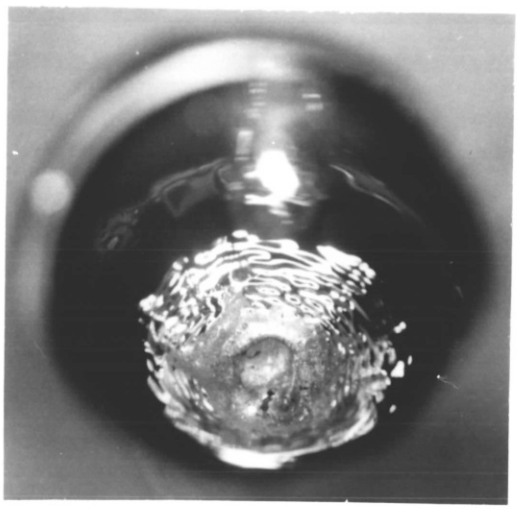

10. t = 6 min

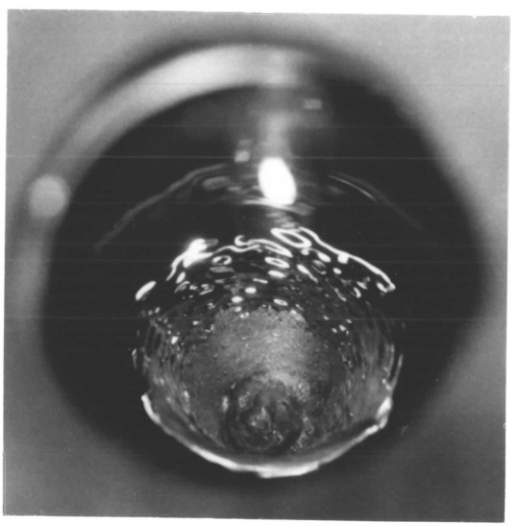

11. t = 7 1/2 min

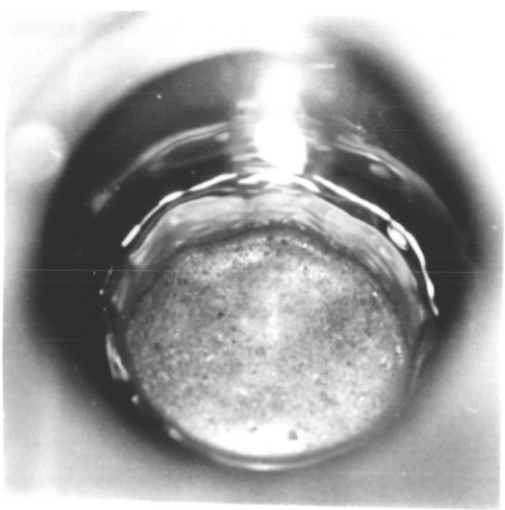

12. After stripping

oxygen potential increased steadily after the slag addition reaching a maximum which is dependent on both the amount of slag added and the concentration of $NaNO_3$ in the slag. Typical changes in the gas and liquid metal oxygen potentials are shown in figs. 3-26 and 3-27B.

Later experiments using NaOH-$NaNO_3$ slags at low mass loadings in the OTB displayed behaviours which differed slightly from the above. The added slags spread rapidly forming a brown slag film which remained as a thin film covering the bubble surfaces. The film later gradually segregated forming islands of coagulated slag blobs surrounded by brown oxide patches (see plate A). At the top surface of the bubble the slag remained as a collection of closely packed oxide particles. No stripping of the slag phase was observed throughout these experiments.

Typical changes in the liquid metal and gas phase oxygen potentials are shown in fig. 3-27B. The liquid metal O_2 potential increased rapidly after slag addition reaching a steady value and later slowly decayed. The gas phase oxygen potential change was characterized by a sharp increase in potential which rapidly returned and finally settled slowly in the region of the original starting potential.

NaOH-$NaNO_3$ slag addition experiments were also done at different oxygen levels in the lead but the observed behaviour was found to be independent of the liquid metal oxygen potential. However, near oxygen saturation in the lead (in run S_{13}; C/C_{sat} = 0.96), there was no appreciable change in the liquid metal oxygen potential after slag addition.

The reaction of NaOH-$NaNO_3$ slag

In run S_6 (fig. 3-26) the OTB pump was switched off soon after the oxygen potential in the lead had reached a steady level. Forming gas (25% H_2, 75% N_2) was then passed through the lead pot to effect deoxidation. The oxygen probe potential rose from about 770 mV (O_2 reference, near Pb/PbO equilibrium potential) to ~1100 mV (just below the Fe/Fe_3O_4 equilibrium) at 450°C, in about 1 hr. This was significantly faster than usually observed at the same temperature.

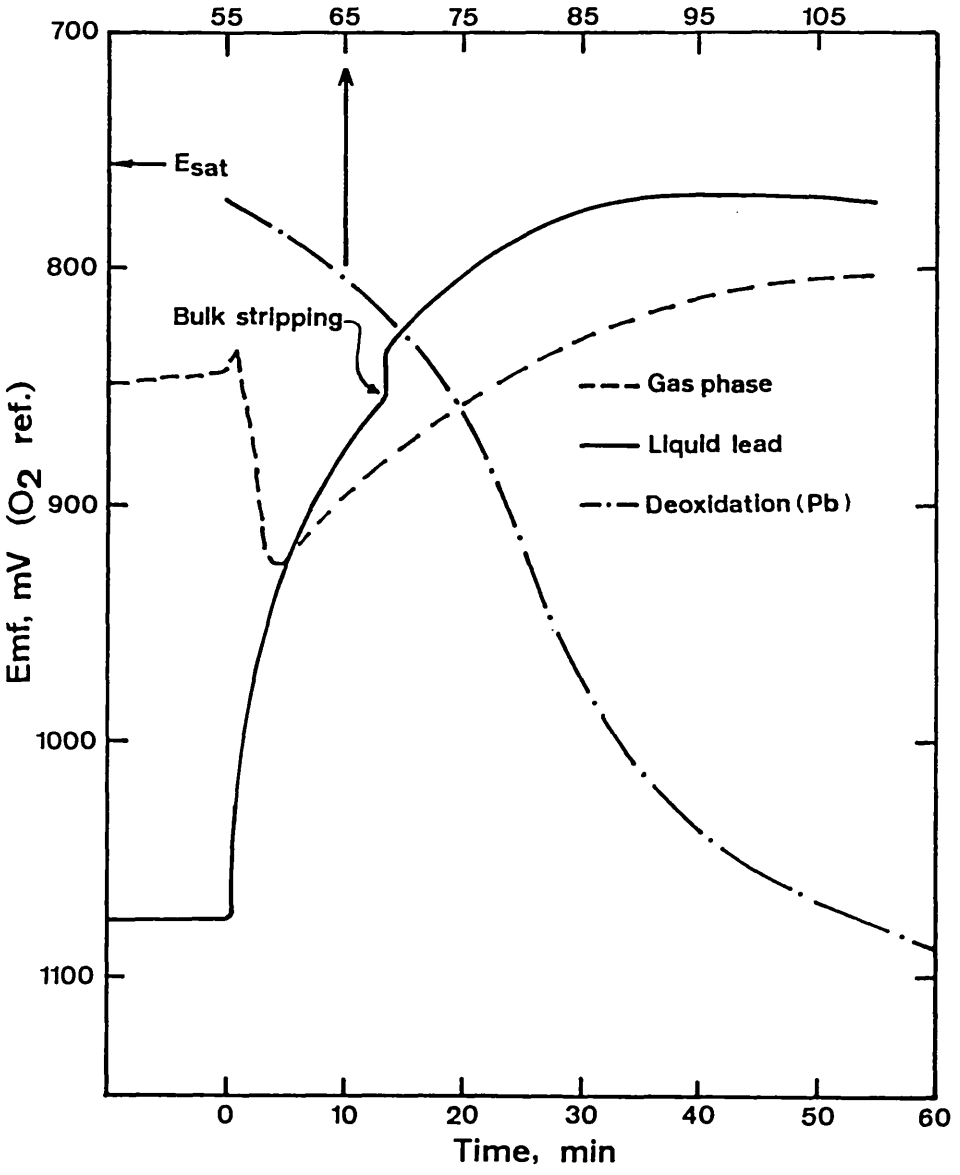

Fig. 3-26: Changes in the oxygen potential due to $NaOH-NaNO_3$ addition to the OTB (Run S_6).

Assuming the sodium nitrate in the slag reacted according to the equation

$$10\ Pb + 4NaNO_3 \rightarrow 2Na_2O + 2N_2 + 10PbO \qquad (3.31)$$

and the oxygen released directly supplied to the lead via the reaction

$$10\ PbO \rightarrow 10[O] + 10\ Pb \qquad (3.32)$$

which would account for the increase in oxygen potential of the lead. In run S_6, 1.2g of $NaOH-NaNO_3$ slag containing 0.3g $NaNO_3$ was added. The amount of oxygen effectively transfered according to the above equations would be ~0.14g, thereby yielding an oxygen concentration increase of 0.47×10^{-3} wt % [O] in lead. This value compares very well with 0.5×10^{-3} wt % [O] required to saturate the lead at 450°C, as measured earlier using the pulse oxygen addition technique discussed in section 3.2.3. The fast deoxidation rate observed in this experiment was attributed to the interaction of the reactive pot, which had not attained equilibrium with oxygen in the course of the experiment. In fig. 3-26 it could be seen that the liquid metal oxygen potential had already started to drop even before the deoxidation gas was passed.

X-ray powder diffraction pattern of slag sample taken from the OTB after $NaOH-NaNO_3$ slag addition confirmed the presence of PbO and hydrolysed NaOH (see table D in appendix A-6). The absence of Na_2O lines in the diffraction pattern is attributed to the effect of the moisture absorbed during the period before X-ray diffraction. Na_2O would react with water at room temperature via the process:

$$Na_2O + H_2O \rightarrow 2NaOH \qquad (3\text{-}33)$$

$$\Delta G^{o}_{298K} = -146.3\ kJ/mol.$$

3.3.3 $NaNO_3$ Addition

The addition of $NaNO_3$ slag to the OTB led to the formation of a dark oxide film which suppressed the ripples on

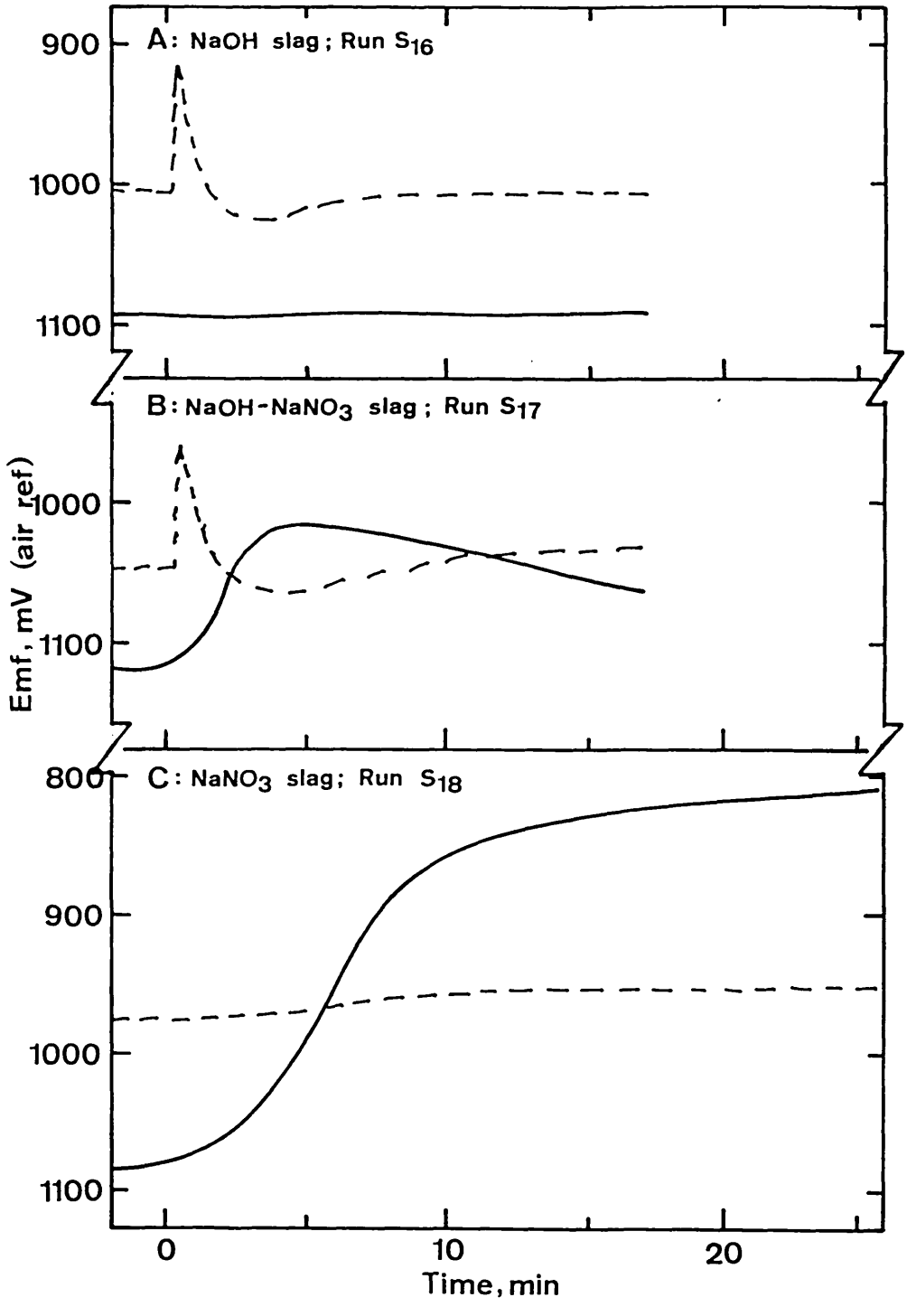

Fig. 3-27: Typical responses of the oxygen probes to slag addition to the OTB.

the bubble base and walls. Typical observations are shown in plate C. The slag pellet, after melting remained as a fairly transparent blob on the dark oxide film on the bubble base. It later slowly reacted forming brown oxide flakes which grew very slowly to cover the bubble walls. After about 5 minutes, the thin oxide flakes grew thicker and became interspaced with reddish-brown oxide flakes. The bubble shape gradually turned conical and the oxide flakes stripped slowly.

The oxygen potential in the liquid metal increased gradually but steadily after each addition of the $NaNO_3$ slag pellet to the OTB. The liquid metal oxygen potential later slowly settled nearer the Pb/PbO equilibrium potential. The gas phase oxygen potentials did not change significantly during $NaNO_3$ addition experiments (see fig. 3-27C). Powder X-ray diffraction of the slag sample taken from the OTB (Table F in appendix A-6) confirmed the formation of Na_2O and PbO, thus confirming a reaction of the type shown by eqn. (3.31).

TABLE 3-3

Summary of Runs - Slag Addition

RUN No.	BUBBLE PARAMETERS		ADDITIVE SLAG		RUN TYPE	COMMENT
	Weir ht (mm)	Base ht (mm)	Slag Type	Slag wt. (g)		
S_1	5.3	10	NaOH	0.80	S_2	Unstable bubble base
S_2	5.1	14	NaOH	0.88	S_2	See Fig. 3-18
S_3	5.3	10	NaOH	1.31	S_2	Unstable bubble base
S_4	5.3	10	NaOH	1.10	S_2	Unstable bubble base
S_5	5.2	12	NaOH	1.00	S_2	Movie picture
S_6	5.2	12	$NaOH/NaNO_3$ (3:1)	1.20	S_8	See Fig. 3-25.
S_7	5.2	14	"	1.10	S_8	-
S_8	5.2	14	"	0.70	S_8	See Fig. 3-25
S_9	5.0	10	"	0.16	S_{14}	Movie pict. $C/C_{sat} \sim 10^{-5}$
S_{10}	5.0	10	"	0.20	S_{14}	Movie pict. $C/C_{sat} \sim 10^{-3}$
S_{11}	5.0	12	"	0.23	S_{14}	$C/C_{sat} = 0.10$
S_{12}	5.0	12	"	0.23	S_{14}	$C/C_{sat} = 0.71$
S_{13}	5.0	12	"	0.24	S_{14}	$C/C_{sat} = 0.96$
S_{14}	5.0	12	"	0.20	S_{14}	See plate A.
S_{15}	5.0	12	$NaOH-NaNO_3$ (4:1)	0.22	S_{15}	See plate B.
S_{16}	5.0	12				
S_{16}	5.0	12	NaOH	0.23	S_2	See plate B.
S_{17}	5.0	10	$NaOH-NaNO_3$ (3:1)	0.32	S_{14}	-
S_{18}	5.0	12	$NaNO_3$	0.24	S_{18}	See plate C.
S_{19}	5.0	10	$NaOH-NaNO_3$ (4:1)	0.25	S_{15}	-
S_{20}	5.0	10	$NaNO_3$	0.13	S_{18}	-

LIST OF PLATES I

PLATE A:

Pure lead system: Run S_{14}

Type of slag: $NaOH-NaNO_3$ (3:1)

Weight of slag: 0.20g

Bubble parameters: Weir height = 5.0 mm
Base depth ~12.0 mm

PLATE B:

Pure lead system: Comparing the behaviour of $NaOH-NaNO_3$ (4:1) and NaOH slags

	Left (S_{15})	Right (S_{16})
Type of slag:	$NaOH-NaNO_3$(4:1)	NaOH
Weight of slag:	0.22 g	0.23g
Bubble parameters:		
Weir height	5.0 mm	5.0 mm
Base depth	~12.0 mm	~12.0 mm

PLATE C:

Pure lead system: Run S_{18}

Type of slag: $NaNO_3$

Weight of slag: 0.24g

Bubble parameters: Weir height = 5.0 mm
Base depth ~12.0 mm

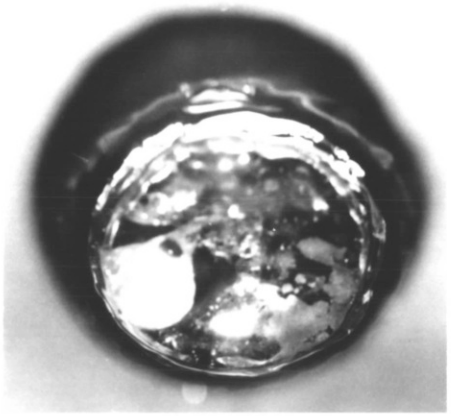

t = 3 s

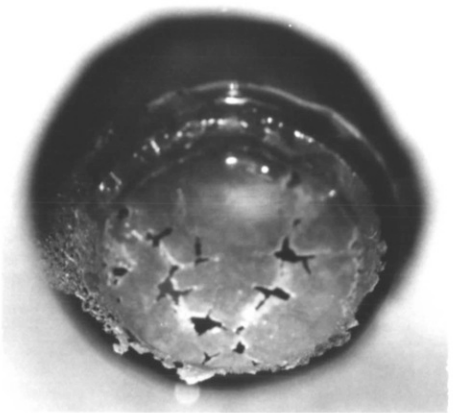

t = 1 min

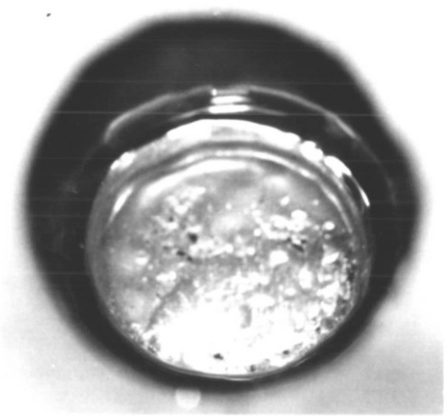

t = 10 s

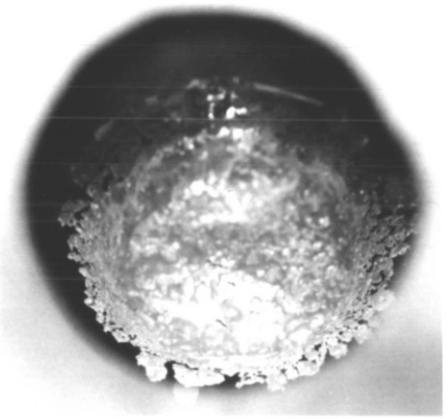

t = 3 mins

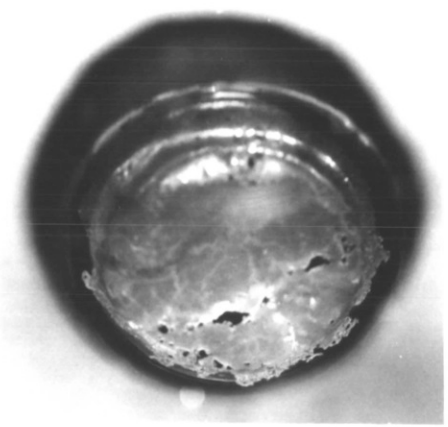

t = 30 s

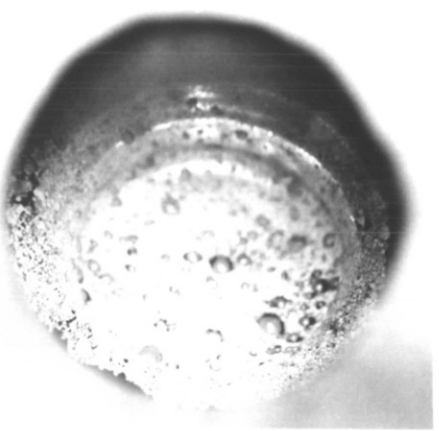

t = 10 mins

PLATE A

$NaOH-NaNO_3$

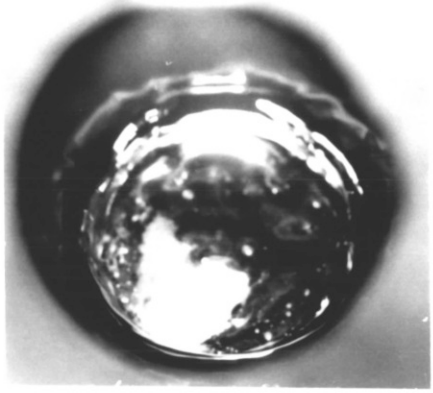

t = 3s

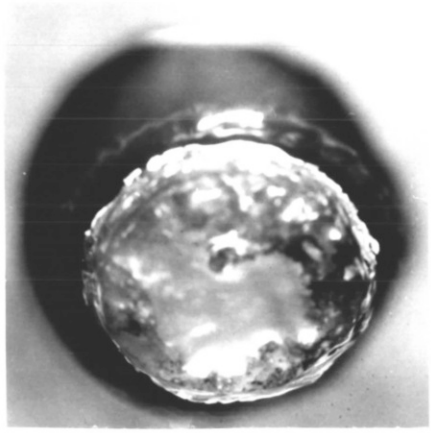

t = 10s

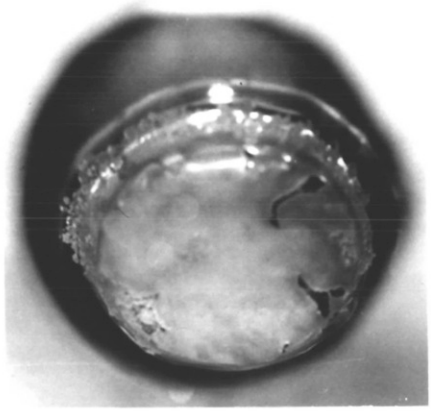

t = 30s

NaOH

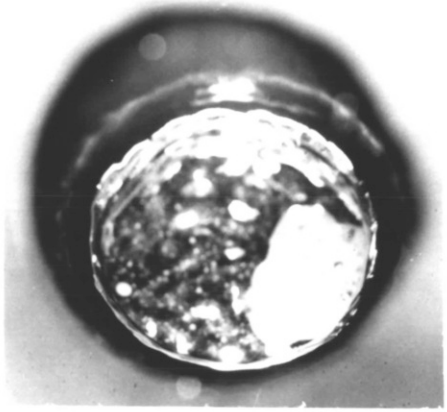

t = 3s

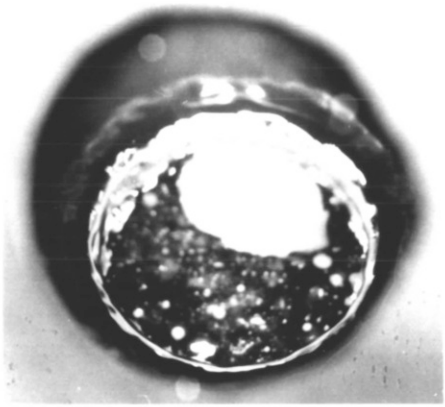

t = 10s

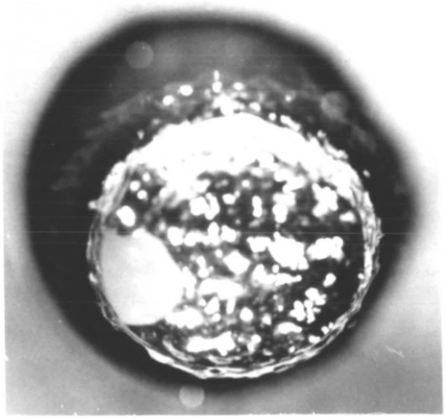

t = 30s

PLATE B

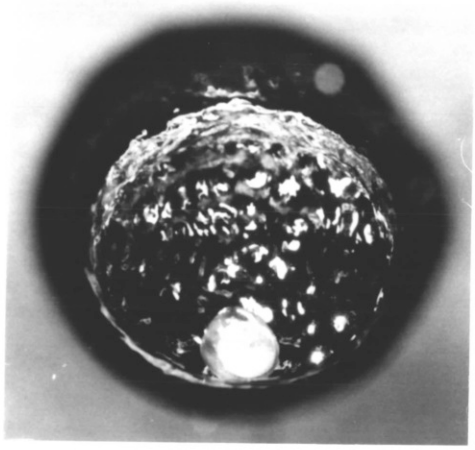

t = 3 s

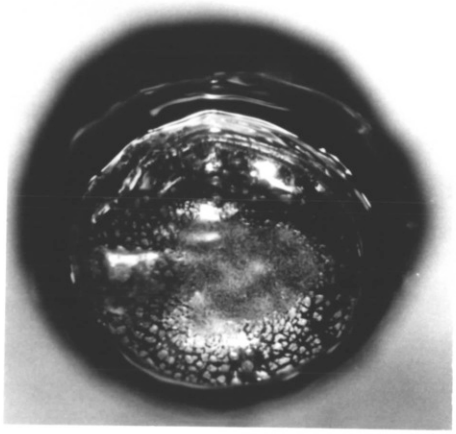

t = 1 min

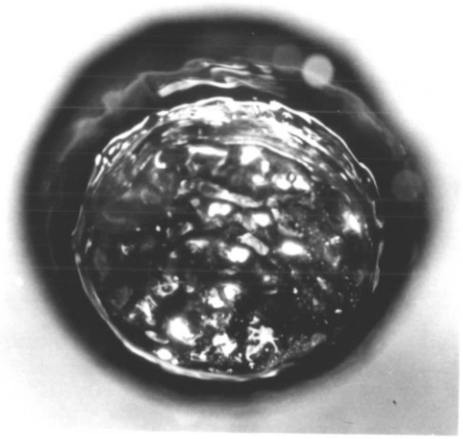

t = 10 s

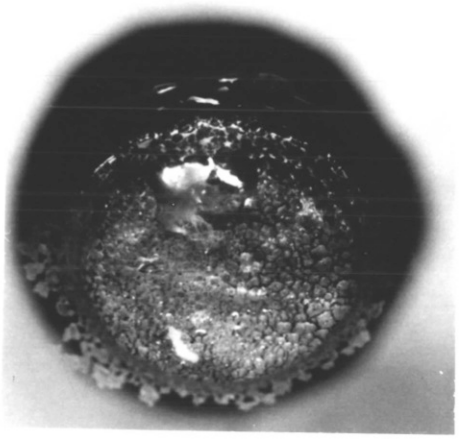

t = 3 mins

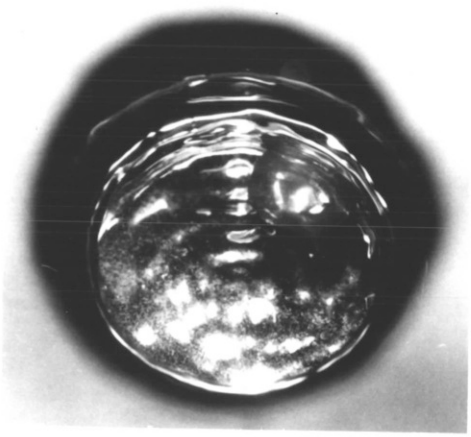

t = 30 s

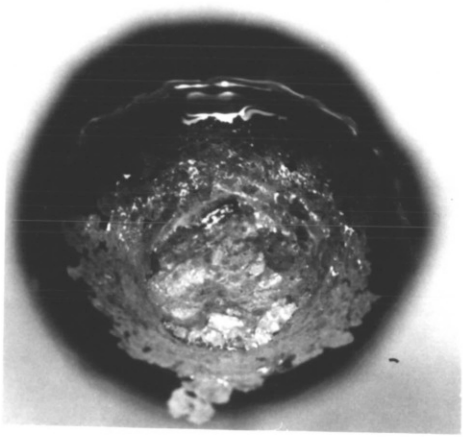

t = 10 mins

PLATE C

3.4 LEAD REFINING: THE HARRIS PROCESS

The behaviour of refining slags carried by bubbles rising in liquid metals was investigated using the open top bubble technique. Antimony and later tin, were added as the impurity elements (~0.06 wt %) in the lead. The removal of these impurities using caustic soda-based slags (as in the Harris process) was then observed in the OTB.

Various types of slags were used in these investigations. The reactive slags displayed interesting spreading characteristics. These observations are illustrated by the sequence of photographs shown in plates D to I. The oxygen potentials of the liquid metal and the outlet gas were also simultaneously monitored during the experiments. These potentials did not change significantly throughout the experiments. In some experiments the slag samples were removed from the OTB using a cold silica rod, and its constitutuent compounds identified by the powder X-ray diffraction technique. Owing to the solid nature of some of the resulting slags, it was not possible to take samples of them from the OTB without significantly oxidizing the lead alloy. Such samples were hence not removed for analysis.

3.4.1 The reactions of antimony

Antimony was added to the deoxidized lead as a solid using the solid dispenser, in the same way as the slags. The metal was observed to melt inside the OTB. Each addition of antimony led to a slight suppression of the ripples in the bubble. The ripples returned after antimony dissolution. There were, however, no changes in the oxygen potential of the liquid metal and the outlet gas. 18g of antimony was added to the lead before slag additions were restarted. The behaviour of the various slags in the OTB after antimony addition is summarised below.

NaOH slag

The addition of NaOH slag to the OTB resulted in a slight suppression of the basal ripples in the bubble. The slag pellet melted within 5 seconds and sat at one end of the

bubble base, stripping very slowly. This behaviour was similar to that of NaOH addition to the OTB before the addition of antimony to the lead, as discussed earlier (section 3.3.1). There was no change in the liquid metal oxygen potential. The gas phase oxygen probe displayed its characteristic change, attributed to the loss of excess water from the NaOH (see section 3.4.3). The observed changes in oxygen probe potentials resulting from NaOH addition to the OTB are shown in fig. 3-28a.

It was, therefore, concluded that the caustic soda did not react significantly with the dissolved antimony in the lead.

NaOH slag + O_2 gas

A 10 ml oxygen gas pulse was later injected onto the OTB containing some NaOH slag. This led to a total suppression of the ripples in the bubble by the resulting dark oxide film. The caustic soda slag in the bubble contracted slightly after oxygen addition but did not react with the oxide film which soon dissolved in the lead leaving small oxide flakes, suspected to be Sb_2O_3. These small oxide flakes took a considerable time to dissolve back into the lead. The ripples in the bubble base reappeared after about 20 seconds of oxygen addition and the NaOH remained virtually unreacted in the bubble base.

In a subsequent experiment an oxygen gas pulse was added to the OTB before the addition of the NaOH slag. The NaOH slag pellet melted and sat immobile on top of the dark oxide film covering the OTB surfaces, apparently unreacted. The ripples at the bubble base returned soon after the slag addition leaving some dark oxide particles dancing about the bubble base, near the liquid slag.

Oxygen potentials in the system changed very little throughout the duration of the experiments. Oxygen input into the system was reflected as a small peak as shown in fig. 3-30. The liquid metal oxygen potential remained virtually unchanged during the experiments.

The reaction of the added oxygen was thought to occur via two processes:

(i) Oxidation of the lead by the reaction

$$Pb(\ell) + \tfrac{1}{2} O_2(g) \rightarrow PbO(s) \qquad (3.1)$$

(ii) Oxidation of the antimony in lead by the lead oxide or dissolved oxygen:

$$3PbO(s) + 2[Sb] \rightarrow Sb_2O_3(s) + Pb(\ell) \qquad (3.34)$$

$$3[O] + 2[Sb] \rightarrow Sb_2O_3(s) \qquad (3.35)$$

Owing to the higher antimony concentration in the lead (0.06 wt %) at such low oxygen potentials ($C/C_{sat} \sim 10^{-5}$), Sb would be readily available at the reaction interface thereby suppressing oxygen dissolution in the lead. Hence the liquid metal probe potential remained virtually unchanged.

The caustic soda in the OTB remained inert since it does not react with PbO[56-58]. Its reaction with Sb_2O_3 is very slow producing complex products, as reported by Aranda[56].

PbO-NaOH slag

The slag pellet melted within 10 seconds of its addition and sat immobile in the bubble base with visible oxide specs suspended in the slag matrix. The slag stripped very slowly but displayed no reactive features (see plate G). The slag behaviour in the OTB was similar to that of the NaOH slag. Changes in the oxygen potential of both the liquid metal and the gas phase were also similar to that observed for NaOH slags (see fig. 3.28A).

$NaOH-NaNO_3$ slags

The reaction of $NaOH-NaNO_3$ (4:1) slags in the OTB produced an interesting spreading behaviour. The slag pellet melted within 5 seconds suppressing the basal ripples and forming a deep brown film which spread rapidly, covering

the bubble base and walls. After about 15 seconds the slag film rapidly contracted and formed a grey viscous blob, which sat on the bubble base. The ripples at the bubble base returned soon after the slag film had started to contract (see frame 7 in plate D). There was no change in the liquid metal oxygen potential. The gas phase probe responded with its characteristic change, the peak usually associated with the addition of an NaOH-based slag (see fig. 3.28B).

The reactions thought to occur were:

(i) the melting and spreading of the NaOH-$NaNO_3$ slag in the manner discussed in section 3.3.2, and

(ii) the oxidation of the impurity antimony in the lead by the oxidizing slag, as in the Harris process, via the reaction:

$$4NaOH+2NaNO_3+2[Sb]\rightarrow 2Na_3SbO_4+N_2+2H_2O \qquad (3.36)$$

The excess caustic soda in the added slag was used as a suspension matrix for the sodium antimonate. Formation of sodium antimonate was confirmed from the powder X-ray diffraction pattern of the slag samples taken from the OTB (see table G in the appendix). The N_2 and H_2O formed during the reaction would be given off as gases. These additional water molecules is probably responsible for the larger peaks observed in the outlet gas oxygen potential (see fig. 3-28).

A mass balance on the slag phase based on reaction (3.36)suggested the presence of an additional element. The results show an average increase in weight of the slag phase of about 13%. Chemical analysis (see also table 3-5) of a slag sample taken from the OTB show that the slag contained 11.47% Sb and 9.40% Pb. It was thus concluded that the pick-up of lead was also responsible for the measured increase in weight.

Reactions observed using $NaOH-NaNO_3$ (1:1) slag in the OTB displayed a different spreading behaviour (see plate E). After melting, the added slag spread rapidly like the $NaOH-NaNO_3$ (4:1) slag but did not contract likewise. It stayed on as a film covering the entire bubble surfaces and slowly grew in thickness with time. After about 60 seconds it started to crack, and finally broke up into grey and white flakes, later confirmed to be antimonate flakes. With an increase in time, the white antimonate flakes became the dominant phase.

The observed changes in oxygen potential of the system are similar to that described above for $NaOH-NaNO_3$ (4:1) slag and are shown in fig. 3-29.

In run R_{11} (see plate H), 0.4g of Sn was added to the OTB soon after the formation of sodium antimonate by the reaction of the previously added $NaOH-NaNO_3$ (4:1) slag with the antimony in the lead. The tin melted and reacted slowly with the antimonate and after about 3 minutes, a white shade appeared at the under surface of the antimonate. The sample was removed after 6 minutes and powder X-ray diffraction confirmed the formation of sodium stannate. The lines observed are similar to those shown in table H in appendix A-6. There were no measured changes in either the liquid metal or gas phase oxygen potentials.

$\underline{NaNO_3}$ $\underline{slag}$

The behaviour of $NaNO_3$ slag in the lead-antimony system was somewhat similar to that in the pure lead system (see section 3.3.3). The slag pellet melted soon after addition, suppressing the rippling of the bubble. It subsequently formed a thin shiny brown film which spread slowly up the bubble walls. The slag film later grew in thickness and its colour gradually turned milky brown (see plate F). This brown paste soon began to accummulate in the bubble base and the bubble shape subsequently turned conical (see frame 6 in plate F). Oxygen potentials of the liquid lead and the gas phase increased slightly during the experiments. Typical changes in oxygen potential are

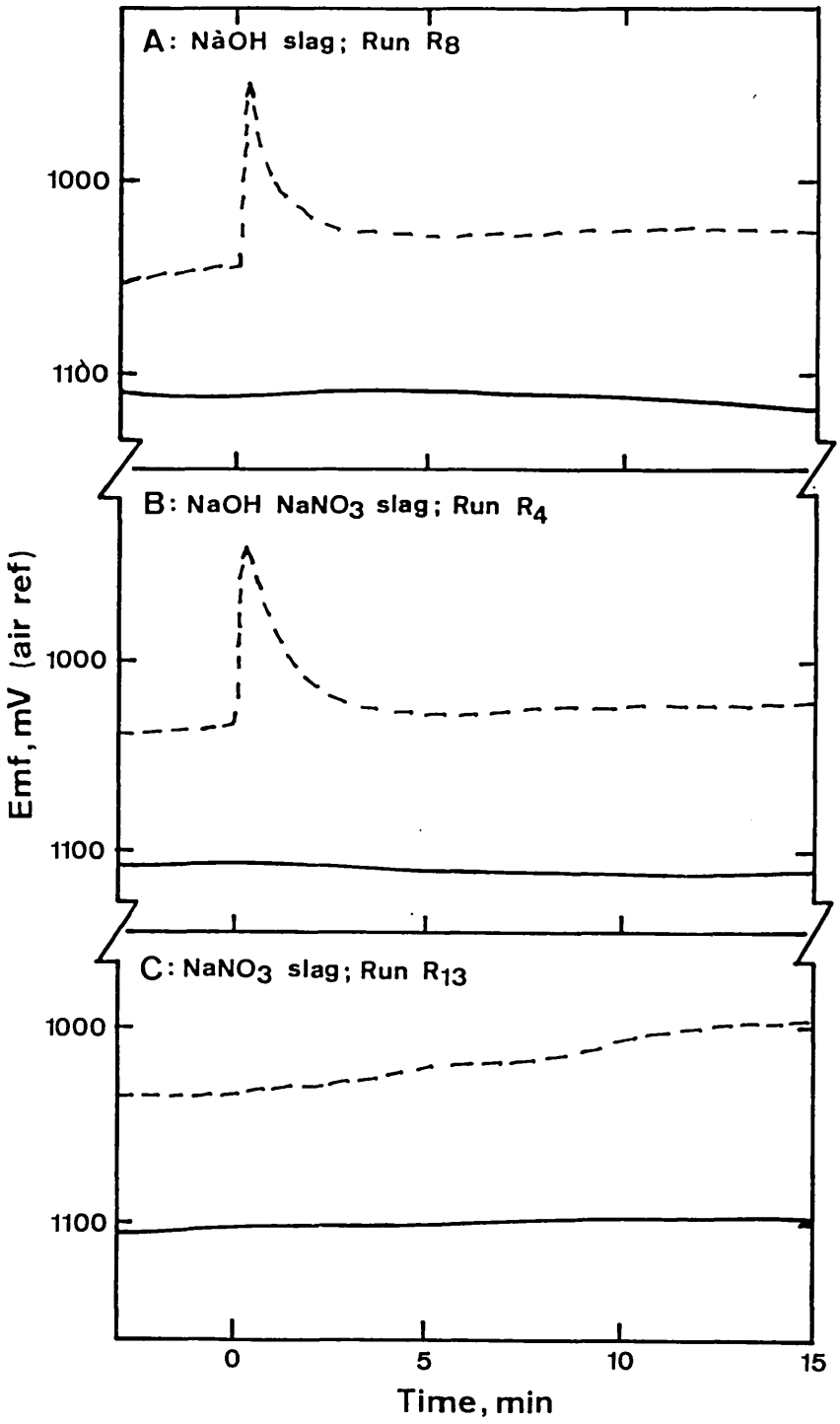

Fig. 3-28: Typical responses of the oxygen probes to slag addition to the OTB, after antimony addition to the lead.

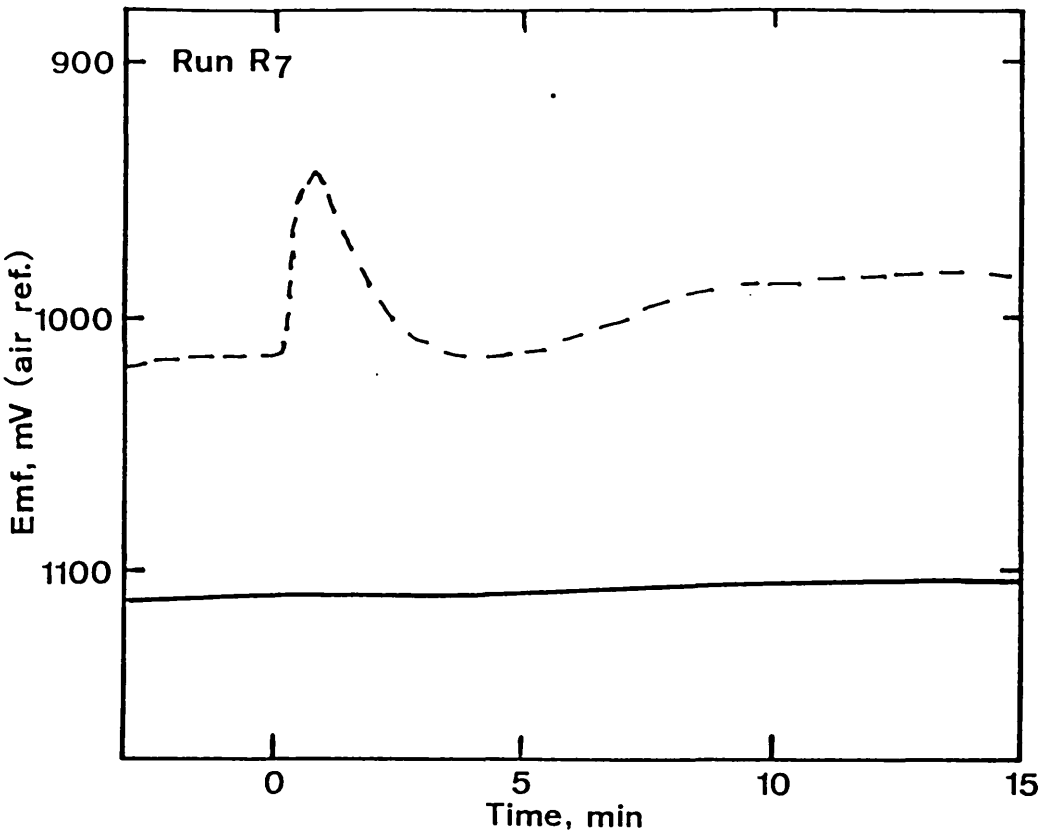

Fig. 3-29: Typical response of the oxygen probes, after the addition of $NaOH-NaNO_3$ (1:1) slag containing Sb.

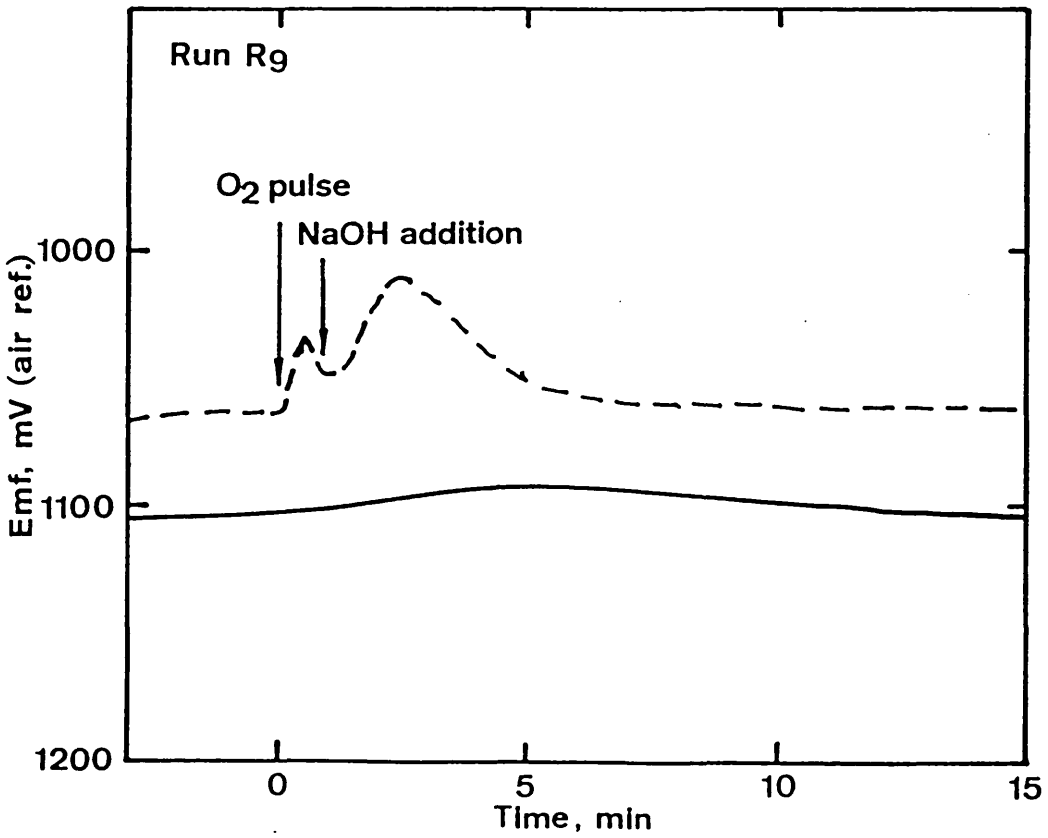

Fig. 3-30: Probe response to the addition of NaOH slag, after the injection of O_2 pulse to lead containing Sb.

shown in fig. 3-28C.

The reactions thought to have occurred after the addition $NaNO_3$ to the system were:

(1) The oxidation of the lead by the nitrate

$$5Pb + 2NaNO_3 \rightarrow 5PbO + Na_2O + N_2 \qquad (3.31)$$

(2) The removal of impurity antimony in the lead via the process

$$3PbO + [Sb] \rightarrow Sb_2O_3 + 3Pb \qquad (3.34)$$

Owing to the high concentration of antimony in the lead, the antimony reaction (3.34) would have occurred faster than the oxygen could dissolve in the lead, hence no net change in the liquid metal oxygen potential, as shown by fig. 3-28C.

3.4.2 The reaction of antimony and tin

18g of tin was later added to the lead-antimony alloy. The tin addition was done exactly in the same way as was done for antimony. The added tin suppressed the basal ripples in the bubble as it dissolved into the lead. There were also no oxygen potential changes in both the gas phase and in the liquid metal phase. The reactions of the added slags with the lead-tin-antimony alloy are summarized below.

NaOH slag

The behaviour of NaOH slag in the Pb-Sb-Sn system was similar to its behaviour in the Pb-Sb system. The slag pellet melted soon after its addition and settled along the basal edge of the bubble. It subsequently stripped very slowly from the bubble base. The observed changes in oxygen potential in both the liquid metal and the outlet gas were similar to those observed with the NaOH slag in pure lead and lead-antimony alloy (see fig. 3-31).

NaOH-$NaNO_3$ slag

NaOH-$NaNO_3$ (4:1) slag pellets melted very quickly in the OTB and spread out forming a greyish-brown slag film which covered the entire bubble surface. Within 20 seconds the slag had contracted again forming a viscous blob, in the same way as was observed for the same slag in the Pb-Sb system (see plate I).

The changes in oxygen potential osberved during the reactions were similar to those observed for the corresponding Pb-Sb system (fig. 3-28B). The slag samples removed from the OTB, after each reaction, were also grey in colour, with white shades on the surface in contact with the lead. Powder X-ray diffraction of the samples confirmed the formation of sodium stannate, but not sodium antimonate (see Table H in appendix A-6). However chemical analysis of the samples (Table 3-5) suggests some antimony reaction. The main reaction thought to have occurred was

$$6NaOH + 4NaNO_3 + 5\,[Sn] \rightarrow 5Na_2\,SnO_3 + 3H_2O + 2N_2 \qquad (3.37)$$

With NaOH-$NaNO_3$ (1:1) slag, a thick greenish yellow slag was formed on the bubble surface, as in the Pb-Sb system. This film, however, did not break likewise. This behaviour was thought to be due to the stoichiometric balance in the slag. The amount of NaOH in the slag was in excess of what was required stoichiometrically by reaction (3.37). In the lead-antimony system, equal weights of NaOH and $NaNO_3$ were stoichiometrically required (see eqn. (3.36)).

$NaNO_3$ slag

$NaNO_3$ slag formed a thin gold coloured film in the OTB after its additions. The film spread very slowly, as was observed with the pure lead and the lead-antimony systems. After about 5 minutes a reddish brown oxide film began to form at the centre of the bubble, and the bubble shape later went conical.

Both the liquid metal and gas phase oxygen potentials remained virtually unchanged during the experiments. The behaviour of the oxygen probes were similar to that observed for $NaNO_3$ slag in the Pb-Sb system, shown in fig. 3-28C.

The likely reactions resulting from the addition of sodium nitrate were the oxidation of the lead in the process:

$$5Pb + 2NaNO_3 \rightarrow 5PbO + Na_2O + N_2 \qquad (3.31)$$

followed by the oxidation of its constituent impurities:

$$2PbO + [Sn] \rightarrow SnO_2 + 2Pb \qquad (3.38)$$

$$3PbO + 2[Sb] \rightarrow Sb_2O_3 + 3Pb \qquad (3.34)$$

The Na_2O may also have reacted with SnO_2 via the process:

$$Na_2O + SnO_2 \rightarrow Na_2SnO_3 \qquad (3.39)$$

However, the above reactions could not be confirmed since it was not possible to sample the slag phase.

$\underline{Na_3SbO_4}$ slag

The "sodium antimonate slag", formed as a result of the reaction of NaOH-$NaNO_3$ (4:1) slag with the lead-antimony system was added to the OTB, after tin had been added to the lead. The behaviour of this slag in the OTB was similar to that of pure NaOH slag, described earlier. The gas phase potential change was also similar to that of NaOH slag, but a smaller peak in oxygen potential was recorded in this case. The sample removed from the bubble was similar in appearance to that removed after the reaction of NaOH-$NaNO_3$ (4:1) slag with Pb-Sb-Sn alloy and a subsequent chemical analysis of the sample confirmed that it contained tin (see table 3-5). The reaction thought to have occurred was

$$5[Sn] + 4Na_3SbO_4 + H_2O \rightarrow 4[Sb] + 2NaOH + 5Na_2SnO_3 \qquad (3.40)$$

3.4.3 Gas phase oxygen potential changes

The sharp change in oxygen potential of the outlet gas observed immediately after each addition of NaOH or $NaOH-NaNO_3$ slag was thought to be due to the evolution of the water absorbed by the slag prior to its addition to the OTB. The response was not observed during experiments with $NaNO_3$ slags (see figs. 3-27C and 3-28C).

Caustic soda is very hygroscopic and would dissolve water even at very high temperatures. Data from Rahmel and Kruger[62] give the water content of molten caustic soda in equilibrium with 1 bar of water to increase from 0.3 wt % to H_2O at ~500°C to about 3 wt % H_2O at 350°C. Thus even at the temperature of slag preparation (500°C), NaOH would still retain up to 0.3 wt % H_2O. Further to this, the slag would pick up more water from the atmosphere during the time it was cast into pellets and subsequently weighed. During the melting of the slag pellets in the OTB this excess water would then be evolved as steam into the gas atmosphere of the lead and hence monitored by the gas phase oxygen probe.

In a separate experiment, drops of water were added to the OTB and the behaviour monitored by both the liquid lead and the outlet gas probes. The observed behaviour, shown in fig. 3-32, is quite similar to that earlier observed. It was thus concluded that the gas phase oxygen probe was sensitive to the H_2/H_2O ratio in the gas phase.

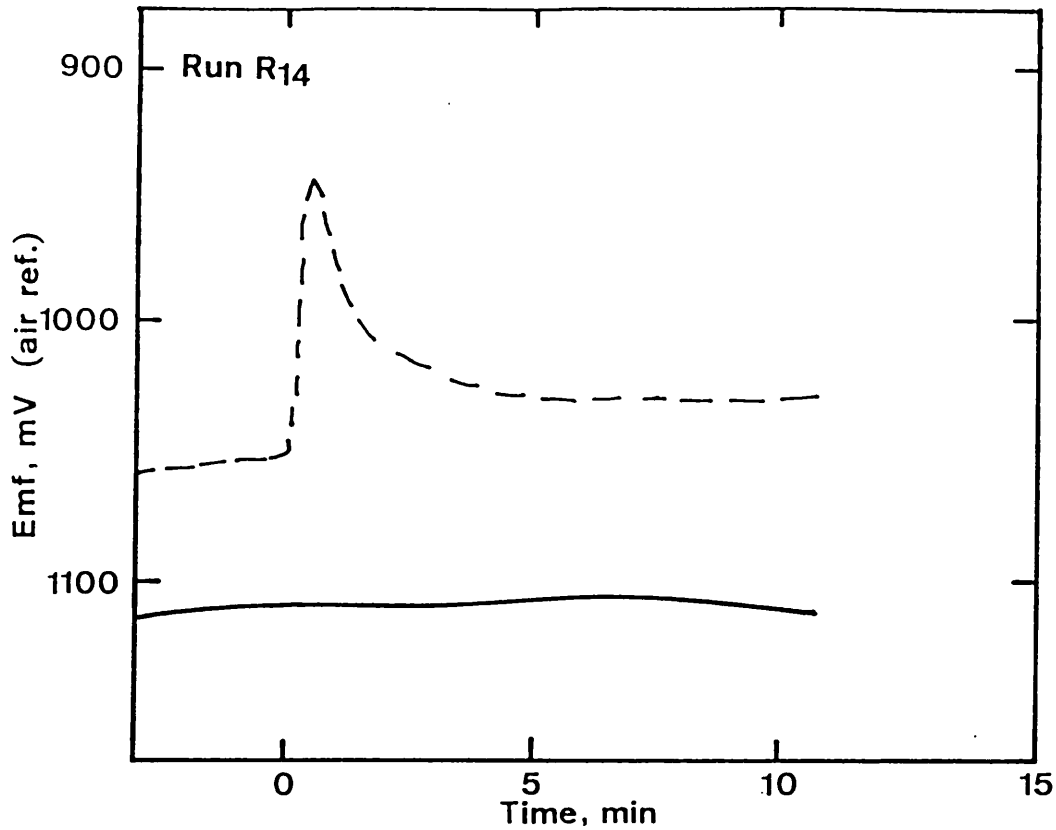

Fig. 3-31: Probes responses to the addition of NaOH slag to the OTB, after Sb and Sn addition to the lead.

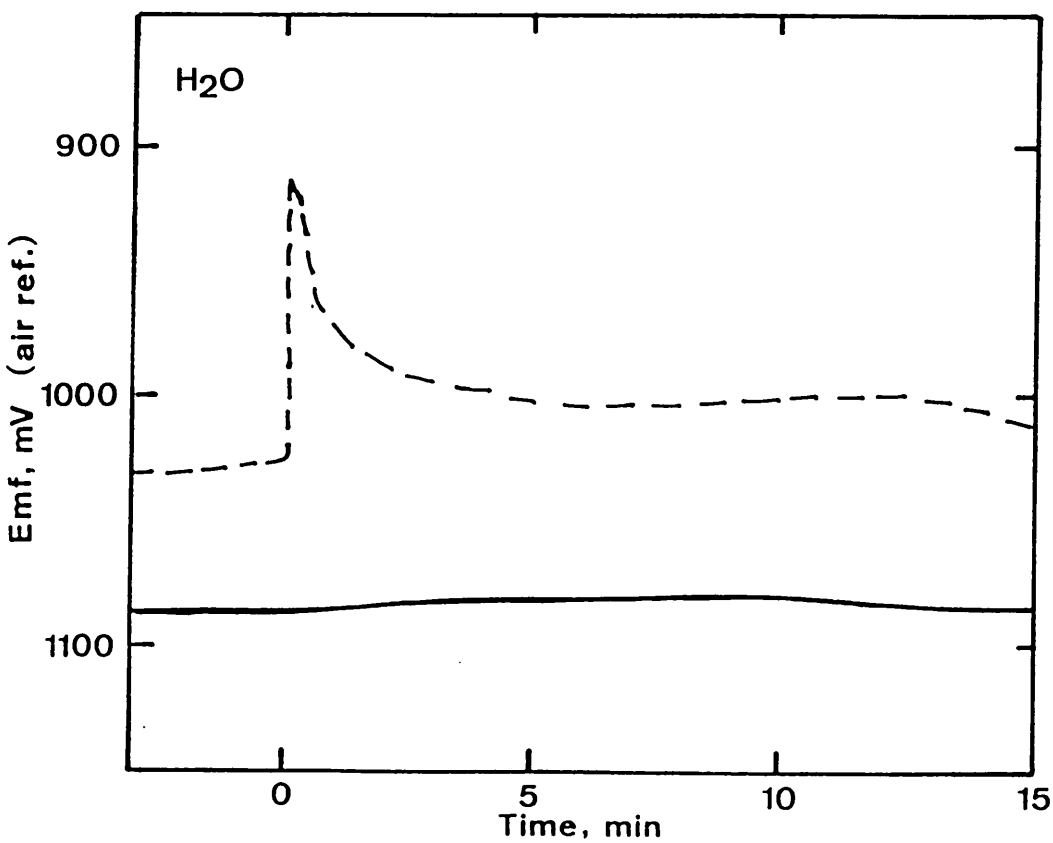

Fig. 3-32: Probes responses to the addition of a drop of water to the OTB, after Sn and Sb addition to the lead.

TABLE 3-4

Summary of Runs - Lead Refining.

RUN No	BUBBLE PARAMETERS		ADDITIVE SLAG		ALLOY	RUN TYPE	COMMENT
	Weir ht (mm)	Base ht (mm)	Slag Type	Weight (g)			
R_1	5.0	10	$NaOH-NaNO_3$ (4:1)	0.16	Sb	R_2	-
R_2	5.0	10	"	0.16	Sb	R_2	See Plate D
R_3	5.0	12	"	0.15	Sb	R_2	Colour slides
R_4	5.0	12	"	0.15	Sb	R_2	"
R_5	5.0	15	"	0.12	Sb	R_2	"
R_6	5.0	10	$NaOH-NaNO_3$ (1:1)	0.15	Sb	R_{12}	-
R_7	5.0	14	"	0.15	Sb	R_{12}	-
R_8	5.0	12	NaOH	0.10	Sb	S_2	See Fig.3-18
R_9	5.0	12	$NaOH+O_2$ gas	0.17	Sb	-	-
R_{10}	5.0	12	PbO-NaOH	0.18	Sb	R_{10}	See plate G
R_{11}	5.0	12	$NaOH-NaNO_3$ (4:1)	0.15	Sb	-	See plate H
R_{12}	5.0	12	$NaOH-NaNO_3$ (1:1)	0.15	Sb	R_{12}	See plate E
R_{13}	5.0	12	$NaNO_3$	0.25	Sb	R_{13}	See plate F
R_{14}	5.0	12	NaOH	0.17	Sb+Sn	S_2	See Fig. 3-18
R_{15}	5.0	12	$NaOH-NaNO_3$ (4:1)	0.15	Sb+Sn	R_{15}	See plate I
R_{16}	5.0	12	$NaOH-NaNO_3$ (1:1)	0.20	Sb+Sn	-	-
R_{17}	5.0	12	$NaNO_3$	0.21	Sb+Sn	R_{13}	-
R_{18}	5.0	12	$NaOH-NaNO_3$ (4:1)	0.16	Sb+Sn	R_{15}	Colour slides
R_{19}	5.0	12	Na_3SbO_4	0.17	Sb+Sn	-	Colour slides
R_{20}	5.0	12	$NaNO_3$	0.15	Sb+Sn	R_{17}	Colour slides

TABLE 3-5

Analysis of Samples*

Sample	Pb	Fe	Na	Sb	Sn
METAL					
A	-	<2ppm	<1ppm	10ppm	-
B	-	<2ppm	<1ppm	1ppm	-
C	-		<1ppm	770ppm	-
D	-	-	-	810ppm	640ppm
SLAG					
E	9.40%	-	-	11.47%	-
F	9.43%	-	-	9.22%	3.27%
G	15.64%	-	-	2.68%	4.69%

METAL:

Sample A - After NaOH addition experiments.

Sample B - After NaOH and $NaNO_3$ addition experiments.

Sample C - After Sb addition to the lead

Sample D - After Sb and Sn addition to the lead.

SLAG:

Sample E - $NaOH-NaNO_3$ (4:1) slag after reaction with lead containing antimony.

Sample F - Sodium antimonate slag after reaction with lead containing tin and antimony.

Sample G - $NaOH-NaNO_3$ (4:1) slag after reaction with lead containing tin and antimony.

* Analysis carried out at the laboratories of Metallurgie Hoboken Overpelt, Belgium.

TABLE OF PLATES II

PLATE D

Lead-antimony alloy:	Run R_2
Type of slag:	$NaOH-NaNO_3$ (4:1)
Weight of slag:	0.16g
Bubble parameters:	Weir height = 5.0 mm Base depth ~ 10.0 mm

PLATE E

Lead-antimony alloy:	Run R_{12}
Type of slag:	$NaOH-NaNO_3$ (1:1)
Weight of slag:	0.15g
Bubble parameters:	Weir height = 5.0 mm Base depth ~ 12.0 mm

PLATE F

Lead-antimony alloy:	Run R_{13}
Type of slag:	$NaNO_3$
Weight of slag:	0.25g
Bubble parameters:	Weir height = 5.0 mm Base depth ~12.0 mm

PLATE G

Lead-antimony alloy:	Run R_{10}
Type of slag:	PbO-NaOH
Weight of slag:	0.18g
Bubble parameters:	Weir height = 5.0 mm Base depth ~12.0 mm

PLATE H

Lead-antimony alloy:	Run R_{11} - the reaction of 0.4g Sn* with Na_3SbO_4
Type of slag:	$NaOH-NaNO_3$ (4:1)
Weight of slag:	0.15g
Bubble parameters:	Weir height = 5.0 mm Base depth ~12.0 mm

*Tin added to the OTB 60 seconds after slag addition (i.e. after the formation of sodium antimonate in the OTB.)

PLATE I

Lead-antimony - tin system:	Run R_{15}
Type of slag:	$NaOH-NaNO_3$ (4:1)
Weight of slag:	0.17g
Bubble parameters:	Weir height = 5.0 mm Base depth ~ 12.0 mm

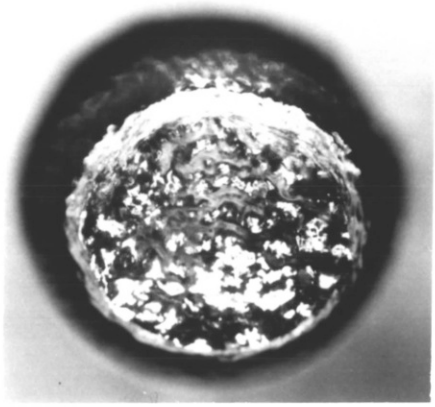

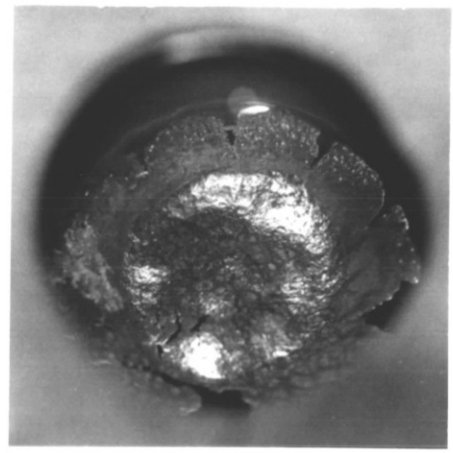

t = 9s

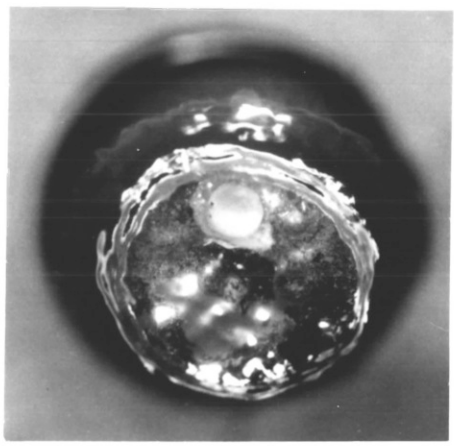

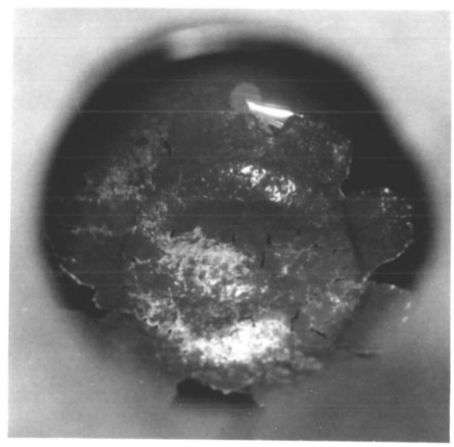

t = 3s

t = 12s

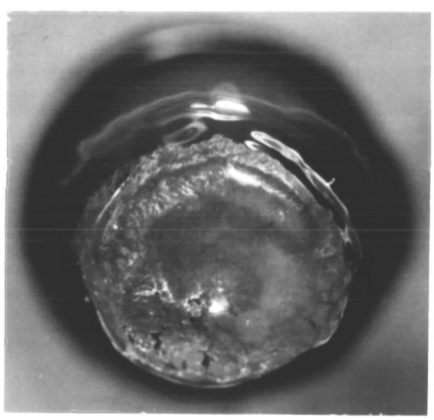

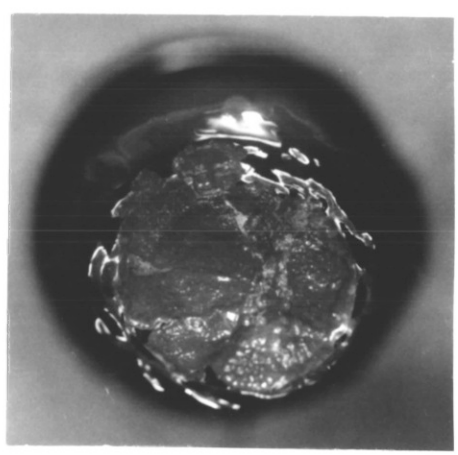

t = 6s

t = 15s

PLATE D

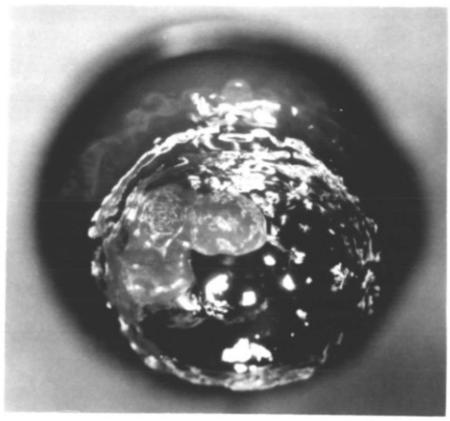

t = 18 s

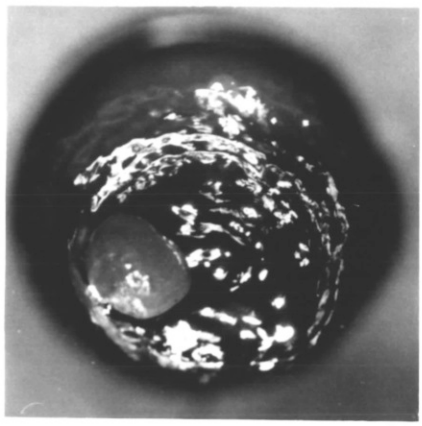

t = 45 s

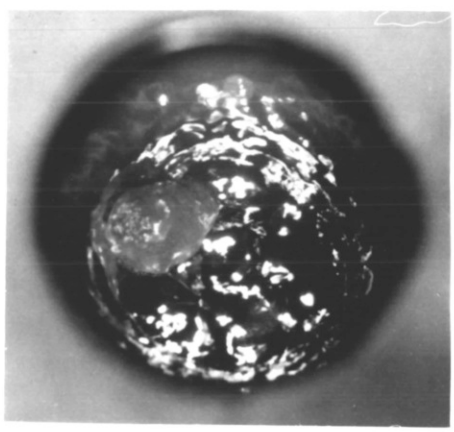

t = 21 s

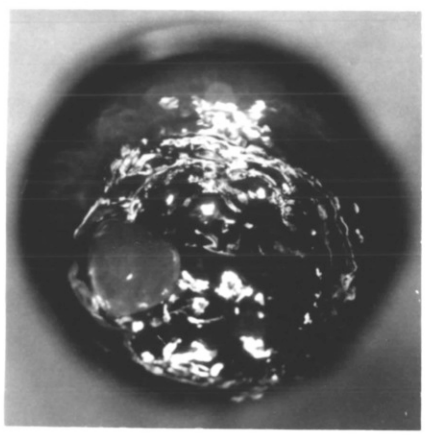

t = 1 min

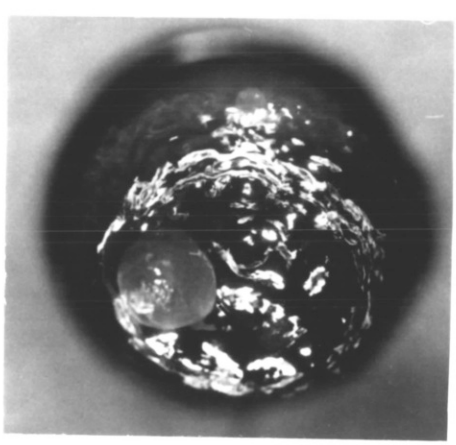

t = 30 s

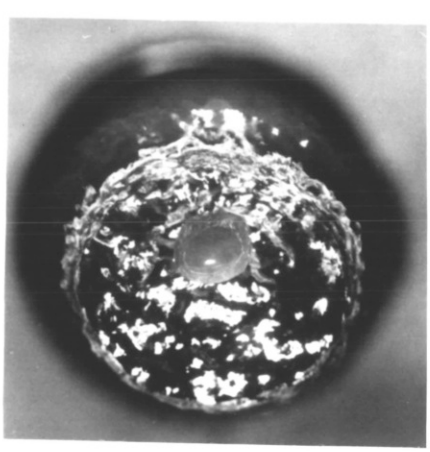

t = 5 mins

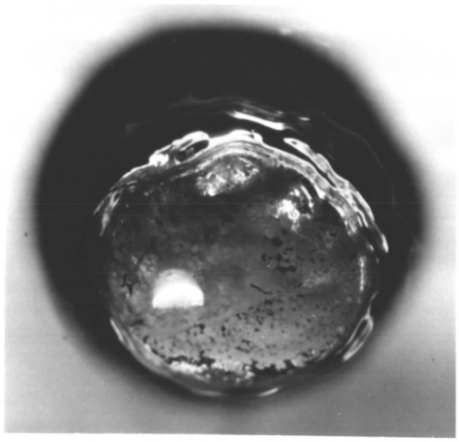

t = 3s

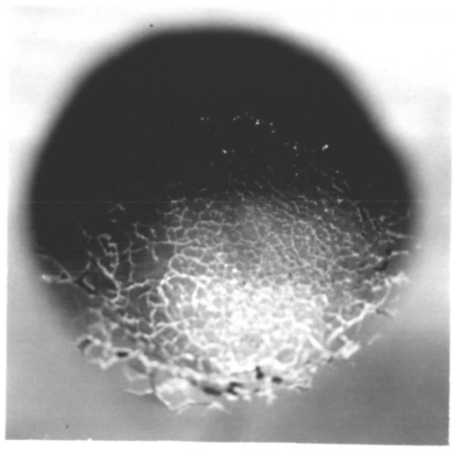

t = 1 min

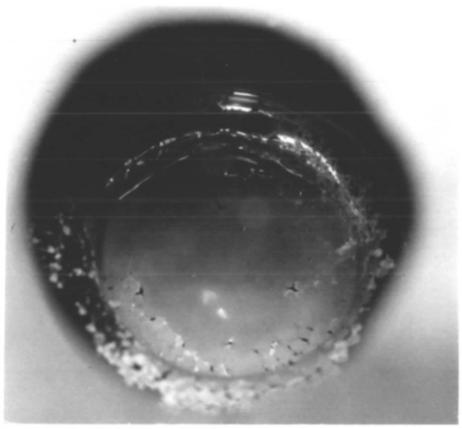

t = 10s

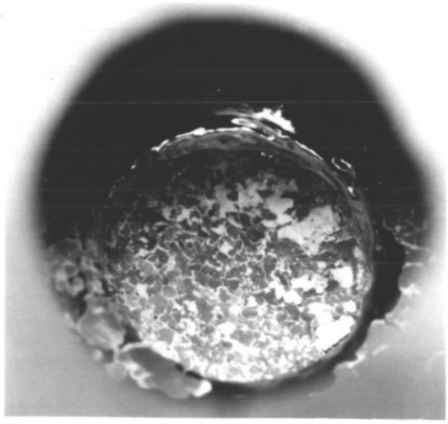

t = 2 mins

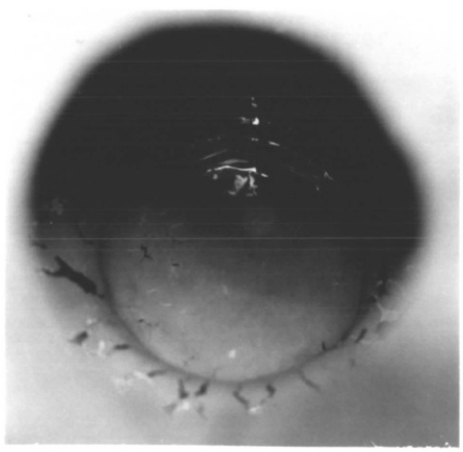

t = 30s

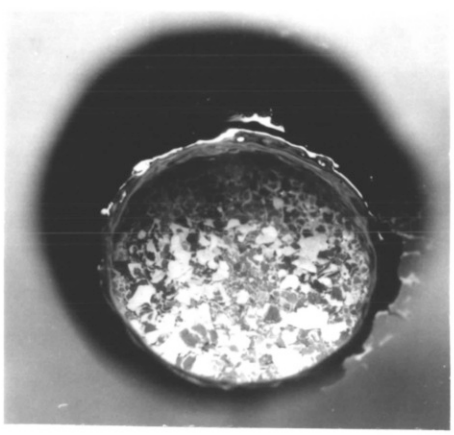

t = 3 mins

PLATE E

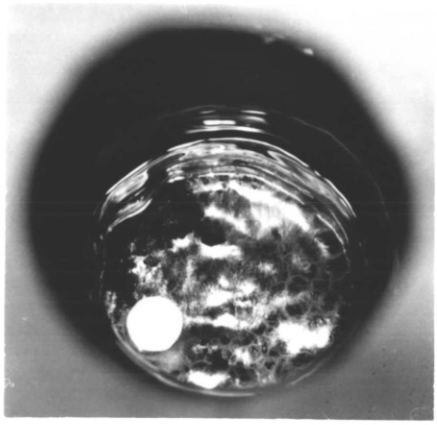

t = 3s

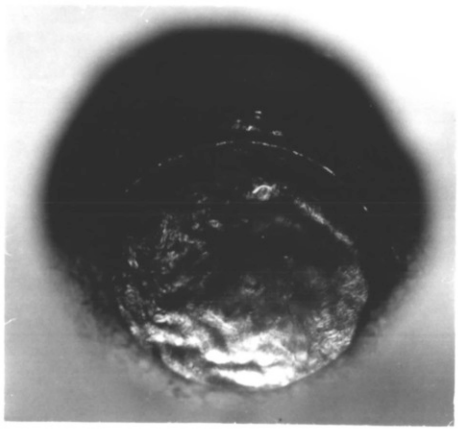

t = 45s

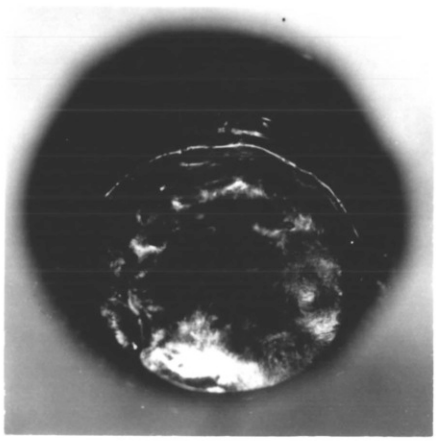

t = 10s

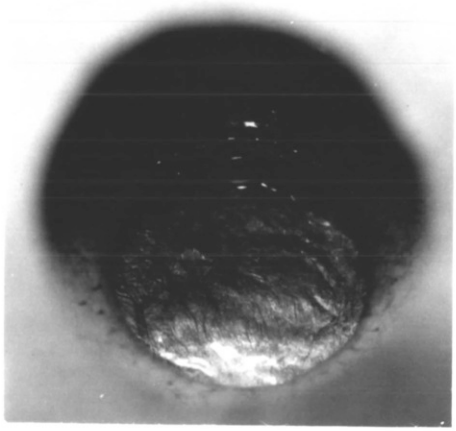

t = 1min

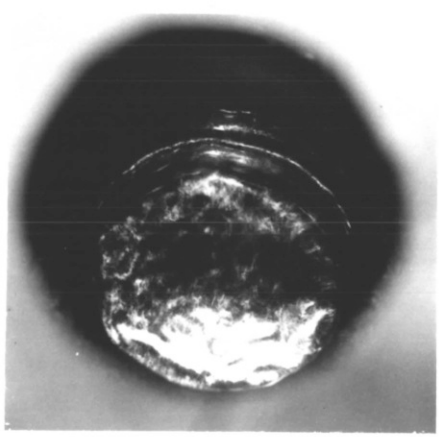

t = 30s

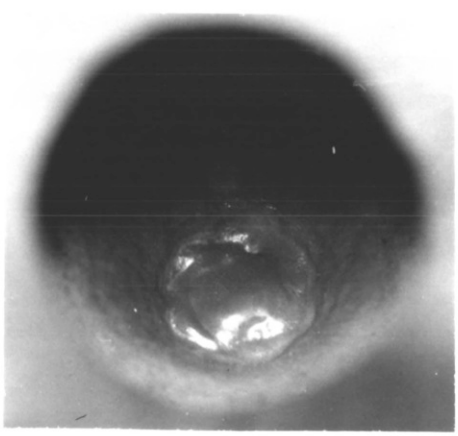

t = 5 mins

PLATE F

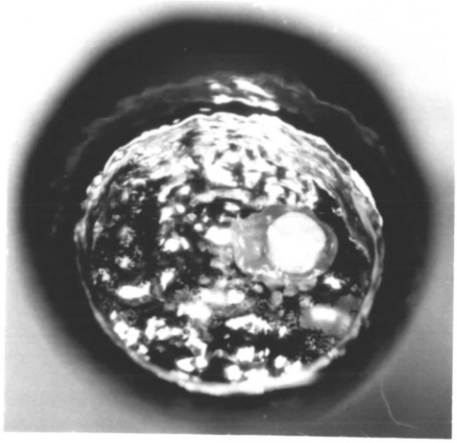

t = 2s

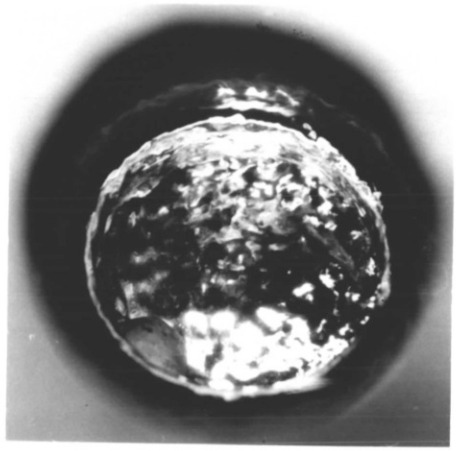

t = 15s

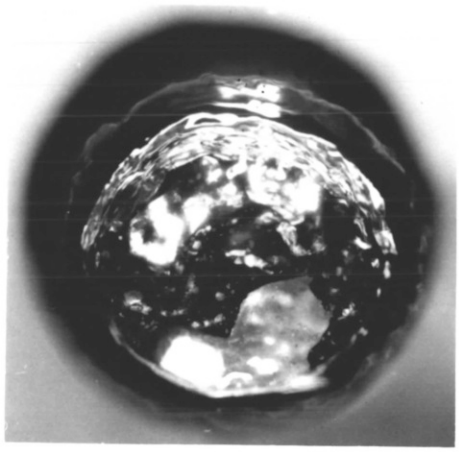

t = 5s

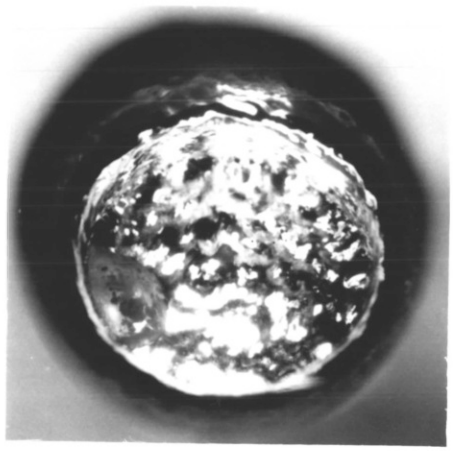

t = 20s

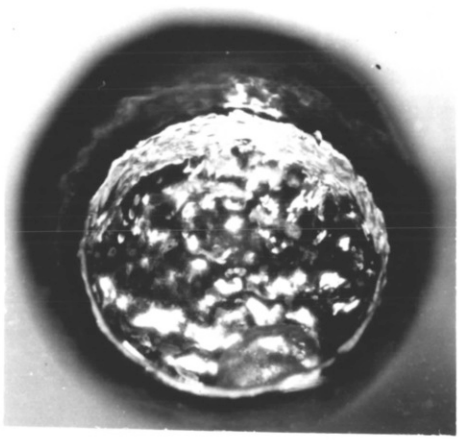

t = 10s

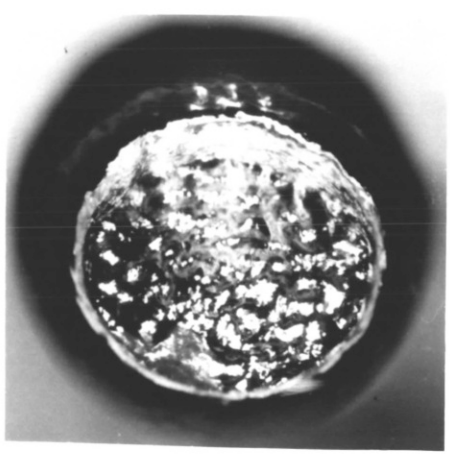

t = 60s

PLATE G

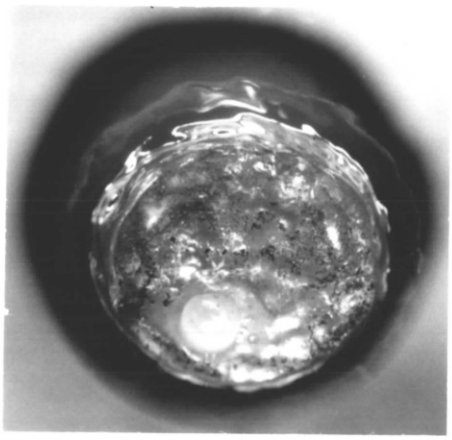

t = 3s

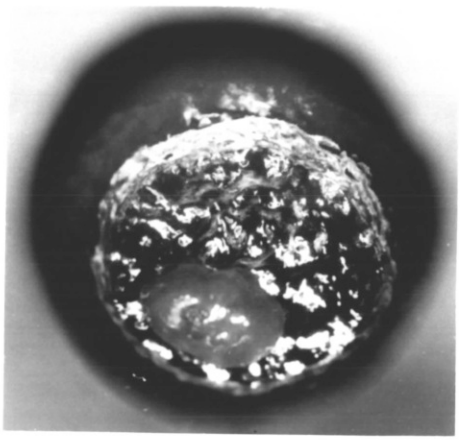

t = 24s

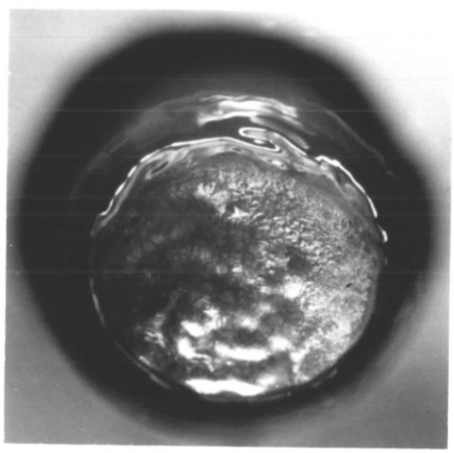

t = 8s

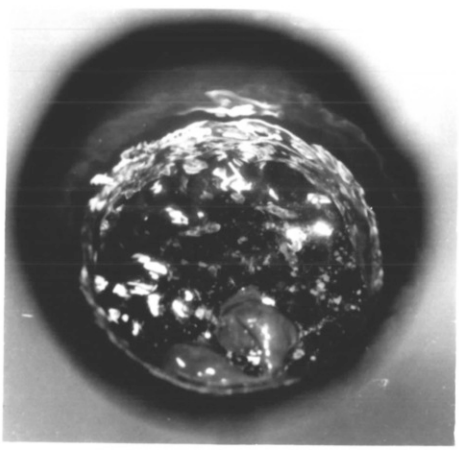

t = 60s

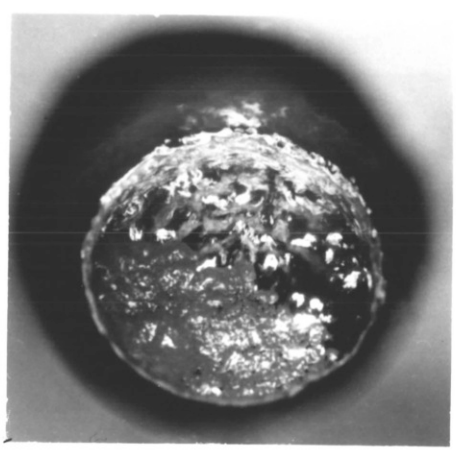

t = 16s

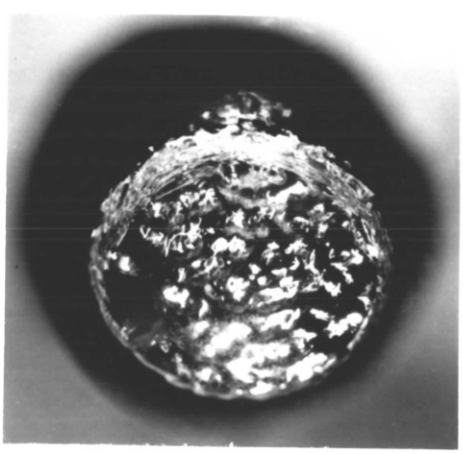

t = 90s

PLATE H

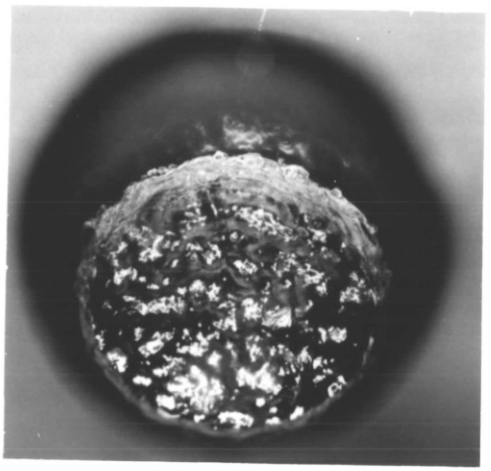

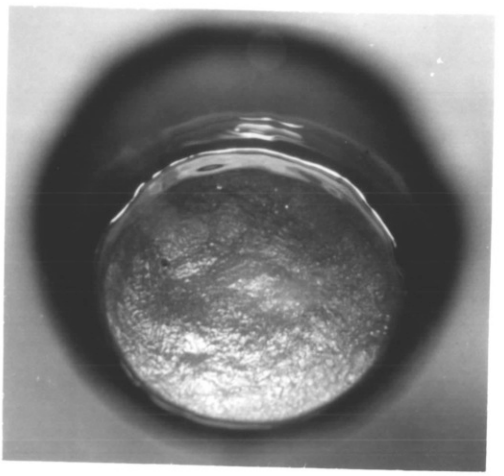

t = 9s

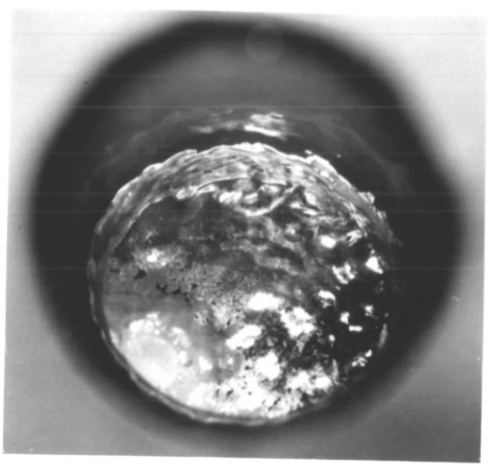

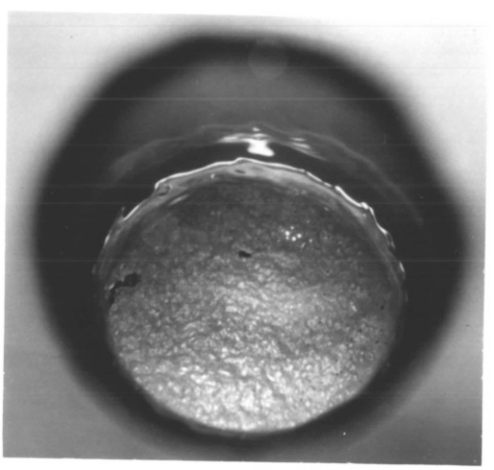

t = 3s

t = 12s

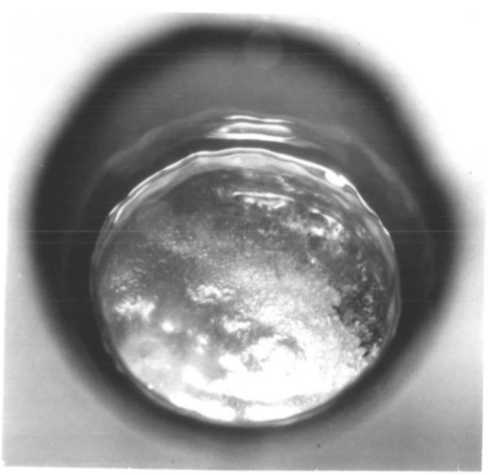

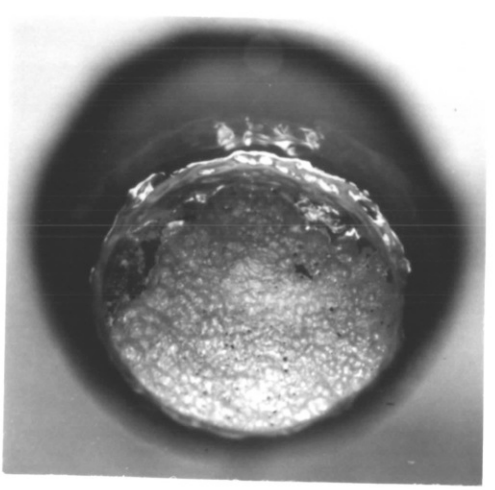

t = 6s

t = 15s

PLATE I

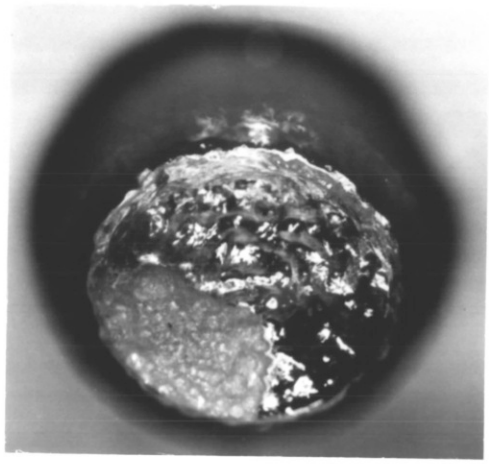

t = 18 s

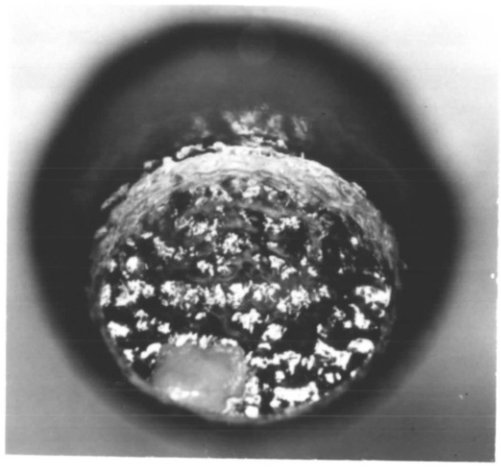

t = 45 s

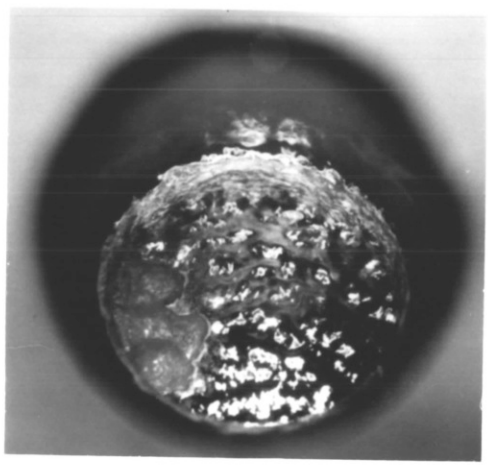

t = 21 s

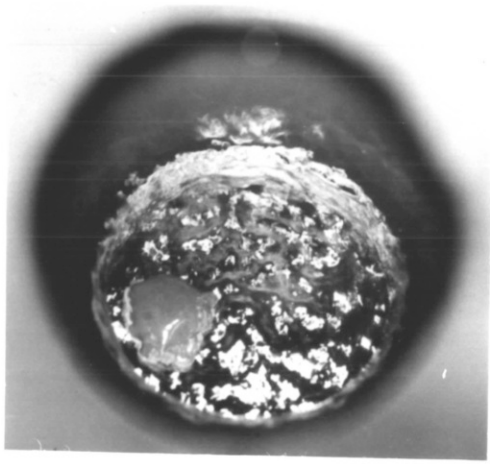

t = 1 min

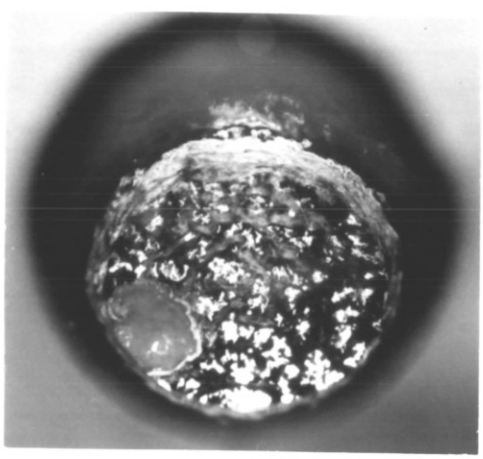

t = 30 s

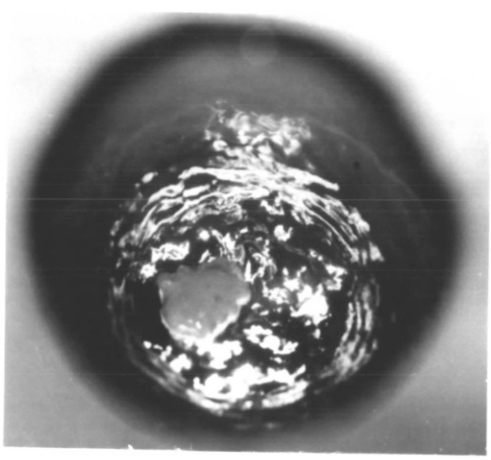

t = 5 mins

CHAPTER 4

DISCUSSION

4.1 THIRD PHASE IN THE ROOM TEMPERATURE OTB

The spreading tendency of solid aluminium particles in the room temperature OTB was found to be very strong, with only a few particles being stripped as they were added to the bubble. The flow pattern observed in the bubble base was asymetric, thus confirming the observations of Robertson and his co-workers[29]. The results obtained in this work (fig. 3-1) suggest that iso-spreading lines exist for the third solid phase inside the OTB. The results also point to the existence of a 'critical depth' at which stripping begins, in agreement with the results of Wiafe[32].

Liquid films inside large bubbles (high total depth (h_b+h_w)) were transported to the bubble rim by the basal flow and stripped. The rates of stripping of these films were found to be dependent on their spreading behaviour and viscosity. This result is also in agreement with those of Wiafe[32], who measured the 'critical depths' of stripping for various liquids in water OTBs and deduced that the rate of stripping was dependent on the viscosity of the film and also on its spreading behaviour. The importance of low melting point powders of good fluidity in practical steel desulphurization[50] may well be connected with these observations.

4.2 THE LEAD-OXYGEN SYSTEM

The five phases likely to be encountered in the open top bubble system without any slag addition were $Pb/PbO/Pb_3O_4$ for the lead, and Fe/Fe_3O_4 for its iron container. With oxygen injection into the apparatus PbO and Fe_3O_4 would be the main oxides formed.

PbO exists in two structural modifications:-

(i) Litharge has a tetragonal structure and is red in colour.

(ii) Massicot is yellow in colour and has a rhombic structure.

Red tetragonal PbO transforms to yellow orthorhombic PbO at 486°C. Pb_3O_4 dissociates in air at 540°C to form PbO[67]. However, with a solution of injected oxygen by the inert gas in the OTB pot, Pb_3O4 formation would not be likely above 400°C once the oxygen and the inert gases were well mixed.

Iron forms three stable oxides: wustite, FeO, magnetic, Fe_3O_4, and hematite, Fe_2O_3. Fe_2O_3 is only formed at high oxygen pressures and FeO is not stable below 570°C[38].

4.2.1 Oxides in the OTB

Three main types of oxides were observed in the open top bubbles in molten lead following oxygen injection, namely: the dark 'oily' film, the thicker lead oxides and the dry grey iron oxide. Each of these oxides was a solid oxide since liquid oxide films would have required temepratures in excess of those used during the experiments. The iron contamination and its subsequent removal provided an interesting example of impurity oxidation.

The 'oily' film gave the lead surface a smooth appearance. It was formed all over the lead surface immediately the oxygen was injected, independent of the bulk oxygen concentration in the lead.

The thicker lead oxide films, which formed more slowly, had various appearances and characteristics. Mellor[37] describes a whole range of colours from yellow through to red-brown for lead monoxide, so it was possible that the various appearances for the oxide described in table 3-1 were for the same oxide. At low oxygen potentials in the lead the thicker oxide formed in a small island in the bubble base was thought to be due to the localised region of the high oxygen potential in the gas phase where the injected oxygen first contacted the lead surface. With an increase in oxygen potential in the lead the oxide island increased in area and a tinge of interference colour appeared around the island. Further increases in oxygen potential caused a change in the oxide appearance to a greenish colour, and later to purple and gold colours characteristic of the oxidation of lead in air.

The third type of oxide formed was the grey oxide which formed at low oxygen potential when the dissolved impurities in the lead were being removed.

The iron container was present at unit activity as discussed in section 3.2.1. Iron dissolved in the liquid lead may have been present at about unit activity after deoxidation and msut have been effectively removed by oxidation. The solubility of iron in molten lead is about 2 ppm at 550°C so that not much iron oxide would be expected to form in the OTB. Most of about 0.06g of iron oxide expected to form on oxidation probably either stuck to the walls of the iron pot or rose to the surface of the lead in the sump. Hence it was not surprising that only a very small amount of grey iron oxide was detected in the OTB. The amount of the grey iron oxide detected increased with temperature, as would be expected from the higher iron solubility.

The solubility of iron in liquid lead was given by Shunk[36] at 600°C as 2.3 ppm, while data from Stevenson and Wulff[40] extrapolate to ~1 ppm at 600°C. Conochie[16] measured two values of Fe in lead at 550°C: 2.9 ppm Fe at a low oxygen potential and 0.25 ppm at a high oxygen potential. The obvious source of this discrepancy was the need to achieve an oxygen potential in the lead itself below the Fe/Fe_3O_4 line.

True iron saturation in the lead can only be measured if the oxygen potential in the lead is below that required for Fe removal by oxidation, i.e. $p_{O_2} < p_{O_2}$ for Fe/Fe_3O_4. This applies to any solubility determinations in which the solute is more readily oxidized than the solvent.

4.2.2 Mass transfer - The rate controlling step

The formation and subsequent dissolution of the 'oily' film and the thicker lead oxide are determined by:

(i) the rate of formation of PbO, dependent on the oxygen potential in the gas phase, the film thickness and mechanism for growth, and

(ii) the rate of dissolution of the oxide into the lead, dependent on the liquid phase masstransfer coefficient and the oxygen potential in the liquid lead.

The rate of transfer of oxygen in the gas phase, per unit area of interface expressed in terms of gram moles of oxygen, is given by

$$N_g = \frac{2k_g}{RT} (p^b_{O_2} - p^i_{O_2}) \qquad (4.1)$$

For there to be an oxide film, $p^b_{O_2}$ must be sufficiently high to keep $p^i_{O_2}$ above the partial pressure of oxygen required to form lead oxide. Only a very low oxygen potential is necessary to form an oxide film on lead ($p_{O_2} \sim 10^{-21}$ at 450°C).

In the presence of an oxide layer the rate of oxygen transfer (per unit area) into the lead is given by

$$N_\ell = k_\ell (C_{sat} - C) \qquad (4.2)$$

where:

N_g is the molar transport rate of oxygen atoms through the gas phase, per unit area of interface.

N_ℓ is the molar transport rate of oxygen atoms in the lead phase per unit area of the interface when covered by an oxide layer.

$P^b_{O_2}, P^i_{O_2}$ are the oxygen partial presures in the bulk and at the gas/PbO interface, respectively.

C, C_{sat} are the molar oxygen concentrations in the bulk lead and at the lead surface.

k_ℓ, k_g are the liquid and gas phase mass transfer coefficients.

The maximum rate of oxygen transfer in the gas phase is given by

$$N_{g,max} = \frac{2k_g}{RT} p^b_{O_2} \qquad (4.3)$$

When a pulse of oxygen was injected onto a clean lead surface the initial oxide film formed immediately because $N_{g,max}$ was greater than N_ℓ. Once an oxide layer was formed oxygen transfer rate to the lead became limited by the liquid phase resistance. This rate is independent of the rate of oxygen transfer through the gas phase and the rate of consumption by the slag film. The amount of oxide at any time was thus dependent on the time integral difference between the rate of oxide formation and its rate of dissolution into the lead. This relationship may be expressed as

$$C_{ox}(d\tau_{ox}/dt) = (2k_g/RT)(p^b_{O_2} - p^i_{O_2}) - k_\ell(C_{sat} - C) \qquad (4\text{-}4)$$

where:

C_{ox} is the molar concentration of oxygen atoms in the oxide, and

τ_{ox} is the oxide thickness.

As the gas phase of the OTB pot was purged by a flow of an inert gas after each oxygen pulse, the rate of oxygen transfer in the gas phase would decrease with time, thus affecting the growth of the oxide layer. When $p^b_{O_2}$ fell below

the value required for oxide formation, the thickness of the oxide layer began to decrease and when it disappeared, the rate of transfer of oxygen was controlled by the resistance in the gas phase. The ripple return therefore corresponded to the start of the gas phase control of oxygen transfer to the lead. As the oxygen content of the lead increased the rate of liquid phase mass transfer decreased and the gas phase resistance became less important as shown by the log plot of the gas phase oxygen potential decay in the OTB in figs. 3-16 and 3-17.

During lead oxidation by a steady supply of oxygen gas, an oxide film was observed on the lead surface immediately after the oxidizing gas was allowed in and the oxide film was seen to thicken during the experiment. The oxygen potential of the gas phase must have been above that in the lead and this affected the probe readings, making the probe indicate too high an oxygen potential. It was also observed (see fig. 3-11) that with a decrease in the flow rate of the oxidizing gas into the pot, the gas phase potential effect on the probe reduced (as oxygen accumulation in the gas phase reduced) and the apparent oxygen solubility value increased. When the part of the probe exposed to the gas atmosphere was shielded with a silica tube, the results obtained were even better.

The continuous oxidation of liquid lead in the OTB pot was, however, not a simple process to predict. The bulk gas phase was not initially well mixed and there was additional consumption of oxygen by the reactive pot.

4.2.3 Oxygen solubility - Comparison with other workers

The available data on oxygen solubility in molten lead at temperatures up to 800°C are summarised in fig. 4-1. A high degree of uncertainty is immediately obvious, especially at temperatures less than 500°C.

Oxygen solubility determinations using the open top bubble apparatus lie somewhere in the middle of the range constituted by the results of earlier workers. Previous determinations have been made by sampling followed by chemical analysis[44], by coulmetric titration involving the use of

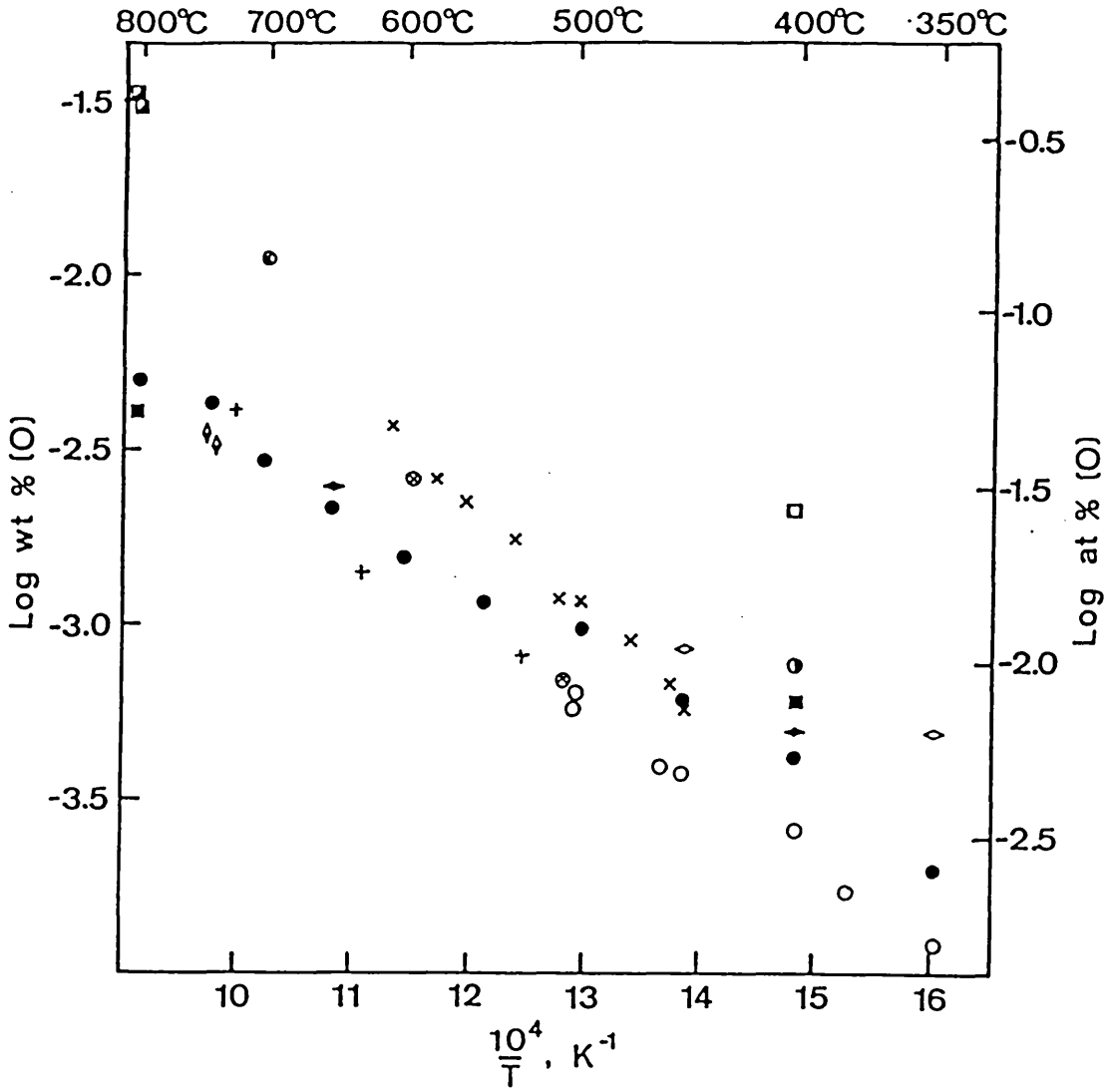

Fig. 4-1: Oxygen solubility - comparison with other workers.

- ⊗ Alcock and Belford[34]
- From ref. 34:
  - ◐ Fischer and Bechtel
  - ■ Sano and Minowa
  - □ Lunge and Schmid
  - ◆ Baker
  - ◇ Grosheím-Krisko, Hofmann & Hanemann
- ◊ Szwarc, Oberg and Rapp[45]
- From ref. 45:
  - ● Barteld and Hofmann
  - \+ Fischer and Ackermann
- ◪ Taskinen[42]
- o Worner[41]
- × This work

solid electrolyte monitors[34,45-47] and by other methods also using solid electrolyte probes[16,40,48]. The technique that has been described here made use of direct measurement of oxygen potential in a large mass of lead (30 kg) in which uniform mixing was achieved within 12s of the oxygen addition[35]. Errors in the measurement of the added oxygen were relatively small; those due to the interactive iron pot and the impurities in the lead were not important at C/C_{sat} values in excess of 0.3. The open top bubble apparatus was thus well suited to the determination of oxygen solubility in liquid lead.

4.3 SLAG - METAL REACTIONS IN THE OTB

The reactions of the added slags with the lead and its impurities were followed by solid electrolyte monitors and also by visual observations of the slag behaviours inside the OTB.

4.3.1 The reactions of the slags with lead

NaOH slags:

After addition to the OTB, NaOH slags sat at one side of the bubble base and stripped very slowly. Their stripping rate was dependent on the 'bubble depth', in agreement with the observations of liquid films in the room temperature model. When the slags were left in the bubble for sufficiently long times their colour gradually darkened. Grange and Heerman[58] have reported that lead in molten alkali hydroxides is oxidized to a bivalent state, which is only slightly soluble in the melt. It is, therefore, likely that the darkening of the caustic soda slags in the OTB was due to a slow oxidation of the lead in contact with it. The resulting PbO was then probably taken up as a suspension in the melt.

$NaNO_3$-based slags:

Both NaOH-$NaNO_3$ and pure $NaNO_3$ slags did react with the lead inside the OTB. Their spreading behaviour was thought to be related to the observations of Brimacombe[5] and Barton and Brimacombe[6] discussed in section 1.1. Oxygen is surface active in lead and reduces the surface tension of molten lead[49]. $NaNO_3$ is a very strong oxidizing agent and would react with the lead to form lead oxide and give rise to regions of reduced interfacial tension which would tend to spread. There was also an increase in oxygen potential in the lead after the addition of a sodium nitrate based slag to the OTB (figs. 3-26 and 3-27).

$NaNO_3$ slags reacted rapidly forming a dark oxide film which suppressed the rippling in the bubble (plate C). Subsequently, tiny yellowish-brown oxide flakes, suspected to be Na_2O, began to appear on the dark oxide film covering the bubble base. As the reaction progressed these oxide flakes

were also observed to be very stable in the OTB as they remained in the bubble even at very low oxygen potentials in the metal. In NaOH-$NaNO_3$ slags they initially formed a homogeneous mixture with the NaOH but later gradually segregated, after the lead oxide must have dissolved back into the metal (plate A). X-ray diffraction patterns of samples taken from the OTB after $NaNO_3$ addition confirmed the formation of Na_2O (see table F in appendix A-6).

Another feature of the reactive slags in the OTB was that NaOH-$NaNO_3$ slags spread faster than $NaNO_3$ slags. This was probably due to the fact that the NaOH-based slags were of better fluidity inside the OTB, as was observed (see plates A, B and C). According to spreading studies[86] with aqueous and organic liquids, the spreading velocity at an interface is linearly dependent on the ratio φ/μ, where μ is the liquid viscosity and φ is the spreading coefficient, defined as

$$\varphi = \sigma_{1/g} - (\sigma_{3/g} + \gamma_{1/3}) \qquad (4.5)$$

which must be positive for spreading; where

$\sigma_{1/g}$ is the surface tension of the continuous phase (phase 1)

$\sigma_{3/g}$ is the surface tension of the third phase (see fig. 1-4), and

$\gamma_{1/3}$ is the interfacial tension of the phase 1 - phase 3 interface.

The spreading behaviours of $NaNO_3$ and NaOH-$NaNO_3$ slags observed in this work are schematically represented in fig. 4-2 in comparison with those of a metal oxide and Cu_2S, reported by Brimacombe[5] and Barton and Brimacombe[6], respectively.

4.3.2 The reactions of the slags during lead refining

NaOH slag:

The behaviour of NaOH slags in Pb-Sb and Pb-Sb-Sn systems was similar to that observed in the 'pure lead'

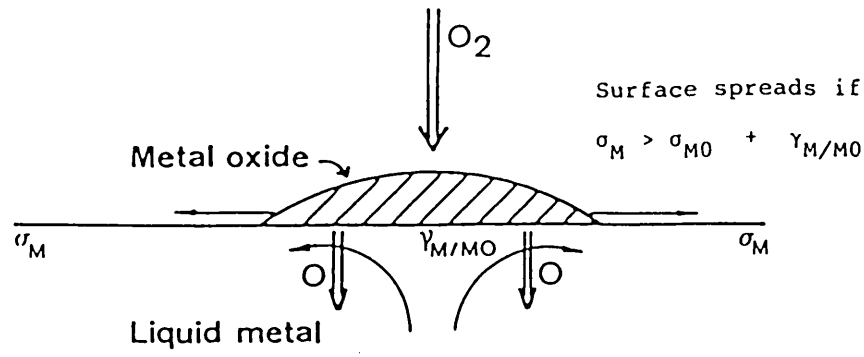

(a) After Brimacombe[5]

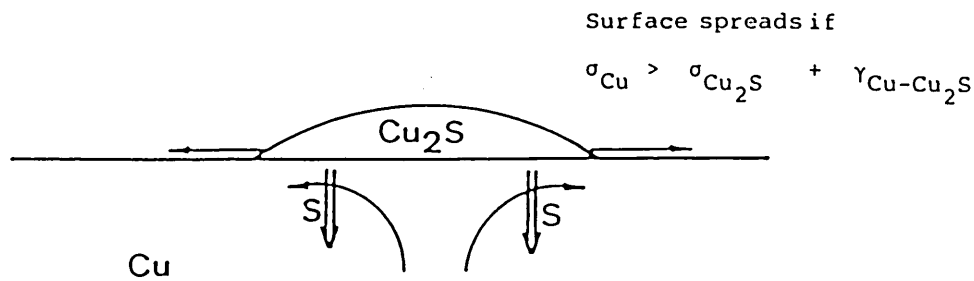

(b) After Barton and Brimacombe[6]

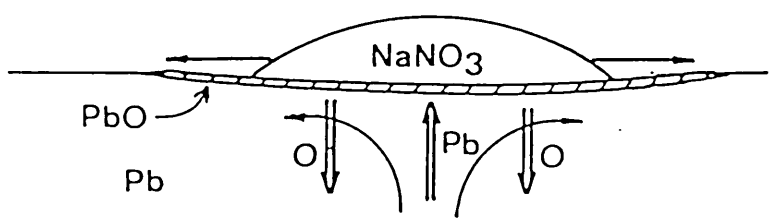

(c) The slow spreading of $NaNO_3$
(This work)

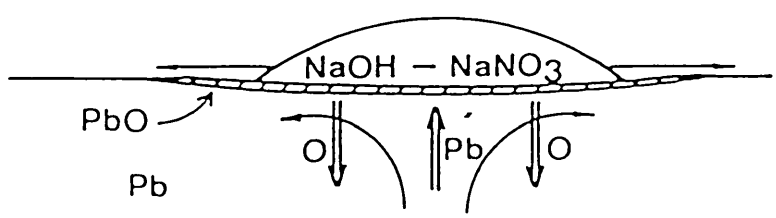

(d) The fast spreading of NaOH-$NaNO_3$
(This work)

Fig. 4-2: The mechanism for spreading.

⟸ Mass transfer; ← Liquid motion

system, discussed in the previous section. According to the report by Davey[53], sodium hydroxide would react with impurity tin in lead even without oxidation, to form sodium stannite, as follows:

$$[Sn] + 2NaOH \rightarrow Na_2SnO_2 + H_2 \qquad (4\text{-}6)$$

The absence of this reaction in this work was attributed to the low tin concentration in the lead (~0.06 wt.% Sn). Data from Emicke and co-workers[52] suggest that the tin concentration in lead before Harris process refining is usually of the order of 1 wt.%.

An interesting feature of the NaOH additions was the absence of a reaction in the lead-antimony system, even after the injection of an oxygen gas pulse. This observation disagrees with the results of Emicke and his co-workers[52] who reported some formation of sodium antimonate via the reaction;

$$4Sb + 5O_2 + 12NaOH \rightarrow 4Na_3SbO_4 + 3H_2O \qquad (4\text{-}7)$$

The absence of this reaction in the OTB system was attributed to the inability to attain a high enough oxygen potential at the slag-metal interface by the addition of a pulse of oxygen to the system at very low oxygen potential. According to Leroy and co-workers[54] antimony cannot be oxidised by air and hence air could be used in the selective oxidation of arsenic and tin with respect to antimony. Dougill and Jeffes[57] studied the heats of reaction of the oxides of tin, arsenic, antimony and lead with molten caustic soda and reported that sodium antimonate could be formed via the reaction

$$6\ NaOH + Sb_2O_5 \rightarrow 2Na_3SbO_4 + 3H_2O \qquad (4\text{-}8)$$

Formation of Sb_2O_5 at the Sb levels in the OTB system (~ 0.07 wt.%) would require oxygen pressures in excess of that required for Pb/PbO equilibrium (see fig. 4-3). Dougill and Jeffes[57] did not observe any reaction between PbO and NaOH. The reaction of NaOH and Sb_2O_3 was slow, producing unidentified products.

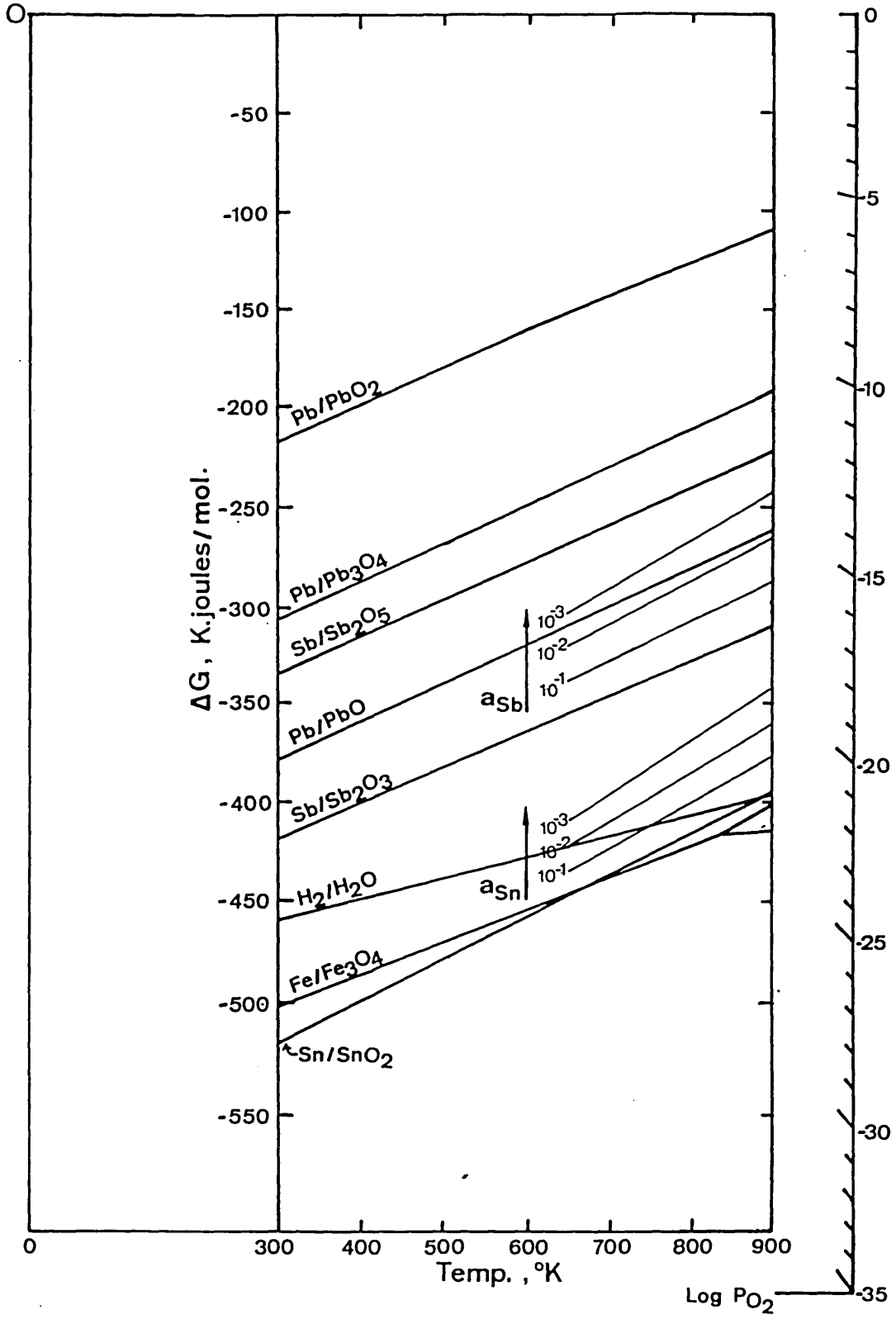

Fig. 4-3: Gibbs free energy diagram for selected oxides in lead refining.

.07 wt % Sb ≡ a_{Sb} of 5×10^{-4}

.06 wt % Sn ≡ a_{Sn} of 10^{-2}

$NaNO_3$-based slags:

Sodium nitrate-based slags reacted in both the Pb-Sb system and the Pb-Sb-Sn systems displaying various spreading characteristics (see plates D, E, F and I). The initial spreading behaviour of each slag in this case was similar to the corresponding behaviour in the 'pure lead' system. However, their later behaviours in the lead-alloy system differed from those in the 'pure lead' system, with the difference depending on the additive slag. Also in the Pb-Sb and the Pb-Sb-Sn systems, the transport of Sb and Sn from the bulk metal to the reaction interface prevented an increase in the bulk oxygen potential of the lead, after the addition of an $NaNO_3$ or $NaOH-NaNO_3$ slag (fig. 3-28).

$NaNO_3$ slags reacted in a similar way as in the 'pure lead' system, initially forming a shiny gold coloured film which later turned light brown. The initial film must have been due to impurity (Sb,Sn) oxidation. The final products of the reactions are, however, unknown since it was not possible to sample these slags. The sampling technique employed during the lead refining experiments was only effective for the removal of slags of certain fluidity which wet the sampler. Slags resulting from $NaNO_3$ addition in the OTB were typically solid and would not stick to the sampler. Their removal by any other means would have led to the leakage of air into the apparatus and contamination of the samples by metallic lead which were not desired.

The reactions of $NaOH-NaNO_3$ (4:1) slags were characterised by their initial rapid spreading followed by a rapid contraction, after the formation of sodium antimonate and/or stannate in the OTB. The rapid contraction of the initially spreading film was thought to be due to the reduction of the lead PbO oxide film and the suspension of the antimonate and/or stannate in the matrix of the excess caustic soda melt, as they are both insoluble in NaOH[52-56]. The formation of sodium antimonate and sodium stannate in the Pb-Sb and Pb-Sb-Sn systems, respectively were confirmed using powder x-ray diffraction technique (see tables G and H in appendix A-6).

The contraction of the slag films observed with NaOH-$NaNO_3$ (4:1) slags was not osberved when NaOH-$NaNO_3$ (1:1) slags were used. In the lead-antimony system the 1:1 slags spread rapidly and later formed a thick grey slag film covering the bubble surfaces which later cracked producing grey and white flakes (see plate E). X-ray diffraction pattern of the initial thick slag film confirmed the formation of sodium antimonate. As the reaction progressed the white antimonate flakes gradually dominated. Emicke and co-workers[52] have listed two types of sodium antimonate: the grey antimonate and the white antimonate. Their analyses show that the white antimonates are richer in antimony content, hence they are in agreement with the gradual change in colour from grey to white as the reaction proceeded in the OTB.

However, in the Pb-Sb-Sn system the NaOH-$NaNO_3$ (1:1) slag showed a similar initial spreading behaviour and remained as a thick film on the bubble surfaces, but did not crack (as in its Pb-Sb counterpart). The film was identified by powder x-ray diffraction technique to consist of mostly sodium stannate (table H in appendix A-6).

The difference in the above behaviours was attributed to the differences in the stoichiometric requirements of the reactions leading to the formation of sodium antimonate and sodium stannate. Antimony removal via the reaction

$$4NaOH(\ell)+2NaNO_3(\ell)+2[Sb]\rightarrow 2Na_3SbO_4(s)+H_2O(g)+N_2(g) \qquad (4.9)$$

requires approximately equal weights of NaOH and $NaNO_3$. For tin removal, less NaOH is required according to the reaction

$$6NaOH(\ell)+4NaNO_3(\ell)+5[Sn) \rightarrow 5Na_2SnO_3(s)+3H_2O(g)+2N_2(g) \qquad (4.10)$$

In reaction (4-10) however, the excess of NaOH was not enough to allow the contraction observed with the NaOH-$NaNO_3$ (4:1) slags.

Results of chemical analysis:

The results of the chemical analysis of the slag samples taken from the OTB (Table 3-5) showed three important facts.

(1) At the concentration levels used there was no appreciable selectivity in the removal of Sb and Sn from the lead-antimony-tin alloy using the OTB system.

(2) There was also substantial oxidation of the lead during the reactions of the impurity antimony and tin in the lead.

(3) That sodium antimonate may react in the Pb-Sb-Sn system to remove tin.

The above facts point to the complex nature of the reactions taking place in the OTB after the addition of a reactive slag, during lead refining. The lack of selectivity in the removal of Sb and Sn from the lead using a sodium nitrate based slag is in agreement with the results of Leroy and his co-workers[54].

The presence of lead in the slag phase may have been due to the initial oxidation of lead prior to the removal of antimony and tin. Lead is present in bulk and must have been oxidized by the reactive slags. Davey[53] has also reported substantial PbO formation at low impurity levels in the lead, during lead refining by the 'modified Harris process'. The variation in the amount of lead identified in the slag phase may be related to the lack of attainment of equilibrium in the system and the mechanism for antimonate or stannate formation, discussed in the next section.

4.3.3 General discussions on reaction mechanism

The exact mode of formation of the antimonate and/or stannate in the Harris process is not known. Davey[53] and Leroy[54] defined Harris softening as the oxidation of antimony, arsenic and tin and the adsorption of the oxides into a caustic soda melt. Jeffes and Aranda[56] proposed that the reaction consisted of three steps, viz:

(i) Oxidation of the lead by air and/or sodium nitrate.

(ii) Oxidation of the impurities in lead by the lead oxides.

(iii) Reaction of the oxides of the impurities with caustic soda.

However, they did not give any evidence in support of the above reaction sequence.

The results obtained in this work suggest the initial formation of lead oxides. The above statement follows from the foregoing observations:

(a) Similarities in the initial behaviour of the slags in the 'pure' lead and in the lead-alloy systems:

The initial spreading behaviour shown by the reactive slags in the lead-alloy system is related to the spreading of similar slags in the 'pure' lead system (see plates A and I). The slight difference in slag colouration may have been due to impurity oxidation which must have also occurred at the same time, thus preventing oxygen dissolution in the bulk metal.

(b) Absence of spreading of the reactive antimonate slag in the Pb-Sb-Sn system:

The reactions of sodium antimonate with tin in the OTB have been confirmed by both the chemical analysis results in table 3-5 and by the powder x-ray diffraction method (section 3.4). The absence of spreading during the reaction was thought to be due to the fact that the reaction

$$5[Sn]+4Na_3SbO_4+H_2O \rightarrow 4[Sb]+2NaOH+Na_3SnO_3 \qquad (4\text{-}11)$$

does not release any oxygen to produce PbO formation and the consequent surface tension gradients necessary for spreading to occur.

(c) Presence of large amount of lead in the slag:

The presence of substantial amounts of lead in the slag (Table 3-5) suggest some oxidation of lead which could not have occurred via its reaction with sodium antimonate. The results of Table 3-5 also suggest a decrease in the amount

of lead oxide, with an increase in the duration of the experiment. Samples E and F (in Table 3-5) were removed from the OTB after about 6 minutes of slag addition to the lead while sample G was removed from the bubble about 4 minutes after reaction. This observation suggests a mechanism whereby lead oxides are initially formed, which then react slowly to form the antimonates and the stannates. Further work would, however, need to be done in order to substantiate this mechanism. Data obtained in this work were not sufficient to provide conclusive evidence for the suggested mechanism.

(d) The need for sodium nitrate:

The results of the earlier experiments with antimony, caustic soda and oxygen gas suggest that sodium nitrate must have contributed in some way towards the formation of sodium antimonate and stannate, at the low concentrations of Sb and Sn used in this work. Sodium nitrate is a very strong oxidizing agent and could have oxidized the lead to oxidation states higher than Pb/PbO equilibrium, thereby enhancing antimonate formation in the lead-alloy system. However, the formation of higher lead oxides in the OTB after $NaNO_3$ addition could not be confirmed from x-ray diffraction pattern of the slag sample.

The release of oxygen from the sodium nitrate in the slag phase did lead to an increase in Na_2O activity in the melt, which could then react with the oxides of the impurity elements to form antimonates and/or stannates:

$$2(O) + 3Na_2O + Sb_2O_3 \rightarrow 2Na_3SbO_4 \qquad (4\text{-}12)$$

$$Na_2O + SnO_2 \rightarrow Na_2SnO_3 \qquad (4\text{-}13)$$

The oxygen in brackets is considered to have been released by the sodium nitrate. There was evidence of production of Na_2O after the reaction of $NaNO_3$ with lead (section 3.3.3).

Stripping:

In this work stripping of a solid slag phase formed as a result of reactions in the OTB was not observed. This observation disagrees with the hypothesis used by Irons and Guthrie[33] to explain their results while studying the desulphurization kinetics of molten iron using magnesium vapour. From our results solid MgS would not be expected to strip. The OTB may, however, be a poor simulation of the behaviour in a highly turbulent system. With bubbles rising in a turbulent environment stripping may occur more easily and slags may also move into a dispersion in the liquid phase when bubbles break up in a turbulent flow.

Future work could be done in exploring ways of making the slag phase of the OTB strip faster, as this may improve reaction kinetics. This may be facilitated by the addition of a surface active agent. Robertson and co-workers[29] added a few drops of liquid detergent to the water OTB and observed an enormous increase in the rate of stripping. Liquid detergent reduces the surface tension of water.

5. CONCLUSIONS

The behaviour of a third phase carried by a gas bubble rising in a liquid column was investigated using the water model of the 'open top bubble' apparatus. Slag film behaviour has been simulated using aluminium flake particles as powdered slag and organic liquids as liquid slags. These materials have been found to strip from the bubble base when a critical 'bubble depth' was reached. The rate of stripping of the liquid films was found to be dependent on their viscosity as well as their spreading coefficient. Less viscous liquid films stripped more easily and the stripping was seen to occur at the bubble rim.

High temperature experiments were carried out using the lead OTB apparatus. This apparatus allowed a visual observation of the open top bubble and provided a well-mixed bath. Slag film formation by gas-metal reaction was investigated by the injection of oxygen gas into the atmosphere-controlled apparatus. The inside surface of the bubble was observed to ripple very strongly when free of oxide. When a thin oxide layer was formed on the lead surface following oxygen injection, the rippling in the bubble was completely suppressed. The initial thin PbO films were dark and gave the surface an oily appearance. With subsequent oxygen additions to the lead thicker oxide layers began to form.

The course of oxygen dissolution in the lead was followed using solid electrolyte oxygen probes. The technique used allowed the simultaneous monitoring of the oxygen potential of the liquid metal as well as that of the gas phase. Very useful measurements were obtained on both the thermodynamics and the kinetics of gas-metal-slag reactions using the oxygen probes, and consequently the oxygen solubility in molten lead was measured in the temperature range 450-610°C. The dissolution of molecular oxygen by the reaction $\frac{1}{2}O_2(g) = [O]$ (wt.% in lead) is described by the standard free energy change ΔG^{o}, J = -60693-21.88T, the standard state being weight percent [O] at infinite dilution. The results obtained were in the centre of the scattered data of other workers. The liquid phase mass transfer coefficient was estimated from oxygen probe

measurements as well as from the time taken for the ripples in the bubble to return, after the addition of an oxygen pulse. The results obtained from the different techniques compared well with each other. At 606°C, the mass transfer coefficient was found to be 3.2×10^{-2} cm/sec.

Analysis of the gas phase oxygen potential provided qualitative information on oxide formation and its subsequent dissolution in the lead pot, following oxygen addition. It was observed that the oxygen level in the gas phase was dependent on the oxygen potential of the liquid metal. There was also very good convectional mixing in the gas atmosphere of the OTB pot.

Slag addition experiments were also carried out using the lead OTB apparatus. The experiments provided the unique opportunity of a direct viewing of slag behaviour in a bubble rising in liquid metal. Sodium nitrate-based slags were very reactive and showed strong spreading tendencies. Caustic soda slags were relatively unreactive and did not spread. Antimony, and later tin were subsequently added as impurity elements in the lead. Their removal using $NaOH-NaNO_3$ slags, as occurs in the Harris process refining of lead, was investigated. The reactions displayed interesting spreading behaviours. It was concluded that lead oxides formed first and that they later reacted with Na_2O and antimony or tin to form sodium antimonate or stannate, respectively.

The OTB technique was found to be very useful for the study of specific metal refining reactions as they occur in many metallurgical processes. A design was completed for the implementation of the open top bubble technique in molten carbon-saturated iron. There was insufficient time for the author to start work on this project.

Recommendations for further work

Following this work, some areas have been selected where it is thought that further work would be of benefit in the understanding of gas-metal-slag reactions in metal refining processes.

(1) Gas phase oxygen potential analysis:

It was concluded in section 3.2.5 that further work is needed in order to provide a quantitative interpretation of the gas phase oxygen potential measurements. This would include the operation of the gas phase oxygen monitor at the same temperature as the liquid lead oxygen monitors as well as providing a simultaneous chemical analysis of the outlet gas using a gas chromatograph, for example. It must, however, be emphasised that,in order to obtain a reasonably fast and reversible response from the gas probe, there is need to work at temperatures in excess of 600°C, which is close to the temperature limit of the OTB apparatus of 650°C[16].

(2) Sampling the slag phase of the OTB:

The difficulty in the interpretation of some of the reactions which were seen to occur in the open top bubble (sections 3.3 and 3.4) could be overcome by devising a suitable sampling technique. The technique used in this work was only suitable for the removal of slag samples of fairly good fluidity. It would be useful to devise such a sampler which could also take solid samples from the OTB.

(3) Kinetic data on lead refining reactions:

The discussions in section 4.3.3 on the mechanism of the reaction of $NaOH-NaNO_3$ slags with Sb and/or Sn during lead refining highlighted the need to obtain more information on the compositions of the resulting slags as a function of time. Such information could be provided by taking samples of the slag phase at various times followed by a chemical

analysis for lead, antimony and/or tin in the various samples. The findings would provide conclusive evidence on the mode of formation of antimonates, stannates and arsenates in Harris process refining reactions.

(4) Stripping:

In this work it was observed that the reactions of a liquid slag carried in the open top bubble, with the impurities in the liquid metal occurred at the bubble surface. Further work could be done in making the slag phase strip and hence continue to react in the bulk metal. This may improve reaction kinetics. The process of stripping could be facilitated by the addition of a surface active agent like sulphur to the lead.

(5) OTB in Fe-C:

The long term objective of this work has been to engineer the open top bubble in molten iron and use it to study some steelmaking reactions. A design has been completed for a new OTB unit that would work in molten carbon-saturated iron (section 2.5). Work has also been completed on most of the components required for its construction. The setting-up of this apparatus will, however, present many potential engineering problems. It is thought that with skill and proper understanding of the existing OTB systems, the iron-carbon OTB unit would become a success and could be invaluable in the development of reagents used in refining steel.

REFERENCES

1. ROBERSTON, D.G.C. and JENKINS, A.E. The reaction of liquid iron and its alloys in 'heterogeneous kinetics at elevated temperatures'. Belton, G.R. and Worrel, W.R. eds. New York, Plenum Press (1970), p. 393.

2. RAO, G.S. 'Kinetics and mechanism of gas-metal-slag reactions relevant to steelmaking'. Ph.D. Thesis, Imperial College, Univ. of London (1979).

3. EMI, T., BOORSTEIN, W.M. and PEHLKE, R.D. 'Absorption of gaseous oxygen by liquid iron'. Met. Trans. 5, (1974), 1959.

4. EMI, T. and PEHLKE, R.D. 'The kinetics of oxidation of iron-silicon and iron-aluminium alloy melts by pure oxygen or oxygen bearing gases'. Met. Trans. B. (1975), 6B, 95.

5. BRIMACOMBE, J.K. 'Interfacial turbulence in liquid-metal systems'. Physical Chemistry of Process Metallurgy: The Richardson Conference, J.H.E. Jeffes and R.J. Tait (eds), I.M.M. London (1974), 175.

6. BARTON, R.G. and BRIMACOMBE, J.K. 'Interfacial turbulence during the dissolution of solid Cu_2S in molten copper'. Met. Trans. B. (1976), 7B, 144.

7. RADZILOWSKI, R.H. and PEHLKE, R.D. 'Absorption of gaseous oxygen by liquid cobalt, copper, iron and nickel'. Met. Trans. B. (1978), 9B, 129.

8. BARTON, R.G. and BRIMACOMBE, J.K. 'Influence of surface tension-driven flow on the kinetics of oxygen absorption in molten copper'. Met. Trans. B. (1977), 8B, 417.

9. HERBERTSON, J.G., ROBERSTON, D.G.C. and BRADSHAW, A.V. 'Critical experiments on the role of surface tension-driven flow in the kinetics of oxygen transfer gases and liquid silver'. Canadian Met. Quarterly 22, 1, 1-8, (1983).

10. PARLANGE, Jean-Yves. 'Spherical cap bubbles with laminar wakes'. J. Fluid Mech. 37 (1969), part 2, 257.

11. DAVIES, R.M. and SIR GEOFFREY TAYLOR, F.R.S. 'The mechanics of large bubbles rising through extended liquids and through liquids in tubes'. Proc. Roy. Soc. (London) A200 (1950), 375.

12. GRACE, J.R., WAREIGI, T. and NGUYEN, T.H. 'Shapes and velocities of single drops and bubbles moving through immiscible liquids'. Trans. Inst. Chem. Engr. (1976), 54, 167.

13. DAVENPORT, W.G., RICHARDSON, F.D. and BRADSHAW, A.V. 'Spherical cap bubbles in low density liquids'. Chem. Eng. Sci. 22 (1967), 1221.

14. GUTHRIE, R.I.L. and BRADSHAW, A.V. 'The stability of gas envelopes trailed behind large spherical cap bubbles rising through viscous liquids'. Chem. Eng. Sci. 24, (1964), 913.

15. FILLA, M., DAVIDSON, J.F., BATES, J.F. and ECCLES, M.A. 'Gas phase controlled mass transfer from a bubble'. Chem. Eng. Sci. 31, (1976), 359.

16. CONOCHIE, D.S. 'Gas-metal-slag reactions in rising bubbles'. Ph.D. Thesis, Imperial College, Univ. of London (1980).

17. COLLINS R. 'A second approximation for the velocity of a large gas bubble rising in an infinite liquid'. J. Fluid Mec. 25 (1966), Part 3, 469.

18. WEGENER, P.P. and PARLANGE, J-Y. 'Spherical-cap bubbles'. Annual Review of Fluid Mechanics (1973), 5, 79.

19. HABERMAN, W.L. and MORTON, R.K. 'David Taylor model basin report. U.S. Dept. of Naval Research'. Report No. 8021, 1953.

20. UNO, S. and KINTER, R.C. 'Effect of wall proximity on the rate of rise of single air bubbles in a quiescent liquid'. A.I. Ch. E.J. (1976), 2, 420.

21. SLAUGHTER, I. and WRAITH, A.E. 'The wake of a large gas bubble'. Chem. Eng. Sc. 23 (1968), 932.

22. MAXWORTHY, T. 'A note on the existence of wakes behind large, rising bubbles'. J. Fluid Mech. 27 (1967), Part 2, 367.

23. COPPUS, J.H.C. 'The structure of the wake behind spherical cap bubbles and its relation to the mass transfer mechanism'. Ph.D. Thesis, Eindhoven University of Technology (1977).

24. PANEMI, M. and DAVENPORT, W.G. 'Dynamics of bubbles in liquid metals: Two-dimensional experiments'. Trans. Met. Soc. AIME 245, (1969) 735.

25. DAVENPORT, W.G. BRADSHAW, A.V. and RICHARDSON, F.D. 'Behaviour of spherical cap bubbles in liquid metals'. J.I.S.I. 205 (Oct. 1967), 1034.

26. GUTHRIE, R.I.L. and BRADSHAW, A.V. 'Behaviour of large bubbles rising in molten silver'. Trans. A.I.M.E. (1969), 245, 285.

27. MINTO, R. and DAVENPORT, W.G. 'Entrapment and floatation of matter in molten slags'. Trans. I.M.M. (Sect. C), (1972), 81, C36.

28. WEBER, M.E. 'The effect of surface active agents on mass transfer from spherical cap bubbles'. Chem. Eng. Sci. (1975), 30, 1507.

29. ROBERTSON, D.G.C., CONOCHIE, D.S. and CASTILLEJOS, A.H. 'Model studies on gas and solid injection and related phenomena in liquid metal baths'. 2nd Conf. on Injection Metallurgy (SCANINJECT II), Lulea, Sweden (1980), 4.

30. CONOCHIE, D.S.. and ROBERTSON, D.G.C. 'Ternary interfacial energy diagram'. Trans. I.M.M. 89 (1980), C61.

31. ENGH, T.A., SANDBERG, H., HULTKVIST, A. and NORBERG, L.G. 'Si deoxidation of steel by injection of slags with low SiO_2 activity'. Scan. J. Met. 1, (1972), 103.

32. WIAFE, J.E. 'The behaviour of third phase in rising gas bubbles in liquid metals'. M.Sc. (Eng.) Thesis, Imperial College, Univ. of London, (1980).

33. IRONS, G. and GUTHRIE, R.I.L. 'The kinetics of molten iron desulphurization using magnesium vapour'. Met. Trans. B. 12B, (1981), 755.

34. ALCOCK, C.B. and BELFORD, T.N. 'Thermodynamics and solubility of oxygen in liquid metals from E.M.F. measurements involving solid electrolytes'. Trans. Faraday Soc. 60 (1964), 822.

35. CONOCHIE, D.S. and ROBERTSTON, D.G.C. 'Behaviour of third phase produced in gas bubble-liquid reactions'. Trans. I.M.M. 89, (1980), C54.

36. SHUNK, F.A. 'Constitution of binary alloys'. 2nd edition. McGraw-Hill, New York (1958).

37. MELLOR, J.W. 'A comprehensive treatise on inorganic and theoretical chemistry', vol. VII, Longman, London (1970).

38. KUBASCHEWSKI, O. and HOPKINS, B.E. 'Oxidation of metals and alloys', 2nd edition. Butterworths, London (1962).

39. KOFSTAD, P. 'High temperature oxidation of metals'. Wiley (1966).

40. STEVENSON, D.A. and WULFF, J. 'Liquid-solid phase distribution studies in systems iron-lead, cobalt-lead, chromium-tin and nickel-silver'. Trans. A.I.M.E. (1961), 221, 271.

41. WORNER, H.W. 'The determination of oxygen in lead and some lead alloys'. J. Inst. Metals, 66 (1940), 131.

42. TASKINEN, A. 'Thermodynamics and solubility of oxygen in liquid lead'. Scan. J. Metall.8, (1979), 185.

43. RICHARDSON, F.D. and WEBB, L.E. 'Oxygen in molten lead and the thermodynamics of lead oxide-silica melts'. Trans. Instn. Min. Metall. 64, (1955), 529.

44. JACOB, K.T. and JEFFES, J.H.E. 'Thermodynamics of oxygen in liquid copper, lead and copper-lead alloys'. Trans. Instn. Min. Metall. 80, (1971), C32.

45. SZWARC, R, OBERG, K.E. and RAPP, R.A. 'The diffusivity and solubility of oxygen in liquid lead from electrochemical measurements'. High Temperature Sci. 4, (1972), 347.

46. OTSUKA, S. and KOZUKA, Z. 'Activities of oxygen in liquid lead and antimony from electrochemical measurements'. Met. Trans. B, 10B, (1979), 565.

47. OTSUKA, S. and KOZUKA, Z. 'Further studies on the activities of oxygen in liquid lead and antimony by a modified coulometric titration method'. Met. Trans. B. 12B (1981), 616.

48. CHARETTE, G.G. and FLENGAS, S.N. 'Thermodynamic properties of the oxides of Fe, Ni, Pb, Cu and Mn by EMF measurements'. J. Electrochem. Soc. 115, (1968), 796.

49. BRADHURST, D.H. and BUCHANAN, A.S. 'The surface properties of liquid lead in contact with uranium dioxide'. J. Phys. Chem. (1959), 63, 1486.

50. TAKENOUCHI, T., SUZIKI, K. and HARA, S. 'Effect of slag composition on the desulphurization and dephosphorization of molten steel'. Trans. I. and S. Inst. Japan 82, (1980), C54.

51. ZUNKEL, A.D. and LARSON, A.H. 'Slag-metal equilibria in the Pb-PbO-Sb_2O_3 system'. Trans. Met. Soc. A.I.M.E. 239 (1967), 473.

52. EMICKE, K., HOLZAPFEL, G. and KNIPRATH, E. 'Lead refining at Norddentsche Affinerie'. AIME World Symposium on Mining and Metallurgy of Lead and Zinc Eds.C.H. Cotterill and J.M. Cigan II (1970), 873.

53. DAVEY, T.R.A. 'The physical chemistry of lead refining'. Lead-Zinc-Tin 1980, Eds. Cigan et al, 477.

54. LEROY, J.L., LENOIR, P.J. and ESCOYEZ, L.E. 'Lead smelter operations at N.V. Metallurgie Hoboken S.A.' AIME World Symposium on Mining and Metallurgy of Lead and Zinc. Eds. C.H. Cotterill and J.M. Cigan, II, (1970), 873.

55. PASCHEN, P. and WINTERHAGEN, H. 'Die Raffination von Blei mit Ätznatron'. Erzmetall. (1968), 21, 14.

56. ARANDA FORNO, S.B. 'Thermodynamics of polyanionic melts with particular reference to sodium systems'. Ph.D. Thesis, Imperial College, Univ. of London (1976).

57. DOUGILL, S.B. and JEFFES, J.H.E. 'Enthalpies of reaction of oxides of tin, antimony, bismuth, arsenic and lead with liquid caustic soda'. Trans. I.M.M. 89, (1980), C37.

58. GRANGE, C. and HEERMAN, L. 'Monitoring of impurities in molten lead by e.m.f. measurements. Application to the Harris process of lead refining'. J. Appl. Electrochem. 4, (1974), 279.

59. BEHL, M., GERLACH, J. and PAIVLER, F. 'Zur kinetik des Harris-Verfahrens'. Erzmetall. (1968), 21, 411.

60. LAUTERBACH, H. 'Beiträge zur bleiaffination nach dem Harris-Verfahren'. Metall. und Erz (1931), 28, 317.

61. McCLINCY, R.J. and LARSON, A.H. 'Activity of Sb_2O_3 in PbO-Sb_2O_3 and PbO-SiO_2-Sb_2O_3 slags'. Trans. Met. Soc. A.I.M.E., 245 (1969), 23.

62. RAHMEL, A. and KRÜGER, H.J. 'Solubility of water in molten caustic soda in the temperature range 350-500°C'. Z. Phys. Chem. Neue Folge, Bd. 55, S25-32 (1967).

63. WILLIAM, D.D., GRAND, J.A. and MILLER, R.R. 'The reactions of molten NaOH with various metals'. J. Amer. Chem. Soc. 78 (1956), 5150.

64. NEWMAN, R.N., SMITH, C.A. and SMITH, R.J. 'The corrosion of steels in molten sodium hydroxide'. J. Electrochem. Soc. 124, No. 8, (1977), 1247.

65. ARCHIBALD, T.F. and GRACE, R.E. 'The oxidation of liquid lead'. Trans. Met. Soc. AIME, (Oct. 1958), 658.

66. CONOCHIE, D.S., EBIOGWU, C. and ROBERTSON, D.G.C. 'Oxygen solubility inmolten lead'. Trans Inst. Min. Metall. Sect. C. (March 1984), C45.

67. WEBER, E. and BALDWIN, Jr. W.M. 'Scaling of lead in air'. J. Metals (August 1952), 854.

68. BANDYOPADHYAY, G.K. and RAY, H.S. 'Kinetics of oxygen dissolution in molten lead'. Met. Trans. 2 (Nov. 1971), 3055.

69. ROBERTSON, D.G.C, DEO, B. and OHGUCHI, S. 'Multicomponent mixed-transport-control theory for kinetics of coupled slag/metal and slag/metal/gas reactions: Application to desulphurization of molten iron'. Ironmaking and Steelmaking (1984), 11, 41.

70. POGGI, D., MINTO, R. and DAVENPORT, W.G. 'Mechanisms of metal entrapment in slags'. J. of Metals (Nov. 1969), 40.

71. URQUHART, R.C. and DAVENPORT, W.G. 'Stabilization of metal-in-slag emulsions'. J. of Metals (June 1970), 36.

72. WEAST, R.C. (Ed.) 'C.R.C. Handbook of Chemistry and Physics'. 63rd edition. G.R.C. Press, Cleveland, Ohio, (1982-83).

73. ALCOCK, C.B. (Ed.). 'Electromotive force measurements in high-temperature systems'. I.M.M. London (1968).

74. KUBASCHEWSKI, O. and ALCOCK, C.B. 'Metallurgical thermochemistry'. 5th edition. Pergamon Press, Oxford (1979).

75. SMITHELLS, C.J. 'Metals Reference Book'. 6th edition. Butterworths, London (1983).

76. HULTGREN, R. et al. 'Selected values of the thermodynamic properties of binary alloys'. Am. Soc. Metals, Metals Park (1973).

77. JANAF Thermochemical Tables, Dow Chemical Co., Midland, Michigan (1970).

78. HANSEN, M. 'Constitution of binary alloys'. 2nd edition. McGraw-Hill, New York (1958).

79. JANZ, G.J. (Ed.). 'Molten salts handbook'. Academic Press (1967).

80. BARD, A.J. (Ed.). 'Encyclopedia of electrochemistry of the elements'. Vol. X: Fused salt systems. Plambeck (1976).

81. PERRY, R.H. et al. 'Chemical engineers handbook'. 5th edition. McGraw-Hill, New York (1973).

82. ELLIOT, J.F. and GLEISER, M. 'Thermochemistry for steelmaking'. Vol. 1, Pergamon (1960).

83. BIRD, R.B., STEWART, W.E. and LIGHTFOOT, L.N. 'Transport phenomena'. Wiley, New York (1960).

84. CLIFT, R., GRACE, J.R. and WEBER, M.E. 'Bubbles, drops and particles'. Academic Press (1978).

85. EBIOGWU, C. 'Gas-slag-metal reactions'. Internal report, John Percy Research Group, Royal School of Mines, Imperial College, London (Oct. 1982).

86. RIDEAL, E.K. and DAVIES, J.T. 'Interfacial phenomena'. Academic Press, New York (1961).

87. GEIGER, G.H. and POIRIER, D.R. 'Transport phenomena in metallurgy'. Addision-Wesley (1980).

88. SZEKELY, J. 'Fluid flow in metals processing'. Academic Press (1979).

89. GASKELL, D.R. 'Introduction to metallurgical thermodynamics'. 2nd edition. McGraw-Hill (1981).

90. Powder Diffraction File, search manual alphabetical listing - inorganic compounds (1973), published by Joint Committee on Powder Diffraction Standards, U.S.A.

91. RICHARDSON, F.D. 'Physical chemistry of melts in metallurgy'. Vol. 2, Academic Press, London (1974).

APPENDICES

A-1 FLOW CALIBRATION IN THE HOTB

The flow parameters of the high temeprature open top bubble (HOTB) rig were varied by adjusting the inlet and/or the outlet flow valves of the apparatus. The inlet flow valve controlled the height of the free lead surface over the weir (weir height), while the outlet flow valve controlled the depth of the resulting open top bubble (base depth). The bubble weir height (h_w) and base depth (h_b) were measured using a specially adapted micrometer screw gauge mounted on the glass window of the apparatus (fig. A-1.1). During the measurement, the glass window was mounted loosely on the lid to allow for easy rotation of the window, depending on what measurement (weir height or base depth) was being taken.

In order to avoid the necessity to measure the flow parameters before each run, they were calibrated against particular settings on the flow control valves of the apparatus. The valve settings were measured using two 'Mercer 216' dial gauges attached to the top surfaces of the control rods. Fig. A-1.2 shows a plot of h_w as a function of the inflow valve setting. The variations of h_b with the outflow valve setting at various weir heights, is shown in fig. A-1.3.

A - Micrometer screw gauge
B - Bulb
C - 1.5V battery
D - OTB window
E - OTB weir (reference point)
F - Liquid lead level

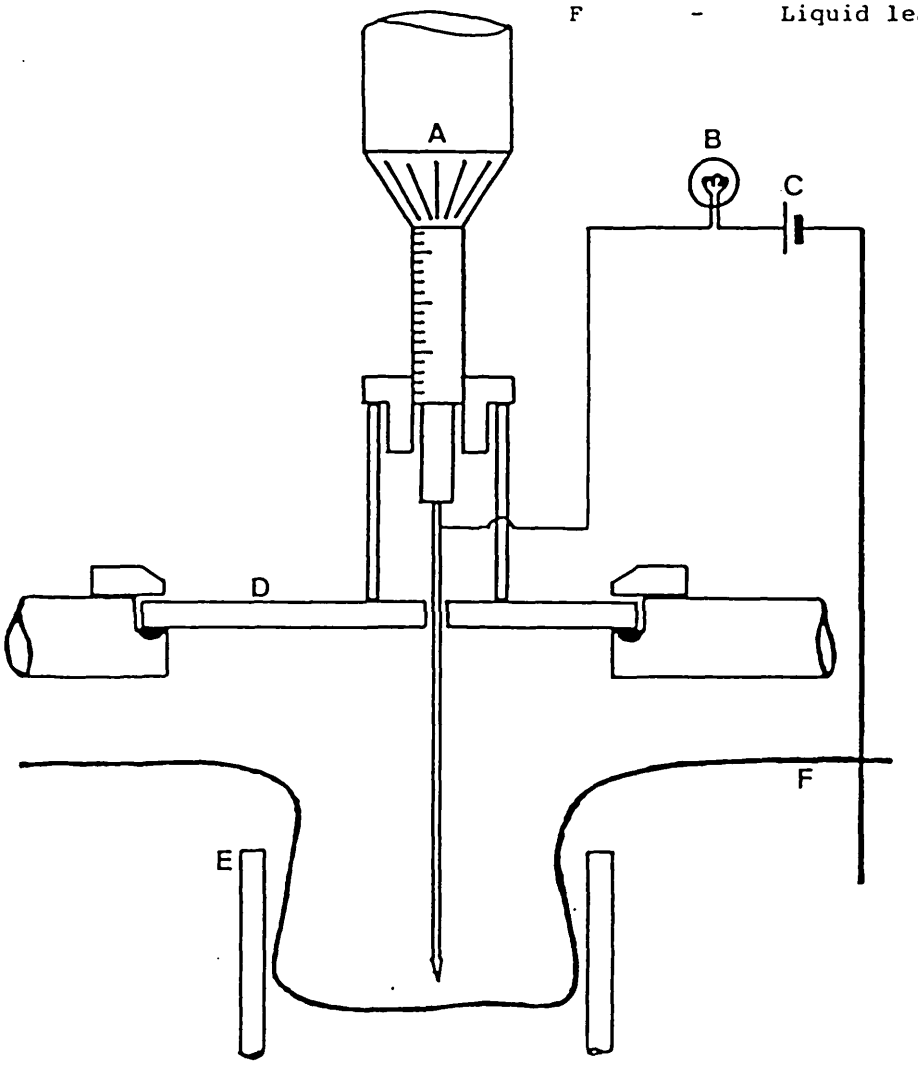

Fig. A-1.1: The arrangement for measuring weir height and base depth in the OTB.

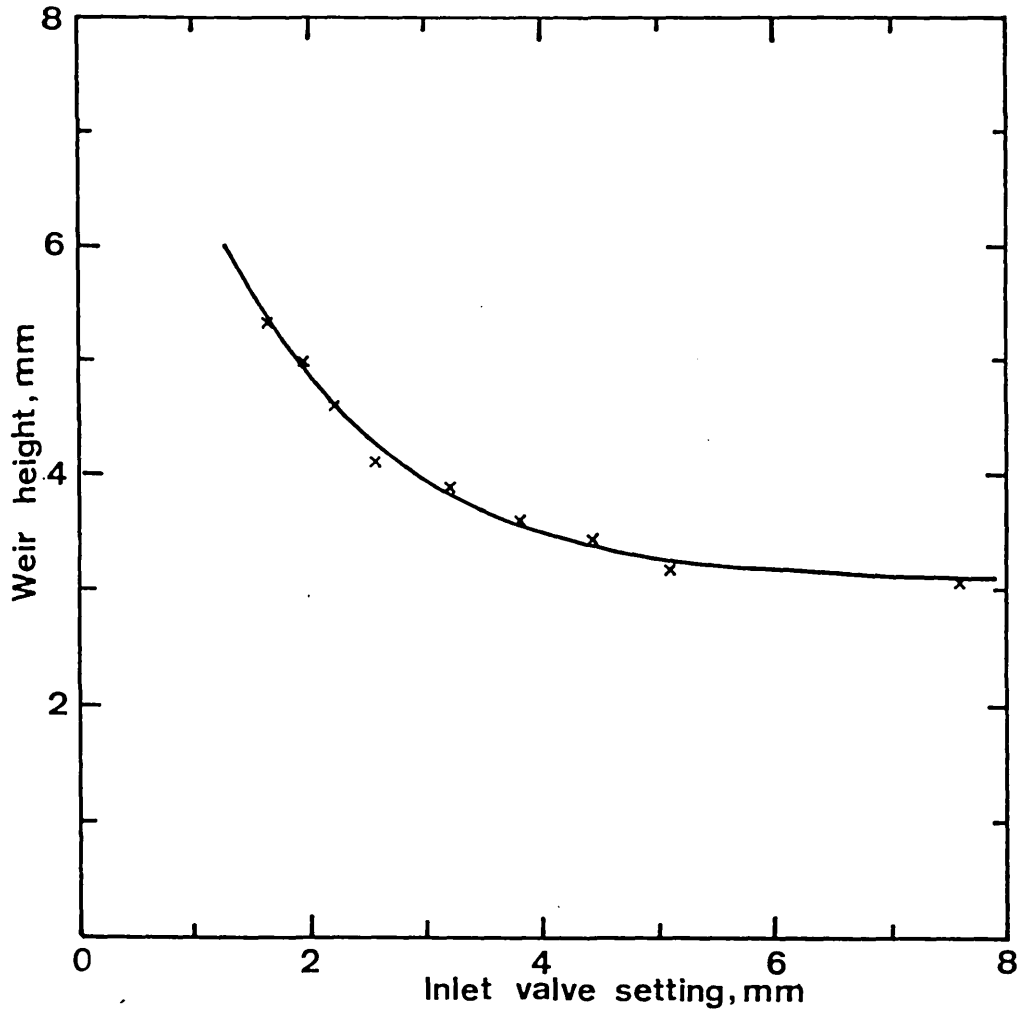

Fig. A-1.2: Flow characteristics of the HOTB - flow outlet valve fully opened.

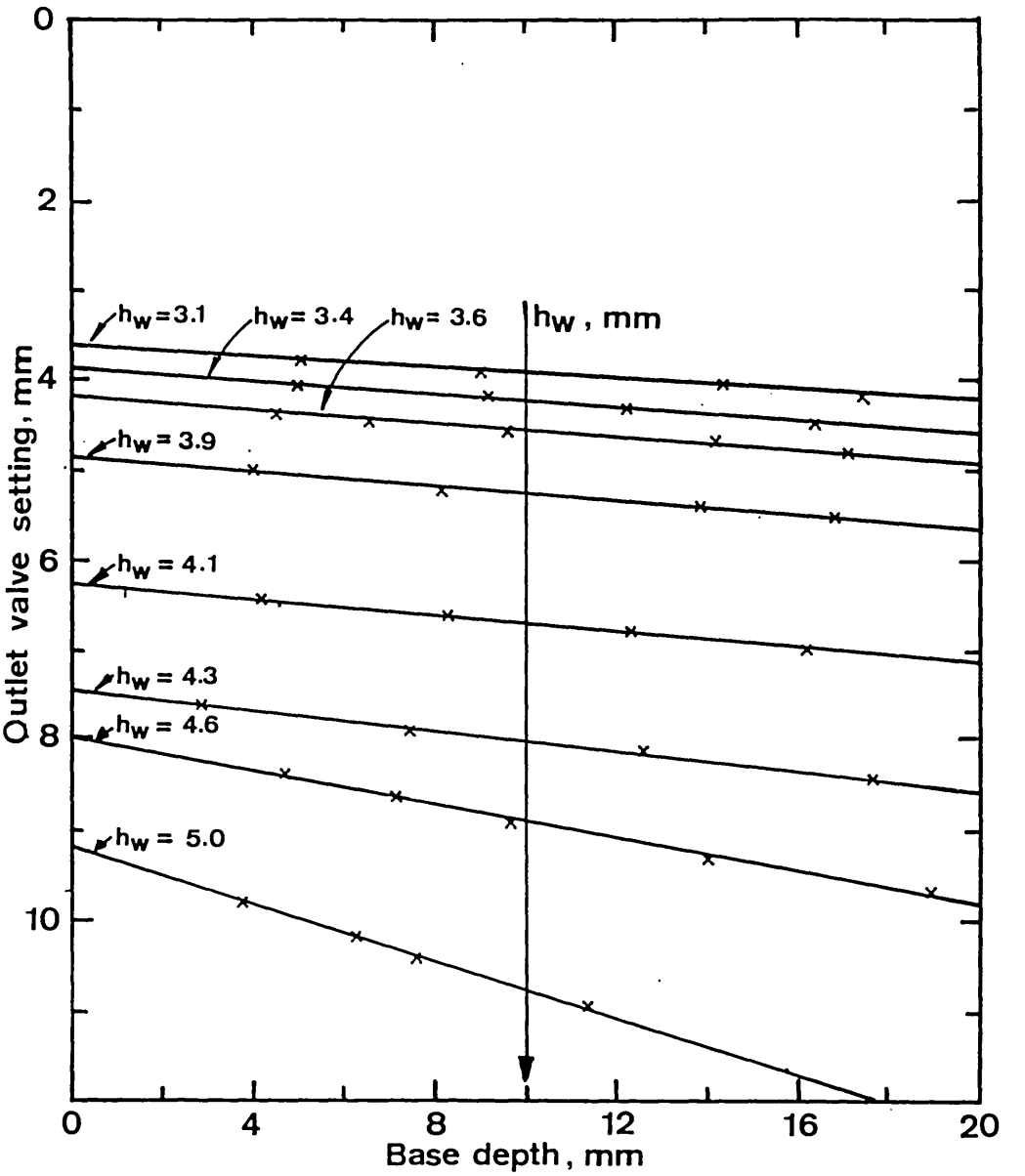

Fig. A-1.3: Flow characteristics of the HOTB.

A-2 GAS TIGHTNESS OF THE HOTB POT

The rate of gas leakage from the HOTB pot was measured. The gas outlet of the lead pot was closed and a steady flow of forming gas was directed into the pot. The manometer (fig. 2.5) measured the pressure build-up in the pot resulting from the gas flow. The final steady pressure was measured at various flow rates of the forming gas.

The results obtained (after the gas seals were changed) showed that there was a leak out of the system of 30 ml/min when the pressure in the pot was 14 cm of water above atmospheric. The main leakage occurred at the pump shaft seal. This leak rate was considered acceptable since the pot was normally operated at a pressure of about 5 cm of water above atmospheric.

A.3 GAS FURNACE DESIGN SPECIFICATIONS

The furnace was designed to operate at temperatures up to 900°C. It consisted of an alumina tube wound with 20G 'Kanthal' wire previously coiled on a 6 mm diameter mild steel mandrel. Details of the design specifications of the furnace are:

Maximum power rating	=	1500 Watts
Voltage source	=	240V AC
Total coil resistance	=	41.67 Ω
Maximum operating current	=	6.25 A
Surface area loading	=	2.77 W/cm^2
Coil length	=	96.7 cm
Stretch length of coil	=	242 cm
Tube diameter	=	55 cm

A cross-section through the furnace is shown in fig. A-3.1.

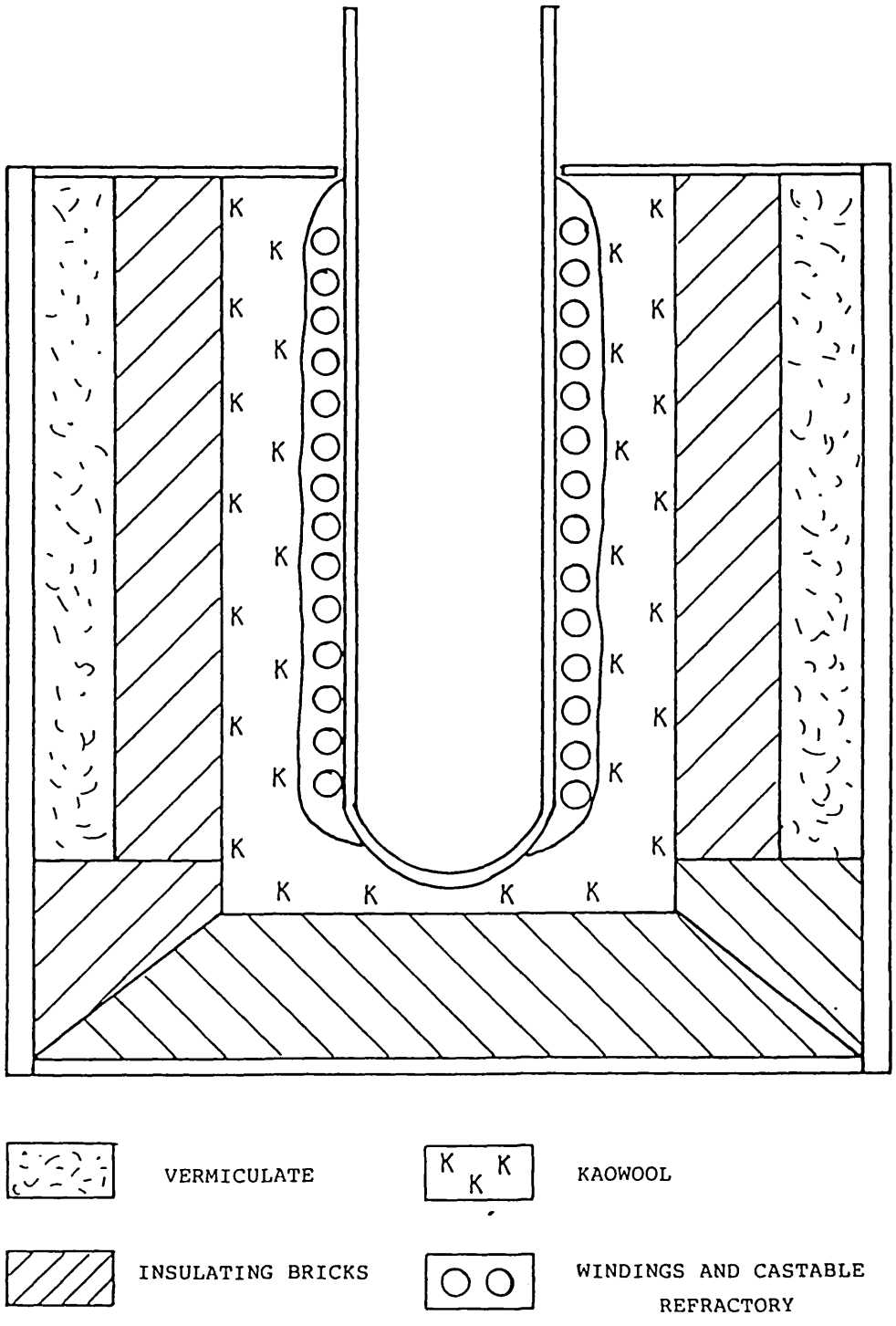

Fig. A-3.1: Furnace construction

A-4 MASS BALANCE ON $NaOH-NaNO_3$

Prior to the start of the slag addition experiments, the stability of $NaNO_3$ in the $NaOH-NaNO_3$ slags was checked at various temperatures in the region of the temperature of slag preparation. Various proportions of NaOH and $NaNO_3$ slags were added to the gold crucible and heated in a muffle furnace. The results obtained are tabulated in table A-4.A

The weight loss observed in each of the experiments was very small and may have been due to the loss of the water picked up by the highly hygroscopic caustic soda. Also, since no brown fumes (usually associated with NO_x oxides) were observed during the tests, it was concluded that the sodium nitrate did not decompose during the heating.

TABLE A-4.A

Weight loss on heating NaOH + $NaNO_3$

Experiment	Duration (min)	Temp. (^oC)	Wt of NaOH (g)	Wt. of $NaNO_3$(g)	Wt of crucible and contents (g)		Wt. loss (g)
					Before heating	After heating	
1	15	400	2.27	2.90	69.87	69.85	0.02
2	15	480	4.01	4.03	73.78	73.73	0.05
3	10	530	4.88	4.59	80.97	80.93	0.04

A-5 SLAG CORROSION TESTS

Before the start of the slag addition experiments in the lead OTB system, the slags intended for use were tested for their reactions with the mild steel container at high temperatures. Two main types of slags were considered, viz: PbO-$PbC\ell_2$ slag and NaOH slag.

A-5.1 PbO-$PbC\ell_2$ slag

The slag pellets were prepared by weighing PbO and $PbC\ell_2$ (in the weight ratio 1:2) into a nickel crucible and heating in a muffle furnace for about 2 hours at 600°C. This was to allow the constituent compounds form a melt. The liquid slag was later quenched on a flat copper plate and later broken down into smaller pellets.

The reaction of the slag with mild steel was investigated by heating 30g of the slag in a mild steel crucible containing some 250g of lead, at 550°C. The experiment was done in a forming gas atmosphere and was left to run for two days.

At the end of the experiment a massive corrosion of the mild steel crucible was observed. It was also observed that some of the $PbC\ell_2$ in the slag had vapourised and condensed on the inner surface of the water-cooled lid of the test rig, partially blocking the gas outlet. Hence the PbO-$PbC\ell_2$ system was rejected for use in the OTB apparatus.

A-5.2 NaOH slag

The reaction of caustic soda with iron was first investigated in an argon atmosphere. 5g of NaOH was heated with 150g of lead in a mild steel crucible at 500°C and later at 600°C. Each experiment lasted for two days at the end of which the crucible was removed and observed for the extent of corrosion.

The results show that at 500°C the degree of corrosion was negligible. Some patches of reddish brown oxides were

observed on the walls of the crucible. The extent of the corrosion was increased at 600°C but still significantly less than observed with PbO-$PbC\ell_2$ slag. In a later experiment in a forming gas atmosphere the extent of corrosion was even less. The caustic soda slag was hence considered safe for addition into the lead OTB pot.

A-6 X-RAY DIFFRACTION PATTERNS

	A.R.	=	As received
	B	=	Broad line
Line intensity decreases ↓	vs	=	Very strong
	s	=	Strong
	ms	=	Medium strong
	m	=	Medium
	mw	=	Medium weak
	w	=	Weak
	vw	=	Very weak
	vvw	=	Very very weak

TABLE A-6.A

Drossed slag before NaOH addition to the OTB

	d A	Int.	PbO (red)		PbO (yellow)		Pb	
	5.90	vw			5.89	6		
	5.00	vw	5.02	5				
B	3.10	vs	3.11	100				
	3.06	s			3.07	100		
	2.95	s			2.95	31		
	2.84	w					2.85	100
	2.80	vs	2.81	62				
	2.72	m			2.74	28		
	2.50	s	2.51	18				
	2.46	vw					2.48	50
	2.36	m			2.38	20		
	2.03	m	2.00	8				
	1.86	s	1.87	37				
	1.84	vw			1.85	14		
	1.79	w			1.80	14		
	1.74	vw					1.75	31
	1.71	w			1.72	15		
	1.69	w						
B	1.66	s	1.67	24				
	1.63	w			1.64	13		
	1.59	m						
	1.55	vw	1.56	6				
	1.53	vw	1.54	11	1.53	9		
	1.52	vw						
	1.48	s			1.47	11	1.49	32
	1.39	m						

TABLE A-6.B

Drossed slag after NaOH addition to the OTB

	d A	Int.	PbO (red)		Pb		α-$NaFeO_2$	
	5.36	vw					5.36	30
	5.00	vw	5.02	5				
	4.55	vw						
	4.30	vw						
	3.18	vw						
B	3.10	vs	3.11	100				
	3.05	w						
	2.84	s			2.85	100		
	2.80	s	2.81	62				
	2.62	vw					2.60	30
	2.52	vw	2.51	18				
	2.50	w					2.49	55
	2.47	m			2.48	50		
	2.20	ms					2.20	100
	2.00	vw	2.00	8				
	1.86	s	1.87	37				
	1.74	w			1.75	31		
B	1.66	s	1.67	24				
	1.52	w					1.51	40
	1.48	m			1.49	32		
	1.42	vw			1.43	9		
	1.39	m						

TABLE A-6.C

$NaOH-NaNO_3$ (3:1) Pellet

	d A	Int.	$NaOH.H_2O$		$NaNO_3$		NaOH(A.R)	
	5.90	vs	5.90	80			5.90	vs
	3.20	m						
	3.02	ms			3.03	100		
B	2.95	s	2.95	100			2.95	vs
	2.70	s	2.70	80			2.69	ms
	2.64	m					2.65	w
	2.50	s	2.51	70			2.50	m
	2.43	m					2.43	m
B	2.32	vs			2.31	25	2.33	vs
B	2.27	ms	2.27	40			2.26	ms
	2.08	m			2.12	10		
B	1.90	ms	1.91	30	1.90	16	1.90	m
	1.88	w	1.88	30	1.88	5	1.87	w
	1.86	w					1.86	w
	1.83	vw						
	1.79	w					1.79	m
	1.69	vw	1.70	10			1.69	ms
	1.66	vw						
	1.64	vw	1.64	10				
	1.63	w						

TABLE A-6.D

Sample taken from OTB after $NaOH-NaNO_3$ addition (Run S_{17})

	d A	Int.	PbO(red)		$NaOH.H_2O$		NaOH(A.R)	
	5.9	m					5.90	vs
	5.5	vs						
	4.9	m						
	4.2	vw						
	3.65	w						
	3.20	w						
B	3.10	vs	3.11	100				
	3.05	m						
B	2.95				2.95	100	2.69	vs
	2.88	m						
	2.80	s	2.81	62				
	2.75	ms						
	2.70	s			2.70	80	2.69	ms
	2.64	w					2.65	w
	2.49	w			2.51	70	2.50	m
B	2.35	vs					2.33	vs
	2.25	w			2.27	40	2.26	ms
	2.20	w					1.9	m
	2.16	m						
	1.87	w	1.87	37	1.88	30	1.87	w
	1.85	vw						
	1.81	w						
	1.79	vw					1.79	m
B	1.67	m	1.67	24			1.69	ms
B	1.65	m			1.64	10		

TABLE A-6.E

$NaNO_3$ Pellet

	d A	Int.	$NaNO_3$ Index		$NaNO_3$ (A.R)	
	3.88	m	3.89	6	3.87	ms
	3.02	vs	3.03	100	3.01	vs
B	2.80	m	2.81	16	2.79	s
	2.52	ms	2.53	10	2.53	s
	2.30	s	2.31	25	2.30	vs
	2.12	ms	2.12	10	2.11	s
	1.94	w	1.95	4	1.94	w
B	1.90	s	1.90	16	1.89	s
	1.84	ms	1.88	8	1.87	s
	1.64	ms	1.65	4	1.64	s
	1.62	m	1.63	4	1.62	s
	1.54	w	1.54	2	1.54	w
	1.53	m	1.52	1	1.52	vw
	1.49	m	1.50	2	1.50	w
	1.48	m	1.48	2	1.46	m
B	1.46	m	1.46	4	1.46	ms
B	1.395	vw	1.40	2	1.395	w
	1.390	vw				

TABLE A-6.F

Sample taken from OTB after $NaNO_3$ addition (Run S_{18})

	d A	Int.	PbO(red)		Pb		Na_2O	
	5.50	w						
	3.32	vw						
	3.20	w					3.19	40
B	3.10	vs	3.11	100				
	2.95	m						
	2.84	w			2.85	100		
B	2.79	vs	2.81	62				
	2.76	w					2.76	40
	2.74	w						
	2.68	m						
	2.62	vw						
	2.50	m	2.51	18				
	2.46	w			2.48	50		
	2.33	m						
	2.15	vw						
	2.02	w						
	2.00	vw	2.00	8				
B	1.97	s					1.95	100
	1.86	s	1.87	37				
	1.77	vw						
	1.74	vw			1.75	31		
	1.66	s	1.67	24			1.67	10
	1.64	vw						
	1.57	vw						
	1.54	ms	1.54	11				
	1.53	ms						
	1.50	vw			1.49	32		
	1.39	s					1.39	30

TABLE A-6.G

Sodium Antimonate Slag (Run R_2)

d A	Int.	Na_3SbO_4		$NaOH.H_2O$		NaOH(A.R.)		NaOH Pellet	
6.60	m	6.61	60						
5.90	vw			5.90	80	5.90	vs	5.90	s
5.50	vs	5.48	85						
4.20	w	4.21	45						
4.03	w	4.04	45						
3.75	m	3.75	55						
2.95	m			2.95	100	2.95	vs	2.95	ms
2.90	vw	2.91	18						
2.78	ms	2.77	30					2.80	ms
2.75	m	2.74	30						
2.72	m			2.70	80			2.71	w
2.68	s					2.69	ms		
2.66	s	2.67	55			2.65	w		
2.58	vw								
2.55	vw	2.55	25						
2.52	vw			2.51	70	2.50	m	2.5	m
2.36	vw								
2.33	s					2.33	vs	2.34	vs
2.31	vs	2.31	100						
2.27	ms	2.28	55						
2.25	vw			2.27	40	2.26	ms	2.25	m
2.17	vw							2.15	w
2.15	vw							2.13	vw
1.92	vw					1.90	m	1.91	ms
1.87	vw			1.88	30	1.87	w	1.87	vw
1.81	w					1.79	m	1.80	w
1.69	m					1.69	ms	1.69	s
1.66	m	1.67	45						
1.64	m							1.645	ms
1.63	m							1.62	w
1.58	w	1.58	30						